General Plasma Physics II: Magnetohydrodynamics

H. Ji

Department of Astrophysical Sciences, Princeton University, 4 Ivy Lane, Princeton, 08544, New Jersey, U.S.A.

E-mail: hji@princeton.edu

Abstract

This is a series of lecture notes from General Plasma Physics (GPP) II (course code AST552) taught by Professor Hantao Ji at Princeton University over 14 years during the 2007-2023 period.

MHD (*10/11/24*)

1 Magnetohydrodynamic (MHD) Models

We begin with a few simple but important clarifications:

MHD: It is obviously incorrect to call anything "hydro" when there is not even a single water molecule present. This comes from a purely historical reason: the plasma fluid models that we are going to learn about are at least partially based on fluid dynamics, which started and matured (successfully!) much earlier than modern plasma physics. In this sense, we will be also learning, to a lesser depth, about the extension of fluid dynamics that includes plasma effects, notably the electric conductivity properties. The correct name should be "Magnetofluiddynamics", or MFD, which is unfortunately rarely used. I note that the term "hydromagnetic" is being used synonymously.

Units: This is another matter that often goes with convention. Over the years, different subareas of each field gradually evolved towards one particular system. In plasma physics, experimentalists tend to use SI while theoreticians tend to use Gaussian. Heliophysics, a relatively new term that includes solar physics, solar wind physics, and magnetospheric space physics, uses SI while astrophysics, including both observation and theory, uses Gaussian regardless. We may choose whatever unit system that we prefer, but we still need to know how to convert from one to the other. Experimentally, there are additional conventions that are being used, such as Torr versus Pascal versus psi versus bar as units for pressure. A standard atmosphere of pressure is 760 Torr or 1.013×10^5 Pascals which is an SI unit, $\mathrm{N/m^2}$. The other unit, bar, is not an SI unit and is defined as 10^5 Pa, giving a standard atmospheric pressure to be slightly over 1 bar.

Constructing Plasma Fluid Models: There are generally two approaches to construct fluid equations for plasma. The first is to follow the hierarchy of plasma models, which will be discussed immediately below. This approach is rigorous (and often tedious) by following first principles. However, it is clear about the assumptions needed for each step. In principle, the consequences of each assumption can be quantified if needed. In reality, however, such consequences or implications are often ignored in favor of simplicity and convenience, which is understandably preferred.

The second approach is based on the continuum hypothesis, which has been hugely successful for fluid dynamics in the collisional limit, where the discreteness of particles can be safely ignored. Here, microscopic origins of macroscopic properties, such as pressure and volume, are not considered. As such, the construction is rather heuristic in nature. Kinetic theory of gases, in contrast, reveals links between microscopic and macroscopic properties, forming the foundation of modern statistical mechanics.

In some senses, plasma models resemble gas models but with inherently richer and deeper physics, involving electromagnetism with wide applications including fusion, astrophysics, and material processing. Regardless of

the method of constructing plasma models, experimental and observational verification or confrontation is always the key to a successful model.

1.1 Hierarchy of Plasma Models

Albert Einstein once famously said, "Everything should be made as simple as possible, but not simpler." This also speaks for plasma models. A hierarchy of plasma models has been developed and applied successfully. Finding the simplest possible model to describe a particular process is always *an art*, but typically one starts with a simple model by adding one ingredient at a time until capturing the necessary feature of that process. What's the initial simple model? Typically, we start with MHD. Below are plasma models in order of increasing simplicity and greater assumptions.

1. Exact microscopic descriptions (Chap.7 in Krall and Trivelpiece, 1973):
   - Klimontovich(-Dupree) equation (Chap. 4 in Klimontovich, 1967; Dupree, 1963),

$$N(\boldsymbol{x}, \boldsymbol{v}, t) = \sum_i \delta\left[\boldsymbol{x} - \boldsymbol{x}_i(t)\right] \delta\left[\boldsymbol{v} - \boldsymbol{v}_i(t)\right] \tag{1}$$

$$\frac{dN}{dt} = 0. \tag{2}$$

   - Distribution function, F, treating all particles statistically and satisfying the Liouville equation,

$$\frac{dF}{dt} = 0. \tag{3}$$

   - Reduced distributions are defined as integrated over coordinates of all but one, two, three, etc. dimensions to obtain one-particle distribution functions, $f_1(\boldsymbol{x}_1, \boldsymbol{v}_1, t)$, two-particle distribution functions, $f_{1,2}(\boldsymbol{x}_1, \boldsymbol{v}_1, \boldsymbol{x}_2, \boldsymbol{v}_2, t)$, and so on. The one-particle distribution does not contain information on interactions between particles. The two-particle distribution contains information on binary interactions only. The three-particle distribution contains information on three-particle interactions, and so on.
   - BBGKY hierarchy (Bogoliubov, Born, Green, Kirkwood, Yvon) in statistical physics for a system with a large number of interacting particles. The one-particle distribution is decided by the two-particle distribution, which is decided by the three-particle distribution, etc., forming an infinite chain of equations for reduced distribution functions.
   - Covered by AST554: Irreversible Processes in Plasma.

2. Boltzman/Vlasov Equations:
   Boltzmann equation: evolution of the one-particle distribution $f_1 \equiv f$ with

binary interactions (collisions):

$$\frac{df}{dt} = \frac{\partial f}{\partial t} + \boldsymbol{v} \cdot \frac{\partial f}{\partial \boldsymbol{x}} + \frac{q}{m} (\boldsymbol{E} + \boldsymbol{v} \times \boldsymbol{B}) \cdot \frac{\partial f}{\partial \boldsymbol{v}} = \left(\frac{\delta f}{\delta t} \right)_{\text{coll}} \tag{4}$$

Vlasov equation: evolution of the one-particle distribution $f_1 \equiv f$ *without* binary interactions (collisions):

$$\frac{df}{dt} = \frac{\partial f}{\partial t} + \boldsymbol{v} \cdot \frac{\partial f}{\partial \boldsymbol{x}} + \frac{q}{m} (\boldsymbol{E} + \boldsymbol{v} \times \boldsymbol{B}) \cdot \frac{\partial f}{\partial \boldsymbol{v}} = 0 \tag{5}$$

3. Drift-kinetic/Gyro-kinetic Models: approximation based on guiding center motion or charge ring motion.
4. Multi-fluid Models: approximation based on fluid descriptions for each species.
5. Single fluid (MHD) Models: approximation based on a combined one fluid description.
6. Mean-field Theory/Models: approximation based on *averaged* fluid quantities over a certain spatial or temporal scale.

1.2 Multiple Scale Nature of Plasma Physics

Magnetized plasmas have a wide range of scales, and usually temporal scales have their counterparts in spatial scales. Ordering spatial scales from large to small:

- Global system dynamics. Typically phenomena on this scale can be described by the MHD model, but not always, such as low-temperature plasmas which may require kinetic models from the outset.
- Local thermal ion (electron) kinetic physics. When magnetized, ion (electron) kinetic physics are in the scale of ion (electron) gyro-radius or ion (electron) skin depth, $d_i \equiv c/\omega_{\text{pi}} = V_A/\Omega_i$ ($d_e \equiv c/\omega_{\text{pe}} = V_A/\Omega_e$), which is the information propagation distance by Alfvén speed in one ion (electron) cyclotron time.
- Debye-scale physics. Above the Debye length, λ_D, quasi-neutral plasma physics applies while below λ_D non-neutral plasma physics applies (Davidson, 2001).
- Atomic scale physics. Some atomic physics processes are important for plasma physics such as ionization/recombination, inelastic processes of atoms including excitation and photon emission, and high-energy particle physics processes like pair plasma (electron positron pairs) creation.

One special case is energetic particles (much more energetic than thermal energies) which can experience multiple scales along their trajectory. Examples include cosmic ray particles in astrophysics and fusion products in laboratory fusion reactors. They are so energetic that they can directly participate in global scale physics, i.e. to cause MHD instabilities to grow or to be influenced

by MHD scale processes directly. Some of these will be covered later in this course.

In magnetized plasmas, the behavior of the magnetic field is part of plasma physics. (In fact, plasmas are almost always magnetized whenever hot and large enough — the so-called "dynamo" problem of plasmas. This will also be covered later in the course.) The magnetic field has some inherent multiscale properties that we will see soon. Locally, they can form X-points or O-points, 3D null-points, separatrices, and separators. Globally, magnetic flux is conserved in ideal MHD, as are magnetic helicity and magnetic topology. Magnetic field lines can form global flux surfaces, and when they don't, they can be stochastic. Some of these will be covered.

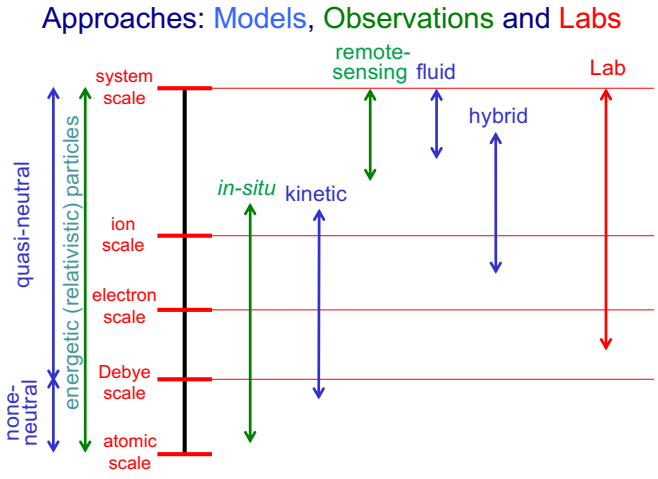

Fig. 1 Multiple scale nature of *magnetized* plasma physics. Scales range from atomic, Debye, electron, ion, and system (MHD) scales. Different approaches cover a range of scales, but none covers all scales.

Currently, no research approach can study the physics of all scales. This is illustrated in Fig. 1. Fluid models, such as MHD models covered here, can be successful in modeling global phenomena, while kinetic models, such as drift-kinetic models or full-particle models, can adequately describe physics on kinetic scales. Sometimes, "hybrid" models, in which electrons are treated as fluid while ions are treated kinetically, can cover much larger scales than thermal ion kinetic scales at the expense of electron kinetic physics. Needless to say, each of these models has necessary simplifying assumptions to be productive, and sometimes these simplifying assumptions are intentional (as in Einstein's quote above) to reveal the underlying essential physics of a particular phenomenon. Nonetheless, because of these assumptions, we can't be too faithful for these models to accurately reproduce every feature of any particular phenomenon.

In space physics and astrophysics, remote sensing technology typically can resolve only global fluid scales while satellites in Earth's magnetosphere or solar wind provide *in-situ* local measurements on ion or electron kinetic scales, with limited information on larger scales. Due to the similar scales that they cover, remote-sensing observations are often modeled by fluid models while *in-situ* measurements are modeled by kinetic models. In contrast, laboratory experiments can advantageously provide both global and local measurements simultaneously, but they are limited by achievable parameters due to available hardware or resources. As such, one of the exciting aspects of plasma physics is that the same phenomena or processes can be created on totally different scales – temporal or spatial – one can be extremely small or short occurring in nanoseconds/micrometers, one can be extremely large and long spanning light years, or in between these extremes, one can play out in human size! Combining the strengths of each of these approaches can tell a very convincing story.

Typically, the protocol to investigate a new phenomenon in either fusion or astrophysical multiscale plasmas is to begin with its global properties using hydrodynamics or magnetohydrodynamics. In fusion plasmas, an MHD equilibrium is established first in a magnetic configuration, such as tokamak or stellarator, followed by testing its MHD stability against various global limits, such as achievable plasma beta or resistive wall time. After passing these "checkups", it is then meaningful to investigate kinetic transport properties, such as (neo)classical transport due to Coulomb collisions or anomalous transport due to drift wave turbulence. This order of protocol follows the logic that equilibrium and global stability are important on short time scales, typically Alfvén time scales, while transport time scales are much longer. For example, the former time scales are typically shorter than one millisecond while the latter time scales or confinement time are typically long, such as 100 milliseconds in hot tokamaks. Other considerations, such as auxiliary heating or power extraction, should be taken into account whenever needed. For simplicity, often some of these steps can be skipped by assuming an idealized configuration, such as slab geometry where a local piece of plasma is considered, but with the understanding that some important physics may be absent due to the limiting assumptions.

A similar protocol can be drawn in astrophysics. Global structures, such as stars, accretion disks, or jets, need to be established first, followed by testing their global hydrodynamic or MHD stability against processes such as convection or shear instability. Then microscopic processes, such as kinetic properties in shocks or dissipation in turbulence, are investigated. During this process, there are other considerations such as observational limitations in the interpretation of the indirectly measured quantities. As in fusion, often idealized configurations are assumed to skip some of these steps to focus on a particular subject of interest, but with the understanding of possible missing physics.

1.3 Constructing Plasma Fluid Equations

Following the hierarchy of plasma models as discussed in Sec. 1.1, macroscopic quantities are obtained by *taking moments* of the Boltzmann equation, Eq. (4), to remove the dependence on velocity $\boldsymbol{v}$,

$$\langle g(\boldsymbol{x},t)\rangle \equiv \int g(\boldsymbol{x},\boldsymbol{v},t) f(\boldsymbol{x},\boldsymbol{v},t) d\boldsymbol{v}, \tag{6}$$

which effectively calculates any quantity (can be a vector or a general tensor), g, with *weighted* contributions based on the distribution f at each location and time. Taking $g = 1$ yields the macroscopic particle density,

$$n(\boldsymbol{x},t) = \int f(\boldsymbol{x},\boldsymbol{v},t) d\boldsymbol{v}, \tag{7}$$

while taking $g = m\boldsymbol{v}$ yields the momentum density,

$$m\langle \boldsymbol{v}(\boldsymbol{x},t)\rangle) = m\int \boldsymbol{v} f(\boldsymbol{x},\boldsymbol{v},t) d\boldsymbol{v}, \tag{8}$$

leading to the macroscopic fluid velocity $\boldsymbol{V}(\boldsymbol{x},t) = \langle \boldsymbol{v}(\boldsymbol{x},t)\rangle / n(\boldsymbol{x},t)$.

When $g = \frac{1}{2} m (\boldsymbol{v}-\boldsymbol{V})(\boldsymbol{v}-\boldsymbol{V})$, *i.e.* the velocity spread after the frame shift to $\boldsymbol{V}$, the corresponding moment of g becomes the pressure tensor,

$$\frac{1}{2} m \langle (\boldsymbol{v}-\boldsymbol{V})(\boldsymbol{v}-\boldsymbol{V})\rangle = p\boldsymbol{I} + \boldsymbol{\Pi}, \tag{9}$$

where p is the *isotropic* macroscopic pressure, $\boldsymbol{I}$ is a unit tensor, and $\boldsymbol{\Pi}$ is the off-diagonal pressure tensor. Thus, macroscopic temperature in *units of energy* can be defined as $T(\boldsymbol{x},t) = p(\boldsymbol{x},t)/n(\boldsymbol{x},t)$. Note that the diagonal components of the pressure here can be *anisotropic* with respect to the magnetic field, *i.e.* pressure in the parallel direction of the field lines can be different from pressure in other directions, $p_\parallel \neq p_\perp$. For simplicity, we take the pressure to be isotropic here.

Now the following MHD equations can be readily derived,

$$\frac{\partial n}{\partial t} + \boldsymbol{\nabla}\cdot(n\boldsymbol{V}) = S, \tag{10}$$

$$mn\left(\frac{\partial}{\partial t} + \boldsymbol{V}\cdot\boldsymbol{\nabla}\right)\boldsymbol{V} - qn(\boldsymbol{E} + \boldsymbol{V}\times\boldsymbol{B}) + \boldsymbol{\nabla}\cdot\boldsymbol{P} = \boldsymbol{R}, \tag{11}$$

$$\frac{3}{2}\frac{\partial p}{\partial t} + \boldsymbol{\nabla}\cdot\left(\frac{3}{2}p\boldsymbol{V}\right) + \boldsymbol{P}:\boldsymbol{\nabla}\boldsymbol{V} + \boldsymbol{\nabla}\cdot\boldsymbol{q} = Q, \tag{12}$$

where $S = \int \left(\frac{\delta f}{\delta t}\right)_{\text{coll}} d\boldsymbol{v}$ is the plasma source via *e.g.* ionization or recombination due to collisions. $\boldsymbol{R} = \int m(\boldsymbol{v}-\boldsymbol{V})\left(\frac{\delta f}{\delta t}\right)_{\text{coll}} d\boldsymbol{v}$ is the frictional force and

$Q = \int \frac{1}{2} m \left(\boldsymbol{v} - \boldsymbol{V}\right)^2 \left(\frac{\delta f}{\delta t}\right)_{\text{coll}} d\boldsymbol{v}$ is the heating due to collisions. $\boldsymbol{\nabla} \cdot \boldsymbol{P}$ includes both of the pressure force and the viscous force (to be discussed later) and $\boldsymbol{P} : \boldsymbol{\nabla} \boldsymbol{V}$ is the work done on or by the fluid.

The terms due to Coulomb collisions can be expressed in fluid quantities in principle if distribution functions are known, but their derivations can be complicated. For local Maxwellians, they have been worked and summarized by Braginskii (1965); also see more concise summaries (Wesson, 2011, p.84) and (Kulsrud, 2005, Ch.8).

The continuity equation, Eq. (10), determines the evolution of density n, but it requires information on the velocity $\boldsymbol{V}$, which is determined by the equation of motion, Eq.(11). Solving Eq. (11) for $\boldsymbol{V}$ evolution requires information on $\boldsymbol{P}$, which is determined by the next energy equation (12). However, solving Eq. (12) requires information on heat flux $\boldsymbol{q} = \frac{1}{2} m \left\langle \left(\boldsymbol{v} - \boldsymbol{V}\right)^2 \left(\boldsymbol{v} - \boldsymbol{V}\right) \right\rangle$ and so on, forming an infinite chain of equations. A standard closure scheme for *ideal* MHD (Ch.4 & 9 Freidberg, 2014) is to introduce an equation of state for an ideal gas, where frequent collisions are required to achieve thermodynamic equilibrium, to replace Eq. (12) and all subsequent equations with,

$$\frac{d}{dt}\left(\frac{p}{\rho^\gamma}\right) = \left(\frac{\partial}{\partial t} + \boldsymbol{V} \cdot \boldsymbol{\nabla}\right)\left(\frac{p}{\rho^\gamma}\right) = 0. \tag{13}$$

Here $\rho = mn$ is the mass density and $\gamma = 5/3$ is the ratio of specific heats of a plasma. Equations (10), (11) and (13) therefore form a complete set of ideal fluid equations for each species of a plasma, after their RHS' are set to zero.

The above set of fluid equations can be constructed for each species in a plasma, and then combined for a single fluid MHD model. For simplicity, we treat electrons and singly charged ions as the only constituents of the plasma. We define macroscopic quantities of a single fluid MHD model by combining electron and ion fluids as

$$\rho = m_i n_i + m_e n_e \approx m_i n_i \approx m_i n, \tag{14}$$

$$\boldsymbol{V} = \frac{m_i n_i \boldsymbol{V}_i + m_e n_e \boldsymbol{V}_e}{\rho} \approx \boldsymbol{V}_i, \tag{15}$$

$$\boldsymbol{j} = en\left(\boldsymbol{V}_i - \boldsymbol{V}_e\right). \tag{16}$$

It is trivial to combine electron and ion continuity equations into a single continuity equation, $\partial\rho/\partial t + \boldsymbol{\nabla} \cdot (\rho \boldsymbol{V}) = 0$, but it is not straightforward for the other two equations. For the energy equation, the energy equilibration time between electrons and ions is typically long for hot plasmas, making it difficult to justify setting their temperatures as equal. In fact, it is rather rare to have equal temperatures in fusion and astrophysical plasmas, except for dense plasmas like stellar interiors. However, if the *total* energy is concerned, the equilibration between different species is not an issue, and Eq.(13) is valid also for the single fluid model after redefining $p = p_e + p_i$. Note that this is

different from the arguments given in Freidberg (2014). A similar strategy can be applied to combine the equation of motion, Eq. (11), for electrons and ions:

$$m_i n \left(\frac{\partial}{\partial t} + \boldsymbol{V}_i \cdot \boldsymbol{\nabla}\right) \boldsymbol{V}_i - en\left(\boldsymbol{E} + \boldsymbol{V}_i \times \boldsymbol{B}\right) + \boldsymbol{\nabla} \cdot \boldsymbol{P_i} = \boldsymbol{R}_i, \tag{17}$$

$$m_e n \left(\frac{\partial}{\partial t} + \boldsymbol{V}_e \cdot \boldsymbol{\nabla}\right) \boldsymbol{V}_e + en\left(\boldsymbol{E} + \boldsymbol{V}_e \times \boldsymbol{B}\right) + \boldsymbol{\nabla} \cdot \boldsymbol{P_e} = \boldsymbol{R}_e, \tag{18}$$

where $\boldsymbol{R}_i$ ($\boldsymbol{R}_e$) is the frictional force on ions (electrons) due to electrons (ions), and thus $\boldsymbol{R}_i + \boldsymbol{R}_e = 0$ when the two fluids are combined. The combined equation of motion, therefore, takes the form

$$\rho \left(\frac{\partial}{\partial t} + \boldsymbol{V} \cdot \boldsymbol{\nabla}\right) \boldsymbol{V} \approx \boldsymbol{j} \times \boldsymbol{B} - \boldsymbol{\nabla} p, \tag{19}$$

where $\boldsymbol{\nabla} \cdot (\boldsymbol{P}_i + \boldsymbol{P}_e) \approx \boldsymbol{\nabla} p$ is assumed. However, the relation to $\boldsymbol{E}$ is lost during this combination. To keep this, the electron equation of motion is used, generally referred as *generalized Ohm's law*, by rearranging terms of Eq. (18) yielding

$$\boldsymbol{E} + \boldsymbol{V} \times \boldsymbol{B} = \eta \boldsymbol{j} + \frac{\boldsymbol{j} \times \boldsymbol{B}}{en} - \frac{\boldsymbol{\nabla} \cdot \boldsymbol{P}_e}{en} - \frac{m_e}{e}\left(\frac{\partial}{\partial t} + \boldsymbol{V}_e \cdot \boldsymbol{\nabla}\right) \boldsymbol{V}_e, \tag{20}$$

where Eq. (16) is used and the plasma resistivity, $\boldsymbol{\eta}$, is based on the frictional force. The resistivity is usually a tensor (Braginskii, 1965) but it is taken to be a scalar here for simplicity as in $\boldsymbol{R} = en\boldsymbol{\eta} \cdot \boldsymbol{j} \approx en\eta \boldsymbol{j}$. Compared with $\boldsymbol{V} \times \boldsymbol{B}$, the magnitudes of the last 3 terms of Eq. (20) respectively scale as

$$\frac{d_i}{L}, \quad \beta_e \frac{d_i}{L}, \quad \sqrt{\frac{m_e}{m_i}} \frac{d_e}{L}, \tag{21}$$

where L is the characteristic length of the plasma and the characteristic speed is taken to be Alfvén speed, $V_A \equiv B/\sqrt{\mu_0 \rho}$. Therefore, if the plasma is sufficiently large, the last three terms in Eq. (20) can be dropped leading to *resistive Ohm's law*

$$\boldsymbol{E} + \boldsymbol{V} \times \boldsymbol{B} = \eta \boldsymbol{j}. \tag{22}$$

(We note that there could be special cases where the resistive term is dominant and the resistive Ohm's law is still largely valid, even for small plasmas which do not necessarily satisfy conditions listed in Eq. (21).) Thus, Faraday's law can be written as the magnetic field evolution equation,

$$\frac{\partial \boldsymbol{B}}{\partial t} = \boldsymbol{\nabla} \times (\boldsymbol{V} \times \boldsymbol{B}) + \frac{\eta}{\mu_0} \nabla^2 \boldsymbol{B} \tag{23}$$

where $\boldsymbol{\nabla} \cdot \boldsymbol{B} = 0$ is used. The first term on the RHS of Eq. (23) represents magnetic field evolution due to the moving plasma to which field lines are

frozen (see GPP I), and the second term represents field diffusion due to finite resistivity. The relative magnitude between these two effects is often identified as the magnetic Reynolds number,

$$Rm \equiv \frac{\mu_0 L V}{\eta} \tag{24}$$

where V is the characteristic speed of the plasma, which in general can be different from V_A. Rm is important for differentially flowing plasmas and will be discussed in detail later in the class. When the plasma has little movement or is static, V is often replaced by V_A leading to the so-called Lundquist number, S. In most fusion and astrophysical plasmas, $Rm \gg 1$ and/or $S \gg 1$, meaning magnetic flux is mostly frozen to the plasma except at some special locations of narrow widths, such as in shock wave layers or magnetic reconnection layers, as will be discussed later in the class.

To complete this section, the remaining Maxwell's equations warrant some discussion. Displacement current is negligible in non-relativistic plasmas,

$$\boldsymbol{\nabla} \times \boldsymbol{B} = \mu_0 \boldsymbol{j} + \frac{1}{c^2} \frac{\partial \boldsymbol{E}}{\partial t}. \tag{25}$$

To see this, the relative importance between electric and magnetic fields can be evaluated via Faraday's law in a plane wave approximation, $E/cB \sim V_{\text{phase}}/c$, where phase velocity $V_{\text{phase}} \equiv \omega/k$; ω and k are the plane wave's angular frequency and wavenumber. Therefore, relative to $\boldsymbol{\nabla} \times \boldsymbol{B}$ the displacement current, $(1/c^2)\partial E/\partial t$, scales proportionally as $(V_{\text{phase}}/c)^2 \to 0$ in non-relativistic plasmas where $V_{\text{phase}} = \mathcal{O}(V_A)$ in MHD (see later).

Note that dropping displacement current is consistent with the quasi-neutrality requirement of a plasma. Taking divergence of Eq. (25) leads to

$$\boldsymbol{\nabla} \cdot \boldsymbol{j} + \epsilon_0 \frac{\partial (\boldsymbol{\nabla} \cdot \boldsymbol{E})}{\partial t} = 0 \tag{26}$$

where the second term is the time derivative of charge density, $\sigma \equiv e(n_i - n_e)$, according to Gauss's law. Therefore, dropping displacement current is equivalent to demanding $\sigma \approx 0$ which is the charge neutrality requirement, as long as this is true for the initial condition at $t = 0$. To appreciate charge neutrality, we can estimate σ/e in a typical tokamak plasma with a size of 1 meter and temperature of 1 keV. The typical magnitude of (radial) electric field measured in such plasmas is 1 kV/m. The mismatch of electron and ion densities or $\sigma/e \sim (\epsilon_0/e)\boldsymbol{\nabla} \cdot \boldsymbol{E} \sim 6 \times 10^{10} \text{m}^{-3}$, which is 9 orders of magnitude lower than the typical density of such a plasma of 10^{20}m^{-3}!

Using Ampere's law, the final set of resistive MHD equations are

$$\frac{\partial \rho}{\partial t} + \boldsymbol{\nabla} \cdot (\rho \boldsymbol{V}) = 0 \tag{27}$$

$$\rho \left(\frac{\partial}{\partial t} + \boldsymbol{V} \cdot \boldsymbol{\nabla} \right) \boldsymbol{V} = \frac{(\boldsymbol{\nabla} \times \boldsymbol{B}) \times \boldsymbol{B}}{\mu_0} - \boldsymbol{\nabla} p \tag{28}$$

$$\left(\frac{\partial}{\partial t} + \boldsymbol{V}\cdot\boldsymbol{\nabla}\right)\left(\frac{p}{\rho^\gamma}\right) = 0 \tag{29}$$

$$\frac{\partial \boldsymbol{B}}{\partial t} = \boldsymbol{\nabla}\times(\boldsymbol{V}\times\boldsymbol{B}) + \frac{\eta}{\mu_0}\nabla^2\boldsymbol{B} \tag{30}$$

with 8 equations for the 8 unknowns: ρ, p, $\boldsymbol{V}$ and $\boldsymbol{B}$. The ideal MHD model refers to the case when $\eta = 0$, or equivalently $Rm \to \infty / S \to \infty$. In order for ideal MHD models to be valid, frequent collisions are needed for plasma to stay near the thermodynamic equilibrium, but not too frequent to cause substantial dissipation of the magnetic field.

1.4 Additional Remarks

We have seen quite a few assumptions or simplifications that went into the derivation of the single-fluid MHD models. This raises legitimate concerns about whether our models are valid when applied to real-world problems. Nonetheless, MHD models are arguably one of the most successful plasma models to capture global behaviors for both fusion and astrophysical plasmas. There could be several reasons for it. MHD models are quite simple, compared with other models in our hierarchy, and attempts have been made to apply it to a wide range of cases. This practice follows Einstein's advice, as the mean-field theory has not been as mature just yet to be practically useful. Even though MHD models are more complicated than their hydrodynamic counterparts, Navier-Stokes equations, the existence of a large volume of literature on the latter subject has served as a solid foundation for MHD models. Experimentally or observationally, global scale phenomena in both fusion and astrophysical plasmas have been the first to be detected and studied, which helped motivate the use of MHD models as well.

Despite these successes, however, we should not take it for granted that MHD models should be also applicable. Detailed discussion on their validity can be found in the reading materials, but Fig. 2 shows a simple and practical flow chart to check the validity of an MHD model. We begin with the question if the plasma is non-relativistic, *i.e.* whether Alfvén speed is much slower than the speed of light. If not, displacement current and charge density need to be included, with corresponding Maxwell's equations. If yes, we move on to whether collision time or mean-free path is much shorter than the time or length of interest. If it is, then the MHD models are valid. Otherwise, we further examine whether the plasma size is much larger than ion kinetic scales in the cross-field directions, and whether the plasma is periodic as in toroidal confinement systems in the parallel direction. If yes, there is a good chance the MHD models can work, but otherwise, more complicated or sophisticated models should be used.

As discussed in Sec.1, MHD models can also be derived based on Navier-Stokes equations by adding the Lorentz force. For example, an incompressible

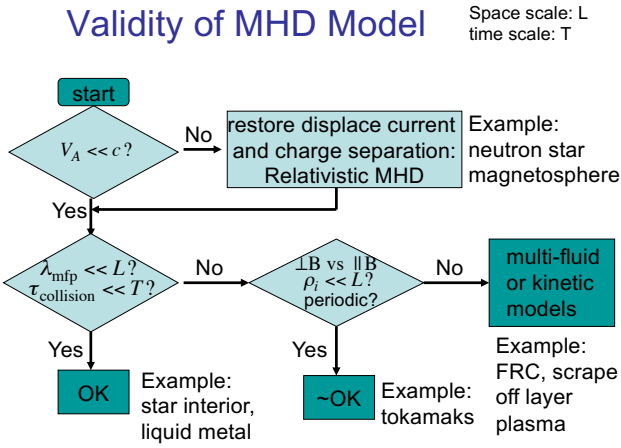

Fig. 2 A flow chart to check the validity of an MHD model.

version is given by

$$\left(\frac{\partial}{\partial t} + \boldsymbol{V}\cdot\boldsymbol{\nabla}\right)\boldsymbol{V} = \frac{\boldsymbol{j}\times\boldsymbol{B}}{\rho} - \frac{\boldsymbol{\nabla}p}{\rho} - \boldsymbol{g} + \nu\nabla^2\boldsymbol{V}, \tag{31}$$

where gravity $\boldsymbol{g}$ and viscous forces are included as a convention. This introduces another dimensionless parameter, the Reynolds number,

$$Re = \frac{LV}{\nu} \tag{32}$$

where ν is the kinematic viscosity. The ratio of Rm to Re is called the magnetic Prandtl number, $Pm = \mu_0\nu/\eta$, which is important in deciding the nature of dissipation on small scales. Refer to (Kundu et al, 2015, Ch.1-4) for fundamentals of Navier-Stokes equations.

Finally, a list of extensions to the simple MHD models is given below for your reference:

Hall MHD: When important physics occurs on length scales comparable to ion kinetic scales, Hall terms are restored in the model. $\boldsymbol{j}\times\boldsymbol{B}/en$ can be added without incurring additional variables, but the electron pressure term, $\boldsymbol{\nabla}p_/en$, is either ignored or needs a link to the total pressure, p.
Electron MHD: When important physics occurs on length scales comparable to electron kinetic scales while ions can be treated as background charge neutralizers, electron MHD models (Bulanov et al, 1992) are employed. See homework.
GR-MHD: When dealing with extreme conditions, such as near black holes, general relativistic effects must be included.

Radiative HD/MHD: When photons play an important role by interacting with plasma, they can be added as an additional massless fluid such as in some laser-generated plasmas and astrophysical plasmas, which can become opaque to photons with certain energies. Quantum effects can be important as well.
General Relativity Radiative HD/MHD (GRRMHD): When both photons and general relativity are important, typically during accretion to black holes such as for the Event Horizon Telescope (EHT) project.
MHD Plus a Neutral Particle Fluid: When plasma is partially ionized, neutral particles participate in MHD through collisions with electrons and ions, introducing effects such as ambipolar diffusion (Mestel and Spitzer, 1956).
MHD Plus Neutrinos: Neutrinos introduce an additional fluid interacting with electron fluid through weak interactions, which is possibly important for supernovae phenomena in astrophysics and in laser-produced laboratory plasmas.

1.5 Summary

- Hierarchy of plasma models from multi-body to kinetic to fluid. MHD models are arguably the most successful model for plasmas.
- Plasma physics is multiscale and no method can cover all scales. Multiple approaches are needed.
- Construction of MHD models requires many assumptions but leads to a set of simple fluid equations.
- Additional Remarks
  - Validity of MHD models is always a concern and should be checked often.
  - Navier-Stokes equation and fluid mechanics provide a solid and useful reference point for MHD.
  - Many extended MHD models exist to take into account of various effects.

1.6 Further Readings

- Chapters 2 & 9 in Freidberg (2014)
- Braginskii (1965), p.84 in Wesson (2011), Chapter 8 in Kulsrud (2005)
- Chapters 1-4 in Kundu et al (2015)

1.7 Homework Problem Set 1

1. Check whether the following line-tied plasmas, in which the field lines intercept conducting boundaries, can be treated properly by MHD models:
   (a) Plasmas in the solar corona often exhibit filamentary field-aligned structures with lengths in the order of 10^6 m and widths in the order of 10^5 m. The typical magnetic field has strength of 10 mT with a temperature of $T \sim 100$eV and number density of $n \sim 10^{15}\text{m}^{-3}$.
   (b) Plasmas in the tokamak scrape-off-layer (SOL) typically have a temperature of $T \sim 100$ eV and a number density of $n \sim 10^{19}\text{m}^{-3}$ at the interface with the bulk plasma. Away from the bulk plasma, T and n fall

off exponentially with a scale length on the order of 1 cm. The magnetic field has a strength of about 1 Tesla and travels for about 100 m before intercepting the divertor plates.

2. Electron MHD Model:
   (a) When ions are regarded as stationary, electrons carry all electric current. Assuming uniform density and incompressible electron flow, derive the Electron MHD (E-MHD) model:

$$\frac{\partial}{\partial t}\left(\boldsymbol{B} - d_e^2 \nabla^2 \boldsymbol{B}\right) = \boldsymbol{\nabla} \times \left[\boldsymbol{V}_e \times \left(\boldsymbol{B} - d_e^2 \nabla^2 \boldsymbol{B}\right)\right] + \eta \nabla^2 \boldsymbol{B} \tag{33}$$

$$\boldsymbol{V}_e = -\frac{1}{\mu_0 e n} \boldsymbol{\nabla} \times \boldsymbol{B} \tag{34}$$

   where d_e is electron skin depth.
   (b) Discuss physical insights that you can develop from these equations for the ideal E-MHD model.

2 Magnetostatic Equilibrium

2.1 Conservation Forms of Ideal MHD Equations

The standard ideal MHD model equations can be summarized as

$$\frac{\partial \rho}{\partial t} + \boldsymbol{\nabla} \cdot (\rho \boldsymbol{V}) = 0, \tag{35}$$

$$\rho \left(\frac{\partial}{\partial t} + \boldsymbol{V} \cdot \boldsymbol{\nabla} \right) \boldsymbol{V} = \frac{(\boldsymbol{\nabla} \times \boldsymbol{B}) \times \boldsymbol{B}}{\mu_0} - \boldsymbol{\nabla} p, \tag{36}$$

$$\left(\frac{\partial}{\partial t} + \boldsymbol{V} \cdot \boldsymbol{\nabla} \right) \left(\frac{p}{\rho^\gamma} \right) = 0, \tag{37}$$

$$\frac{\partial \boldsymbol{B}}{\partial t} = \boldsymbol{\nabla} \times (\boldsymbol{V} \times \boldsymbol{B}.) \tag{38}$$

Note that they do not contain any dissipative effects, and as a result, many conservation laws should hold.

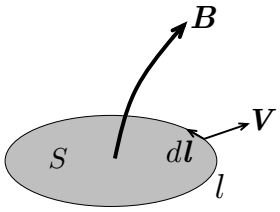

Fig. 3 Magnetic field $\boldsymbol{B}$ passes through a surface S encircled by the loop l in a plasma moving with a velocity of $\boldsymbol{V}$ ($d\boldsymbol{l}$ is an element of $\boldsymbol{l}$).

Magnetic flux conservation. Conservation of magnetic flux is also called the "frozen-in" law of magnetic field to the plasma. The magnetic flux passing through surface S is given by

$$\Psi = \int \boldsymbol{B} \cdot d\boldsymbol{S}, \tag{39}$$

and its time derivative moving with the plasma is given by

$$\frac{d\Psi}{dt} = \int \frac{\partial \boldsymbol{B}}{\partial t} \cdot d\boldsymbol{S} + \oint \boldsymbol{B} \cdot (\boldsymbol{V} \times d\boldsymbol{l}). \tag{40}$$

The second term is due to the rate of change in S by the loop element $d\boldsymbol{l}$ swept with velocity $\boldsymbol{V}$ and can be written as

$$\oint \boldsymbol{B} \cdot (\boldsymbol{V} \times d\boldsymbol{l}) = -\oint (\boldsymbol{V} \times \boldsymbol{B}) \cdot d\boldsymbol{l} = -\int \boldsymbol{\nabla} \times (\boldsymbol{V} \times \boldsymbol{B}) \cdot d\boldsymbol{S}. \tag{41}$$

Using Faraday's law, we have

$$\frac{d\Psi}{dt} = -\int \boldsymbol{\nabla}\times\boldsymbol{E}\cdot d\boldsymbol{S} - \int \boldsymbol{\nabla}\times(\boldsymbol{V}\times\boldsymbol{B})\cdot d\boldsymbol{S} = -\int \boldsymbol{\nabla}\times(\boldsymbol{E}+\boldsymbol{V}\times\boldsymbol{B})\cdot d\boldsymbol{S} = 0. \tag{42}$$

Mass and momentum conservation. The conservation of mass is trivial from Eq. (35), which can then be used to derive momentum conservation. Multiplying Eq. (35) with $\boldsymbol{V}$ and adding to Eq. (36) yield the LHS,

$$\boldsymbol{V}\frac{\partial\rho}{\partial t} + \rho\frac{\partial\boldsymbol{V}}{\partial t} + (\rho\boldsymbol{V}\cdot\boldsymbol{\nabla})\,\boldsymbol{V} + \boldsymbol{V}\boldsymbol{\nabla}\cdot(\rho\boldsymbol{V}) = \frac{\partial(\rho\boldsymbol{V})}{\partial t} + \boldsymbol{\nabla}\cdot(\rho\boldsymbol{V}\boldsymbol{V})\,. \tag{43}$$

The RHS of Eq. (36) can then be written in a tensor form, since $\boldsymbol{\nabla}\cdot\boldsymbol{B} = 0$,

$$\frac{(\boldsymbol{\nabla}\times\boldsymbol{B})\times\boldsymbol{B}}{\mu_0} - \boldsymbol{\nabla}p = \boldsymbol{\nabla}\cdot\left[\left(p+\frac{B^2}{2\mu_0}\right)\boldsymbol{I} - \frac{\boldsymbol{B}\boldsymbol{B}}{\mu_0}\right], \tag{44}$$

leading to the momentum conservation,

$$\frac{\partial(\rho\boldsymbol{V})}{\partial t} + \boldsymbol{\nabla}\cdot\left[\left(p+\frac{B^2}{2\mu_0}\right)\boldsymbol{I} + \rho\boldsymbol{V}\boldsymbol{V} - \frac{\boldsymbol{B}\boldsymbol{B}}{\mu_0}\right] = 0. \tag{45}$$

The first term in the divergence is the force due to plasma and magnetic pressure. The second and third terms are the forces due to Reynolds and Maxwell stresses, respectively.

Energy conservation. Performing dot product of Eq. (36) with $\boldsymbol{V}$ yields an energy conservation equation. The first term becomes,

$$\begin{aligned}
\rho\boldsymbol{V}\cdot\left(\frac{\partial}{\partial t}+\boldsymbol{V}\cdot\boldsymbol{\nabla}\right)\boldsymbol{V} &= \frac{\partial}{\partial t}\left(\frac{1}{2}\rho V^2\right) - \frac{V^2}{2}\frac{\partial\rho}{\partial t} + \rho\boldsymbol{V}\cdot\boldsymbol{\nabla}\left(\frac{V^2}{2}\right) \\
&= \frac{\partial}{\partial t}\left(\frac{1}{2}\rho V^2\right) - \frac{V^2}{2}\left[\frac{\partial\rho}{\partial t} + \boldsymbol{\nabla}(\rho\boldsymbol{V})\right] + \boldsymbol{\nabla}\left(\frac{1}{2}\rho V^2\boldsymbol{V}\right) \\
&= \frac{\partial}{\partial t}\left(\frac{1}{2}\rho V^2\right) + \boldsymbol{\nabla}\left(\frac{1}{2}\rho V^2\boldsymbol{V}\right),
\end{aligned} \tag{46}$$

where we have used the mass conservation in Eq. (35). The second term becomes

$$\begin{aligned}
\boldsymbol{V}\cdot(\boldsymbol{j}\times\boldsymbol{B}) &= -\boldsymbol{j}\cdot(\boldsymbol{V}\times\boldsymbol{B}) = \boldsymbol{j}\cdot\boldsymbol{E} \\
&= -\boldsymbol{\nabla}\left(\frac{\boldsymbol{E}\times\boldsymbol{B}}{\mu_0}\right) + \frac{\boldsymbol{B}}{\mu_0}\cdot\boldsymbol{\nabla}\times\boldsymbol{E} \\
&= -\boldsymbol{\nabla}\left(\frac{\boldsymbol{E}\times\boldsymbol{B}}{\mu_0}\right) - \frac{\partial}{\partial t}\left(\frac{B^2}{2\mu_0}\right),
\end{aligned} \tag{47}$$

where the ideal Ohm's law and Faraday's law have been used. The first term on RHS represents the Poynting vector for electromagnetic energy flux while the second term represents the rate of change for the magnetic energy. The last term of Eq. (36) after being dotted by $\boldsymbol{V}$ is

$$\boldsymbol{V}\cdot\boldsymbol{\nabla}p=\boldsymbol{\nabla}\cdot(p\boldsymbol{V})-p\boldsymbol{\nabla}\cdot\boldsymbol{V}. \tag{48}$$

We will then replace $\boldsymbol{\nabla}\cdot\boldsymbol{V}$ in terms of p using the continuity and energy equations, Eq. (35) and Eq. (37). To do this, we divide Eq. (37) by p/ρ^γ to yield,

$$\frac{d}{dt}\left[\ln\left(\frac{p}{\rho^\gamma}\right)\right]=\frac{d}{dt}\left(\ln p-\gamma\ln\rho\right)=\frac{1}{p}\frac{dp}{dt}-\frac{\gamma}{\rho}\frac{d\rho}{dt}=0. \tag{49}$$

Similarly, Eq. (35) can be written as

$$\frac{1}{\rho}\frac{d\rho}{dt}+\boldsymbol{\nabla}\cdot\boldsymbol{V}=0, \tag{50}$$

which can be used to replace $d\rho/dt$ in Eq. (49) yielding

$$\frac{dp}{dt}=\frac{\partial p}{\partial t}+\boldsymbol{V}\cdot\boldsymbol{\nabla}p=-\gamma p\boldsymbol{\nabla}\cdot\boldsymbol{V}. \tag{51}$$

Finally, using this equation to eliminate $\boldsymbol{\nabla}\cdot\boldsymbol{V}$ in Eq. (48) leads to

$$\boldsymbol{V}\cdot\boldsymbol{\nabla}p=\frac{1}{\gamma-1}\frac{\partial p}{\partial t}+\frac{\gamma}{\gamma-1}\boldsymbol{\nabla}\cdot(p\boldsymbol{V}). \tag{52}$$

Combining all three terms, the energy conservation equation becomes

$$\frac{\partial W}{\partial t}+\boldsymbol{\nabla}\cdot\boldsymbol{S}=0, \tag{53}$$

$$W=\frac{1}{2}\rho V^2+\frac{p}{\gamma-1}+\frac{B^2}{2\mu_0}, \tag{54}$$

$$\boldsymbol{S}=\left(\frac{1}{2}\rho V^2+\frac{p}{\gamma-1}\right)\boldsymbol{V}+p\boldsymbol{V}+\frac{\boldsymbol{E}\times\boldsymbol{B}}{\mu_0}. \tag{55}$$

The total energy contains plasma kinetic energy, internal thermal energy 3p/2 when $\gamma=5/3$, and magnetic energy. The energy flux contains the flux of plasma kinetic and internal thermal energy, work done on plasma $p\boldsymbol{V}$, and electromagnetic energy flux given by the Poynting vector.

Boundary conditions. Global properties of a system, such as its equilibrium or stability, can critically depend on its boundary conditions. For plasma, the normal boundaries can either be fixed and non-penetrating or free. For a fixed boundary, like a solid wall, the normal component of velocity vanishes

$$\boldsymbol{n}\cdot\boldsymbol{V}=0, \tag{56}$$

where $\boldsymbol{n}$ is the normal unit vector of the boundary. In contrast, the free surface boundary deforms at the rate given by the normal component of the plasma's velocity.

In the tangential direction, the boundaries can either be slippery, for an inviscid fluid or non-slippery, for a viscous fluid. Assuming stationary boundaries, the tangential components of plasma's velocity must also vanish in the non-slip condition,

$$\boldsymbol{n} \times \boldsymbol{V} = 0. \tag{57}$$

Electromagnetic boundary conditions can either be perfectly conducting or insulating. For perfect conductors, both the perpendicular magnetic field and tangential electric field must vanish,

$$\boldsymbol{n} \cdot \boldsymbol{B} = 0, \tag{58}$$

$$\boldsymbol{n} \times \boldsymbol{E} = 0. \tag{59}$$

For insulating boundaries, the normal current density must vanish

$$\boldsymbol{n} \cdot (\boldsymbol{\nabla} \times \boldsymbol{B}) = 0. \tag{60}$$

More detailed discussion on various boundary conditions can be found in (Ch.3 Freidberg, 2014).

2.2 Virial Theorem

A closely related subject to global energy conservation is the virial theorem, which is used to appreciate the required confinement by either magnetic fields in laboratory magnetic fusion experiments or self-gravity in astrophysics.

We begin with a tensor identity (the proof is part of Homework 2),

$$\boldsymbol{\nabla} \cdot (\boldsymbol{r} \cdot \boldsymbol{T}) = \boldsymbol{r} \cdot (\boldsymbol{\nabla} \cdot \boldsymbol{T}) + \mathrm{Trace}(\boldsymbol{T}) \tag{61}$$

where $\boldsymbol{T}$ is a tensor and $\boldsymbol{r}$ is the position vector. For the momentum conservation in Eq. (45), we have

$$\frac{d\,(\rho \boldsymbol{V})}{dt} = -\boldsymbol{\nabla} \cdot \boldsymbol{T} = 0, \tag{62}$$

where

$$\boldsymbol{T} = \left(p + \frac{B^2}{2\mu_0}\right) \boldsymbol{I} + \rho \boldsymbol{V}\boldsymbol{V} - \frac{\boldsymbol{B}\boldsymbol{B}}{\mu_0}. \tag{63}$$

The first term on the RHS from Eq. (61) vanishes in a steady state. It is also straightforward to calculate

$$\mathrm{Trace}(\boldsymbol{T}) = \rho V^2 + 3p + \frac{B^2}{2\mu_0}. \tag{64}$$

Since $\int \boldsymbol{\nabla}\cdot(\boldsymbol{r}\cdot\boldsymbol{T})\,dV = \int(\boldsymbol{r}\cdot\boldsymbol{T})\cdot d\boldsymbol{S}$, where the surface $\boldsymbol{S}$ encloses the volume V, the identity Eq. (61) becomes

$$\int(\boldsymbol{r}\cdot\boldsymbol{T})\cdot d\boldsymbol{S} = \int\left(\rho V^2 + 3p + \frac{B^2}{2\mu_0}\right)dV. \tag{65}$$

This equation leads to a contradiction when $r\to\infty$. Because the integrand of the RHS is positive definite, the volume integration remains positive and finite even when $r\to\infty$. In contrast, under the same condition, the LHS

$$\int(\boldsymbol{r}\cdot\boldsymbol{T})\cdot d\boldsymbol{S} \propto \int rB^2 dS \propto \frac{1}{r^3}\to 0, \tag{66}$$

where we have assumed that the magnetic dipoles decay the slowest, $B\propto r^{-3}$, and the surface area $S\propto r^2$. This contradiction means the magnetic field generated by the plasma cannot confine the plasma itself! However, it is possible to confine plasma using its gravitational force (Homework 2). Therefore to magnetically confine plasma in a laboratory, we need external magnetic fields generated by coils.

2.3 Magnetostatic Equilibrium in Toroidal Configurations

2.3.1 Grad-Shafranov Equation

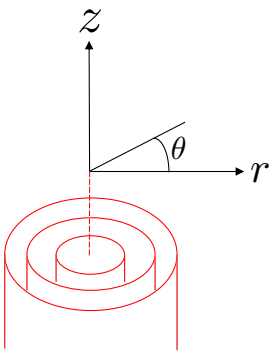

Fig. 4 Nested magnetic flux surfaces in cylindrical coordinate system (r,θ,z) where θ is the azimuthal angle.

The equation to determine steady-state static magnetic confinement of plasma is simply given by

$$\boldsymbol{j}\times\boldsymbol{B} = \boldsymbol{\nabla}p, \tag{67}$$

which implies

$$\boldsymbol{B}\cdot\boldsymbol{\nabla}p = \boldsymbol{j}\cdot\boldsymbol{\nabla}p = 0. \tag{68}$$

Therefore, both vectors $\boldsymbol{j}$ and $\boldsymbol{B}$ must lie on the constant pressure contours forming nested magnetic flux surfaces as illustrated in Fig. 4. We can use the plasma pressure p to index the magnetic flux surfaces, and p is a (magnetic) flux surface quantity. There exist many other flux surface quantities when plasma is in magnetostatic equilibrium. Examples include plasma density, electron and ion temperatures, as well as poloidal flux Ψ and toroidal flux Φ when properly integrated (see below).

We begin with a cylindrical coordinate system (r, θ, z), pictured in Fig. 4, formed by the radial, azimuthal, and axial directions. We assume axisymmetry for simplicity. Consider the 1D case when all quantities, including p, depend on only r. Then, the pressure force $-\boldsymbol{\nabla} p$ is only in the radial direction, and both $\boldsymbol{B}$ and $\boldsymbol{j}$ must have no radial component depending on only r,

$$\boldsymbol{B} = (0, B_\theta, B_z), \tag{69}$$

$$\mu_0 \boldsymbol{j} = \left(0, -\frac{dB_z}{dr}, \frac{1}{r}\frac{d\,(rB_\theta)}{dr}\right). \tag{70}$$

Therefore, the force balance equation, Eq. (67), can be expressed as

$$\frac{d}{dr}\left(\frac{B_\theta^2 + B_z^2}{2\mu_0}\right) + \frac{B_\theta^2}{\mu_0 r} = -\frac{dp}{dr}. \tag{71}$$

The plasma pressure is confined by a combination of magnetic pressure and magnetic tension force, as shown in the LHS of the above equation.

This confinement system is called **screw pinch** due to the presence of both B_z and B_θ. **Z pinch** is a special case with $B_z = 0$ and the plasma is confined purely by B_θ generated by j_z. Another special case is the **theta pinch** when the plasma is confined purely by B_z generated by j_θ and $B_\theta = 0$.

Confining plasma without open field lines requires the flux surfaces to take a toroidal (doughnut) shape. For simplicity, we assume axisymmetry as illustrated in Fig. 5. This configuration is called **toroidal pinch** with major radius R_0 and minor radius a reduces the system into a 2D system. The original cylindrical coordinate system (r, θ, z) shown in Fig. 4 now becomes a toroidal coordinate system (r, θ, ϕ) where ϕ is toroidal angle and is related to z through $z = -\phi R_0$. Figure 5 also introduces a new cylindrical coordinate system (R, ϕ, Z) which is related to the toroidal coordinate system via

$$R = R_0 + r\cos\theta, \tag{72}$$

$$\phi = -z/R_0, \tag{73}$$

$$Z = r\sin\theta. \tag{74}$$

Note that all coordinates here are right-handed. Flux surfaces (in red) are nested but shifted radially outwards (called Shafranov Shift (Shafranov, 1966)). This shift is due to the hoop force difference from a stronger poloidal field on the inner side of the torus than that on the outside (Ch.4 in Freidberg,

2014). The center of flux surfaces when its area approaches zero is the magnetic axis at $R = R_a$ which is also typically the location of maximum plasma pressure. On the other side, the last closed flux surface is a circle with a radius of a.

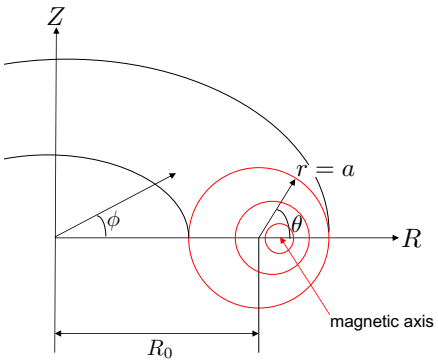

Fig. 5 Magnetic configuration of toroidal confinement system. Cylindrical coordinate system is defined as (R, ϕ, Z) while the toroidal coordinate system is defined as (r, θ, ϕ). Here toroidal angle is ϕ and poloidal angle is θ. Other definitions: major radius is R_0 and minor radius is a. Magnetic axis is also shown in the figure.

As in any 2D systems, a stream function, ψ, can be introduced as,

$$B_R = -\frac{1}{R}\frac{\partial \psi}{\partial Z}, \tag{75}$$

$$B_Z = \frac{1}{R}\frac{\partial \psi}{\partial R}, \tag{76}$$

to satisfy

$$\boldsymbol{\nabla} \cdot \boldsymbol{B} = \frac{1}{R}\frac{\partial (RB_R)}{\partial R} + \frac{\partial B_Z}{\partial Z} = -\frac{1}{R}\frac{\partial^2 \psi}{\partial R \partial Z} + \frac{1}{R}\frac{\partial^2 \psi}{\partial Z \partial R} = 0. \tag{77}$$

By comparing to the definition of the vector potential $\boldsymbol{A}$ in an axisymmetric cylindrical system, ψ can be readily identified as $\psi = RA_\phi$. ψ is also closely related to poloidal flux Ψ defined as

$$\Psi(R) = 2\pi \int_{R_a}^{R} B_Z(R', 0) R' dR' = 2\pi \left[\psi(R, 0) - \psi(R_a, 0)\right] = 2\pi \psi(R, 0), \tag{78}$$

where Eq. (76) is used and $\psi(R_a, 0)$ is set to be zero. Therefore, instead of using pressure p, we can use poloidal flux ψ to uniquely label the flux surfaces. (The plasma pressure p might not provide unique labels of the flux surfaces.) Similarly, toroidal flux Φ can also be defined for each closed flux surface. Both Ψ and Φ are flux surface quantities.

Using ψ and toroidal field component, B_ϕ, and introducing $F = RB_\phi$, we can express current density via Ampere's law:

$$\boldsymbol{B} = \left(-\frac{1}{R}\frac{\partial\psi}{\partial Z}, B_\phi, \frac{1}{R}\frac{\partial\psi}{\partial R}\right), \tag{79}$$

$$\mu_0\boldsymbol{j} = \left(-\frac{\partial B_\phi}{\partial Z}, -\frac{\Delta^*\psi}{R}, \frac{1}{R}\frac{\partial F}{\partial R}\right), \tag{80}$$

$$\Delta^*\psi = R\frac{\partial}{\partial R}\left(\frac{1}{R}\frac{\partial\psi}{\partial R}\right) + \frac{\partial^2\psi}{\partial Z^2} = R^2\boldsymbol{\nabla}\cdot\left(\frac{\boldsymbol{\nabla}\psi}{R^2}\right). \tag{81}$$

By applying Stokes's theorem to Ampere's law, $F(R)$ is shown to be related to the total *poloidal* current passing through the circle with a radius of R, $I_{pol}(R)$,

$$I_{pol}(R) = 2\pi\mu_0\int_0^R j_Z(R')R'dR' = \oint B_\phi(R)Rd\phi = 2\pi RB_\phi(R) = 2\pi F(R). \tag{82}$$

Finally, the R component of the force balance in Eq. (67) is given by

$$j_\phi B_Z - j_Z B_\phi = \frac{\partial p}{\partial R}, \tag{83}$$

or

$$-\frac{\Delta^*\psi}{\mu_0 R^2}\frac{\partial\psi}{\partial R} - \frac{F}{\mu_0 R^2}\frac{\partial F}{\partial R} = \frac{\partial p}{\partial R}. \tag{84}$$

Multiplying by $-\mu_0 R^2$ and using chain rule of differentiation yield the **Grad-Shafranov equation** by Grad & Rubin (1958) and Shafranov (1960) (Shafranov, 1966),

$$\Delta^*\psi + F\frac{dF}{d\psi} + \mu_0 R^2\frac{dp}{d\psi} = 0. \tag{85}$$

This equation can also be written in the toroidal coordinate system (r, θ, ϕ) but in a somewhat more complicated form,

$$\begin{aligned}\Delta^*\psi &= \frac{1}{r}\frac{\partial}{\partial r}\left(r\frac{\partial\psi}{\partial r}\right) + \frac{1}{r^2}\frac{\partial^2\psi}{\partial\theta^2} - \frac{1}{R_0 + r\cos\theta}\left(\cos\theta\frac{\partial\psi}{\partial r} - \frac{\sin\theta}{r}\frac{\partial\psi}{\partial\theta}\right)\\ &= -F\frac{dF}{d\psi} - \mu_0\left(R_0 + r\cos\theta\right)^2\frac{dp}{d\psi}.\end{aligned} \tag{86}$$

Analytical solutions of Grad-Shafranov equation exist, such as those by Solov'ev (1968). In practice, the equation is solved numerically by specifying F and p as functions of ψ with appropriate boundary conditions.

2.3.2 Characteristics of Toroidal Configurations

We should recognize that a toroidal system cannot confine plasma by using a purely toroidal field B_ϕ. This limitation is because the charge-dependent

guiding center drifts in the Z direction caused by the ∇B and the field curvature. For example, the vacuum toroidal field generated by the toroidal field coil current, I_{TF}, decreases with R and is given by

$$B_\phi = \frac{\mu_0 I_{TF}}{2\pi R} = 0.2 \left(\frac{I_{TF}}{\text{MA}}\right) \left(\frac{R}{\text{m}}\right)^{-1} \text{Tesla}, \tag{87}$$

where I_{TF} is in the unit of mega ampere and R is in the meter unit. Usually, we calculate I_{TF} by multiplying the coil current by the number of turns of the toroidal field coil system. The equation gives ∇B that is in the R direction so does the field line curvature vector. Since the magnetic field is in the toroidal direction, both ∇B and field curvature drifts are in the Z direction, but with opposite signs for electrons and ions. This difference leads to charge buildup at opposite ends of the Z direction generating an electric field E_Z. The resulting $E_Z \times B_\phi$ drift will cause ions and electrons to move radially outward and losing confinement. A poloidal component of the magnetic field, B_θ, is therefore needed to short out the charge buildup along the field line direction to prevent the loss of confinement. This B_θ can be generated either by current flowing in the plasma (called plasma current, I_p) as in toroidal pinches, such as tokamaks or reversed field pinches (RFPs), or by external coils as in stellarators.

Once B_θ is added to the existing B_ϕ, magnetic field lines on the flux surface go around not only toroidally but also poloidally in helical paths. "Safety factor" of a given flux surface ψ, $q(\psi)$, is introduced to quantify the twistedness of the field lines on that particular flux surface, *i.e.* the number of toroidal turns for field lines to finish one poloidal turn,

$$q(r) \equiv \frac{1}{2\pi} \oint \frac{B_\phi}{R B_\theta} ds = \frac{2\pi}{\iota}, \tag{88}$$

where s is the distance along a field line. Here ι is called rotational transform, defined as the poloidal angle it travels per toroidal turn of a field line. Conventionally, q is used for toroidal pinches while ι is used for stellarators. In the large aspect ratio limit $R_0/r \gg 1$ of a circular plasma,

$$q(r) = \frac{\#\text{ of toroidal turn}}{\#\text{ of poloidal turn}} \approx \frac{B_\phi/2\pi R_0}{B_\theta/2\pi r} = \frac{r B_\phi}{R_0 B_\theta}. \tag{89}$$

Now we are ready to introduce the three different types of field line trajectories in toroidal systems. Field line in the plasma can either be:

Rational when the q is a rational number, *i.e.* $q = n/m$ (n and m are positive integers). The field line stays not only on a single flux surface but also on a closed loop on the flux surface. For example, $q = 3/2$ means the field line wraps around toroidally for exactly 3 turns for every 2 poloidal turns. Rational flux surfaces are also important for MHD instabilities relating to the resonances of n and m mode numbers.

Ergodic when the q is an irrational number. In this case, a field line maps an entire flux *surface* without closing the loop. This trajectory is an ideal situation for flux surfaces without rational resonances.
Stochastic when a field line occupies a *volume* due to the loss of geometric symmetry. This is undesirable for plasma confinement as parallel transport along field lines is much faster than perpendicular transport, leading to constant p in the stochastic volume, *i.e.* loss of confinement. It should be noted that sometimes stochastic field lines are intentionally introduced to reduce pressure gradient, such as to mediate disruptive behavior due to strong Edge-Localized Mode or ELM, or to spread heat to a large volume in the divertor region.

Finally, an important figure of merit for plasma confinement, the globally defined plasma β warrants some discussion here. It makes sense to calculate volume-averaged pressure rather than the local pressure,

$$\langle p \rangle = \frac{1}{V_p} \int p dV, \tag{90}$$

where V_p is the plasma volume. The toroidal beta, β_t, is the beta value when vacuum toroidal field at $R = R_0$, B_0, is often used for convenience,

$$\beta_t \equiv \frac{\langle p \rangle}{B_0^2/2\mu_0}. \tag{91}$$

In contrast, the poloidal beta, defined as

$$\beta_p \equiv \frac{\langle p \rangle}{B_\theta^2(r=a)/2\mu_0}, \tag{92}$$

has more physical meanings. This can be illustrated using the cylindrical approximation given by Eq. (71) which is valid when $R_0/a \gg 1$. Multiplying πr^2 to Eq. (71) and integrating from $r = 0$ to $r = a$ yields

$$\int_0^a \pi r^2 \frac{d}{dr}\left(p + \frac{B_\theta^2 + B_z^2}{2\mu_0}\right) dr + \int_0^a 2\pi r \frac{B_\theta^2}{2\mu_0} dr = 0. \tag{93}$$

The first integration can be written as

$$\left[\pi r^2 \left(p + \frac{B_\theta^2 + B_z^2}{2\mu_0}\right)\right]_0^a - \int_0^a 2\pi r \left(p + \frac{B_\theta^2 + B_z^2}{2\mu_0}\right) dr, \tag{94}$$

which can be combined with the second integration to yield

$$\pi a^2 \left(\frac{B_\theta^2(a) + B_z^2(a)}{2\mu_0}\right) = \int_0^a 2\pi r \left(p + \frac{B_z^2}{2\mu_0}\right) dr, \tag{95}$$

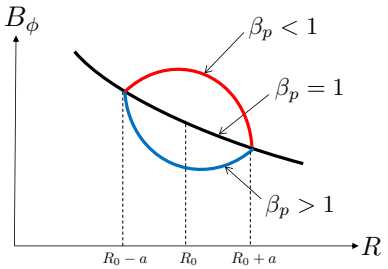

Fig. 6 Diamagnetism versus paramagnetism as indicated by poloidal beta, β_p.

where $p(a) = 0$ is used. Since volume averaged quantity here means $\langle x \rangle = \int_0^a x 2\pi dr / \pi a^2$, we have

$$\langle p \rangle + \frac{\langle B_z^2 \rangle}{2\mu_0} = \frac{B_\theta^2(a) + B_z^2(a)}{2\mu_0}, \tag{96}$$

which can be rearranged to

$$\beta_p \equiv \frac{\langle p \rangle}{B_\theta^2(a)/2\mu_0} = 1 + \frac{B_z^2(a) - \langle B_z^2 \rangle}{B_\theta^2(a)}. \tag{97}$$

Therefore, when $\beta_p < 1$, $\langle B_z^2 \rangle$ is larger than its edge value, $B_z^2(a)$, implying the plasma is *paramagnetic*. In contrast, when $\beta_p > 1$, the plasma is *diamagnetic*, *i.e.* $\langle B_z^2 \rangle$ is smaller than $B_z^2(a)$. This is illustrated in Fig. 6 where B_z is replaced by B_ϕ in the toroidal system.

Total β, or β_t in strong toroidal field systems like tokamaks, depends strongly on geometry. This can be seen in

$$\beta \approx \beta_t = \frac{\langle p \rangle}{B_\phi^2/2\mu_0} = \beta_p \frac{a^2}{R^2 q_a^2}, \tag{98}$$

where $q_a = q(a)$. Given $\beta_p \sim 1$, β is higher for a smaller aspect ratio or a lower edge safety factor, q_a. However, lower q_a can lead to MHD instabilities (see later). Instead, elongating plasma cross-section, shown in Fig. 7, can increase β without lowering q_a. With a non-circular cross-section, q_a is given by

$$q_a \approx \frac{\sqrt{(a^2 + b^2)/2}}{R} \frac{B_\phi}{B_\theta(a)} = \frac{aB_\phi}{RB_\theta(a)} \sqrt{\frac{1 + \kappa^2}{2}}, \tag{99}$$

where elongation $\kappa \equiv b/a$. Therefore, β increases with κ as in

$$\beta \approx \beta_p \frac{a^2}{R^2 q_a^2} \sqrt{\frac{1 + \kappa^2}{2}}. \tag{100}$$

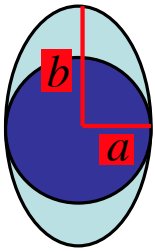

Fig. 7 Elongated plasma cross section $\kappa = b/a > 1$.

2.3.3 Force Balance in the Major Radius Direction

As implied by the virial theorem, some forms of the magnetic field by external coils are required to confine the plasma. This requirement is not obvious in the Grad-Shafranov equation as the magnetic field is assumed to be generated by currents in both the plasma and the external coils. Here we discuss the force balance in the R direction to explicitly calculate the required vertical field to be generated by external sources.

The three forces acting on the toroidal plasma in the R direction are:

1. Hoop force, F_h, due to poloidal field, which is expanding,
2. Plasma pressure force, F_p, which is expanding,
3. Force due toroidal field, F_m, which can be either expanding or contracting depending on β_p.

The required vertical field, B_V, can then be calculated by balancing $I_p \times B_V$ with the sum of the above three forces. Below, we calculate each of these three forces.

Hoop Force, F_h. The energy of a current-carrying loop is given by $\frac{1}{2}L_pI_p^2$ where L_p is the self-inductance of the current ring,

$$L_p = \mu_0 R\left(\ln\frac{8R}{a} - 2 + \frac{l_i}{2}\right); \quad l_i = \frac{\langle B_\theta^2\rangle}{B_\theta^2(a)}. \tag{101}$$

The hoop force can be calculated from the radial expansion of the current ring to reduce its energy while keeping its flux L_pI_p constant,

$$\begin{aligned} F_h &= -\frac{\partial}{\partial R}\left(\frac{L_pI_p^2}{2}\right)\bigg|_{L_pI_p=\text{const}} = -\frac{1}{2}\frac{\partial}{\partial R}\left(\frac{(L_pI_p)^2}{L_p}\right)\bigg|_{L_pI_p=\text{const}} \\ &= -\frac{(L_pI_p)^2}{2}\frac{\partial}{\partial R}\left(\frac{1}{L_p}\right) = \frac{I_p^2}{2}\frac{\partial L_p}{\partial R} = \frac{\mu_0 I_p^2}{2}\left(\ln\frac{8R}{a} - 1 + \frac{l_i}{2}\right). \end{aligned} \tag{102}$$

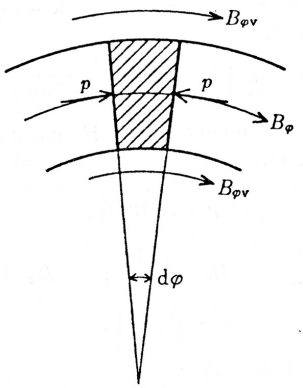

Fig. 8 Forces acting on a toroidal plasma.

Pressure Force, F_p. The plasma pressure force acting on its cross-section is $\langle p \rangle \pi a^2$. From Fig. 8, for each small wedge of $d\psi$, the pressure forces from both sides do not exactly cancel due to toroidal curvature, leading to a residual radial force of $\langle p \rangle \pi a^2 d\psi$. Integrating over 2π, we have

$$F_p = \langle p \rangle \pi a^2 2\pi = \frac{\langle p \rangle}{B_\theta^2(a)/2\mu_0} \frac{B_\theta^2(a)}{2\mu_0} 2\pi^2 a^2 = \frac{\mu_0 I_p^2}{4} \beta_p, \tag{103}$$

where $2\pi a B_\theta(a) = \mu_0 I_p$ and we have used the definition of β_p.

Force due toroidal field, F_m. The expanding force of a toroidal field is due to larger B_ϕ pressure on the inner side of the torus (recall $B_\phi \propto 1/R$), and the contracting force is due to the B_ϕ tension force. In a vacuum, they exactly balance but in plasma, the net radial force depends on whether β_p is larger or smaller than unity, see Fig. 6. When $\beta_p > 1$, $\left\langle B_\phi^2 \right\rangle$ is smaller than $B_\phi^2(a)$, causing the net force points radially outward due to a weaker tension force. The opposite happens when $\beta_p < 1$. Using Eq. (97), we have

$$F_m = \frac{B_\phi^2(a)}{2\mu_0} \pi a^2 2\pi - \frac{\left\langle B_\phi^2 \right\rangle}{2\mu_0} \pi a^2 2\pi = \frac{\mu_0 I_p^2}{4} \left(\beta_p - 1\right), \tag{104}$$

where the first term is due to the expanding B_ϕ pressure force while the second term is due to the contracting tension force.

A vertical field, B_V, is needed to balance all three forces,

$$2\pi R I_p B_V = F_h + F_p + F_m. \tag{105}$$

Substituting the forces that we have calculated before, we get

$$B_V = \frac{\mu_0 I_p}{4\pi R}\left(\ln\frac{8R}{a} + \beta_p + \frac{l_i}{2} - \frac{3}{2}\right). \tag{106}$$

This vertical field can either be provided by a set of "vertical field coils" or by the eddy currents flowing in a conducting shell that encloses plasma. In the latter case, however, the eddy currents will eventually decay, resulting in a merely transient vertical field.

2.3.4 Various Toroidal Configurations

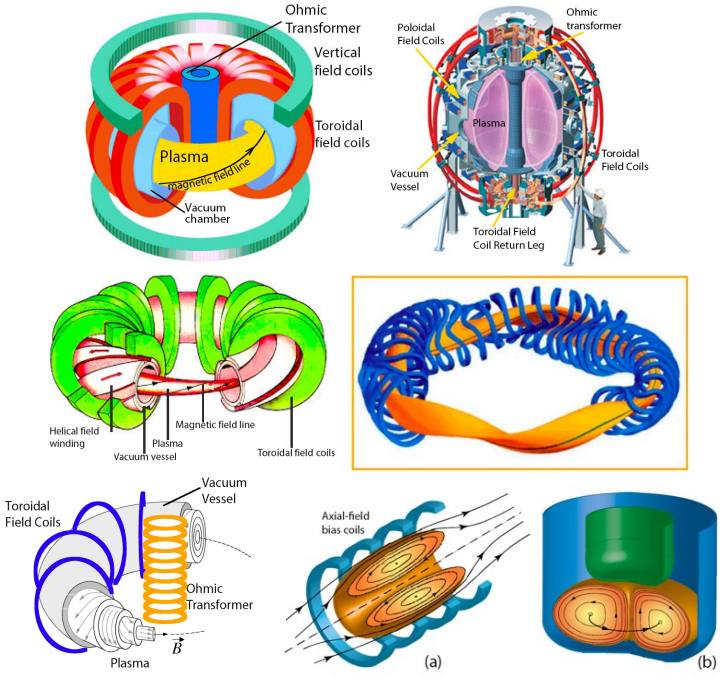

Fig. 9 Configurations for tokamak, Spherical Torus (ST), two versions of stellarators, Reversed Field Pinch (RFP), Field Reversed Configuration (FRC), and spheromak.

Below we briefly comment on several toroidal confinement configurations.

Tokamak is the most advanced and mature configuration that the ITER project is based. However, it is relatively large and complex with a moderate confinement efficiency. In addition, it requires plasma current to be driven for steady-state operation.

Spherical Torus (ST) is a tokamak at lower aspect ratios making it more compact. It has higher betas or better confinement efficiencies, thus possibly

more economical for fusion reactors. But it is less developed than tokamaks and more restrictive in available space.

Stellarator provides rotational transform via external coils that can be necessarily complicated with larger devices. This configuration does not require current drive and has less free energy for instabilities.

Reversed Field Pinch (RFP) is a tokamak at a much larger ($\sim$ 10 times) plasma current or low q. It requires much weaker external toroidal fields giving a significant advantage but has many MHD instabilities to avoid.

Spheromak is an RFP at the unity aspect ratio. Its main advantage is that it does not require a center stack. However, it also suffers more global instabilities.

Field Reversed Configuration (FRC) is a spheromak without a toroidal field. It has the highest plasma beta closer to unity but more free plasma energy for instabilities. Classical FRCs do not have flux surfaces due to their field lines forming loops within their poloidal planes.

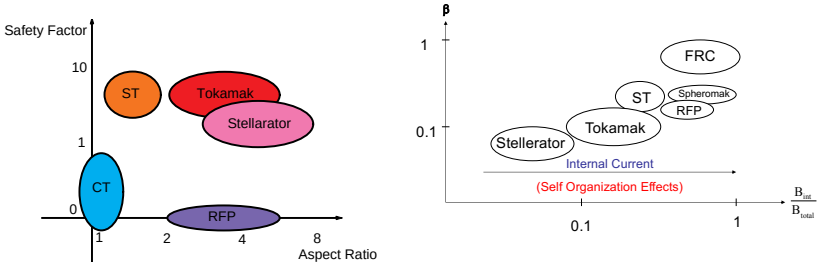

Fig. 10 Locations of various configurations in the parameter space of aspect ratio and safety factor, and also in the parameter space of ratio of the magnetic field generated internally to the total field and plasma beta.

Figure 10 shows rough locations of these configurations in the parameter space of the aspect ratio and the safety factor and the parameter space of the ratio of internal to total magnetic field and the plasma beta. There is a general tendency for higher plasma beta in systems with a higher proportion of internally generated magnetic fields. The plasmas in such systems are more often "self-organized" with the magnetic configurations strongly influenced by the plasma dynamics. We will discuss this concept further later in the class.

2.4 Summary

- Conservation laws of ideal MHD plasmas on flux, mass, momentum, and energy.
- Virial theorem: A plasma cannot be confined by its self-generated magnetic field but can by self-generated gravity.

- Magnetostatic equilibrium is generally given by the Grad-Shafranov equation in 2D for axisymmetric toroidal systems. General cases in 1D are screw pinches which include theta pinch and Z pinch as special cases.
- Characteristics of toroidal confinement systems
  - A simple toroidal field cannot confine plasma.
  - Safety factor and three types of field lines in toroidal plasmas.
  - Poloidal beta informs paramagnetism or diamagnetism of the plasma.
  - Plasma total beta or toroidal beta depends on the geometry and shape of a toroidal plasma.
- A vertical field is needed to balance the expanding radial forces.
- Various toroidal configurations are briefly discussed.

2.5 Further Readings

- Chapters 3-6 in Freidberg (2014)
- Chapter 4 in Kulsrud (2005)
- Chapters 4 and 15 in Miyamoto (2016)
- Chapter 3 in Wesson (2011)

2.6 Homework Problem Set 2

1. Virial theorem with self-gravity
   (a) Prove the identity:

$$\boldsymbol{\nabla} \cdot (\boldsymbol{r} \cdot \boldsymbol{T}) = \boldsymbol{r} \cdot (\boldsymbol{\nabla} \cdot \boldsymbol{T}) + \text{Trace}(\boldsymbol{T}). \tag{107}$$

   (b) When gravity is important such as in the sun, we need to add the gravitational force density $\rho \boldsymbol{g}$ to the equation of motion. In the presence of a nearby massive body, $\boldsymbol{g}$ is a constant vector. When the system is influenced by its gravity (also known as a self-gravitating system), $\boldsymbol{g}$ will vary according to

$$\boldsymbol{g} = -\boldsymbol{\nabla}\phi, \tag{108}$$

   where gravitational potential ϕ satisfies

$$\nabla^2 \phi = 4\pi G \rho. \tag{109}$$

   Here G is the gravitational constant. Prove the corresponding stress tensor is given by

$$\boldsymbol{T}_g = \frac{\boldsymbol{\nabla}\phi\boldsymbol{\nabla}\phi}{4\pi G} - \frac{(\boldsymbol{\nabla}\phi)^2}{8\pi G}\boldsymbol{I}. \tag{110}$$

   (c) Generalize Virial Theorem to include self-gravity and show that gravity can confine plasma (and magnetic field!).

2. Z-pinch equilibrium and virial theorem
   Consider a static ideal MHD Z-pinch equilibrium with

$$j(r) = j_0 \frac{r^2/a^2}{(1 + r^2/a^2)^3}, \tag{111}$$

   where j_0 is a constant.
   (a) Calculate $B_\theta(r)$ and $p(r)$. Express your answers in terms of I, the total current. Sketch the fields and the currents as a function of r.
   (b) Calculate the averaged "engineering beta", which is the ratio of the average plasma pressure to the external magnetic field pressure, as a figure of merit for reactor design.
   (c) Since $j(r)$ vanishes when $r \to \infty$, Z-pinch is apparently confined by its own current. Doesn't this violate the virial theorem? Explain.

3 Steady Flows

In this lecture, we will discuss **steady flows**, which have no time dependence, in a variety of situations of both fluid mechanics and plasma physics, including liquid metals, solar wind, and tokamaks. Steady flows serve as the "base state", based on which stability analyses are performed as the time-dependent response to initial perturbations. This phenomenon is equivalent to the equilibrium states of a magnetically confined plasma, which is subject to stability analysis against initial perturbations.

3.1 Some Useful Concepts in Fluid Dynamics

3.1.1 Bernoulli's Equation

We begin with a set of useful concepts in fluid dynamics governed by Navier-Stokes equation (Kundu et al, 2015, Ch.4),

$$\left(\frac{\partial}{\partial t} + \boldsymbol{V}\cdot\boldsymbol{\nabla}\right)\boldsymbol{V} = -\frac{\boldsymbol{\nabla} p}{\rho} - \boldsymbol{\nabla}\boldsymbol{\Phi} + \nu\nabla^2\boldsymbol{V}, \tag{112}$$

where Φ is the gravitational potential. For simplicity, here we assume incompressibility, which also reduces the continuity equation to constant density, ρ, and divergence free of $\boldsymbol{V}$,

$$\boldsymbol{\nabla}\cdot\boldsymbol{V} = 0. \tag{113}$$

Using vector identity

$$(\boldsymbol{V}\cdot\boldsymbol{\nabla})\,\boldsymbol{V} = \boldsymbol{\nabla}\left(\frac{V^2}{2}\right) - \boldsymbol{V}\times\boldsymbol{\nabla}\times\boldsymbol{V}, \tag{114}$$

Eq. (112) becomes,

$$\frac{\partial\boldsymbol{V}}{\partial t} + \boldsymbol{\nabla}\left(\frac{V^2}{2} + \frac{p}{\rho} + \Phi\right) = \boldsymbol{V}\times\boldsymbol{\omega}, \tag{115}$$

for inviscid flows with $\nu = 0$ and defining $\boldsymbol{\omega} \equiv \boldsymbol{\nabla}\times\boldsymbol{V}$ as the vorticity. For irrotational flows where $\boldsymbol{\omega} = 0$, velocity can be expressed using velocity potential ϕ such that $\boldsymbol{V} = \boldsymbol{\nabla}\phi$. The above equation reduces to the **Bernoulli's equation**,

$$\boldsymbol{\nabla}\left(\frac{\partial\phi}{\partial t} + \frac{V^2}{2} + \frac{p}{\rho} + \Phi\right) = 0, \tag{116}$$

which states that the sum of the four quantities within the parentheses remains constant throughout the flow. Bernoulli's equation has been used widely in fluid dynamics, for example, in Pitot tube that measures velocity in a flow by comparing pressure at a stagnation point where $\boldsymbol{V} = 0$ to the ambient pressure with flow while keeping other quantities unchanged.

3.1.2 Kelvin's Circulation Theorem

We can define the circulation Γ of the velocity-field of a flow along a closed loop C as

$$\Gamma \equiv \oint_C \boldsymbol{V} \cdot d\boldsymbol{l} = \int \boldsymbol{\omega} \cdot d\boldsymbol{S}, \tag{117}$$

which is also equivalent to the flux of vorticity passing through a surface $\boldsymbol{S}$ enclosed by C. **Kelvin's circulation theorem** states that Γ remain conserved in inviscid flows such that,

$$\frac{d\Gamma}{dt} = 0. \tag{118}$$

The proof of this theorem is as follows. The rate of change for the circulation can be written into two parts:

$$\frac{d\Gamma}{dt} = \oint_C \frac{d\boldsymbol{V}}{dt} \cdot d\boldsymbol{l} + \oint_C \boldsymbol{V} \cdot \frac{d\,(d\boldsymbol{l})}{dt}. \tag{119}$$

Using the inviscid version of Eq. (112), the first part will vanish:

$$\oint_C \frac{d\boldsymbol{V}}{dt} \cdot d\boldsymbol{l} = -\oint_C \left(\frac{\boldsymbol{\nabla} p}{\rho} + \boldsymbol{\nabla \Phi} \right) \cdot d\boldsymbol{l} = -\frac{1}{\rho} \oint_C dp - \oint_C d\Phi = 0. \tag{120}$$

The proof completes as the second part will also vanish as

$$\oint_C \boldsymbol{V} \cdot \frac{d\,(d\boldsymbol{l})}{dt} = \oint_C \boldsymbol{V} \cdot d\boldsymbol{V} = \frac{1}{2} \oint_C d\left(V^2\right) = 0. \tag{121}$$

Kelvin's circulation theorem in the ideal fluid is analogous to the magnetic flux conservation in the ideal MHD. The vorticity field behaves similarly to the magnetic field as both are divergence-free. The vortex line and the vortex tube correspond to the magnetic field line and the flux tube. In addition, they share many other important concepts as well.

3.1.3 Vorticity Equation

One such example of the similarity can be seen from the time evolution of vorticity. Equation (114) can be rewritten as

$$(\boldsymbol{V} \cdot \boldsymbol{\nabla})\, \boldsymbol{V} = \boldsymbol{\nabla} \left(\frac{V^2}{2} \right) + \boldsymbol{\omega} \times \boldsymbol{V}. \tag{122}$$

Using this equation and taking the curl of Eq. (112) in the nearly incompressible limit, or the so-called Boussinesq approximation (Kundu et al, 2015, Ch.4), yield

$$\frac{\partial \boldsymbol{\omega}}{\partial t} = \boldsymbol{\nabla} \times (\boldsymbol{V} \times \boldsymbol{\omega}) + \frac{\boldsymbol{\nabla} \rho \times \boldsymbol{\nabla} p}{\rho^2} + \nu \nabla^2 \boldsymbol{\omega}, \tag{123}$$

where we have used

$$\boldsymbol{\nabla} \times \left(\frac{\boldsymbol{\nabla} p}{\rho} \right) = \boldsymbol{\nabla} \left(\frac{1}{\rho} \right) \times \boldsymbol{\nabla} p + \frac{1}{\rho} \boldsymbol{\nabla} \times (\boldsymbol{\nabla} p) = - \frac{\boldsymbol{\nabla} \rho \times \boldsymbol{\nabla} p}{\rho^2}. \tag{124}$$

The first and third terms on the RHS of Eq. (123) have exactly the same shapes as the terms in the magnetic field evolution equation of resistive MHD. The second term on the RHS of Eq. (123) represents the vorticity generation due to baroclinic effects, *i.e.* the gradient of ρ does not align with the gradient of p. This second term explains vortex ring generation when a gas is heated locally.

However, there is also an analog of the baroclinic effects in MHD. Consider a simplified generalized Ohm's law,

$$\boldsymbol{E} + \boldsymbol{V} \times \boldsymbol{B} = \eta \boldsymbol{j} - \frac{\boldsymbol{\nabla} p_e}{e n_e}, \tag{125}$$

where the electron pressure term is kept due to the conditions such as high β_e. Substituting $\boldsymbol{E}$ in Faraday's law yields a similar term called the Biermann battery effect in

$$\frac{\partial \boldsymbol{B}}{\partial t} = \boldsymbol{\nabla} \times (\boldsymbol{V} \times \boldsymbol{B}) + \frac{\boldsymbol{\nabla} n_e \times \boldsymbol{\nabla} p_e}{e n_e^2} + \frac{\eta}{\mu_0} \nabla^2 \boldsymbol{B}. \tag{126}$$

The Biermann battery term can be used to explain magnetic field generation in plasmas produced by lasers heating a local spot on a solid target.

3.1.4 Boundary Layer

One of the important concepts in fluid dynamics is the boundary layer connecting ideal fluid to non-slippery boundaries. This concept was introduced by Ludwig Prandtl, who wanted to explain the finite drag force measured in flows where viscosity should be negligibly small. Globally, fluid can be nearly ideal with negligible viscosity (or resistivity in MHD fluids), meaning that Reynolds number Re (or magnetic Reynolds number Rm or Lundquist number S) defined globally is large. However, locally close to the boundary, flow needs to slow down to match the non-slip condition. The slowed-down flow forms a surface layer next to the boundary with a large shear that can generate the measured drag force. Thus, the locally defined Reynolds number becomes small. The boundary layer concept separates flow into two regions: the outer region where viscosity is unimportant and the inner region where viscosity is important. This idea spreads into other fields including plasma physics.

In two dimension, the components of Navier-Stokes equation for velocity field (u, v) are given by

$$u \frac{\partial u}{\partial x} + v \frac{\partial u}{\partial y} = - \frac{1}{\rho} \frac{\partial p}{\partial x} + \nu \left(\frac{\partial^2 u}{\partial x^2} + \frac{\partial^2 u}{\partial y^2} \right), \tag{127}$$

$$u\frac{\partial v}{\partial x} + v\frac{\partial v}{\partial y} = -\frac{1}{\rho}\frac{\partial p}{\partial y} + \nu\left(\frac{\partial^2 v}{\partial x^2} + \frac{\partial^2 v}{\partial y^2}\right), \tag{128}$$

$$\frac{\partial u}{\partial x} + \frac{\partial v}{\partial y} = 0 \tag{129}$$

for the three variables u, v, and p. Instead of solving these equation exactly, we will perform *boundary layer analysis* focusing on the relative magnitudes between the variables.

First, the length scale in x direction is L, which is much longer than the boundary layer thickness δ shown in Fig. 11. Therefore, from the continuity equation, u should be much larger than v with $u \sim U_\infty \gg v$ such that

$$\frac{\delta}{L} \sim \frac{v}{U_\infty} \;\rightarrow\; v \sim \frac{\delta}{L}U_\infty. \tag{130}$$

Using these relations, Eq. (127) can be evaluated as

$$\frac{U_\infty^2}{L} + \frac{\delta}{L}U_\infty^2\frac{1}{\delta} = -\frac{1}{\rho}\frac{\partial p}{\partial x} + \nu\left(\frac{U_\infty}{L^2} + \frac{U_\infty}{\delta^2}\right), \tag{131}$$

where the two left terms are comparable while the last term on RHS dominates over the second to last term. The pressure term $(1/\rho)\partial p/\partial x$ should be comparable in the region away from the boundary and scale as U_∞^2/L. Therefore, the required δ in the boundary layer to make the viscous term important is

$$\frac{U_\infty^2}{L} \sim \nu\frac{U_\infty}{\delta^2} \;\rightarrow\; \delta \sim \sqrt{\frac{\nu L}{U_\infty}} = \frac{L}{\sqrt{Re}}. \tag{132}$$

Since typically $Re \gg 1$, the corresponding δ is very thin. Therefore, even if the global system is nearly ideal, local dissipation can be important by forming thin (boundary) layers. Note that if we use δ instead of L to define the "local" Reynolds number, $Re_{\rm local} = \sqrt{Re}$ becomes much smaller than the global Re. However, this $Re_{\rm local}$ can still be large, causing the boundary layer to be unstable and even turbulent. In MHD, boundary layers are important for tearing mode instability and magnetic reconnection, which we will discuss later in the class.

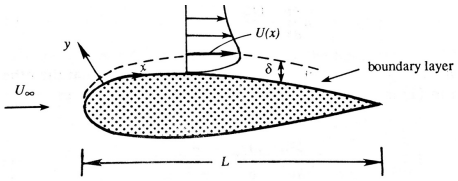

Fig. 11 Boundary layer with a thickness of δ and its coordinate system (x, y).

3.2 Steady Flows in Fluid Dynamics

A few representative one-dimensional laminar steady flows are described first, followed by liquid metal flows under the influence of a magnetic field.

3.2.1 Flows Between Parallel Plates

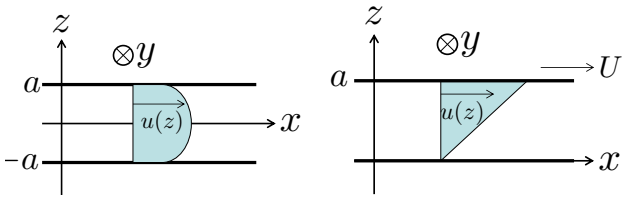

Fig. 12 Flows driven between parallel plates. (left panel) Plane Poiseuille flow driven by a constant pressure gradient in x direction. (right panel) Plane Couette flow driven by a moving plate and a stationary plate.

Starting from the simplified one-dimensional Navier-Stokes equation, Eq. (112), without gravity

$$\left(\frac{\partial}{\partial t}+u\frac{\partial}{\partial x}\right)u=-\frac{1}{\rho}\frac{\partial p}{\partial x}+\nu\left(\frac{\partial^2}{\partial x^2}+\frac{\partial^2}{\partial z^2}\right)u, \tag{133}$$

all terms except the first and last ones on the RHS will vanish when the flow is driven only by a pressure gradient,

$$\frac{\partial^2 u}{\partial z^2}=\frac{1}{\rho\nu}\frac{\partial p}{\partial x}. \tag{134}$$

This equation has solutions for plane Poiseuille flows,

$$u=\frac{1}{2\rho\nu}\frac{\partial p}{\partial x}z^2+Az+B=\frac{1}{2\rho\nu}\frac{\partial p}{\partial x}\left(z^2-a^2\right), \tag{135}$$

where the constant A is zero due to the symmetry and the constant B can be determined using the non-slip boundary conditions $u(a)=u(-a)=0$ at the two parallel plates.

The plane Couette flow is when the flow is driven by a moving plate at $z=a$ with a speed of U with a stationary plate at $z=0$ with no pressure gradient ($\partial p/\partial x=0$). For this case, the constants of integration becomes $A=U/a$ and $B=0$, which can be determined by substituting $u(0)=0$ and $u(a)=U$ giving:

$$u=\frac{U}{a}z. \tag{136}$$

3.2.2 Pipe Flows

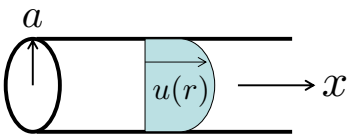

Fig. 13 Flow driven by a constant pressure gradient in a pipe.

To derive the solution for flow driven by the pressure gradient in a circular pipe, we need to use the Navier-Stokes equation in cylindrical coordinates:

$$\left(\frac{\partial}{\partial t}+u\frac{\partial}{\partial x}\right)u=-\frac{1}{\rho}\frac{\partial p}{\partial x}+\frac{\nu}{r}\frac{\partial}{\partial r}\left(r\frac{\partial u}{\partial r}\right). \tag{137}$$

The solution is given by,

$$u(r)=\frac{1}{4\rho\nu}\frac{\partial p}{\partial x}+A\ln r+B. \tag{138}$$

Here, the constants of integration $A=0$ and $B=-a^2/4\rho\nu(\partial p/\partial x)$ can be determined by enforcing $u(a)=0$ and $u(0)$ is finite, leading to the parabolic solution

$$u(r)=\frac{1}{4\rho\nu}\frac{\partial p}{\partial x}\left(r^2-a^2\right). \tag{139}$$

3.2.3 Circular Couette Flows

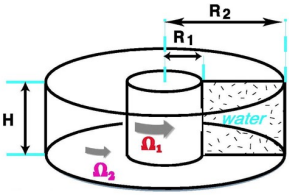

Fig. 14 Circular Couette flow between concentric cylinders.

Rotating flow between two infinitely long concentric cylinders needs to satisfy the force balance in the radial direction,

$$\frac{u_\theta^2}{r}=\frac{1}{\rho}\frac{\partial p}{\partial r}. \tag{140}$$

The flow profile is then determined by the azimuthal component of the Navier-Stokes equation, Eq. (112),

$$\frac{\partial u_\theta}{\partial t} + \frac{u_r}{r}\frac{\partial (r u_\theta)}{\partial r} + \frac{u_\theta}{r}\frac{\partial u_\theta}{\partial \theta} + u_z \frac{\partial u_\theta}{\partial z} = -\frac{1}{\rho r}\frac{\partial p}{\partial \theta} + \nu\left(\frac{1}{r^2}\frac{\partial}{\partial r}\left[r^3 \frac{\partial}{\partial r}\left(\frac{u_\theta}{r}\right)\right] + \frac{1}{r^2}\frac{\partial^2 u_\theta}{\partial \theta^2} + \frac{\partial^2 u_\theta}{\partial z^2} + \frac{2}{r^2}\frac{\partial u_r}{\partial \theta}\right). \quad (141)$$

Under the conditions that $u_r = 0$, $\partial/\partial t = 0$, and $\partial/\partial\theta = \partial/\partial z = 0$, this equation simplifies to

$$\frac{\partial}{\partial r}\left[r^3 \frac{\partial}{\partial r}\left(\frac{u_\theta}{r}\right)\right] = 0. \quad (142)$$

This can then be solved to give

$$u_\theta = Ar + \frac{B}{r}, \quad (143)$$

where the constants A and B are determined by boundary conditions given in Fig. 14,

$$u_\theta(R_1) = \Omega_1 R_1, \quad (144)$$
$$u_\theta(R_2) = \Omega_2 R_2, \quad (145)$$

to yield

$$A = \frac{\Omega_2 R_2^2 - \Omega_1 R_1^2}{R_2^2 - R_1^2}, \quad (146)$$
$$B = \frac{R_1^2 R_2^2 (\Omega_1 - \Omega_2)}{R_2^2 - R_1^2}. \quad (147)$$

3.2.4 Hartmann Flow

When a magnetic field, B_0, is imposed in the z direction to plane Poiseuille flow shown in Fig. 15, the profile is significantly modified due to Lorentz force if the liquid is electrically conducting. The resulting flow is called Hartmann flow in steady state (Müller and Bühler, 2001, Ch.4). Adding the Lorentz force, Eq. (134) becomes

$$\frac{\partial^2 u}{\partial z^2} = \frac{1}{\rho\nu}\frac{\partial p}{\partial x} - \frac{j_y B_0}{\rho\nu}, \quad (148)$$

where j_y can be determined by the resistive MHD Ohm's law in the y direction

$$j_y = \frac{E_y - u B_0}{\eta}. \quad (149)$$

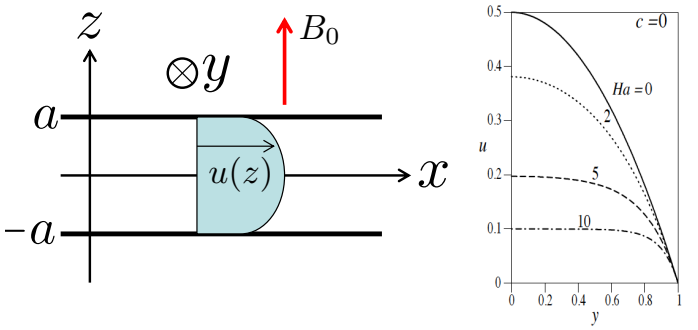

Fig. 15 (left panel) Hartmann flow between parallel plates driven by a constant pressure gradient in the x direction across magnetic field in the z direction. (right panel) Hartmann flow profile flattens as Ha increases.

Here E_y is a constant in the steady state, which can be seen from Faraday's law in the x direction,

$$0 = \frac{\partial B_x}{\partial t} = (\boldsymbol{\nabla} \times \boldsymbol{E})_x = -\frac{\partial E_y}{\partial z}. \tag{150}$$

Therefore, Eq. (148) becomes

$$\frac{\partial^2 u}{\partial z^2} = \frac{1}{\rho\nu}\frac{\partial p}{\partial x} - \frac{E_y B_0}{\rho\nu\eta} + \frac{B_0^2}{\rho\nu\eta}u, \tag{151}$$

where the first two terms on RHS are constant and can be combined. The solutions to this equation depend on the conductivities of the two parallel plates, which for insulating parallel plates simplifies to (Müller and Bühler, 2001, Ch.4)

$$u(z) = u_0\left(1 - \frac{\cosh Ha(z/a)}{\cosh Ha}\right), \tag{152}$$

where the Hartmann number is defined

$$Ha \equiv \frac{aB_0}{\sqrt{\rho\nu\eta}}. \tag{153}$$

As shown in Fig. 15, the flow profile significantly flattens as Ha increases. The resulting boundary layers, called Hartmann layers, appear at $z = \pm a$ with the thickness of $\mathcal{O}(a/Ha)$.

3.3 Solar Wind

The first question that came up for the solar atmosphere is whether it is confined statically by gravity as in Earth's atmosphere. The answer to the solar atmosphere confinement problem is, surprisingly, related to its hot temperature, which in itself is a well-known and well-studied but still unsolved puzzle.

Assuming a spherically symmetric system in a steady state, the continuity and momentum equations for radial velocity u are given by

$$\frac{d\left(\rho u r^2\right)}{dr} = 0, \tag{154}$$

$$\rho u \frac{du}{dr} = -\frac{dp}{dr} - \rho \frac{GM_\odot}{r^2}, \tag{155}$$

where $G = 6.6743 \times 10^{-11}\mathrm{m}^3\mathrm{kg}^{-1}\mathrm{s}^{-2}$ is the gravitational constant and $M_\odot = 1.99 \times 10^{30}\mathrm{kg}$ is the solar mass. For simplicity, we assume $T_e = T_i = T$ such that $\rho = (m/2T)p$ with m denoting the ion mass. To seek static solutions, we set $u = 0$ that leads to radial force balance

$$\frac{1}{p}\frac{dp}{dr} = -\frac{GM_\odot m}{2T}\frac{1}{r^2}. \tag{156}$$

This equation has solutions in the form of

$$\ln p = \frac{GM_\odot m}{2T}\frac{1}{r} + C. \tag{157}$$

The constant C is determined by the plasma pressure p_0 at the solar surface of $r = R_\odot = 6.96 \times 10^8\mathrm{m}$ giving us,

$$p(r) = p_0 \exp\left[\frac{GM_\odot m}{2T}\left(\frac{1}{r} - \frac{1}{R_\odot}\right)\right]. \tag{158}$$

Assuming $h = r - R_\odot \ll R_\odot$, we can approximate

$$\frac{1}{r} = \frac{1}{R_\odot + h} = \frac{1}{R_\odot(1 + h/R_\odot)} \approx \frac{1}{R_\odot}\left(1 - \frac{h}{R_\odot}\right), \tag{159}$$

giving us

$$p(r) \approx p_0 \exp\left(-\frac{h}{\lambda}\right), \tag{160}$$

where $\lambda = 2TR_\odot^2/GM_\odot m$ is the gravitational pressure scale height. If we use a coronal temperature of 100 eV, λ is about $R_\odot/10$ that is roughly consistent with observations.

In the opposite limit when $r \gg R_\odot$, Eq. (158) becomes

$$p(\infty) = p_0 \exp\left(-\frac{GM_\odot m}{2TR_\odot}\right) \approx p_0 \exp(-8) \approx 5\mathrm{Pa}, \tag{161}$$

assuming $T = 100$ eV. This value is several orders of magnitude higher than the interstellar medium pressure of $10^{-13} - 10^{-14}$ Pa (Kivelson and Russell, 1995). The mismatch shows that a static solar atmosphere cannot exist; plasma must constantly flow out as the solar wind, as predicted by Parker in 1958.

Let's return to the Eqs. (154) and (155) to solve for u. From Eq. (154), nur^2 is a constant c such that $n = c/ur^2$, which leads to

$$\frac{dn}{dr} = -\frac{2c}{ur^3} - \frac{c}{u^2r^2}\frac{du}{dr} = -\frac{2n}{r} - \frac{n}{u}\frac{du}{dr}. \tag{162}$$

Rewriting Eq. (155) using $\rho = (m/2T)p$ yields

$$u\frac{du}{dr} = -\frac{2T}{mn}\frac{dn}{dr} - \frac{GM_\odot}{r^2} \tag{163}$$

$$= \frac{2T}{m}\left(\frac{2}{r} + \frac{1}{u}\frac{du}{dr}\right) - \frac{GM_\odot}{r^2}, \tag{164}$$

which can be reorganized to

$$\left(u^2 - \frac{2T}{m}\right)\frac{1}{u}\frac{du}{dr} = \frac{4T}{mr} - \frac{GM_\odot}{r^2}. \tag{165}$$

On the other hand, Eq. (164) can be directly integrated to

$$\frac{1}{2}u^2 = \frac{4T}{m}\ln r + \frac{2T}{m}\ln u + \frac{GM_\odot}{r} + c', \tag{166}$$

where constant c' is determined by the special solution of $u_c = \sqrt{2T/m}$ at $r_c = GM_\odot m/4T$ to yield the full solutions:

$$u^2 - u_s^2\left[1 + \ln\left(\frac{u}{u_s}\right)^2\right] = 4u_s^2 \ln\frac{r}{r_c} + 2GM_\odot\left(\frac{1}{r} - \frac{1}{r_c}\right), \tag{167}$$

where we define sound speed as $u_s = \sqrt{2T/m}$. These numerical solutions were given by Parker (1958) at the age of 30 in Fig. 16 where case 1 is the solar breeze solution and case 2 is the solar wind solution. In the very next year, the solar wind was discovered by the Luna 1 satellite of the Soviet Union, the first satellite to escape from the Earth's gravity in January 1959. Recently, 60 years later, Parker Solar Probe was launched on August 12, 2018, to reach the closest distance from the sun at $\sim 10R_\odot$ with the aim to study solar coronal heating and solar wind acceleration.

Despite the solar wind velocity profile being purely radial, its streamlines are not. This is because the sun rotates once every 25.4 days on average. As a result, the streamline forms a spiral, called Parker spiral, as shown in Fig. 17, behaving similarly to a rotating water sprinkler. The trajectory of the spiral is determined by

$$\frac{u_\phi}{u_r} = \frac{\omega r}{u} = \frac{r d\phi}{dr}, \tag{168}$$

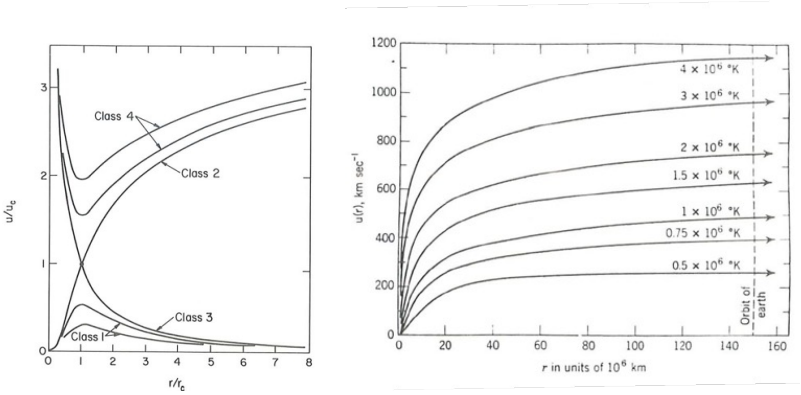

Fig. 16 Solar breeze (case 1) and solar wind (case 2) solutions.

where ω is the angular speed of solar rotation. We can then solve this equation to give,

$$r - R_\odot = \frac{u}{\omega}(\phi - \phi_0), \tag{169}$$

where ϕ_0 is the angle where the solar wind is first launched. The streamline of solar wind is purely radial when it is launched from the solar surface and gradually picks up azimuthal speed when it is further out. By the time it reaches Earth, the angle is about 45° and becomes more azimuthal further away from the sun.

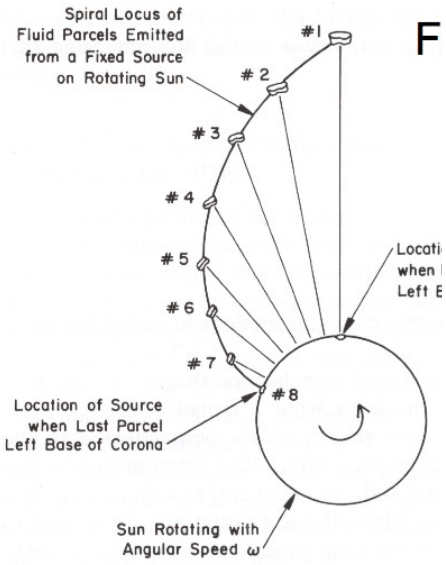

Fig. 17 Parker spiral.

On large scales, the solar wind plasma is nearly ideal, causing its magnetic field lines to be frozen-in to the streamlines,

$$\frac{B_\phi}{B_r} = \frac{u_\phi}{u_r} = \frac{\omega r}{u}. \tag{170}$$

The radial magnetic field decreases from B_0 at $r = R_\odot$ following

$$B_r(r) = B_0 \left(\frac{R_\odot}{r}\right)^2. \tag{171}$$

In contrast, the azimuthal field decreases less as a function of r,

$$B_\theta(r) = B_0 \frac{\omega R_\odot}{u} \frac{R_\odot}{r}. \tag{172}$$

In summary, when $r/R_\odot \gg 1$, $u \sim$ const, and $u_\phi \propto r$, the components of magnetic field scale as $B_r \propto r^{-2}$ and $B_\phi \propto r^{-1}$. The amplification of magnetic fields caused the solar wind to not only become supersonic but also to become super-Alfvénic. Currently, the Parker Solar Probe mission aims to reach the point where the solar wind becomes Alfvénic.

3.4 Rotation in Toroidal Confinement System

Flow in magnetically confined plasma is closely related to the electric field in the system. In toroidal pinches, the plasma current is driven inductively by the toroidal electric field via an Ohmic transformer. The Lorentz force (between the toroidal current and the poloidal field it generates) balances the radially outward pressure force. On the timescales of the transport, the inward $\boldsymbol{E} \times \boldsymbol{B}$ drift balances the radially outward particle diffusion. Both inward forces form the bases of "pinching" that support and confine plasma.

Fusion plasmas are fairly collisionless. Sometimes, it is beneficial to consider the physics picture of such plasma in the two-fluid models, describing the electron and ion fluids separately. The electric field enters radial force balance for each fluids,

$$-en_e \left[E_r + (\boldsymbol{V}_e \times \boldsymbol{B})_r\right] = \frac{dp_e}{dr}, \tag{173}$$

$$en_i \left[E_r + (\boldsymbol{V}_i \times \boldsymbol{B})_r\right] = \frac{dp_i}{dr}, \tag{174}$$

where E_r depends on the chosen frame. Therefore, even at the rest frame of a given species, E_r is finite and is in the order of

$$E_r \sim \frac{1}{en}\frac{dp}{dr} \sim \frac{eT(0)}{a} \sim 10 \text{ keV/m}, \tag{175}$$

where $T(0)$ is the temperature at the center and a is the minor radius. Here E_r is the so-called ambipolar electric field that arises via communications between ions and electrons to maintain charge neutrality. E_r is electrostatic in nature and can be expressed as the gradient of electrostatic potential in the order of $T(0)/e$ at the plasma center relative to its edge value. The sign of E_r contains information on which species is preferably lost through the edge.

Neutral Beam Injection can also deliberately inject angular momentum to cause the plasma to rotate with finite $V_{i\phi}$ in the laboratory frame. Sometimes plasma can "spontaneously" rotate without apparent angular momentum input due to asymmetric momentum losses by ions in the toroidal direction.

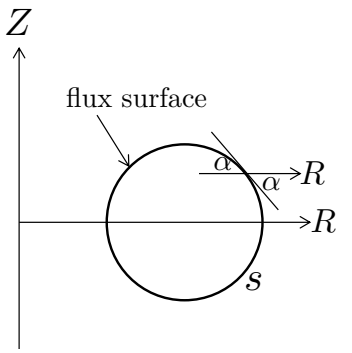

Fig. 18 Finite rotation causes density non-uniformity on the flux surface due to centrifugal effects.

With a finite plasma rotation, due to the centrifugal force, the magnetic axis shifts radially outward beyond the Shafranov shift that we discussed before. For the same reason, the finite ion rotation causes pressure non-uniformity on the flux surfaces. The change is mostly in the plasma density as heat transport is fast along the parallel direction. This invalidates the Grad-Shafranov equation that was derived based on the constant pressure (density) on the flux surfaces.

For a constant angular velocity Ω in the laboratory frame, density and the associated ambipolar electric potential ϕ_a profiles on a given flux surface can be calculated as follows. Since centrifugal force acts only on $+R$ direction shown in Fig. 18), its projection on the tangential direction of a given flux surface s with an angle α is $nm\Omega^2 R\cos\alpha$. Therefore, the force balance on the surface for a constant temperature, T, is given by

$$T\frac{dn}{ds} = nm\Omega^2 R\cos\alpha - qnE_a, \tag{176}$$

where $dn/ds = (dn/dR)\cos\alpha$ and $E_a = -(d\phi_a/dR)\cos\alpha$. Removing $\cos\alpha$ from the above equation yields

$$\frac{1}{n}\frac{dn}{dR} = \frac{m\Omega^2}{T}R - \frac{q}{T}\frac{d\phi_a}{dR}, \tag{177}$$

which can be rewritten as

$$d\ln n = \frac{1}{2}\frac{m\Omega^2 d\left(R^2\right)}{T} - \frac{q d\phi_a}{T}. \tag{178}$$

Integrating this equation yields

$$n = n_0 \exp\left[\frac{\frac{1}{2}m\Omega^2\left(R^2 - R_0^2\right) - q\phi_a}{T}\right], \tag{179}$$

where $n = n_0$ and $\phi_0 = 0$ at $R = R_0$. Therefore, we have an equation for each species, and by ignoring electron mass,

$$n_i = n_0 \exp\left[\frac{\frac{1}{2}m_i\Omega^2\left(R^2 - R_0^2\right) - e\phi_a}{T_i}\right], \tag{180}$$

$$n_e = n_0 \exp\left(\frac{e\phi_a}{T_e}\right). \tag{181}$$

Ambipolar electric potential ϕ_a can be solved by setting $n_e = n_i$,

$$e\phi_a = \frac{T_e}{T_e + T_i}\frac{1}{2}m_i\Omega^2\left(R^2 - R_0^2\right), \tag{182}$$

and the density profile,

$$n = n_0 \exp\frac{M^2}{2}\left[\left(\frac{R}{R_0}\right)^2 - 1\right], \tag{183}$$

where $M = \Omega R_0/\sqrt{(T_e + T_i)/m_i}$ is the Mach number of rotation. If $M \ll 1$ and the minor radius of a flux surface $r \ll R_0$, the density variation on the flux surface is given by

$$\frac{\Delta n}{n_0} \approx M^2\frac{2r}{R_0}. \tag{184}$$

3.5 Summary

- Useful fluid dynamics concepts: Bernoulli's equation, Kelvin's circulation theorem, vorticity equation and its similarity to MHD, and boundary layers formed on non-slip boundaries.
- Steady flows in fluid dynamics: flows between parallel plates, pipe flow, circular Couette flow.
- MHD (liquid metal) flows across the magnetic field in a channel: Hartmann flow and Hartmann layer.
- Solar wind must exist: Parker spiral.
- Rotation and electric field in toroidal pinches.

3.6 Further Readings

- Chapters 5,9,10 in Kundu et al (2015)
- Chapter 4 in Müller and Bühler (2001)
- Chapter 4 in Kivelson and Russell (1995)
- Chapter 3 in Wesson (2011)

3.7 Homework Problem Set 3

1. de Laval nozzle
   (a) The de Laval nozzle is a tube that has a throat in the middle to accelerate a hot gas from a subsonic speed to a supersonic speed, as widely used in rocket engine nozzles and supersonic jet engines. Derive and solve the equation for the gas flow speed.
   (b) Show that de Laval nozzle shares the same working principle with the solar wind acceleration.

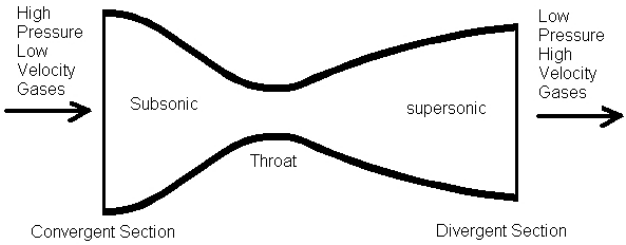

2. Two-fluid model of solar wind
   (a) Derive equations for ion and electron fluids for solar wind and show that the ion equation reduces to Parker's original equation while the electron equation defines ambipolar electric potential. Assuming uniform solar wind temperature of $T_i = T_e = 10\text{eV}$, and plasma density at the solar surface is $n_s = 10^{20}\text{m}^{-3}$ while at local interstellar medium is $n_{lism} = 10^5\text{m}^{-3}$, estimate electric potential at the solar surface relative to that of the local interstellar medium.
   (b) Illustrate how this electric potential modifies gravitational potential for ions and electrons, especially during solar wind acceleration. Discuss the physical insights that you can get by noting that the ion and electron thermal speeds satisfy $v_{th,i} \ll v_\infty \ll v_{th,e}$ in the solar corona where $T_i = T_e = 100\text{eV}$. Here $v_\infty = 6 \times 10^5\text{m s}^{-1}$ is the escape velocity from the solar surface.

3. Hartmann flow
   (a) In the one-dimensional Hartmann flow problem, derive and solve the governing equation for the flow profile.

(b) When boundaries are electrically insulating, the return current has to flow within the MHD fluid. In this case, the total current within the MHD fluid in the direction perpendicular to both the magnetic field and flow vanishes. Determine the maximum flow at the channel center and total flow rate as a function of the Hartmann number. Where does the return current flow? Does it impede or accelerate the flow?

4 Waves, Discontinuities, and Shocks

4.1 Linear MHD Waves

We begin with a local approximation of a large MHD system such that locally the plasma is homogeneous (all spatial derivatives vanish so that ρ_0, p_0, $\boldsymbol{V}_0$ and $\boldsymbol{B}_0$ are constant), static (by taking the local moving frame so $\boldsymbol{V}_0 = 0$), magnetized ($\boldsymbol{B}_0 \neq 0$), and ideal ($\eta = 0$). Then, we assume a given variable, a, deviates from its equilibrium value, a_0, by an infinitesimally small linear perturbation, a_1, such that

$$a = a_0 + a_1; \quad a_1 \ll a_0. \tag{185}$$

When two variables, say a and b, multiply, we have

$$ab = a_0 b_0 + (a_1 b_0 + a_0 b_1) + a_1 b_1 \tag{186}$$

where $a_0 b_0$, $a_1 b_0 + a_0 b_1$, and $a_1 b_1$ are the zeroth (equilibrium), first (linear), and second (nonlinear) order terms, respectively, satisfying

$$a_0 b_0 \gg a_1 b_0 + a_0 b_1 \gg a_1 b_1. \tag{187}$$

Because of these separations between orders, we can formulate equations only within each order, *i.e.*, zeroth order equations involving only equilibrium quantities before perturbations, first-order or linear equations only involving first-order perturbation and higher order terms, etc. Here we are interested in small-amplitude waves in ideal MHD fluid, or linear MHD waves, and thus, we will construct first-order or *linearized* MHD equations.

Substituting all MHD variables with the breakdowns of equilibrium values and perturbed values, the linearized ideal MHD equations are given by

$$\frac{\partial \rho_1}{\partial t} + \boldsymbol{\nabla} \cdot (\rho_0 \boldsymbol{V}_1) = 0, \tag{188}$$

$$\frac{\partial}{\partial t}\left(\frac{p_1}{\rho_0^\gamma} - \gamma \frac{p_0}{\rho_0^{\gamma+1}} \rho_1 \right) = 0, \tag{189}$$

$$\rho_0 \frac{\partial \boldsymbol{V}_1}{\partial t} = \frac{(\boldsymbol{\nabla} \times \boldsymbol{B}_1) \times \boldsymbol{B}_0}{\mu_0} - \boldsymbol{\nabla} p_1, \tag{190}$$

$$\frac{\partial \boldsymbol{B}_1}{\partial t} = \boldsymbol{\nabla} \times (\boldsymbol{V}_1 \times \boldsymbol{B}_0), \tag{191}$$

where all variables have their usual meanings.

Now let us introduce the displacement vector of the fluid as a function of space and time, $\boldsymbol{\xi}(\boldsymbol{r}, t)$. This displacement vector comes from integrating the perturbed velocity, $\boldsymbol{V}_1$, over time as the fluid is displaced from its original

position at $t = 0$

$$\boldsymbol{\xi}(\boldsymbol{r}, t) \approx \int_0^t \boldsymbol{V}_1(\boldsymbol{r}, t')dt', \tag{192}$$

or conversely

$$\boldsymbol{V}_1(\boldsymbol{r}, t) = \frac{d\boldsymbol{\xi}(\boldsymbol{r}, \boldsymbol{t})}{dt} \approx \frac{\partial \boldsymbol{\xi}(\boldsymbol{r}, \boldsymbol{t})}{\partial t}. \tag{193}$$

The approximation here refers to the linearized equations with more elaborate discussions on the displacement vector given in Kulsrud (2005, Ch.4).

Using $\boldsymbol{V}_1$ expressed in $\boldsymbol{\xi}$, all other linear perturbations can also be expressed conveniently in $\boldsymbol{\xi}$:

$$\rho_1 = -\rho_0 \boldsymbol{\nabla} \cdot \boldsymbol{\xi}, \tag{194}$$

$$p_1 = \gamma \frac{p_0}{\rho_0} \rho_1 = -\gamma p_0 \boldsymbol{\nabla} \cdot \boldsymbol{\xi}, \tag{195}$$

$$\boldsymbol{B}_1 = \boldsymbol{\nabla} \times (\boldsymbol{\xi}_1 \times \boldsymbol{B}_0). \tag{196}$$

Thus, the equation of motion, Eq. (190), can be fully expressed in $\boldsymbol{\xi}$,

$$\begin{aligned} \rho_0 \frac{\partial^2 \boldsymbol{\xi}}{\partial t^2} &= \frac{1}{\mu_0} (\boldsymbol{\nabla} \times \boldsymbol{B}_1) \times \boldsymbol{B}_0 - \boldsymbol{\nabla} p_1 \\ &= \frac{1}{\mu_0} \{\boldsymbol{\nabla} \times [\boldsymbol{\nabla} \times (\boldsymbol{\xi} \times \boldsymbol{B}_0)]\} \times \boldsymbol{B}_0 + \gamma p_0 \boldsymbol{\nabla} (\boldsymbol{\nabla} \cdot \boldsymbol{\xi}). \end{aligned} \tag{197}$$

Let us assume all perturbed quantities are the real parts of complex functions of angular frequency ω and wavenumber $\boldsymbol{k}$ in the plane wave decomposition

$$\boldsymbol{\xi} = \Re \left[\tilde{\boldsymbol{\xi}} e^{i(\boldsymbol{k} \cdot \boldsymbol{r} - \omega t)} \right]. \tag{198}$$

Then, the spatial and time derivatives of such quantities are equivalent to the factors of $i\boldsymbol{k}$ and $-i\omega$, respectively. Equation (197) therefore becomes

$$\rho_0 \omega^2 \boldsymbol{\xi} = \frac{1}{\mu_0} \{\boldsymbol{k} \times [\boldsymbol{k} \times (\boldsymbol{\xi} \times \boldsymbol{B}_0)]\} \times \boldsymbol{B}_0 + \gamma p_0 \boldsymbol{k} (\boldsymbol{k} \cdot \boldsymbol{\xi}), \tag{199}$$

or

$$V_{\rm ph}^2 \boldsymbol{\xi} = V_{\rm A}^2 \left\{ \hat{\boldsymbol{k}} \times \left[\hat{\boldsymbol{k}} \times \left(\boldsymbol{\xi} \times \hat{\boldsymbol{b}} \right) \right] \right\} \times \hat{\boldsymbol{b}} + V_{\rm s}^2 \hat{\boldsymbol{k}} \left(\hat{\boldsymbol{k}} \cdot \boldsymbol{\xi} \right), \tag{200}$$

where $V_{\rm ph} (\equiv \omega/k)$, $V_{\rm s} (\equiv \sqrt{\gamma p_0/\rho_0})$, and $V_{\rm A} (\equiv B_0/\sqrt{\mu_0 \rho_0})$, are the wave phase speed, sound speed, and Alfvén speed, respectively. $\hat{\boldsymbol{k}}$ and $\hat{\boldsymbol{b}}$ are the unit vectors of $\boldsymbol{k}$ and $\boldsymbol{B}_0$.

Without loss of generality, we choose the coordinate shown in Fig. 19 where the vectors are given by

$$\hat{\boldsymbol{b}} = (0, 0, 1), \tag{201}$$

$$\boldsymbol{k} = (k_\perp, 0, k_\parallel) = k(\sin\theta, 0, \cos\theta), \tag{202}$$

$$\hat{\boldsymbol{k}} = (\sin\theta, 0, \cos\theta), \tag{203}$$

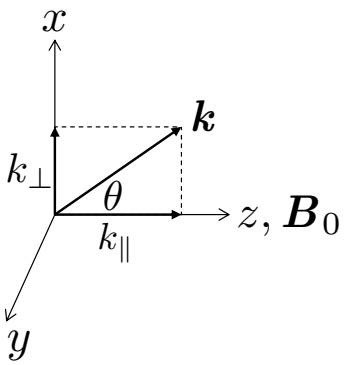

Fig. 19 Coordinate for the magnetic field and wavenumber directions.

$$\boldsymbol{\xi} = (\xi_x, \xi_y, \xi_z). \tag{204}$$

Therefore, we have:

$$\begin{aligned}
\boldsymbol{\xi} \times \hat{\boldsymbol{b}} &= (\xi_y, -\xi_x, 0), \\
\hat{\boldsymbol{k}} \times \left(\boldsymbol{\xi} \times \hat{\boldsymbol{b}}\right) &= (\xi_z \cos\theta, \xi_y \cos\theta, -\xi_x \sin\theta), \\
\hat{\boldsymbol{k}} \times \left[\hat{\boldsymbol{k}} \times \left(\boldsymbol{\xi} \times \hat{\boldsymbol{b}}\right)\right] &= \left(-\xi_y \cos^2\theta, \xi_x \cos^2\theta + \xi_x \sin^2\theta, \xi_y \sin\theta \cos\theta\right), \\
\left\{\hat{\boldsymbol{k}} \times \left[\hat{\boldsymbol{k}} \times \left(\boldsymbol{\xi} \times \hat{\boldsymbol{b}}\right)\right]\right\} \times \hat{\boldsymbol{b}} &= \left(\xi_x, \xi_y \cos^2\theta, 0\right), \\
\hat{\boldsymbol{k}} \cdot \boldsymbol{\xi} &= \xi_x \sin\theta + \xi_z \cos\theta, \\
\hat{\boldsymbol{k}} \left(\hat{\boldsymbol{k}} \cdot \boldsymbol{\xi}\right) &= (\xi_x \sin\theta + \xi_z \cos\theta)(\sin\theta, 0, \cos\theta).
\end{aligned}$$

Equation (200) can then be written as

$$V_{\rm ph}^2 \begin{bmatrix} \xi_x \\ \xi_y \\ \xi_z \end{bmatrix} = V_{\rm A}^2 \begin{bmatrix} \xi_x \\ \xi_y \cos\theta \\ 0 \end{bmatrix} + V_{\rm s}^2 \begin{bmatrix} \xi_x \sin^2\theta + \xi_z \sin\theta\cos\theta \\ 0 \\ \xi_x \sin\theta\cos\theta + \xi_z \cos^2\theta \end{bmatrix}, \tag{205}$$

and rearranged to

$$\begin{bmatrix} V_{\rm ph}^2 - V_{\rm A}^2 - V_{\rm s}^2 \sin^2\theta & 0 & -V_{\rm s}^2 \sin\theta\cos\theta \\ 0 & V_{\rm ph}^2 - V_{\rm A}^2 \cos^2\theta & 0 \\ -V_{\rm s}^2 \sin\theta\cos\theta & 0 & V_{\rm ph}^2 - V_{\rm s}^2 \cos^2\theta \end{bmatrix} \begin{bmatrix} \xi_x \\ \xi_y \\ \xi_z \end{bmatrix} = 0. \tag{206}$$

Thus, the dispersion relation of MHD waves is given by

$$\left(V_{\rm ph}^2 - V_{\rm A}^2 \cos^2\theta\right)\left[V_{\rm ph}^4 - V_{\rm ph}^2\left(V_{\rm s}^2 + V_{\rm A}^2\right) + V_{\rm A}^2 V_{\rm s}^2 \cos^2\theta\right] = 0. \tag{207}$$

The first pair of roots of this dispersion relation,

$$V_{\rm ph} = \pm V_{\rm A} \cos\theta, \tag{208}$$

represents the shear Alfvén waves, also known as the intermediate waves, derived by Alfvén in 1942. The phase speed of the waves is in between the phase speeds of the two magnetosonic waves (see below). Alfvén waves involve only wavenumbers in the magnetic field direction due to the bending field lines. Only the displacement component in the y direction, ξ_y, participates in the wave motion. Thus, Alfvén waves are transverse waves without compression, propagating in the direction of the field line and not in the perpendicular direction.

The other two pairs of roots of the dispersion relation are given by

$$V_{\rm ph}^2 = \frac{V_{\rm A}^2 + V_{\rm s}^2}{2} \pm \frac{1}{2}\sqrt{\left(V_{\rm A}^2 - V_{\rm s}^2\right)^2 + 4V_{\rm A}^2 V_{\rm s}^2 \sin^2\theta}, \tag{209}$$

representing the fast and slow magnetosonic waves derived by Spitzer in 1962, involving both the Alfvén waves and the sound waves. Magnetosonic waves' perturbations are finite only for ξ_x and ξ_z: ξ_x along the $k_\perp$ direction as in the sound waves but also compressing or decompressing magnetic field while ξ_z along $k_\parallel$ direction compressing the plasma. The relative phase between the two directions of perturbation determines the type of waves. When the two of them work in concert, *i.e.* restoring forces are constructive to each other, phase velocity increases resulting in fast waves. When the restoring forces are destructive to each other, phase velocity decreases and can even vanish, resulting in slow waves.

Magnetosonic waves are described by

$$\begin{bmatrix} V_{\rm ph}^2 - V_{\rm A}^2 - V_{\rm s}^2 \sin^2\theta & -V_{\rm s}^2 \sin\theta\cos\theta \\ -V_{\rm s}^2 \sin\theta\cos\theta & V_{\rm ph}^2 - V_{\rm s}^2\cos^2\theta \end{bmatrix} \begin{bmatrix} \xi_x \\ \xi_z \end{bmatrix} = 0, \tag{210}$$

which reduces to the two decoupled waves

$$\begin{bmatrix} V_{\rm ph}^2 - V_{\rm A}^2 & 0 \\ 0 & V_{\rm ph}^2 - V_{\rm s}^2 \end{bmatrix} \begin{bmatrix} \xi_x \\ \xi_z \end{bmatrix} = 0, \tag{211}$$

when $\theta = 0$. The waves with only nonzero ξ_x bend the magnetic field lines and propagate at $V_{\rm ph} = \pm V_{\rm A}$, which are the transverse shear Alfvén waves. In contrast, the waves with only nonzero ξ_z compress the plasma and propagate at $V_{\rm ph} = \pm V_{\rm s}$, which are the longitudinal sound waves. The fast wave phase speed takes whichever is larger between $V_{\rm A}$ and $V_{\rm s}$.

When $\theta = \pi/2$, Eq. (210) becomes

$$\begin{bmatrix} V_{\rm ph}^2 - \left(V_{\rm A}^2 + V_{\rm s}^2\right) & 0 \\ 0 & V_{\rm ph}^2 \end{bmatrix} \begin{bmatrix} \xi_x \\ \xi_z \end{bmatrix} = 0, \tag{212}$$

resulting in fast longitudinal waves with nonzero ξ_x that compress both the magnetic field and the plasma propagating at $V_{\rm ph} = \pm\sqrt{V_{\rm A}^2 + V_{\rm s}^2}$. At any other angles between $\theta = 0$ and $\theta = \pi/2$, both the transverse and the longitudinal modes of magnetosonic waves are mixed as shown by Friedricks in 1957 in Fig. 20 for both $V_{\rm A} > V_{\rm s}$ ($\beta < 1$) and $V_{\rm A} < V_{\rm s}$ ($\beta > 1$) cases.

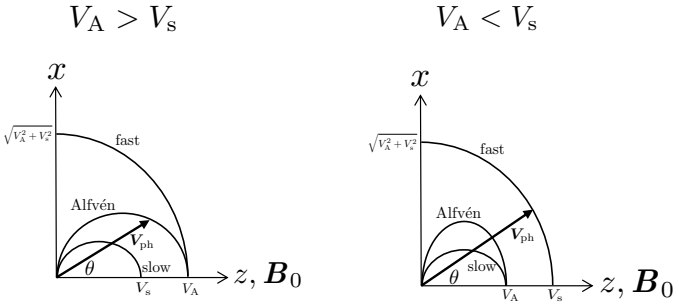

Fig. 20 Friedricks diagrams for both $V_{\rm A} > V_{\rm s}$ and $V_{\rm A} < V_{\rm s}$ cases.

Finally, we will discuss the total number of waves in MHD. According to our ideal MHD model, there are 8 variables with 8 equations, and thus there should be 8 waves available. However, our dispersion relation has only 6 waves: two Alfvén waves and four magnetosonic waves. The missing waves are called "entropy waves" (Kulsrud, 2005, Ch.5). These waves are trivial, involving only perturbations in density and pressure but without plasma motions nor magnetic field compression resulting in zero frequencies.

4.2 Surface Gravity Waves

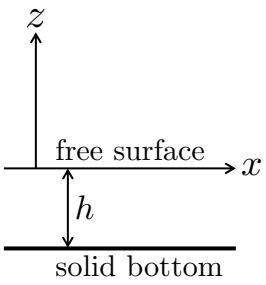

Fig. 21 Coordinate system for surface gravity waves.

We turn our attention to surface gravity waves which are illustrative for many common wave properties, including MHD waves. In this case, the static

fluid has a free-surface on the top and a solid bottom supported by a vertical pressure gradient,

$$\frac{dp_0}{dz} = -\rho g. \tag{213}$$

Linear perturbations give free surface deformation $\delta(x,t)$, pressure perturbation $p_1(x,z,t)$, and 2D velocity perturbation $\boldsymbol{V}_1 = (u,0,v)$, where u and v are the functions of x, z, and t. Assuming incompressibility $\boldsymbol{\nabla}\cdot\boldsymbol{V}_1 = 0$, we can introduce a stream function $\psi(x,z,t)$ so that

$$u = \frac{\partial\psi}{\partial z}; \quad v = -\frac{\partial\psi}{\partial x}. \tag{214}$$

As before, we further assume that the linear mode decomposition of waves,

$$\psi = \Re\left[\psi e^{i(kx-\omega t)}\right]. \tag{215}$$

The equation for ψ can then be derived from the equation of motion,

$$\rho\frac{\partial\boldsymbol{V}_1}{\partial t} = -\boldsymbol{\nabla}p_1. \tag{216}$$

Taking the y component from the curl of this equation we have:

$$(\boldsymbol{\nabla}\times\boldsymbol{V}_1)_y = \frac{\partial u}{\partial z} - \frac{\partial v}{\partial x} = \frac{\partial^2\psi}{\partial z^2} + \frac{\partial^2\psi}{\partial x^2} = 0, \tag{217}$$

which leads to

$$\frac{\partial^2\psi}{\partial z^2} = -\frac{\partial^2\psi}{\partial x^2} = k^2\psi, \tag{218}$$

with solutions in the form of

$$\psi(z) = Ae^{kz} + Be^{-kz}. \tag{219}$$

Here A and B are determined by the boundary conditions at the bottom of the fluid $z=-h$,

$$v|_{z=-h} = -\left.\frac{\partial\psi}{\partial x}\right|_{z=-h} = 0 \tag{220}$$

or

$$Ae^{-kh} + Be^{kh} = 0; \quad B = -Ae^{-2kh}. \tag{221}$$

Substituting to Eq. (219) yields

$$\psi(z) = 2Ae^{-kh}\frac{e^{k(z+h)} - e^{-k(z+h)}}{2} = A\sinh\left[k\left(z+h\right)\right], \tag{222}$$

where we have redefined $2Ae^{-kh} \to A$ for simplicity. p_1 can then be determined by using the x component of Eq. (216),

$$-i\rho\omega\frac{\partial\psi}{\partial z} = -\frac{\partial p_1}{\partial x} = -ikp_1, \tag{223}$$

and thus,

$$p_1 = \rho\omega A\cosh\left[k\left(z+h\right)\right]. \tag{224}$$

Kinematic Boundary Condition. The surface deformation δ can be related to the velocity of the free surface in the following way,

$$v|_{z=0} = -\left.\frac{\partial\psi}{\partial x}\right|_{z=0} = -ik\psi|_{z=0} = -ikA\sinh\left(kh\right)e^{i(kx-\omega t)} = \frac{\partial\delta}{\partial t} = -i\omega\delta, \tag{225}$$

which leads to,

$$\delta = \frac{k}{\omega}A\sinh\left(kh\right)e^{i(kx-\omega t)}. \tag{226}$$

Dynamic Boundary Condition. The force across the massless free surface should vanish,

$$p_1|_{z=0} + \left.\frac{\partial p_0}{\partial z}\right|_{z=0}\delta + T\frac{\partial^2\delta}{\partial x^2} = 0, \tag{227}$$

where T is the surface tension coefficient. Using vertical force balance and the solution for p_1, we have

$$A\rho\omega\cosh\left(kh\right) - \rho g\delta - k^2T\delta = 0, \tag{228}$$

which can be rewritten to obtain the dispersion relation by substituting δ,

$$\rho\omega^2 = \left(\rho g + k^2T\right)k\tanh kh. \tag{229}$$

For $T = 0$, we have two limiting cases of this dispersion:

$$\frac{\omega}{k} = \sqrt{gh} \quad \text{when } kh \ll 1; \quad \text{shallow water limit} \tag{230}$$

$$\frac{\omega}{k} = \sqrt{\frac{g}{k}} \quad \text{when } kh \gg 1; \quad \text{deep water limit.} \tag{231}$$

4.3 Wave Dispersion, Nonlinearity, and Hydraulic Jumps

When the phase velocity of a wave, $\boldsymbol{V}_{\rm ph} = \omega/\boldsymbol{k}$, is equal to its group velocity, $\boldsymbol{V}_{\rm g} = \partial\omega/\partial\boldsymbol{k}$, the wave is said to be non-dispersive, *i.e.*, the waveform does not change during its propagation. When the two velocities differ, the wave is dispersive, *i.e.*, the waveform spreads during its propagation. The non-dispersive waves include light waves in a vacuum, sound waves in the air, MHD waves,

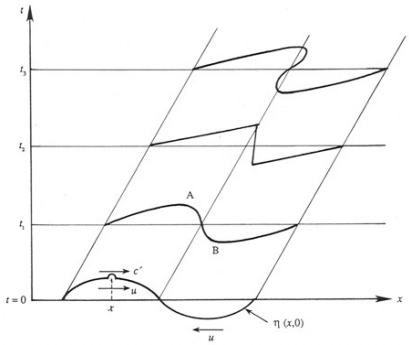

Fig. 22 Wave steepening due to its large amplitude.

and surface gravity waves in shallow water or long wavelength limit. Dispersive waves include surface gravity waves in deep water or short wavelength limit. Many non-MHD plasma waves are dispersive such as Whistler waves or ion acoustic waves in the short wavelength limit.

Some waves can be non-dispersive when they are linear but turn dispersive or steepen (the opposite of dispersive) due to the nonlinear effects when their amplitudes are large enough. Illustrations in Fig. 22 (Kundu et al, 2015, Ch.7) show the time evolution of a surface wave with large amplitude. Since the phase velocity is given by $\sqrt{gh}$, the part with high elevation will have a faster phase velocity and can catch up with the depressed part with a slower phase velocity. This leads to the steepening of wave gradient between the elevation and depression, eventually forming a hydraulic jump (see below) that breaks the wave. A similar situation occurs for a sound wave with phase velocity given by $\sqrt{\gamma p/\rho}$. Locally increased pressure due to compression can lead to a faster phase velocity that can catch up with the part with decreased pressure due to decompression. Magnetosonic waves can exhibit similar steepening since they compress the magnetic field (and plasma), resulting in the change of phase velocity when the amplitude is large.

The nonlinear steepening of finite-amplitude waves can be balanced by their linear wave dispersion so that the combined effects lead to non-dispersive behavior. A well-known example (Kundu et al, 2015, Ch.7) is the "soliton" solutions of a finite-amplitude surface gravity wave with a long wavelength when compared to the depth, governed by Korteweg-de Vries (KdV) equation which was derived in 1895 to explain the observation by Russell in 1844.

Many cases of the nonlinear steepening of finite-amplitude waves are balanced by finite dissipation generated on the steepened wavefront, as exemplified in Fig. 22. Consider the case of a hydraulic jump formed by steepening of surface gravity waves shown in the initial frame of the jump in Fig. 23. The dimensionless parameter (*c.f.* Mach number in the case of shock) controlling hydraulic jumps is the Froude number $Fr \equiv u/V_{\rm ph} = u/\sqrt{gh}$. The flow is supercritical if $Fr > 1$ and subcritical if $Fr < 1$. Therefore in Fig. 23, we must have $Fr_1 = u_1/\sqrt{gh_1} > 1$ and $Fr_2 = u_2/\sqrt{gh_2} < 1$.

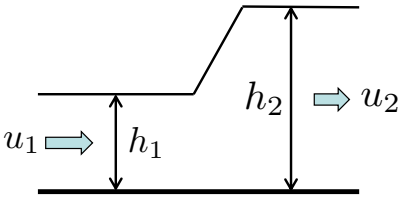

Fig. 23 Hydraulic jump in a stationary frame.

Mass and horizontal momentum conservation demand their fluxes are unchanged

$$u_1 h_1 = u_2 h_2 = Q, \tag{232}$$

$$\rho g \frac{h_1}{2} \cdot h_1 + \rho u_1 Q = \rho g \frac{h_2}{2} \cdot h_2 + \rho u_2 Q, \tag{233}$$

where the forces on the upstream and downstream of the jump come from the averaged pressure, $\rho g h_1/2$ and $\rho g h_2/2$, multiplied by the height h_1 and h_2, respectively. Using Q to eliminate $u_1 = Q/h_1$ and $u_2 = Q/h_2$ from the second equation yields

$$\frac{g}{2}\left(h_1^2 - h_2^2\right) = Q\left(\frac{Q}{h_2} - \frac{Q}{h_1}\right). \tag{234}$$

Removing the trivial solution of $u_1 = u_2$ simplifies the above equation to

$$g h_1 h_2 \left(h_1 + h_2\right) = 2Q^2. \tag{235}$$

Treating $Fr_1^2 = u_1^2/g h_1 = Q^2/g h_1^3$ as a given value, the above equation becomes an equation for h_2/h_1:

$$\left(\frac{h_2}{h_1}\right)^2 + \left(\frac{h_2}{h_1}\right) - 2Fr_1^2 = 0, \tag{236}$$

which can be solved to find

$$\frac{h_2}{h_1} = \frac{\sqrt{8Fr_1^2 + 1} - 1}{2} \approx \sqrt{2} Fr_1 - \frac{1}{2} \tag{237}$$

in the $Fr_1 \gg 1$ limit.

A fluid parcel will lose its mechanical and gravitational potential energy as it goes through the hydraulic jump. To see this, we can calculate the mechanical and gravitational energy change through the jump:

$$\frac{1}{2}u_1^2 + \frac{1}{2}g h_1 - \left(\frac{1}{2}u_2^2 + \frac{1}{2}g h_2\right) = \frac{Q^2}{2}\left(\frac{1}{h_1^2} - \frac{1}{h_2^2}\right) + \frac{g}{2}\left(h_1 - h_2\right)$$

$$= \frac{h_1 - h_2}{2}\left(g - Q^2 \frac{h_1 + h_2}{h_1^2 h_2^2}\right)$$
$$= \frac{g\,(h_1 - h_2)}{2}\left(1 - \frac{1}{2}\frac{(h_1 + h_2)^2}{h_1 h_2}\right)$$
$$= \frac{g\,(h_2 - h_1)\left(h_1^2 + h_2^2\right)}{4 h_1 h_2} > 0, \qquad (238)$$

where Eq. (235) was used. The lost energy becomes heat due to dissipation by eddies in the hydraulic jump, as the total energy must be conserved. In general, entropy is generated by dissipation when waves break.

4.4 Gas Dynamic Shock Waves

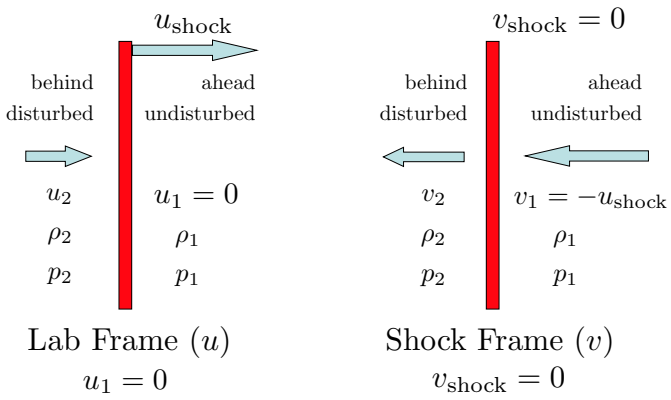

Fig. 24 Lab frame and shock frame of a shock front.

Nonlinear steepening in compressible gas generates a shock wave. In the shock front, dissipation produces entropy similar to a hydraulic jump. Figure 24 shows two commonly used frame-of-references when the flow is normal to the shock front: the lab frame using u and the shock frame using v. In either frame, subscript 1 denotes the undisturbed region ahead or upstream of the shock while subscript 2 denotes the disturbed region behind or downstream of the shock.

In the lab frame, the undisturbed gas is at rest with $u_1 = 0$ while the shock front propagates at speed u_{shock}, faster than sound speed. In the shock frame, the shock front is at rest with $v_{\text{shock}} = 0$ so that the undisturbed gas moves towards the shock at $v_1 = -u_{\text{shock}}$. It is more common and convenient to analyze shock waves based on the shock frame.

In a steady state, the relations between upstream and downstream parameters follow conservation laws (continuity, momentum, and energy):

$$\rho_2 v_2 = \rho_1 v_1, \tag{239}$$

$$p_2 + \rho_2 v_2^2 = p_1 + \rho_1 v_1^2, \tag{240}$$

$$\left(\frac{1}{2}\rho_2 v_2^2 + \frac{\gamma}{\gamma-1}p_2\right) v_2 = \left(\frac{1}{2}\rho_1 v_1^2 + \frac{\gamma}{\gamma-1}p_1\right) v_1. \tag{241}$$

Assuming $X \equiv \rho_2/\rho_1$, from the continuity equation (239), we have $v_2/v_1 = 1/X$. Now, it is convenient to define Mach number, $M \equiv v_1/v_s$, where sound speed $v_s = \sqrt{\gamma p_1/\rho_1}$ or $\rho_1/p_1 = \gamma/v_s^2$. From the momentum equation (240), we have:

$$\begin{aligned}
\frac{p_2}{p_1} &= 1 + \frac{\rho_1 v_1^2}{p_1} - \frac{\rho_2 v_2^2}{p_1} \\
&= 1 + \frac{\gamma v_1^2}{v_s^2} - \frac{\gamma v_1^2}{v_s^2}\cdot\frac{\rho_2}{\rho_1}\cdot\frac{v_2^2}{v_1^2} \\
&= 1 + \gamma M^2 - \gamma M^2 \cdot X \cdot \frac{1}{X^2} \\
&= 1 + \gamma M^2 \left(1 - \frac{1}{X}\right).
\end{aligned} \tag{242}$$

We need an equation to solve for X as a function of M. To do so, we divide the energy conservation equation (241) by continuity equation (239) to have

$$\frac{1}{2}v_2^2 + \frac{\gamma}{\gamma-1}\frac{p_2}{\rho_2} = \frac{1}{2}v_1^2 + \frac{\gamma}{\gamma-1}\frac{p_1}{\rho_1}. \tag{243}$$

Using $p_1/\rho_1 = v_s^2/\gamma$ and

$$\begin{aligned}
\frac{p_2}{\rho_2} &= \frac{p_1}{\rho_1}\cdot\frac{\rho_1}{\rho_2}\cdot\frac{p_2}{p_1} \\
&= \frac{v_s^2}{\gamma}\cdot\frac{1}{X}\left[1 + \gamma M^2\left(1 - \frac{1}{X}\right)\right],
\end{aligned} \tag{244}$$

then after dividing by v_s^2, Eq. (243) becomes

$$\frac{1}{2}\frac{M^2}{X^2} + \frac{1}{\gamma-1}\frac{1}{X}\left[1 + \gamma M^2\left(1 - \frac{1}{X}\right)\right] = \frac{1}{2}M^2 + \frac{1}{\gamma-1}. \tag{245}$$

Removing the trivial solution of $X - 1$, we get

$$X = \frac{\rho_2}{\rho_1} = \frac{(\gamma+1)M^2}{2 + (\gamma-1)M^2} = 1 + \frac{2(M^2-1)}{2 + (\gamma-1)M^2} \tag{246}$$

and therefore

$$\frac{v_2}{v_1} = \frac{1}{X} = 1 - \frac{2(M^2-1)}{(\gamma+1)M^2},$$
$$\frac{p_2}{p_1} = 1 + \gamma M^2\left(1 - \frac{1}{X}\right) = 1 + \frac{2\gamma(M^2-1)}{\gamma+1}. \tag{247}$$

As a result, the ratio between downstream quantities to their upstream values can be expressed by the upstream Mach number. Both density and pressure will increase while the velocity will decrease when $M > 1$.

How much does the velocity decrease relative to the local sound speed? The Mach number at the downstream, $M_2 \equiv v_2/v_{s,2}$, and the downstream sound speed, $v_{s,2} = \sqrt{\gamma p_2/\rho_2}$, can be calculated by rewriting the momentum equation (240) as

$$p_2 + \gamma p_2 M_2^2 = p_1 + \gamma p_1 M^2. \tag{248}$$

After some algebra and by using Eq. (247) this leads to,

$$M_2^2 = \frac{(\gamma-1)M^2+2}{2\gamma M^2 - \gamma + 1} = 1 - \frac{(\gamma+1)(M^2-1)}{2\gamma(M^2-1)+\gamma+1}, \tag{249}$$

which is < 1 as long as $M > 1$. This means that the flow transitions from being supersonic to subsonic by passing through the shock.

It is useful to calculate u_2 in the lab frame after the shock wave,

$$\frac{u_2}{u_{\rm shock}} = \frac{v_1 - v_2}{v_1} = 1 - \frac{v_2}{v_1} = \frac{2(M^2-1)}{(\gamma+1)M^2} = 1 - \frac{(\gamma-1)M^2+2}{(\gamma+1)M^2}. \tag{250}$$

Rankine and Hugoniot relations determines the relations between upstream and downstream quantities of the shock wave which are named after their independent derivation. In principle, there should not be an upper limit in M, and in the limit of $M \to \infty$, we have

$$\frac{\rho_2}{\rho_1} \to \frac{\gamma+1}{\gamma-1}; \quad \frac{v_2}{v_1} \to \frac{\gamma-1}{\gamma+1}; \quad \frac{p_2}{p_1} \to \infty. \tag{251}$$

For $\gamma = 5/3$, they simplify to

$$\frac{\rho_2}{\rho_1} \to 4; \quad \frac{v_2}{v_1} \to \frac{1}{4}; \quad \frac{u_2}{u_{\rm shock}} \to \frac{3}{4}. \tag{252}$$

It is interesting to note that the downstream pressure can increase without a bound under a strong shock. Yet, density and velocity can not do so due to the conservation of mass and momentum.

Global conservation laws based on the ideal fluid equations do not contain the physics within the shock layer. The shock layer has a finite thickness which

is determined by the dissipation inside of it. In gas dynamics, the viscous effects are important and reflected in the Reynolds number of the shock,

$$Re_{\text{shock}} = \frac{\delta \Delta v}{\nu} \sim 1, \tag{253}$$

where δ is the shock layer thickness, Δv is the velocity change across the shock, and ν is the kinematic viscosity. Estimating $\Delta v \sim v_s$ and

$$\nu \sim \frac{\lambda_{\text{mfp}}^2}{\tau_{\text{collision}}} = \frac{\lambda_{\text{mfp}}}{\tau_{\text{collision}}} \lambda_{\text{mfp}} = v_s \lambda_{\text{mfp}}, \tag{254}$$

we have,

$$\delta \sim \lambda_{\text{mfp}}. \tag{255}$$

The result means that the thickness of a shock is on the order of mean-free-path of the gas molecules. In room-temperature air, the mean free path is very short, typically below 1 micron, and thus the shock layers are very thin.

4.5 MHD Discontinuities and Shocks

As seen from the discussion of gas dynamic shock, conservation laws can directly lead to the Rankine and Hugoniot relations between upstream and downstream quantities regardless of the details within the shock front. This method is powerful as it can determine the global structures of a large system in its steady state without requiring us to know the specific form of the dissipation processes. Using the conservative forms of the ideal MHD system given in Lecture 2, we can derive the corresponding Rankine and Hugoniot relations for MHD dicontinuities and shocks.

Instead of using subscript 1 and 2 for the upstream and downstream quantities, we introduce a pair of square brackets to denote changes across the shock, *i.e.*, $[a] = a_2 - a_1$ for any quantities a. When the quantity a is conserved across the shock, we have $[a] = 0$.

Therefore, the three jump conditions from ideal MHD conservation laws are:

$$[\rho \boldsymbol{V} \cdot \boldsymbol{n}] = 0, \tag{256}$$

$$\left[\rho \boldsymbol{V} (\boldsymbol{V} \cdot \boldsymbol{n}) + \left(p + \frac{B^2}{2\mu_0}\right) \boldsymbol{n} - \frac{\boldsymbol{B}}{\mu_0} (\boldsymbol{B} \cdot \boldsymbol{n})\right] = 0, \tag{257}$$

$$\left[\left(\frac{1}{2}\rho V^2 + \frac{\gamma}{\gamma - 1} p\right) \boldsymbol{V} \cdot \boldsymbol{n} + \frac{\boldsymbol{E} \times \boldsymbol{B}}{\mu_0} \cdot \boldsymbol{n}\right] = 0, \tag{258}$$

where $\boldsymbol{n}$ is the normal unit vector of the shock layer (or discontinuity layer, see below). Additional jump conditions come from the Maxwell's equations,

$$[\boldsymbol{E} \times \boldsymbol{n}] = [-(\boldsymbol{V} \times \boldsymbol{B}) \times \boldsymbol{n}] = 0, \tag{259}$$

$$[\boldsymbol{B}\cdot\boldsymbol{n}] = 0, \tag{260}$$

where the first jump condition states that the tangential component of the electric field must be continuous in a steady state due to Faraday's law. The second condition enforces that the normal component of the magnetic field must be continuous due to its divergence-free nature.

More useful forms of these jump conditions can be derived (Gurnett and Bhattacharjee, 2017, Ch.8). We will use subscripts "n" and "t" to denote a vector's normal and tangential components to the shock front. Equations (256) and (260) can then be written as,

$$[\rho V_n] = 0, \tag{261}$$
$$[B_n] = 0. \tag{262}$$

The second equation leads to $\left[B_n^2\right] = 0$ and therefore $\left[B^2\right] = \left[B_n^2 + B_t^2\right] = \left[B_t^2\right]$. Using this relation, the momentum equation (257) can be split to its normal component,

$$\left[\rho V_n^2 + p + \frac{B_t^2}{2\mu_0}\right] = 0, \tag{263}$$

and its tangential component,

$$\left[\rho V_n \boldsymbol{V}_t - B_n \frac{\boldsymbol{B}_t}{\mu_0}\right] = 0. \tag{264}$$

Since

$$\boldsymbol{E}\times\boldsymbol{B} = -(\boldsymbol{V}\times\boldsymbol{B})\times\boldsymbol{B} = \boldsymbol{B}\times(\boldsymbol{V}\times\boldsymbol{B}) = B^2\boldsymbol{V} - (\boldsymbol{B}\cdot\boldsymbol{V})\,\boldsymbol{B}$$

the energy jump condition Eq. (258) can be written as

$$\left[\left(\frac{1}{2}\rho V^2 + \frac{\gamma}{\gamma-1}p + \frac{B^2}{\mu_0}\right)V_n - (\boldsymbol{B}\cdot\boldsymbol{V})\,\frac{B_n}{\mu_0}\right] = 0. \tag{265}$$

Lastly, the tangential electric field jump condition is

$$[\boldsymbol{V}_n\times\boldsymbol{B}_t + \boldsymbol{V}_t\times\boldsymbol{B}_n] = 0. \tag{266}$$

Equations (261) to (266) form a complete set of 6 jump conditions (Rankine and Hugoniot relations) across discontinuities or shocks for ideal MHD system with 6 unknowns: ρ, p, V_n, V_t, B_n, and B_t.

Different types of MHD discontinuities can be classified according to the difference in density and normal velocity as shown in Table 1.

The first non-trivial discontinuity is the *contact discontinuity* where the density changes ($[\rho] \neq 0$), but the normal velocity vanishes ($V_n = 0$), *i.e.* no plasma passes across the layer. There are two cases of contact discontinuities:

Table 1 Classification of MHD discontinuities and shocks according to (Landau and Lifshitz, 1960, Ch.8).

	$V_n = 0$	$V_n \neq 0$
$[\rho] = 0$	Trivial	Rotational discontinuity
$[\rho] \neq 0$	Contact discontinuity	Shock wave

$B_n \neq 0$ and $B_n = 0$. For the case with $B_n \neq 0$, most of the quantities do not change across the shock front:

- $[V_t] = 0$ based on the electric field jump condition Eq. (266).
- $[B_t] = 0$ based on the tangential component of momentum jump condition Eq. (264).
- $[p] = 0$ based on the normal component of momentum jump condition Eq. (263) where $\left[B_t^2\right] = 0$ is used.

Since $[\rho] \propto [n] \neq 0$ while $[p] = 0$, $[T] \neq 0$ must occur in cases such as when a heat source is suddenly applied. However, it is typically difficult for such contact discontinuity to form in a plasma when the heat transport is fast.

The second case of contact discontinuity, often called *tangential discontinuity*, occurs when $B_n = 0$. Contrary to the first case, many quantities *do jump* across the discontinuity front:

- $[V_t] \neq 0$ in general since $B_n = 0$ in the electric field jump condition Eq. (266).
- $[B_t] \neq 0$ in general since $B_n = 0$ in the tangential component of momentum jump condition Eq. (264).
- $\left[p + \frac{B_t^2}{2\mu_0}\right] = 0$ based on the normal component of momentum jump condition Eq. (263) even when $\left[B_t^2\right] \neq 0$ in general.

In this case, the plasma flow and the magnetic field parallel to the discontinuity surface can change their magnitude and direction while maintaining the force balance. An example of this case is Earth's magnetopause where (the shocked) solar wind plasma in contact with Earth's magnetosphere as shown in Fig. 25. The tangential discontinuity maintains a sharp boundary between these two plasmas, parallel to the majority of the flow and magnetic field of solar wind plasma. Occasionally, this approximation is violated by magnetic reconnection (see later) at sporadic places. A similar tangential discontinuity, called the heliopause, exists when solar wind plasma meets interstellar plasma in the galaxy.

The second non-trivial discontinuity in Table 1 is the *rotational discontinuity* where the density is continuous but the normal component of velocity has a finite value, *i.e.* plasma flows across the layer. In this case, since the mass flow must be continuous $[\rho V_n] = 0$ according to Eq. (261), the normal velocity needs to be continuous, $[V_n] = 0$. Since $[B_n] = 0$ according to Eq. (262), the tangential component of momentum continuity Eq. (264) leads to

$$\rho V_n \left[\boldsymbol{V}_t\right] = \frac{B_n}{\mu_0} \left[\boldsymbol{B}_t\right]. \tag{267}$$

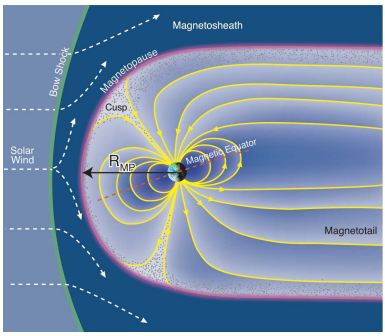

Fig. 25 Earth's magnetopause as a tangential discontinuity between the magnetosphere and magnetosheath, containing the shocked plasma from the solar wind.

From the continuous tangential electric field Eq. (266), we have

$$\boldsymbol{V}_n \times [\boldsymbol{B}_t] + [\boldsymbol{V}_t] \times \boldsymbol{B}_n = 0, \tag{268}$$

which can be rewritten by substituting $[\boldsymbol{V}_t]$ from Eq. (267) as

$$V_n \boldsymbol{V}_n \times [\boldsymbol{B}_t] = \frac{B_n}{\mu_0 \rho} \boldsymbol{B}_n \times [\boldsymbol{B}_t] \tag{269}$$

or

$$\boldsymbol{V_n} = \pm \frac{\boldsymbol{B}_n}{\sqrt{\mu_0 \rho}} = \pm \boldsymbol{n} V_{\mathrm{A}} \cos\theta, \tag{270}$$

where θ is the angle between the normal direction of the discontinuity and magnetic field. Magnetic field and flow change directions by rotation across the discontinuity but not their magnitude. This can be identified as Alfvén waves propagating in the direction θ away from the magnetic field, as we discussed earlier in the linear waves section. However, the tangential discontinuity is actually a result of Alfvén waves in the nonlinear regime.

From this example, it is natural to expect that different types of MHD discontinuities or shocks can develop based on the different types of MHD waves via nonlinear steepening. Since there are three different types of MHD waves, there are three general types of MHD discontinuities or shocks. For discontinuities that we have discussed so far, the contact discontinuity with $B_n = 0$ corresponds to the fast or slow mode since any increase in p needs to be compensated by the decrease in $B^2/2\mu_0$ and vice versa. However, the contact discontinuity with $B_n \neq 0$ is a special case corresponding to entropy wave as there is no quantities to have a jump other than the density and temperature. The rotational discontinuity belongs to the Alfvén mode as just discussed above.

Three different types of MHD shocks are illustrated in their shock frames in Fig. 26. Just like solving the dispersion relation for linear MHD waves, these three solutions can be found in a cubic equation (Anderson, 1963) by systematically solving (Gurnett and Bhattacharjee, 2017, Ch.8) the jump condition

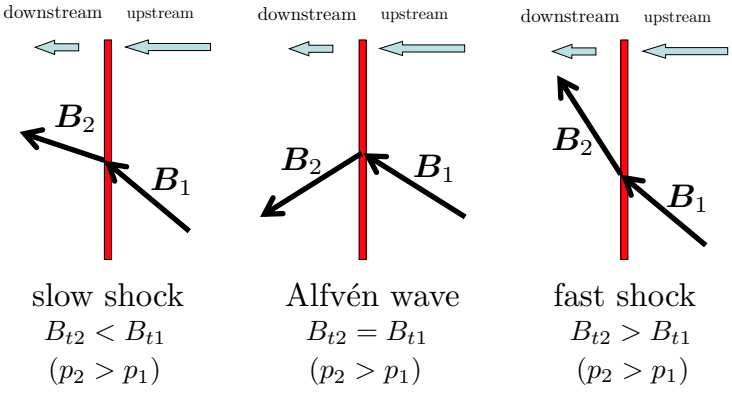

Fig. 26 Three types of MHD shocks.

Eqs. (261) to (266), similar to the gas dynamic case above, which has only one solution. In addition to the sonic Mach number, M, Alfvén Mach number, $M_{\rm A}$, is also introduced as a control parameter with its relation to M determined by the plasma beta. All three cases have the downstream pressure increasing over the shock front, converted from the flow and magnetic energy. The normal component of the magnetic field needs to be kept constant. However, there are three possibilities for the tangential component of the magnetic field, B_t. If B_t increases such that $B_{t2} > B_{t1}$ in concert with the pressure increase ($p_2 > p_1$), the resulting shock is a fast mode shock. It can be thought as if the shock front propagates so fast that B_t piles up after the shock front. The bow shock in front of Earth facing the solar wind is a fast mode shock as shown in Fig. 25. The opposite happens when B_t decreases downstream $B_{t2} < B_{t1}$ during the slow mode shock even if the plasma pressure still increases $p_2 > p_1$. In between these modes, there is an intermediate Alfvén wave mode where $B_{t2} = B_{t1}$ while the $\boldsymbol{B}_t$ vector rotates 180° as a special case of rotational discontinuity. However, intermediate mode shocks have a finite density jump $[\rho] \neq 0$, which is absent in the rotational discontinuities. Both cases are the manifestations of nonlinear Alfvén waves.

As in linear MHD waves, the shock front orientation with respect to the upstream magnetic field is important. Figure 26 shows the cases for oblique shocks when $0 < \theta < \pi/2$. When the shock's normal direction is parallel to the magnetic field, $\theta = 0$, the shock is called parallel shock. Sometimes, even θ can be not exactly zero, but the shocks behave quite similarly to the case of $\theta = 0$. These cases are often called quasi-parallel shocks ($\theta \approx 0$). In such cases, charged particles in collisionless plasmas freely pass through the shock front over a long distance without any constraints from the large-scale magnetic field. As a result, the thin shock layers can affect the large volume of plasmas both upstream and downstream, causing complicated plasma kinetic dynamics called "foreshock".

In contrast, perpendicular ($\theta = \pi/2$) or quasi-perpendicular ($\theta \approx \pi/2$) shocks have their charged particles strongly constrained by the large-scale magnetic field with their kinetic dynamics relatively concentrated in the shock layer. Quasi-perpendicular shocks tend to form as a result of rapidly expanding upstream plasma (such as supernova explosion), which sweeps the downstream magnetic field to align with the parallel direction of the shock front. In all cases, however, the large-scale magnetic field matters such that the plasma beta is a key control parameter that will determine not only relative speeds between V_A and V_s (thus M and M_A) but also the acceleration of charged particles due to the different degrees of magnetization. Charged particle acceleration by collisionless shocks (where collisions are negligible during the shock transition time) is an active and rich area of research as many solar energetic particles and high-energy cosmic rays are considered the direct results of kinetic dynamics occurring around the shock fronts.

4.6 Summary

- Linear MHD waves: Alfvén waves, fast and slow magnetosonic waves.
- Surface gravity waves are dispersive in the short wavelength limit and non-dispersive in the long wavelength limit.
- Nonlinear steepening can balance the wave dispersion, but in many cases, it causes waves to form discontinuities and shocks.
- Derivation of Rankine-Hugoniot relations for the gas dynamic shocks.
- MHD discontinuities: contact (tangential) discontinuities and rotational discontinuities.
- MHD shocks include fast and slow mode shocks and Alfvén mode shocks. Charged particle acceleration occurs during MHD shocks.

4.7 Further Readings

- Chapters 5 and 6 in Kulsrud (2005)
- Chapters 7 and 15 in Kundu et al (2015)
- Chapters 6 and 8 in Gurnett and Bhattacharjee (2017)
- Chapter 5 in Kivelson and Russell (1995)

4.8 Homework Problem Set 4

1. Phase velocity of intermediate waves.
   Prove that the phase velocity of intermediate waves (shear Alfvén waves) is always not slower than that of slow waves and simultaneously not faster than that of fast waves:

$$V_{\mathrm{ph,slow}} \le V_{\mathrm{ph,A}} \le V_{\mathrm{ph,fast}}. \tag{271}$$

2. Interfacial waves between two fluids.

(a) Derive the dispersion relation of angular frequency, ω, and wave vector, k, for interfacial waves between two fluids with different densities, ρ_1 and ρ_2, under gravity. Each fluid is considered to occupy half of the whole space and the surface tension is ignored.
(b) Under what condition does either ω or k have to be complex, indicating the existence of an instability (Rayleigh-Taylor Instability)?
(c) How does this instability condition change when the surface tension is included?

3. Perpendicular MHD shock.
(a) When $\boldsymbol{B}$ is parallel to the shock front, show that the Rankine-Hugoniot relation can be written as

$$\begin{aligned}
\rho_2 V_2 &= \rho_1 V_1, \\
p_2 + \rho_2 V_2^2 + \frac{B_2^2}{2\mu_0} &= p_1 + \rho_1 V_1^2 + \frac{B_1^2}{2\mu_0}, \\
\left(\frac{\gamma}{\gamma-1} p_2 + \frac{\rho_2 V_2^2}{2} + \frac{B_2^2}{\mu_0}\right) V_2 &= \left(\frac{\gamma}{\gamma-1} p_1 + \frac{\rho_1 V_1^2}{2} + \frac{B_1^2}{\mu_0}\right) V_1, \\
B_2 V_2 &= B_1 V_1.
\end{aligned}$$

(b) Defining $\rho_2/\rho_1 \equiv X$ such that $V_2/V_1 = 1/X$ and $B_2/B_1 = X$. Show that for $\beta_1 \equiv p_1/(B_1^2/2\mu_0)$: we have p_2/p_1 given by

$$\frac{p_2}{p_1} = 1 + \gamma M^2 \left(1 - \frac{1}{X}\right) + \frac{1 - X^2}{\beta_1}. \tag{272}$$

(c) Show that X satisfies

$$2(2-\gamma)X^2 + \left[2\beta_1 + (\gamma-1)\beta_1 M^2 + 2\right]\gamma X - \gamma(\gamma+1)\beta_1 M^2 = 0, \tag{273}$$

which will always have a positive root as long as $1 < \gamma < 2$. We can also recover the gas dynamic case in the large β_1 limit.
(d) In the small β_1 limit, however, instead of M it makes better sense to use the magnetosonic Mach number defined as

$$M_{\rm MS} \equiv \frac{V_1}{\sqrt{V_s^2 + V_A^2}}. \tag{274}$$

Revise the equation in part (c) using $M_{\rm MS}$. What value should X take in the large $M_{\rm MS}$ limit? How does it compare with the gas dynamic case?

5 Energy Principle

5.1 Stability Analysis

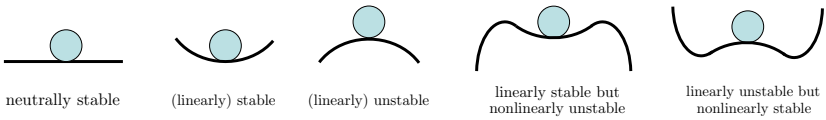

Fig. 27 Stability of a system at equilibrium.

It is important to know the stability properties of a given (magneto)static equilibrium or a base state flow, both of which we have learned in previous lectures. Different kinds of system stability at equilibrium are illustrated in Fig. 27, where a ball is placed on different surfaces under a constant gravitational force:

- If the surface is flat, the ball is at a neutrally stable position. If we place the ball away from its original location, it will not move toward its original position.
- If the surface is in the form of a valley, the ball is at a stable against (infinitesimally) small linear perturbations at the bottom of it. If we place the ball away from its original location at the bottom of the valley, it will return to its original position. The ball will eventually settle at the bottom of the surface if it has finite friction.
- If the surface is in the form of a hill, the ball is at an unstable position on top of it. If we move the ball away from the peak, the distance to its original location will increase over time.
- However, if there is a hill outside the valley, even if the ball can be stable linearly, it will be nonlinearly unstable against finite-amplitude perturbations if the perturbation is sufficiently large, pushing the ball beyond the edge of the valley.
- Conversely, if there is a valley outside the hill, the ball can be nonlinearly stable as the distance from the original location will not increase further after the initial growth.

In general, different combinations of the surface landscape can exhibit different stability properties. Among these, however, the linear stability of a given system against infinitesimally small perturbations is by far the first question that will be asked. Fortunately, answering this question will also be the easiest. As such, in this lecture, we will focus on linear stability analysis.

To study the stability of a system, there are three different approaches. The most practical way is to treat it as an initial value problem, which is often performed numerically. Experimental research on stability can also be regarded as taking this approach, although with some subtleties. Usually, it is difficult to set up an unstable system in the first place. Some techniques can be used to

mediate the difficulties. For example, by starting with a stable system, we can gradually adjust the system toward the desired state through a sequence of equilibrium states. When an instability with a growth rate comparable to the adjustment rate is encountered, the system will not change further despite the adjustment. If the growth rate is large, we may be able to see a sudden onset of instability which may disrupt the system depending on the nature of the instability. This is a practical approach as it can be implemented numerically and experimentally. However, it is often inefficient as it tests one particular initial condition at a time. Of course, one should not forget that the experimental investigations do provide the "final" answers.

The second approach is based on the normal mode analysis. Any linear perturbations can be decomposed as a summation of normal modes of the system. In principle, since linear normal modes are independent of each other, we can examine the system stability against each mode one by one. It is still inefficient as the number of normal modes is close to infinite. However, the approach is systematic, which often results in the identification of clear trends during the process. This approach is usually performed numerically and occasionally analytically.

The third approach is based on the variational analysis, which is the subject of this lecture with the name "energy principle". Using a minimization process, we can find the least stable perturbation to a particular system. If such a perturbation is still stable, the system is stable against all perturbations. Therefore, this method is powerful as it leads to such sweeping statements. The details of this approach can sometimes be difficult and less accurate in determining growth rates. However, once we can do it successfully, the energy principle can easily determine stability boundaries and often provide physically intuitive insights that are otherwise difficult to obtain.

The statement of energy principle (Bernstein et al, 1958; Hain et al, 1957) is,

> When the total energy of a system is conserved, the growth of perturbation kinetic energy at the expense of the magnetic, thermal, or gravitational potential energy corresponds to instability*.
>
> *There are some exceptions.

5.2 Linear Force Operator

When we analyze a linear wave, we used the plane wave decomposition for each wavenumber vector, $\boldsymbol{k}$, and angular frequency, ω, to derive the dispersion relation relating them. Typically, we treat $\boldsymbol{k}$ as a real vector to solve the dispersion relation for ω, which is generally a complex numbers. Assuming $\omega = \omega_r + i\gamma$, we have the displacement vector $\boldsymbol{\xi}$ given by

$$\boldsymbol{\xi} \propto e^{i\boldsymbol{k}\cdot\boldsymbol{r} - i\omega_r t + \gamma t}, \tag{275}$$

which shows that the displacement grows exponentially in time as a linear instability when $\gamma > 0$. From the linear wave analysis, all solutions that we

obtained are real with $\gamma = 0$. This is expected since we have assumed local spatial homogeneity of the plasma, which contains no free energy for the waves to grow unstable.

However, if we are concerned with the plasma at a large system scale, spatial homogeneity is no longer a reasonable assumption. This prevents the plane wave decomposition in the space of wavenumber $\boldsymbol{k}$. Therefore, all equilibrium quantities: ρ_0, p_0, and $\boldsymbol{B}_0$ can have spatial dependencies. Only the equilibrium velocity can still be homogeneous such that $\boldsymbol{V}_0 = 0$ in a proper frame where the plasma is in static equilibrium. This choice of $\boldsymbol{V}_0 = 0$ will be discussed later.

In this case, using linear velocity perturbation $\boldsymbol{V}_1$ expressed as a function of the linear displacement vector $\boldsymbol{\xi}$ (similar to the previous lecture), all other linear perturbations can be expressed conveniently in $\boldsymbol{\xi}$ but with modifications due to spatial in-homogeneity:

$$\rho_1 = -\boldsymbol{\nabla} \cdot (\rho_0 \boldsymbol{\xi}), \tag{276}$$

$$p_1 = -\gamma p_0 \boldsymbol{\nabla} \cdot \boldsymbol{\xi} - \boldsymbol{\xi} \cdot \boldsymbol{\nabla} p_0, \tag{277}$$

$$\boldsymbol{Q} \equiv \boldsymbol{B}_1 = \boldsymbol{\nabla} \times (\boldsymbol{\xi} \times \boldsymbol{B}_0). \tag{278}$$

The equation of motion then becomes

$$\begin{aligned} \rho_0 \frac{\partial^2 \boldsymbol{\xi}}{\partial t^2} &= \frac{1}{\mu_0} (\boldsymbol{\nabla} \times \boldsymbol{Q}) \times \boldsymbol{B}_0 + \frac{1}{\mu_0} (\boldsymbol{\nabla} \times \boldsymbol{B}_0) \times \boldsymbol{Q} + \boldsymbol{\nabla} (\gamma p_0 \boldsymbol{\nabla} \cdot \boldsymbol{\xi} + \boldsymbol{\xi} \cdot \boldsymbol{\nabla} p_0) \\ &\equiv \boldsymbol{F}(\boldsymbol{\xi}), \end{aligned} \tag{279}$$

where $\boldsymbol{F}(\boldsymbol{\xi})$ is called *force operator* which is a function of the displacement vector $\boldsymbol{\xi}$.

$\boldsymbol{F}(\boldsymbol{\xi})$ is self-adjoint, which is a special mathematical property for linear operators. This means the adjoint of $\boldsymbol{F}$ is itself: $\boldsymbol{F}^\dagger = \boldsymbol{F}$. In other words, for any pair of displacement vectors, $\boldsymbol{\eta}$ and $\boldsymbol{\xi}$, satisfying the same boundary conditions, the self-adjoint property of $\boldsymbol{F}$ demands

$$\int \boldsymbol{\eta} \cdot \boldsymbol{F}(\boldsymbol{\xi}) d\boldsymbol{r} = \int \boldsymbol{\xi} \cdot \boldsymbol{F}(\boldsymbol{\eta}) d\boldsymbol{r}. \tag{280}$$

The self-adjoint property of the force operator places ideal MHD spectral theory on the same solid ground as in quantum mechanics (Goedbloed and Poedts, 2004, Ch.6). To see this, we can define an inner product by treating plasma density $\rho(\boldsymbol{r})$ as a weight function,

$$\langle \boldsymbol{\xi}, \boldsymbol{\eta} \rangle \equiv \frac{1}{2} \int \rho \, (\boldsymbol{\xi}^* \cdot \boldsymbol{\eta}) \, d\boldsymbol{r}, \tag{281}$$

so that

$$\left\langle \boldsymbol{\eta}, \frac{\boldsymbol{F}(\boldsymbol{\xi})}{\rho} \right\rangle \equiv \frac{1}{2} \int \boldsymbol{\eta}^* \cdot \boldsymbol{F}(\boldsymbol{\xi}) d\boldsymbol{r} = \frac{1}{2} \int \boldsymbol{\xi} \cdot \boldsymbol{F}(\boldsymbol{\eta}^*) d\boldsymbol{r} \equiv \left\langle \frac{\boldsymbol{F}(\boldsymbol{\eta})}{\rho}, \boldsymbol{\xi} \right\rangle. \tag{282}$$

Therefore, as long as the norm, $||\boldsymbol{\xi}|| \equiv \sqrt{\langle \boldsymbol{\xi}, \boldsymbol{\xi} \rangle}$, is bounded or finite, a Hilbert space can be defined. Furthermore, we can consider normal modes of the solution,

$$\boldsymbol{\xi} = \hat{\boldsymbol{\xi}} e^{-i\omega t} \tag{283}$$

such that the equation of motion, Eq. (279), can be written as

$$\boldsymbol{F}(\hat{\boldsymbol{\xi}}) = -\rho\omega^2 \hat{\boldsymbol{\xi}}. \tag{284}$$

We use $\boldsymbol{\xi}$ for $\hat{\boldsymbol{\xi}}$ interchangeably, depending on the context without the loss of generality. With this definition, we have a complete set of correspondence between the equation of motion in static ideal MHD and the Schrödinger equation in quantum mechanics. We summarize the correspondence in Table 2 below.

Table 2 Correspondence between ideal MHD and quantum mechanics in Hilbert space.

Quantum Mechanics	Static Ideal MHD
Hamiltonian, H	Force operator, $\boldsymbol{F}(\boldsymbol{\xi})/\rho$
Energy level, E	Frequency or growth rate, $-\omega^2$
Wave function, ψ	Displacement vector, $\boldsymbol{\xi}$
Schrödinger equation, $H\psi = E\psi$	Equation of motion, $\boldsymbol{F}(\boldsymbol{\xi}) = -\rho\omega^2\boldsymbol{\xi}$
Inner product, $\langle \psi_1, \psi_2 \rangle \equiv \frac{1}{2}\int \psi_1^* \psi_2 d\boldsymbol{r}$	Weighed inner product, $\langle \boldsymbol{\xi}, \boldsymbol{\eta} \rangle \equiv \frac{1}{2}\int \rho\,(\boldsymbol{\xi}^* \cdot \boldsymbol{\eta})\, d\boldsymbol{r}$
Self-adjoint, $\langle H\psi_1, \psi_2 \rangle = \langle \psi_1, H\psi_2 \rangle$	Self-adjoint, $\left\langle \frac{\boldsymbol{F}(\boldsymbol{\eta})}{\rho}, \boldsymbol{\xi} \right\rangle = \left\langle \boldsymbol{\eta}, \frac{\boldsymbol{F}(\boldsymbol{\xi})}{\rho} \right\rangle$
Norm, $\|\psi\| \equiv \sqrt{\langle \psi, \psi \rangle}$	Norm, $\|\boldsymbol{\xi}\| \equiv \sqrt{\langle \boldsymbol{\xi}, \boldsymbol{\xi} \rangle}$

Compared to quantum mechanics, where the wave function and its norm have specific physical interpretations as the probability of finding the desired particle, the physical interpretation of the norm in ideal MHD, $||\boldsymbol{\xi}||$, is less clear. However, $||\dot{\boldsymbol{\xi}}||^2$ has a clear physical meaning,

$$||\dot{\boldsymbol{\xi}}||^2 \equiv \left\langle \dot{\boldsymbol{\xi}}, \dot{\boldsymbol{\xi}} \right\rangle = \frac{1}{2}\int \rho \dot{\boldsymbol{\xi}}^2 d\boldsymbol{r} = \frac{1}{2}\int \rho V_1^2 d\boldsymbol{r}, \tag{285}$$

which is the kinetic energy of perturbed velocity. By establishing this full correspondence, all mathematical techniques that were developed in spectral theory from quantum mechanics can be directly applied to ideal MHD spectral analysis. Details can be found in Goedbloed and Poedts (2004).

Among these, there are two important consequences of the self-adjoint property of the linear force operator, $\boldsymbol{F}(\boldsymbol{\xi})$. Multiplying $\boldsymbol{\xi}^*$ to Eq. (284) and integrating over space yield

$$-\omega^2 \int \rho \boldsymbol{\xi}^* \cdot \boldsymbol{\xi} d\boldsymbol{r} = \int \boldsymbol{\xi}^* \cdot \boldsymbol{F}(\boldsymbol{\xi}) d\boldsymbol{r}. \tag{286}$$

Alternatively, we can take the complex conjugate of Eq. (284) first,

$$\boldsymbol{F}(\boldsymbol{\xi}^*) = -\rho\omega^{*2}\boldsymbol{\xi}^*, \tag{287}$$

then multiply it with $\boldsymbol{\xi}$ before integrating over space, leading to

$$-\omega^{*2}\int \rho\boldsymbol{\xi}\cdot\boldsymbol{\xi}^* d\boldsymbol{r} = \int \boldsymbol{\xi}\cdot\boldsymbol{F}(\boldsymbol{\xi}^*)d\boldsymbol{r}. \tag{288}$$

This is identical to Eq. (286) due to the self-adjointness of $\boldsymbol{F}$, Eq. (280). Therefore, we have

$$\omega^2 = \omega^{*2}. \tag{289}$$

This means that ω is either real (stability), as in our linear MHD wave analysis, or purely imaginary, representing a purely growing (instability) or purely damping system without any oscillation. This is in contrast to the cases where ω is complex with both nonzero real and imaginary parts. Sometimes, the instability with nonzero real frequency is called "overstability". While many non-MHD plasma instabilities have nonzero real frequencies, ideal MHD instabilities discussed here must be purely growing. Therefore, when the system transitions from stability to instability by varying $\boldsymbol{\xi}$, ω^2 must go through the origin of the complex plane. In other words, the stability boundary can be determined by $\omega^2 = 0$ or $\boldsymbol{F}(\boldsymbol{\xi}) = 0$.

The second important consequence of self-adjointness of $\boldsymbol{F}(\boldsymbol{\xi})$ is to establish the orthogonality of its eigenfunctions. Suppose that m and n are any two of eigenmodes such that

$$-\rho\omega_m^2\boldsymbol{\xi}_m = \boldsymbol{F}(\boldsymbol{\xi}_m) \tag{290}$$

$$-\rho\omega_n^2\boldsymbol{\xi}_n = \boldsymbol{F}(\boldsymbol{\xi}_n). \tag{291}$$

Taking dot products of the first equation by $\boldsymbol{\xi}_n$ and the second equation by $\boldsymbol{\xi}_n$, and then taking their differences leads to

$$\left(\omega_m^2 - \omega_n^2\right)\int \rho\boldsymbol{\xi}_n\cdot\boldsymbol{\xi}_m d\boldsymbol{r} = \int \left[\boldsymbol{\xi}_m\cdot\boldsymbol{F}(\boldsymbol{\xi}_n) - \boldsymbol{\xi}_n\cdot\boldsymbol{F}(\boldsymbol{\xi}_m)\right] d\boldsymbol{r} = 0, \tag{292}$$

where self-adjointness of $\boldsymbol{F}$ is used. Therefore, the eigenfunctions form a complete set of mutually orthogonal eigenmodes.

Proof of the self-adjoint property of force operator, Eq. (280), can be done in three different ways:

- The first way is by performing vector operations of $\boldsymbol{\eta}\cdot\boldsymbol{F}(\boldsymbol{\xi})$ and $\boldsymbol{\xi}\cdot\boldsymbol{F}(\boldsymbol{\eta})$ to show that they are equal. This approach was taken by the original authors (Bernstein et al, 1958) and also by most of the textbooks such as in Goedbloed and Poedts (2004). But the process is quite tedious and prone to errors.
- The second way is to purposely rearrange a large number of terms in groups of symmetric forms between $\boldsymbol{\eta}$ and $\boldsymbol{\xi}$ so that they are obviously equal. This has been done nicely by Freidberg (2014). The process still involves quite a lot of vector operations.

- The third way is an indirect but formal and elegant proof by Kulsrud in 1964 (Kulsrud, 2005), which we reproduce below in a short form.

We begin by defining the total energy in the system,

$$\mathcal{E} = K + W; \quad K \equiv \int \frac{1}{2}\rho V^2 d\boldsymbol{r}; \quad W \equiv \int \left(\frac{B^2}{2\mu_0} + \frac{p}{\gamma - 1} + \rho\phi\right) d\boldsymbol{r}, \tag{293}$$

where K is the total kinetic energy, W is the total potential energy including magnetic, thermal and gravitational energy. ϕ is the gravitational potential. The system is perturbed at $t = 0$ by some adjustments which can occur before $t < 0$ and up to $t = 0$. This initial perturbation may or may not change $\mathcal{E}$ but as soon as the initial imposition of perturbation ends for $t \geq 0$, the energy is conserved such that $\mathcal{E}(t \geq 0) = \text{const.}$, while allowing the conversion of energy from one form to another. As stated previously, instability will occur if the initial perturbation can grow to lower potential energy in favor of perturbed kinetic energy without bounds. If the initial perturbation is infinitesimally small, the instability is linear instability.

Now we expand both K and W to the second order of infinitesimally small displacement $\boldsymbol{\xi}$ after the initial perturbation is imposed,

$$\mathcal{E} = K_0 + K_1(\boldsymbol{\xi}) + K_2(\boldsymbol{\xi}, \boldsymbol{\xi}) + ... + W_0 + W_1(\boldsymbol{\xi}) + W_2(\boldsymbol{\xi}, \boldsymbol{\xi}) + ... \tag{294}$$

with each terms can be calculate below:

$$\begin{aligned}
K_0 &= \frac{1}{2}\int \rho_0 V_0^2 d\boldsymbol{r} = 0, \\
K_1(\boldsymbol{\xi}) &= \int \left(\rho_0 \boldsymbol{V}_0 \cdot \frac{\partial \boldsymbol{\xi}}{\partial t} + \frac{1}{2}\rho_1 V_0^2\right) d\boldsymbol{r} = 0, \\
K_2(\boldsymbol{\xi}, \boldsymbol{\xi}) &= \frac{1}{2}\int \left[\rho_0 \left(\frac{\partial \boldsymbol{\xi}}{\partial t}\right)^2 + 2\rho_1 \boldsymbol{V}_0 \cdot \frac{\partial \boldsymbol{\xi}}{\partial t}\right] d\boldsymbol{r} = \frac{1}{2}\int \rho_0 \left(\frac{\partial \boldsymbol{\xi}}{\partial t}\right)^2 d\boldsymbol{r}, \qquad (295) \\
W_0 &= \int \left(\frac{B_0^2}{2\mu_0} + \frac{p_0}{\gamma - 1} + \rho_0\phi\right) d\boldsymbol{r}, \qquad (296) \\
W_1(\boldsymbol{\xi}) &= \frac{\partial W}{\partial \boldsymbol{\xi}} \cdot \boldsymbol{\xi} = 0, \\
W_2(\boldsymbol{\xi}, \boldsymbol{\xi}) &= \frac{\partial^2 W}{\partial \boldsymbol{\xi} \partial \boldsymbol{\xi}} : \boldsymbol{\xi}\boldsymbol{\xi}, \qquad (297)
\end{aligned}$$

where $\boldsymbol{V}_0 = 0$ is from the assumption used and $\partial W/\partial \boldsymbol{\xi} = 0$ is due to the fact that the system is in an equilibrium residing at an extremum of the potential energy W with regard to $\boldsymbol{\xi}$. As a result, we have

$$\mathcal{E} = \frac{1}{2}\int \rho_0 \left(\frac{\partial \boldsymbol{\xi}}{\partial t}\right)^2 d\boldsymbol{r} + W_0 + W_2(\boldsymbol{\xi}, \boldsymbol{\xi}), \tag{298}$$

which is conserved for $t \geq 0$. Therefore,

$$\frac{\partial \mathcal{E}}{\partial t} = \int \rho_0 \frac{\partial \boldsymbol{\xi}}{\partial t} \cdot \frac{\partial^2 \boldsymbol{\xi}}{\partial t^2} d\boldsymbol{r} + W_2\left(\frac{\partial \boldsymbol{\xi}}{\partial t}, \boldsymbol{\xi}\right) + W_2\left(\boldsymbol{\xi}, \frac{\partial \boldsymbol{\xi}}{\partial t}\right) = 0. \tag{299}$$

Defining $\boldsymbol{\eta} \equiv \partial \boldsymbol{\xi}/\partial t$, which is an independent vector from $\boldsymbol{\xi}$ at least at $t = 0$[1], and using the equation of motion Eq. (279), we finally have

$$\int \boldsymbol{\eta} \cdot \boldsymbol{F}(\boldsymbol{\xi}) d\boldsymbol{r} + W_2(\boldsymbol{\eta}, \boldsymbol{\xi}) + W_2(\boldsymbol{\xi}, \boldsymbol{\eta}) = 0. \tag{300}$$

Swapping $\boldsymbol{\eta}$ and $\boldsymbol{\xi}$ in this equation leads to

$$\int \boldsymbol{\xi} \cdot \boldsymbol{F}(\boldsymbol{\eta}) d\boldsymbol{r} + W_2(\boldsymbol{\xi}, \boldsymbol{\eta}) + W_2(\boldsymbol{\eta}, \boldsymbol{\xi}) = 0. \tag{301}$$

which can be compared with the previous equation. This leads to the elegant proof of self-adjointness of $\boldsymbol{F}$ from the symmetry of equations, Eq. (280): $\int \boldsymbol{\eta} \cdot \boldsymbol{F}(\boldsymbol{\xi}) d\boldsymbol{r} = \int \boldsymbol{\xi} \cdot \boldsymbol{F}(\boldsymbol{\eta}) d\boldsymbol{r}$. An additional consequence of the above equation is obtained by setting $\boldsymbol{\eta} = \boldsymbol{\xi}$ such that

$$W_2(\boldsymbol{\xi}, \boldsymbol{\xi}) = -\frac{1}{2} \int \boldsymbol{\xi} \cdot \boldsymbol{F}(\boldsymbol{\xi}) d\boldsymbol{r} \equiv \delta W(\boldsymbol{\xi}, \boldsymbol{\xi}), \tag{302}$$

where the latter expression of δW is called *energy integral*. This equation provides a convenient way to calculate the energy integral.

5.3 Energy Principle

The energy principle states

> The system is stable if and only if for all possible $\boldsymbol{\xi}$, $\delta W(\boldsymbol{\xi}, \boldsymbol{\xi}) > 0$.

Proving sufficient conditions for stability is straightforward by using energy conservation after initial perturbation $t \geq 0$,

$$\mathcal{E} - W_0 = \frac{1}{2} \int \rho_0 \left(\frac{\partial \boldsymbol{\xi}}{\partial t}\right)^2 d\boldsymbol{r} + \delta W(\boldsymbol{\xi}, \boldsymbol{\xi}), \tag{303}$$

which is a constant. Since δW is positive definite for all possible $\boldsymbol{\xi}$, the perturbed kinetic energy, which is also positive definite, cannot grow. Thus, the system is stable.

Proving necessary conditions of the energy principle is less straightforward. Among many versions of the proof, an elegant theorem by Laval et al (1965)

[1] One might argue that for $t > 0$, $\partial \boldsymbol{\xi}/\partial t$ may not be an independent vector as it satisfies ideal MHD equations. However, at $t = 0$, $\partial \boldsymbol{\xi}/\partial t$ can be imposed as part of initial perturbation, independent from the choice of $\boldsymbol{\xi}$.

is described below. The necessary condition statement reads: a stable system leads to positive δW for all possible $\boldsymbol{\xi}$. This is equivalent to the statement: if there exists a $\boldsymbol{\xi}_0$ such that $\delta W(\boldsymbol{\xi}_0, \boldsymbol{\xi}_0) < 0$, then the system is unstable. This is what we intend to prove.

Define γ_0 such that

$$\gamma_0^2 \equiv \frac{-\delta W(\boldsymbol{\xi}_0, \boldsymbol{\xi}_0)}{\frac{1}{2}\int \rho \xi_0^2 d\boldsymbol{r}} = \frac{-\delta W(\boldsymbol{\xi}_0, \boldsymbol{\xi}_0)}{I(\boldsymbol{\xi}_0, \boldsymbol{\xi}_0)} > 0, \tag{304}$$

where the integral $I(\boldsymbol{\xi}, \boldsymbol{\xi})$ is defined as

$$I(\boldsymbol{\xi}, \boldsymbol{\xi}) \equiv \frac{1}{2}\int \rho \boldsymbol{\xi} \cdot \boldsymbol{\xi} d\boldsymbol{r} = \frac{1}{2}\int \rho \xi^2 d\boldsymbol{r}. \tag{305}$$

Consequently, we have

$$\dot{I}(\boldsymbol{\xi}, \boldsymbol{\xi}) = \int \rho \boldsymbol{\xi} \cdot \dot{\boldsymbol{\xi}} d\boldsymbol{r}, \tag{306}$$

$$\begin{aligned} \ddot{I}(\boldsymbol{\xi}, \boldsymbol{\xi}) &= \int \rho \left(\dot{\xi}^2 + \boldsymbol{\xi} \cdot \ddot{\boldsymbol{\xi}} \right) d\boldsymbol{r} \\ &= 2\left[I(\dot{\boldsymbol{\xi}}, \dot{\boldsymbol{\xi}}) - \delta W(\boldsymbol{\xi}, \boldsymbol{\xi}) \right], \end{aligned} \tag{307}$$

where

$$\int \rho \boldsymbol{\xi} \cdot \ddot{\boldsymbol{\xi}} d\boldsymbol{r} = \int \boldsymbol{\xi} \cdot \boldsymbol{F}(\boldsymbol{\xi}) d\boldsymbol{r} = -2\delta W(\boldsymbol{\xi}, \boldsymbol{\xi}) \tag{308}$$

is used according to Eqs. (279) and (302). Now we are ready to calculate Eq. (303) as follows

$$\begin{aligned} \mathcal{E} - W_0 &= I\left[\dot{\boldsymbol{\xi}}(t), \dot{\boldsymbol{\xi}}(t) \right] + \delta W\left[\boldsymbol{\xi}(t), \boldsymbol{\xi}(t) \right] && (309) \\ &= I\left[\dot{\boldsymbol{\xi}}(0), \dot{\boldsymbol{\xi}}(0) \right] + \delta W\left[\boldsymbol{\xi}(0), \boldsymbol{\xi}(0) \right] \\ &= \gamma_0^2 I\left(\boldsymbol{\xi}_0, \boldsymbol{\xi}_0 \right) + \delta W\left(\boldsymbol{\xi}_0, \boldsymbol{\xi}_0 \right) && (310) \\ &= 0, && (311) \end{aligned}$$

where we used the choice of $\dot{\boldsymbol{\xi}}(0) \equiv \gamma_0 \boldsymbol{\xi}(0) = \gamma_0 \boldsymbol{\xi}_0$ for the step in Eq. (310) and the definition of γ_0 in Eq. (304) for the step in Eq. (311). (Note that the choice of $\dot{\boldsymbol{\xi}}(0) \equiv \gamma_0 \boldsymbol{\xi}_0$ is consistent with the expected purely growing modes when the system is unstable). Therefore, from the steps in Eq. (309) and Eq. (311), we have

$$\delta W(\boldsymbol{\xi}, \boldsymbol{\xi}) = -I(\dot{\boldsymbol{\xi}}, \dot{\boldsymbol{\xi}}), \tag{312}$$

which can be substituted into Eq. (307) to yield

$$\ddot{I}(\boldsymbol{\xi}, \boldsymbol{\xi}) = 4I(\dot{\boldsymbol{\xi}}, \dot{\boldsymbol{\xi}}). \tag{313}$$

Now by using Schwarz inequality:

$$\left[\int \rho\boldsymbol{\xi}\cdot\dot{\boldsymbol{\xi}}d\boldsymbol{r}\right]^2 \leq \left[\int \rho\xi^2 d\boldsymbol{r}\right]\left[\int \rho\dot{\xi}^2 d\boldsymbol{r}\right] \tag{314}$$

and Eq. (306) for $\dot{I}(\boldsymbol{\xi},\boldsymbol{\xi})$, we have

$$\begin{aligned}\left[\dot{I}(\boldsymbol{\xi},\boldsymbol{\xi})\right]^2 &\leq 2I(\boldsymbol{\xi},\boldsymbol{\xi})\cdot 2I(\dot{\boldsymbol{\xi}},\dot{\boldsymbol{\xi}}) \\ &= I(\boldsymbol{\xi},\boldsymbol{\xi})\ddot{I}(\boldsymbol{\xi},\boldsymbol{\xi}),\end{aligned} \tag{315}$$

where Eq. (313) is used. This inequality can be simply written as $\dot{I}^2 \leq I\ddot{I}$, which can be divided by I^2 to yield

$$\frac{\ddot{I}}{I} - \left(\frac{\dot{I}}{I}\right)^2 \geq 0 \quad \text{or} \quad \frac{d}{dt}\left(\frac{\dot{I}}{I}\right) \geq 0. \tag{316}$$

$\dot{I}/I$ is a growing function of time for $t > 0$.Therefore,

$$\left.\frac{\dot{I}}{I}\right|_{t=t} \geq \left.\frac{\dot{I}}{I}\right|_{t=0} = 2\gamma_0. \tag{317}$$

The last equal sign of this equation is due to

$$\begin{aligned}\dot{I}(\boldsymbol{\xi}_0,\boldsymbol{\xi}_0) &= \int \rho\boldsymbol{\xi}_0\cdot\dot{\boldsymbol{\xi}}(0)d\boldsymbol{r} \\ &= \gamma_0\int \rho\xi_0^2 d\boldsymbol{r} \\ &= 2\gamma_0 I(\boldsymbol{\xi}_0,\boldsymbol{\xi}_0).\end{aligned} \tag{318}$$

Solving Eq. (317) yields a solution which grows at least exponentially, indicating instability,

$$I\left[\boldsymbol{\xi}(t),\boldsymbol{\xi}(t)\right] \geq e^{2\gamma_0 t} I(\boldsymbol{\xi}_0,\boldsymbol{\xi}_0). \tag{319}$$

5.4 Additional Remarks

Now that we have proved the energy principle, let us summarize its advantages:

- Finding one trial displacement vector $\boldsymbol{\xi}$ such that $\delta W < 0$ is sufficient to show that the system is unstable.
- Marginal stability can be determined by using the $\boldsymbol{F}(\boldsymbol{\xi}) = 0$ contour.
- The energy integral $\delta W < 0$ has a physically intuitive form which can provide physical understanding (next lecture).
- There exists a practical method to numerically test ideal MHD stability.

Furthermore, the energy principle can be extended to include a vacuum region surrounding the plasma with contributions from the surface that separates them, see (Freidberg, 2014, Ch.8). This is called *Extended Energy Principle*. Energy principle can also be extended to other MHD models (Freidberg, 2014, Ch.10) other than the ideal MHD model discussed here.

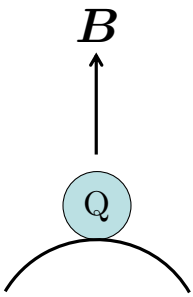

Fig. 28 Stability of an electrically charged ball on the top of hill in a vertical magnetic field.

Finally, the energy principle can fail. One particular example is when the force operator $\boldsymbol{F}$ is a function of not only $\boldsymbol{\xi}$ but also $\dot{\boldsymbol{\xi}}$ or velocity. An example of this is the case of an electrically charged ball on a hill under a vertical magnetic field, shown in Fig. 28 (Kulsrud, 2005, Ch.7). Without the magnetic field, the ball is unstable to the downward gravitational potential energy ($\delta W < 0$). With a strong enough field, however, the ball can initially go down the hill but when it picks up some speed, the Lorentz force (which is a function of velocity) acts to turn it around and eventually returns it to its original position. Therefore, finding a particular displacement to lower its potential energy ($\delta W < 0$) is insufficient to guarantee its instability. Another case is when the system has an equilibrium flow. Contradicting cases can occur: the system can be unstable even if δW is always positive because the growing perturbation flow energy was mistaken as increased potential energy or a flow shear can stabilize instabilities that are due to $\delta W < 0$.

5.5 Summary

- The basic idea of stability analysis and energy principle are powerful tools for analyzing MHD systems.
- The self-adjoint property of the force operator in ideal MHD systems is fundamental to the energy principle.
- Advantages and caveats of using energy principle.

5.6 Further Readings

- Chapter 7 in Kulsrud (2005)
- Chapters 8, 9 and 10 in Freidberg (2014)

- Chapter 4 in Miyamoto (2016)

5.7 Homework Problem Set 5

1. Complex argument for energy integral.
   Given the energy principle for any real displacement, prove that it can be extended to any complex displacement $\boldsymbol{\xi}$: The system is stable if and only if

$$\delta W(\boldsymbol{\xi}^*, \boldsymbol{\xi}) > 0 \tag{320}$$

   where $\boldsymbol{\xi}^*$ is the complex conjugate of $\boldsymbol{\xi}$.

2. Simple proof of the energy principle.
   Consider a case with some displacement $\boldsymbol{\xi}_0$ such that the change in potential energy $\delta W(\boldsymbol{\xi}_0, \boldsymbol{\xi}_0) \equiv -a < 0$, causing the system to be unstable.

   (a) By choosing initial conditions at $t = 0$: $\boldsymbol{\xi}(0) = \boldsymbol{\xi}_0$ and $\dot{\boldsymbol{\xi}}(0) = 0$, calculate the total perturbation energy at $t \geq 0$,

$$\epsilon(t) = \frac{1}{2}\int \rho \dot{\boldsymbol{\xi}}^2 d\boldsymbol{r} + \delta W(\boldsymbol{\xi}, \boldsymbol{\xi}), \tag{321}$$

   and show that $\epsilon(t) < 0$.

   (b) Prove that the system is unstable by showing that

$$I(\boldsymbol{\xi}, \boldsymbol{\xi}) \equiv \frac{1}{2}\int \rho \xi^2 d\boldsymbol{r} \tag{322}$$

   grows at least as fast as at^n when $t \to \infty$. What is the value of n?

   (c) Why is the total perturbation energy not conserved ($\epsilon(t) < 0$) in this case? What does the existence of this case mean to the energy principle proof given in the class?

6 Applications of Energy Principle

In this lecture, we will illustrate the usefulness of the energy principle by applying it to generic cases in astrophysics and fusion plasmas. Including gravity, $\boldsymbol{g}$, the force operator, $\boldsymbol{F}$, acting on the displacement vector $\boldsymbol{\xi}$ is given by

$$\boldsymbol{F}(\boldsymbol{\xi}) = \frac{1}{\mu_0}(\boldsymbol{\nabla}\times\boldsymbol{Q})\times\boldsymbol{B} + \boldsymbol{j}\times\boldsymbol{Q} + \boldsymbol{\nabla}(\gamma p\boldsymbol{\nabla}\cdot\boldsymbol{\xi} + \boldsymbol{\xi}\cdot\boldsymbol{\nabla}p) - \boldsymbol{g}\boldsymbol{\nabla}\cdot(\rho\boldsymbol{\xi}), \quad (323)$$

where $\mu_0\boldsymbol{j} = \boldsymbol{\nabla}\times\boldsymbol{B}$, $\boldsymbol{Q} = \boldsymbol{\nabla}\times(\boldsymbol{\xi}\times\boldsymbol{B})$, and all subscript "0" have been dropped for equilibrium quantities. The energy integral δW can be calculated using $\delta W = -\frac{1}{2}\int\boldsymbol{\xi}\cdot\boldsymbol{F}(\boldsymbol{\xi})dV$. The first term of the integrand is

$$\begin{aligned}\frac{1}{\mu_0}\boldsymbol{\xi}\cdot[(\boldsymbol{\nabla}\times\boldsymbol{Q})\times\boldsymbol{B}] &= -\frac{1}{\mu_0}(\boldsymbol{\nabla}\times\boldsymbol{Q})\cdot(\boldsymbol{\xi}\times\boldsymbol{B}) \\ &= -\frac{Q^2}{\mu_0} + \frac{1}{\mu_0}\boldsymbol{\nabla}\cdot[(\boldsymbol{\xi}\times\boldsymbol{B})\times\boldsymbol{Q}], \end{aligned} \quad (324)$$

where the contribution from the last term on RHS to the δW integration vanishes with proper boundary conditions. The second term of the integrand is

$$\boldsymbol{\xi}\cdot(\boldsymbol{j}\times\boldsymbol{Q}) = -\boldsymbol{j}\cdot(\boldsymbol{\xi}\times\boldsymbol{Q}). \quad (325)$$

The third term of the integrand is

$$\boldsymbol{\xi}\cdot\boldsymbol{\nabla}(\gamma p\boldsymbol{\nabla}\cdot\boldsymbol{\xi}) = \boldsymbol{\nabla}\cdot(\boldsymbol{\xi}\gamma p\boldsymbol{\nabla}\cdot\boldsymbol{\xi}) - \gamma p(\boldsymbol{\nabla}\cdot\boldsymbol{\xi})^2, \quad (326)$$

where the first term on RHS vanishes in the δW integration with proper boundary conditions. The fourth term of the integrand is

$$\boldsymbol{\xi}\cdot\boldsymbol{\nabla}(\boldsymbol{\xi}\cdot\boldsymbol{\nabla}p) = \boldsymbol{\nabla}\cdot(\boldsymbol{\xi}(\boldsymbol{\xi}\cdot\boldsymbol{\nabla}p)) - (\boldsymbol{\xi}\cdot\boldsymbol{\nabla}p)(\boldsymbol{\nabla}\cdot\boldsymbol{\xi}), \quad (327)$$

where the first term on RHS vanishes again. The last term of the integrand is simply,

$$-\boldsymbol{\xi}\cdot\boldsymbol{g}(\rho\boldsymbol{\nabla}\cdot\boldsymbol{\xi} + \boldsymbol{\xi}\cdot\boldsymbol{\nabla}\rho). \quad (328)$$

Combining all terms yields

$$\begin{aligned}2\delta W = \int\Big[&\frac{Q^2}{\mu_0} + \boldsymbol{j}\cdot(\boldsymbol{\xi}\times\boldsymbol{Q}) + \gamma p(\boldsymbol{\nabla}\cdot\boldsymbol{\xi})^2 + (\boldsymbol{\xi}\cdot\boldsymbol{\nabla}p)(\boldsymbol{\nabla}\cdot\boldsymbol{\xi}) \\ &+\boldsymbol{\xi}\cdot\boldsymbol{g}(\rho\boldsymbol{\nabla}\cdot\boldsymbol{\xi} + \boldsymbol{\xi}\cdot\boldsymbol{\nabla}\rho)\Big]dV. \end{aligned} \quad (329)$$

6.1 Convective Instability

We will first consider convective instability, which occurs when plasma is purely confined by the gravitational force with no magnetic field involved,

$$\rho \boldsymbol{g} = \boldsymbol{\nabla} p. \tag{330}$$

Using this equation, the energy integral Eq. (329) simplifies to

$$\begin{aligned}
2\delta W &= \int \left[\gamma p \left(\boldsymbol{\nabla}\cdot\boldsymbol{\xi}\right)^2 + \left(\boldsymbol{\xi}\cdot\boldsymbol{\nabla} p\right)\left(\boldsymbol{\nabla}\cdot\boldsymbol{\xi}\right) + \boldsymbol{\xi}\cdot\boldsymbol{g}\left(\rho\boldsymbol{\nabla}\cdot\boldsymbol{\xi} + \boldsymbol{\xi}\cdot\boldsymbol{\nabla}\rho\right)\right] dV \\
&= \int \left[\gamma p \left(\boldsymbol{\nabla}\cdot\boldsymbol{\xi}\right)^2 + 2\left(\boldsymbol{\xi}\cdot\boldsymbol{\nabla} p\right)\left(\boldsymbol{\nabla}\cdot\boldsymbol{\xi}\right) + \frac{(\boldsymbol{\xi}\cdot\boldsymbol{\nabla} p)(\boldsymbol{\xi}\cdot\boldsymbol{\nabla}\rho)}{\rho}\right] dV \\
&= \int \left[\gamma p \left(\boldsymbol{\nabla}\cdot\boldsymbol{\xi} + \frac{\boldsymbol{\xi}\cdot\boldsymbol{\nabla} p}{\gamma p}\right)^2 - \frac{(\boldsymbol{\xi}\cdot\boldsymbol{\nabla} p)^2}{\gamma p} + \frac{(\boldsymbol{\xi}\cdot\boldsymbol{\nabla} p)(\boldsymbol{\xi}\cdot\boldsymbol{\nabla}\rho)}{\rho}\right] dV \\
&= \int \left[\gamma p \left(\boldsymbol{\nabla}\cdot\boldsymbol{\xi} + \frac{\boldsymbol{\xi}\cdot\boldsymbol{\nabla} p}{\gamma p}\right)^2 - \frac{\boldsymbol{\xi}\cdot\boldsymbol{\nabla} p}{\gamma}\boldsymbol{\xi}\cdot\left(\frac{\boldsymbol{\nabla} p}{p} - \frac{\gamma\boldsymbol{\nabla}\rho}{\rho}\right)\right] dV \\
&= \int \left[\gamma p \left(\boldsymbol{\nabla}\cdot\boldsymbol{\xi} + \frac{\boldsymbol{\xi}\cdot\boldsymbol{\nabla} p}{\gamma p}\right)^2 - \frac{\boldsymbol{\xi}\cdot\boldsymbol{\nabla} p}{\gamma}\boldsymbol{\xi}\cdot\boldsymbol{\nabla}\ln\left(\frac{p}{\rho^\gamma}\right)\right] dV.
\end{aligned} \tag{331}$$

The first term is positive definite and can be made zero by choosing $\boldsymbol{\nabla}\cdot\boldsymbol{\xi}$ to minimize δW. The second term, however, can have either sign. For stability, the pressure gradient, $\boldsymbol{\nabla} p$, and entropy gradient, $\boldsymbol{\nabla} s \equiv C_V \boldsymbol{\nabla}\ln(p/\rho^\gamma)$, should be in opposite directions. This requirement is the same as the Schwarzchild criterion (Schwarzschild, 1906) for stellar convection, which we have reproduced here in a few lines using the energy principle.

6.2 Interchange Instability

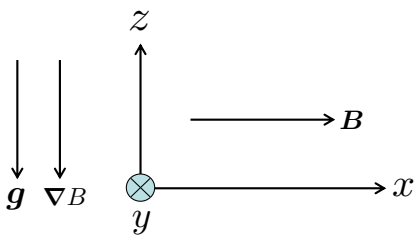

Fig. 29 The coordinate system for interchange instability and Parker instability: the magnetic field is in the x direction, ($\boldsymbol{g}$) and magnetic field gradient are in the $-z$ direction.

Now, let us consider the case when a 1D cold plasma is supported by a magnetic field against constant gravitational force as shown in Fig. 29. When

the plasma pressure is negligible, the force balance is given by,

$$\rho \boldsymbol{g} = \frac{\boldsymbol{\nabla} B^2}{2\mu_0}. \tag{332}$$

Ignoring the pressure terms, the energy integral becomes

$$2\delta W = \int \left[\frac{Q^2}{\mu_0} + \boldsymbol{j} \cdot (\boldsymbol{\xi} \times \boldsymbol{Q}) + \boldsymbol{\xi} \cdot \boldsymbol{g} \left(\rho \boldsymbol{\nabla} \cdot \boldsymbol{\xi} + \boldsymbol{\xi} \cdot \boldsymbol{\nabla} \rho \right) \right] dV. \tag{333}$$

We first focus on displacement that does not vary along the magnetic field direction. The magnetic field does not bend, $(\boldsymbol{B} \cdot \boldsymbol{\nabla})\boldsymbol{\xi} = 0$, *i.e.* $\boldsymbol{\xi}$ does not vary in the x direction but is only compressed or decompressed in the $y - z$ plane. Under this condition, expanding $\boldsymbol{Q}$ yields

$$\begin{aligned} \boldsymbol{Q} &= \boldsymbol{\nabla} \times (\boldsymbol{\xi} \times \boldsymbol{B}) \\ &= (\boldsymbol{B} \cdot \boldsymbol{\nabla})\boldsymbol{\xi} + \boldsymbol{\xi}(\boldsymbol{\nabla} \cdot \boldsymbol{B}) - \boldsymbol{B}(\boldsymbol{\nabla} \cdot \boldsymbol{\xi}) - (\boldsymbol{\xi} \cdot \boldsymbol{\nabla})\boldsymbol{B} \\ &= -\boldsymbol{B}(\boldsymbol{\nabla} \cdot \boldsymbol{\xi}) - (\boldsymbol{\xi} \cdot \boldsymbol{\nabla})\boldsymbol{B}. \end{aligned} \tag{334}$$

We further restrict the displacement from compressing or decompressing magnetic field such that $\boldsymbol{Q} = 0$ by choosing plasma compressibility $\boldsymbol{\nabla} \cdot \boldsymbol{\xi}$ to be

$$\boldsymbol{\nabla} \cdot \boldsymbol{\xi} = -\frac{(\boldsymbol{\xi} \cdot \boldsymbol{\nabla})B}{B}. \tag{335}$$

Then, from Eq. (333) we have,

$$\begin{aligned} 2\delta W &= \int \boldsymbol{\xi} \cdot \boldsymbol{g} \left(\rho \boldsymbol{\nabla} \cdot \boldsymbol{\xi} + \boldsymbol{\xi} \cdot \boldsymbol{\nabla} \rho \right) dV \\ &= \int \boldsymbol{\xi} \cdot \boldsymbol{g} \left[-\rho \frac{(\boldsymbol{\xi} \cdot \boldsymbol{\nabla})B}{B} + \boldsymbol{\xi} \cdot \boldsymbol{\nabla} \rho \right] dV \\ &= \int \rho \left(\boldsymbol{\xi} \cdot \boldsymbol{g} \right) \boldsymbol{\xi} \cdot \left(\frac{\boldsymbol{\nabla} \rho}{\rho} - \frac{\boldsymbol{\nabla} B}{B} \right) dV \\ &= \int \rho \left(\boldsymbol{\xi} \cdot \boldsymbol{g} \right) \left(\boldsymbol{\xi} \cdot \boldsymbol{\nabla} \right) \ln \frac{\rho}{B} dV. \end{aligned} \tag{336}$$

Therefore, $\boldsymbol{g}$ and $\boldsymbol{\nabla} \ln \frac{\rho}{B}$ need to be in the same direction for stability. This requirement is a sufficient condition for stability as we limit the choices of $\boldsymbol{\xi}$ such that $\boldsymbol{Q} = 0$. It turns out that this is also the necessary condition (Kulsrud, 2005, Ch.7) (also see Homework Set 6) as long as there is no bent field lines, *i.e.* $(\boldsymbol{B} \cdot \boldsymbol{\nabla})\boldsymbol{\xi} = 0$.

The physical picture of this instability is shown in Fig. 30. Total magnetic energy will not change when we swap the locations of two tubes with the same flux at different heights without bending. The magnetic energy of a flux tube

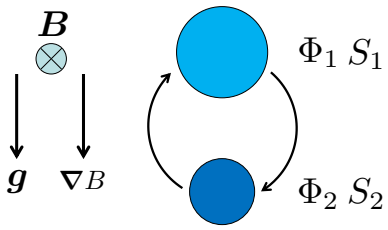

Fig. 30 Interchange instability as an MHD analog of Rayleigh-Taylor instability. The darker color indicates a stronger magnetic field and denser plasma.

is given by

$$W_{\rm B} = \int \frac{B^2}{2\mu_0} S dl = \frac{\Phi^2}{2\mu_0} \int \frac{dl}{S}, \tag{337}$$

where B is assumed to be uniform within a sufficiently small tube of cross-section area S. $\int S dl$ is the volume integral along the tube and $\Phi = BS$ is the magnetic flux.

Consider flux tube 1 with flux Φ_1 and cross-section area of S_1 and flux tube 2 with flux Φ_2 and cross-section area of S_2. The change in magnetic field energy due to interchanging them is

$$\begin{aligned}
\delta W_{\rm B} &= (W_{\rm B1} + W_{\rm B2})_{\rm after} - (W_{\rm B1} + W_{\rm B2})_{\rm before} \\
&= \left(\frac{\Phi_1^2}{2\mu_0} \int \frac{dl}{S_2} + \frac{\Phi_2^2}{2\mu_0} \int \frac{dl}{S_1} \right) - \left(\frac{\Phi_1^2}{2\mu_0} \int \frac{dl}{S_1} + \frac{\Phi_2^2}{2\mu_0} \int \frac{dl}{S_2} \right) \\
&= \left(\frac{\Phi_1^2}{2\mu_0} - \frac{\Phi_2^2}{2\mu_0} \right) \left(\int \frac{dl}{S_2} - \int \frac{dl}{S_1} \right) = 0.
\end{aligned} \tag{338}$$

The change vanishes when $\Phi_1 = \Phi_2$, even in the case when $S_1 \neq S_2$. According to the equilibrium force balance, Eq. (332), B needs to increase in the same direction as gravity. However, if plasma density ρ does not increase as fast as B, the quantity ρ/B will *decrease*, causing the plasma mass per magnetic flux to decrease in the direction of gravity.

In other words, interchanging two identical flux tubes at different heights can lower the gravitational potential energy, even if the magnetic energy does not change. The potential energy is lowered because the mass moving downward is more than the mass moving upward. This instability is therefore called *interchange instability*, which is essentially a Rayleigh-Taylor instability (see Homework Set 4) in ideal MHD (Kruskal and Schwarzschild (1954)) with a heavy fluid (plasma) sitting on top of a light fluid (magnetic field) against gravity.

The physical picture of this instability with a sharp boundary between plasma and vacuum is illustrated in Fig. 31 (Miyamoto, 2016, Ch.6). The magnetic field is higher on the vacuum side to support the plasma against gravity pointing towards the vacuum side. Under the gravitational potential, both ions

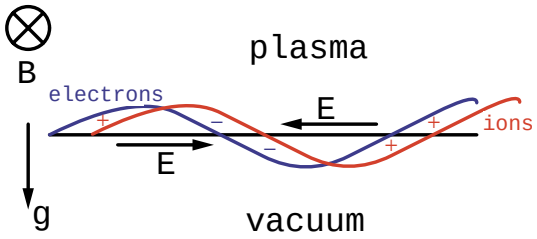

Fig. 31 Interchange instability in plasma with a sharp boundary against vacuum.

and electrons undergo $g \times B$ drift in opposite directions along the surface, maintaining the shape of the unperturbed surface. After the perturbation, the ions' surface will differ from the electrons' surface, shown in Fig. 31. The difference will create charge separation, and therefore electric field parallel the surface. The $E \times B$ drift from this electric field is the same for both species and has a phase that reinforces the initial perturbation, resulting in instability.

6.3 Parker Instability

In the previous section on interchange instability, we did not allow displacement to vary along the magnetic field direction. One may wonder what would happen if we did. We might think that this would lead to a more stable system because bending field lines increase magnetic potential energy or δW. It turns out this is not the case, but instead, we will encounter a new instability called *Parker instability* (Parker, 1966, 1967). Allowing the plasma to slide down along the field line can lower the gravitational potential energy more than the increase in magnetic energy via field line bending. Below, we illustrate how this can happen (Kulsrud, 2005, Ch.7).

We relax $(\boldsymbol{B}\cdot\boldsymbol{\nabla})\boldsymbol{\xi} = 0$ by allowing $\boldsymbol{\xi}$ to vary in the x direction bending the field lines. In addition, we imposed the previous condition on the perpendicular components $\boldsymbol{\xi}_\perp$ (ξ_y and ξ_z):

$$\boldsymbol{\nabla}\cdot\boldsymbol{\xi}_\perp = -\frac{(\boldsymbol{\xi}\cdot\boldsymbol{\nabla})B}{B}. \tag{339}$$

Then we have

$$\begin{aligned}\boldsymbol{Q} &= (\boldsymbol{B}\cdot\boldsymbol{\nabla})\boldsymbol{\xi} - \boldsymbol{B}(\boldsymbol{\nabla}\cdot\boldsymbol{\xi}) - (\boldsymbol{\xi}\cdot\boldsymbol{\nabla})\boldsymbol{B} \\ &= (\boldsymbol{B}\cdot\boldsymbol{\nabla})(\xi_x\hat{\boldsymbol{x}} + \boldsymbol{\xi}_\perp) - \boldsymbol{B}\left(\frac{\partial\xi_x}{\partial x} + \boldsymbol{\nabla}\cdot\boldsymbol{\xi}_\perp\right) - (\boldsymbol{\xi}\cdot\boldsymbol{\nabla})\boldsymbol{B} \\ &= (\boldsymbol{B}\cdot\boldsymbol{\nabla})\boldsymbol{\xi}_\perp,\end{aligned} \tag{340}$$

giving $Q_\parallel = 0$ and $\boldsymbol{Q}_\perp = (\boldsymbol{B}\cdot\boldsymbol{\nabla})\boldsymbol{\xi}_\perp$ due to field line bending. $\hat{\boldsymbol{x}}$ is the unit vector in the x or $\boldsymbol{B}$ direction. Therefore, the first term of δW integrand in

Eq. (333) is

$$\frac{Q_\perp^2}{\mu_0} = \frac{\left[(\boldsymbol{B}\cdot\boldsymbol{\nabla})\boldsymbol{\xi}_\perp\right]^2}{\mu_0}. \tag{341}$$

Since the equilibrium $\boldsymbol{j}$ is in the y direction, the second term of δW integrand is

$$\boldsymbol{j}\cdot(\boldsymbol{\xi}\times\boldsymbol{Q}_\perp) = j_y(\boldsymbol{\xi}\times\boldsymbol{Q}_\perp)_y, \tag{342}$$

where $j_y = (1/\mu_0)\partial B/\partial z$. Therefore we have

$$\begin{aligned}
\boldsymbol{Q}_\perp &= \left(0, B\frac{\partial\xi_y}{\partial x}, B\frac{\partial\xi_z}{\partial x}\right),\\
(\boldsymbol{\xi}\times\boldsymbol{Q}_\perp)_y &= -\xi_x B\frac{\partial\xi_z}{\partial x},\\
j_y(\boldsymbol{\xi}\times\boldsymbol{Q}_\perp)_y &= -\frac{1}{2\mu_0}\frac{\partial B^2}{\partial z}\xi_x\frac{\partial\xi_z}{\partial x} = -\rho g\xi_x\frac{\partial\xi_z}{\partial x},
\end{aligned} \tag{343}$$

where the force balance Eq. (332) is used. Integrating by parts and removing the surface terms as before, we obtain

$$\int \boldsymbol{j}\cdot(\boldsymbol{\xi}\times\boldsymbol{Q}_\perp)dV = \int \rho g\xi_z\frac{\partial\xi_x}{\partial x} = \int \rho\boldsymbol{\xi}\cdot\boldsymbol{g}\frac{\partial\xi_x}{\partial x}. \tag{344}$$

Since ξ_x now depends on x, the third term in the integrand of δW, Eq. (333), has another identical term. We have

$$2\delta W = \int\left[\frac{\left[(\boldsymbol{B}\cdot\boldsymbol{\nabla})\boldsymbol{\xi}_\perp\right]^2}{\mu_0} + \rho\,(\boldsymbol{\xi}\cdot\boldsymbol{g})\,(\boldsymbol{\xi}\cdot\boldsymbol{\nabla})\ln\frac{\rho}{B} + 2\rho\boldsymbol{\xi}\cdot\boldsymbol{g}\frac{\partial\xi_x}{\partial x}\right]dV. \tag{345}$$

Comparing the δW for interchange instability, there are two extra terms. The first term is due to the increased magnetic energy from bending the field lines, while the second term is due to the change of gravitational energy, which can be made negative by choosing the proper parameters. Assuming the wavenumber in the x direction is k_x, the first term scales like $(Bk_x\xi_z)^2/\mu_0$ while the second term scales like $2\rho g k_x\xi_x\xi_z = 2B^2k_x\xi_x\xi_z/h_z\mu_0$, given that

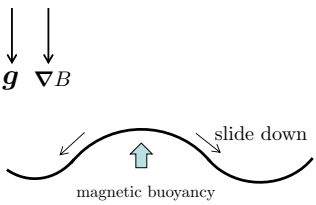

Fig. 32 Parker instability or magnetic buoyancy instability.

$\rho g = B^2/h_z\mu_0$ with h_z as the vertical scale height. Taking the ratio of these two terms yields the condition for δW to be negative,

$$\frac{2\xi_x}{k_x h_z \xi_z} > 1 \quad \text{or} \quad \xi_x > \frac{1}{2} k_x h_z \xi_z. \tag{346}$$

It means that for each choice of h_z, k_x, and ξ_z, the plasma can always be made unstable for a sufficiently large parallel displacement, ξ_x. In this scenario, the plasma will slide down along the bent field lines to the lower gravitational potential with a change greater than the increased magnetic potential energy. Sometimes this instability is called magnetic buoyancy instability. The depleted field lines rise upward, given that they are lighter than the surroundings, reinforcing the plasma to slide downward, see Fig. 32.

6.4 Interchange Instability Without Gravity

The last combination of forces is the case when the plasma with finite pressure is confined by a magnetic field without gravity,

$$\boldsymbol{\nabla} p = \boldsymbol{j} \times \boldsymbol{B} \tag{347}$$

We have described this case with the Grad-Shafranov equation in Lecture 2. Even neglecting the gravity, a magnetically confined plasma will experience an effective "gravity" due to the curved field lines, as indicated in the guiding center motion of a charged particle (Miyamoto, 2016, Ch.6),

$$\boldsymbol{V}_{\rm gc} = \frac{\boldsymbol{E} \times \boldsymbol{b}}{\boldsymbol{B}} + \frac{\boldsymbol{b}}{\Omega} \times \left(\boldsymbol{g} + \frac{v_\perp^2/2 + v_\parallel^2}{R} \boldsymbol{n} \right) + v_\parallel \boldsymbol{b} \tag{348}$$

where $\boldsymbol{b} \equiv \boldsymbol{B}/B$. Ω is the cyclotron angular frequency including the sign of charge, $\boldsymbol{n}$ is the unit vector of the field line curvature with radius R. When a charged particle moves along the curved field line, it experiences an effective gravity due to the centrifugal force. Therefore, the effective gravity is in the opposite direction of field line curvature vector.

There are two possibilities for field line curvature shown in Fig. 33. When the field line curvature vector points away from plasma or effective gravity points towards the plasma, the situation is similar to the case where a light fluid (magnetic field) sits on top of a heavy fluid (plasma). This is because the magnetic curvature vector is in the same direction of field strength gradient vector, especially in the low beta system where $\boldsymbol{j} \times \boldsymbol{B} = (\boldsymbol{B} \cdot \boldsymbol{\nabla})\boldsymbol{B} - \boldsymbol{\nabla}(B^2/2\mu_0) \approx 0$. In this case, the plasma is stable against interchange instability or Rayleigh-Taylor instability. The field line curvature in this case is labeled as "good curvature", confining the plasma in a low magnetic field region or the *(absolute) minimum-B* configuration.

In contrast, when the effective gravity points away from the plasma, the system is unstable to interchange instability. This configuration is similar to

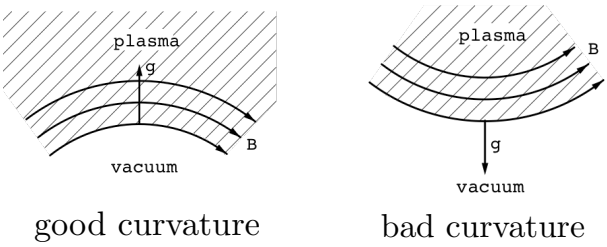

Fig. 33 Good and bad curvatures of field lines for confining plasma.

the case with a heavy fluid sitting on top of a light fluid corresponding to the "bad curvature", confining the plasma in a high magnetic field region.

The concept of good and bad field line curvatures for interchange instability can be applied to stability analysis of magnetically confined plasmas, see Fig. 34. The middle section of a mirror configuration has a bad curvature, while the cusp configuration has good curvatures everywhere. However, both suffer from losing particles due to the loss-cones along the field lines. The toroidal configuration does not have the loss-cones, but its field line curvatures can be mixed. The field lines on the outer side will always have bad curvatures. The inner side curvature can be good when the q is large enough. Since the field lines pass through both inner and outer sides within the same flux surface, the concept of *(average) minimum-B* configuration is needed to analyze its stability against interchange instability (see later).

Previously when we described the interchange instability under gravity, we demonstrated the importance of examining whether the gravitational potential energy can be lowered as we interchange the two magnetic flux tubes without changing the total magnetic energy. Here, we can follow the same procedure to determine the stability by examining whether the plasma internal energy, $pV/(\gamma - 1)$ where V is the flux tube volume, can be lowered by interchanging two magnetic flux tubes without changing the magnetic energy. Consider two flux tubes, 1 and 2, with their pressure and volume, (p_1, V_1) and (p_2, V_2), respectively. When the plasma follows the adiabatic process to

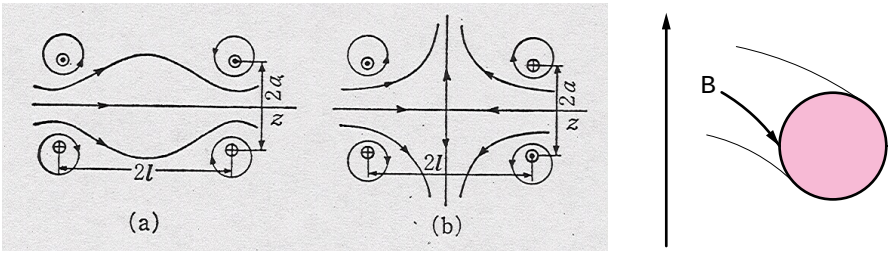

Fig. 34 Good and bad curvatures of field lines in mirror, cusp, and toroidal configurations.

preserve entropy, the pressure after the interchange needs to satisfy,

$$p_1' V_2^\gamma = p_1 V_1^\gamma, \tag{349}$$
$$p_2' V_1^\gamma = p_2 V_2^\gamma, \tag{350}$$

where p_α' is the pressure after plasma in tube α has been swapped to the other tube's location. Therefore, we have

$$p_1' = p_1 \left(\frac{V_1}{V_2}\right)^\gamma, \tag{351}$$
$$p_2' = p_2 \left(\frac{V_2}{V_1}\right)^\gamma. \tag{352}$$

The change in plasma internal energy can be calculated as

$$(\gamma-1)\delta W = (p_1' V_2 - p_1 V_1) + (p_2' V_1 - p_2 V_2) \tag{353}$$
$$= p_1 V_1^\gamma V_2^{1-\gamma} - p_1 V_1 + p_2 V_1^{1-\gamma} V_2^\gamma - p_2 V_2. \tag{354}$$

Now, we assume that tube 2 is located right next to tube 1, such that

$$p_2 = p_1 + \delta p, \tag{355}$$
$$V_2 = V_1 + \delta V. \tag{356}$$

Up to the quadratic terms, this leads to the following relations:

$$V_1^\gamma V_2^{1-\gamma} = V_1^\gamma \left[V_1\left(1+\frac{\delta V}{V_1}\right)\right]^{1-\gamma}$$
$$= V_1 \left[1 + (1-\gamma)\frac{\delta V}{V_1} + \frac{(1-\gamma)(-\gamma)}{2}\left(\frac{\delta V}{V_1}\right)^2\right], \tag{357}$$
$$V_1^{1-\gamma} V_2^\gamma = V_1^{1-\gamma} \left[V_1\left(1+\frac{\delta V}{V_1}\right)\right]^{\gamma}$$
$$= V_1 \left[1 + \gamma\frac{\delta V}{V_1} + \frac{\gamma(\gamma-1)}{2}\left(\frac{\delta V}{V_1}\right)^2\right], \tag{358}$$
$$p_2 V_2 = p_1 V_1 \left(1+\frac{\delta p}{p_1}\right)\left(1+\frac{\delta V}{V_1}\right)$$
$$= p_1 V_1 \left(1 + \frac{\delta p}{p_1} + \frac{\delta V}{V_1} + \frac{\delta p \delta V}{p_1 V_1}\right). \tag{359}$$

Then, the internal energy change is

$$(\gamma-1)\delta W = p_1 V_1 \left[1 + (1-\gamma)\frac{\delta V}{V_1} - \frac{\gamma(1-\gamma)}{2}\left(\frac{\delta V}{V_1}\right)^2\right] - p_1 V_1 \tag{360}$$

$$+p_1\left(1+\frac{\delta p}{p_1}\right)V_1\left[1+\gamma\frac{\delta V}{V_1}+\frac{\gamma(\gamma-1)}{2}\left(\frac{\delta V}{V_1}\right)^2\right] \tag{361}$$

$$-p_1V_1\left(1+\frac{\delta p}{p_1}+\frac{\delta V}{V_1}+\frac{\delta p\delta V}{p_1V_1}\right) \tag{362}$$

$$= (\gamma-1)p_1V_1\left[\gamma\left(\frac{\delta V}{V_1}\right)^2+\frac{\delta p\delta V}{p_1V_1}\right], \tag{363}$$

which simplifies to

$$\delta W = p_1\left[\frac{\delta p\delta V}{p_1}+\gamma\frac{(\delta V)^2}{V_1}\right] = p_1\delta V\delta\ln\left(pV^\gamma\right). \tag{364}$$

This reminds us of Schwarzschild criterion if we identify V with $1/\rho$.

In the edge of a magnetically confined plasma, pressure p must eventually decrease to zero. As such, δp should lower p towards the plasma boundary. As a sufficient condition for plasma to be stable against interchange instability, $\delta p\delta V$ needs to be positive. Thus, δV needs to be negative to compensate for the negative δp,

$$\delta V = \int \delta S dl = \int \frac{\delta\Phi}{B}dl = \delta\Phi\int\frac{dl}{B} < 0. \tag{365}$$

Here S is the cross-sectional area of the flux tube, dl is the element length along the tube, and $\delta\Phi = B\delta S$ is the increment of magnetic flux. Therefore, the magnetic field strength needs to increase towards the boundary to lower the volume occupied by a given flux tube. This is equivalent to the requirement for the minimum-B configuration.

The volume per flux or specific volume is formally defined as

$$U \equiv \frac{dV}{d\Phi} = \int\frac{dl}{B}, \tag{366}$$

which can be calculated for a magnetically confined toroidal plasma as a function of flux surface. In this case, V is considered as the volume inside a given flux surface containing the toroidal flux Φ. Therefore, the stability condition against interchange instability can be expressed as

$$\frac{dU}{d\Phi} = \frac{d^2V}{d\Phi^2} \equiv V'' < 0. \tag{367}$$

Since the integration in Eq. (366) is along the field lines, passing through both the inner and outer sides of a torus, the configurations satisfying the above condition are called *average minimum-B* or magnetic well configurations (Miyamoto, 2016, Ch.6). The magnetic well depth is defined

as

$$\frac{\Delta U}{U} = \frac{U_0 - U_a}{U_0}, \tag{368}$$

where U_0 and U_a are the specific volumes at the magnetic axis and the outermost magnetic surface. This is another figure of merit for a given confinement configuration.

6.5 Ballooning Instability

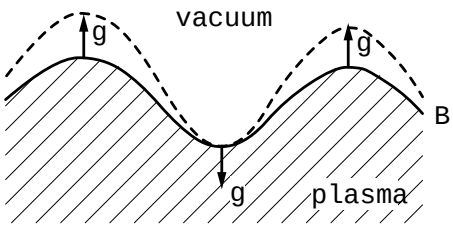

Fig. 35 Effective gravity in magnetically confined plasma and ballooning instability.

There are no direct counterparts of Parker instability when we allow the bending of field lines for the case with finite plasma pressure confining magnetic field without gravity. As illustrated in Fig. 35, the direction of effective gravity changes following the good and bad curvatures. Bending the field lines on the bad curvature sides reduces the energy integral as the change in plasma internal energy or pressure can overcome the increase in magnetic energy. In contrast, we do not want to bend at good curvature locations where plasma pressure has to increase.

The corresponding instability is called *ballooning instability* which can occur even when the plasma is stable to the interchange instability, similar to the Parker instability. The confinement performance for modern tokamak is typically limited by the ballooning instabilities. We can stabilize this instability by introducing a large magnetic shear across the flux surfaces or imposing a large radial derivative of the safety factor $dq/dr = q'$, which we will discuss later.

6.6 Summary

- Pressure-driven instabilities include convective instability and interchange instability (similar to Rayleigh-Taylor instability) without bending field lines, as summarized in the left panel of Fig. 36.
- When field lines can be bent, Parker instability can occur when gravity force is dominant while ballooning instability on bad curvature locations can occur when the pressure is dominant, as summarized in the right panel of Fig. 36.
- For magnetically confined plasma, field lines can have locations of good and bad curvatures.

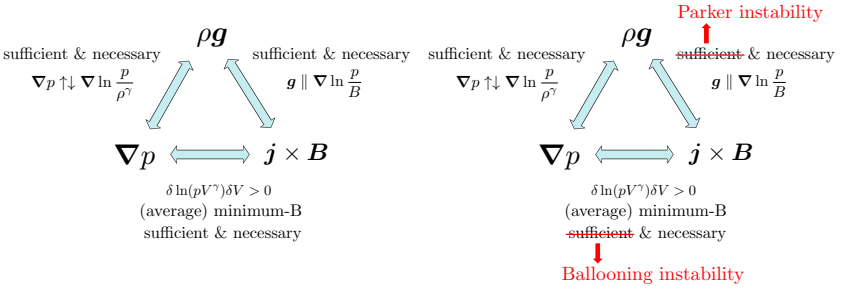

Fig. 36 Summary of stability conditions against interchange instability for each pair of forces (left panel) and the modifications in red due to field line bending (right panel)

- The absolute and average minimum-B configurations are defined for stability against interchange instability in magnetically confined plasmas.

6.7 Further Readings

- Chapter 7 in Kulsrud (2005)
- Chapter 8 in Freidberg (2014)
- Chapter 6 in Miyamoto (2016)

6.8 Homework Problem Set 6

Stability condition for a magnetized plasma confined by gravity.

An ideal MHD plasma occupies half of the space from $z = 0$ and $z = \infty$, supported by a superconducting and solid boundary at $z = 0$. Plasma mass density ρ, pressure p, and magnetic field strength are functions of z only, and the static equilibrium is given by

$$\frac{d}{dz}\left(p + \frac{B^2}{2\mu_0}\right) = -\rho g, \tag{369}$$

where $\boldsymbol{B}$ is in the x direction and $\boldsymbol{g}$ is a constant gravity pointing in the $-z$ direction.

1. Assume that the displacement vector is given by $\boldsymbol{\xi} = (\xi_x, \xi_y, \xi_z)\exp(ik_x x + ik_y y)$ where $i\xi_x(\equiv \zeta)$, $i\xi_y(\equiv \eta)$, and $\xi_z(\equiv \xi)$ are real functions of z. Note here that ξ_x and ξ_y are out of the phase of ξ_z to allow Parker instabilities. Substitute the real part of the complex displacement vector ($\boldsymbol{\xi}$) into the energy integral (δW), and make use of the equilibrium, Eq.(1), to show

$$\delta W = \frac{1}{2}\int_0^\infty dz \left\{ \frac{B^2}{\mu_0}\left[k_x^2\left(\xi^2 + \eta^2\right) + \left(\frac{d\xi}{dz} + k_y\eta\right)^2\right] \right.$$
$$\left. +\gamma p\left(\frac{d\xi}{dz} + k_x\zeta + k_y\eta\right)^2 - 2\rho g\xi\left(\frac{d\xi}{dz} + k_x\zeta + k_y\eta\right) - g\xi^2\frac{d\rho}{dz}\right\},$$

where γ is the adiabatic index.

2. When $k_x = 0$, only interchange instabilities are possible and ζ drops out from δW.
   (a) Show in this case that the energy integral reduces to

$$\delta W = \frac{1}{2}\int_0^\infty dz \left[-g\xi^2 \left(\frac{d\rho}{dz} + \frac{\rho^2 g}{\gamma p + B^2/\mu_0} \right) + \left(\gamma p + \frac{B^2}{\mu_0} \right) \left(\frac{d\xi}{dz} + k_y \eta - \frac{\rho g \xi}{\gamma p + B^2/\mu_0} \right)^2 \right].$$

   (b) What is the necessary and sufficient condition for interchange stability?
   (c) Show that this condition reduces to $\boldsymbol{g} \cdot \boldsymbol{\nabla} \ln(\rho/B) \geq 0$ in the cold plasma limit.
   (d) Show that this condition reduces to Schwarzschild Criterion in the unmagnetized limit.

3. When $k_x \neq 0$, Parker instabilities also become possible.
   (a) Show in this case that the energy integral can be expressed as

$$\delta W = \frac{1}{2}\int_0^\infty dz \left[\left(k_x^2 \frac{B^2}{\mu_0} - \frac{\rho^2 g^2}{\gamma p} - g\frac{d\rho}{dz} \right) \xi^2 + \frac{B^2}{\mu_0} \frac{k_x^2}{k_x^2 + k_y^2} \left(\frac{d\xi}{dz} \right)^2 + \gamma p \left(\frac{d\xi}{dz} + k_x \zeta + k_y \eta - \frac{\rho g \xi}{\gamma p} \right)^2 + \left(k_x^2 + k_y^2 \right) \frac{B^2}{\mu_0} \left(\eta + \frac{k_y (d\xi/dz)}{k_x^2 + k_y^2} \right)^2 \right].$$

   (b) Show that the necessary and sufficient condition against both interchange and Parker stabilities are given by

$$-\frac{d\rho}{dz} > \frac{\rho^2 g}{\gamma p}. \tag{370}$$

   (c) Discuss this condition in the following three limits:
      (i) cold plasma limit
      (ii) unmagnetized limit
      (iii) zero gravity limit.

4. Find an example of a warm plasma which is stable to interchange instabilities but unstable to Parker instabilities.

7 MHD Instabilities in Cylindrical Plasmas

Now that we have seen the usefulness of the energy principle in evaluating the ideal MHD stability of a given system, we will systematically use it to examine magnetically confined fusion plasmas in these two following lectures. The ideal MHD equilibrium is given by $\nabla p = \boldsymbol{j} \times \boldsymbol{B}$ and the corresponding energy integral is given by

$$2\delta W = \int \left[\frac{Q^2}{\mu_0} + \boldsymbol{j} \cdot (\boldsymbol{\xi} \times \boldsymbol{Q}) + \gamma p \left(\nabla \cdot \boldsymbol{\xi} \right)^2 + (\boldsymbol{\xi} \cdot \nabla p) \left(\nabla \cdot \boldsymbol{\xi} \right) \right] dV. \tag{371}$$

For our purpose here, we will rearrange the energy integral into different terms with direct physical meanings.

Define $\boldsymbol{\xi} = \boldsymbol{\xi}_\perp + \xi_\parallel \boldsymbol{b}$ where $\boldsymbol{b}$ is the unit vector along $\boldsymbol{B}$. Then, we have

$$\begin{aligned} \boldsymbol{Q} &= \nabla \times (\boldsymbol{\xi} \times \boldsymbol{B}) = \nabla \times (\boldsymbol{\xi}_\perp \times \boldsymbol{B}), \\ (\boldsymbol{\xi} \cdot \nabla p) \left(\nabla \cdot \boldsymbol{\xi} \right) &= (\boldsymbol{\xi}_\perp \cdot \nabla p) \left(\nabla \cdot \boldsymbol{\xi} \right) = \nabla \cdot (\boldsymbol{\xi} (\boldsymbol{\xi}_\perp \cdot \nabla p)) - \boldsymbol{\xi} \cdot \nabla (\boldsymbol{\xi}_\perp \cdot \nabla p), \\ \boldsymbol{j} \cdot (\boldsymbol{\xi} \times \boldsymbol{Q}) &= -\boldsymbol{\xi} \cdot (\boldsymbol{j} \times \boldsymbol{Q}) = -(\boldsymbol{\xi}_\perp + \xi_\parallel \boldsymbol{b}) \cdot (\boldsymbol{j} \times \boldsymbol{Q}). \end{aligned}$$

After dropping the $\nabla \cdot (\boldsymbol{\xi} (\boldsymbol{\xi}_\perp \cdot \nabla p))$ term, which vanishes by taking $\boldsymbol{\xi} = 0$ on the volume surface, the second and fourth terms of the integrand in Eq. (371) become

$$\boldsymbol{j} \cdot (\boldsymbol{\xi} \times \boldsymbol{Q}) + (\boldsymbol{\xi} \cdot \nabla p) \left(\nabla \cdot \boldsymbol{\xi} \right) = - \left(\boldsymbol{\xi}_\perp + \xi_\parallel \boldsymbol{b} \right) \cdot \left[\boldsymbol{j} \times \boldsymbol{Q} + \nabla (\boldsymbol{\xi}_\perp \cdot \nabla p) \right], \tag{372}$$

where the terms proportional to $\xi_\parallel$ vanish as they can also be written as

$$\begin{aligned} \boldsymbol{B} \cdot (\boldsymbol{j} \times \boldsymbol{Q}) &= -\boldsymbol{Q} \cdot (\boldsymbol{j} \times \boldsymbol{B}) = -\boldsymbol{Q} \cdot (\nabla p) = -\nabla \cdot (p \boldsymbol{Q}), \\ \boldsymbol{B} \cdot \nabla (\boldsymbol{\xi}_\perp \cdot \nabla p) &= \nabla \cdot \left[(\boldsymbol{\xi}_\perp \cdot \nabla p) \boldsymbol{B} \right], \end{aligned}$$

since $\nabla \cdot \boldsymbol{Q} = 0$. Therefore, Eq. (371) becomes

$$2\delta W = \int \left[\frac{Q^2}{\mu_0} + \gamma p \left(\nabla \cdot \boldsymbol{\xi} \right)^2 + (\boldsymbol{\xi}_\perp \cdot \nabla p) \left(\nabla \cdot \boldsymbol{\xi}_\perp \right) - \boldsymbol{\xi}_\perp \cdot (\boldsymbol{j} \times \boldsymbol{Q}) \right] dV. \tag{373}$$

Now we break down $\boldsymbol{Q}$ and $\boldsymbol{j}$ into their parallel and perpendicular components,

$$\begin{aligned} \boldsymbol{Q} &= \boldsymbol{Q}_\perp + Q_\parallel \boldsymbol{b}, \\ \boldsymbol{j} &= \boldsymbol{j}_\perp + j_\parallel \boldsymbol{b} = \frac{\boldsymbol{b} \times \nabla p}{B} + j_\parallel \boldsymbol{b}, \end{aligned}$$

where

$$Q_\parallel = \frac{\boldsymbol{B} \cdot \nabla \times (\boldsymbol{\xi}_\perp \times \boldsymbol{B})}{B}$$

$$
\begin{aligned}
&= \frac{\boldsymbol{\nabla}\cdot[(\boldsymbol{\xi}_\perp\times\boldsymbol{B})\times\boldsymbol{B}]+(\boldsymbol{\xi}_\perp\times\boldsymbol{B})\cdot\boldsymbol{\nabla}\times\boldsymbol{B}}{B}\\
&= -\frac{\boldsymbol{\nabla}\cdot\left(B^2\boldsymbol{\xi}_\perp\right)+\mu_0\boldsymbol{\xi}_\perp\cdot(\boldsymbol{j}\times\boldsymbol{B})}{B}\\
&= -\frac{B^2(\boldsymbol{\nabla}\cdot\boldsymbol{\xi}_\perp)+(\boldsymbol{\xi}_\perp\cdot\boldsymbol{\nabla})B^2+\mu_0(\boldsymbol{\xi}_\perp\cdot\boldsymbol{\nabla})p}{B}\\
&= -B(\boldsymbol{\nabla}\cdot\boldsymbol{\xi}_\perp+2\boldsymbol{\xi}_\perp\cdot\boldsymbol{\kappa})-\frac{\mu_0}{B}(\boldsymbol{\xi}_\perp\cdot\boldsymbol{\nabla})p. \qquad (374)
\end{aligned}
$$

Here, we have used the magnetic curvature vector $\boldsymbol{\kappa}=\boldsymbol{b}\cdot\boldsymbol{\nabla}\boldsymbol{b}$ which is related to the curvature radius of field lines (Freidberg, 2014, Appendix D). Now, we are ready to calculate the last term of the integrand in Eq. (373) as follows,

$$
\begin{aligned}
\boldsymbol{\xi}_\perp\cdot(\boldsymbol{j}\times\boldsymbol{Q}) &= \boldsymbol{\xi}_\perp\cdot\left[\boldsymbol{j}\times(\boldsymbol{Q}_\perp+Q_\parallel\boldsymbol{b})\right]\\
&= \boldsymbol{\xi}_\perp\cdot(\boldsymbol{j}\times\boldsymbol{Q}_\perp)+Q_\parallel\boldsymbol{\xi}_\perp\cdot(\boldsymbol{j}\times\boldsymbol{b})\\
&= \boldsymbol{Q}_\perp\cdot(\boldsymbol{\xi}_\perp\times\boldsymbol{j})+Q_\parallel\boldsymbol{\xi}_\perp\cdot(\boldsymbol{j}_\perp\times\boldsymbol{b})\\
&= \boldsymbol{Q}_\perp\cdot\left(\boldsymbol{\xi}_\perp\times j_\parallel\boldsymbol{b}\right)+Q_\parallel\boldsymbol{\xi}_\perp\cdot\left(\frac{\boldsymbol{b}\times\boldsymbol{\nabla}p}{B}\times\boldsymbol{b}\right)\\
&= \frac{j_\parallel}{B}(\boldsymbol{\xi}_\perp\times\boldsymbol{B})\cdot\boldsymbol{Q}_\perp-\frac{Q_\parallel}{B}(\boldsymbol{\xi}_\perp\cdot\boldsymbol{\nabla})\,p. \qquad (375)
\end{aligned}
$$

Substituting the equation above and Eq. (374) for $Q_\parallel$ both to Eq. (373), after some algebra, we finally get,

$$
\begin{aligned}
2\delta W = \int\Bigg[&\frac{|Q_\perp|^2}{\mu_0}+\frac{B^2}{\mu_0}\left|\boldsymbol{\nabla}\cdot\boldsymbol{\xi}_\perp+2\boldsymbol{\xi}_\perp\cdot\boldsymbol{\kappa}\right|^2+\gamma p\left|\boldsymbol{\nabla}\cdot\boldsymbol{\xi}\right|^2\\
&-2\left(\boldsymbol{\xi}_\perp\cdot\boldsymbol{\nabla}p\right)\left(\boldsymbol{\xi}_\perp\cdot\boldsymbol{\kappa}\right)-\frac{j_\parallel}{B}\left(\boldsymbol{\xi}_\perp\times\boldsymbol{B}\right)\cdot\boldsymbol{Q}_\perp\Bigg]dV, \qquad (376)
\end{aligned}
$$

which is a physically intuitive form of energy integral (Freidberg, 2014, Ch.8). Each of these terms represents the contribution of a particular physical effect to the energy integral:

- $|Q_\perp|^2$ represents the increase in magnetic energy due to the field line bending and is associated with Alfvén waves.
- $\left|\boldsymbol{\nabla}\cdot\boldsymbol{\xi}_\perp+2\boldsymbol{\xi}_\perp\cdot\boldsymbol{\kappa}\right|^2$ represents the increase in magnetic energy due to the field compression and is associated with magnetosonic waves.
- $\gamma p\left|\boldsymbol{\nabla}\cdot\boldsymbol{\xi}\right|^2$ represents the increase in plasma internal energy due to compression.
- $-2\left(\boldsymbol{\xi}_\perp\cdot\boldsymbol{\nabla}p\right)\left(\boldsymbol{\xi}_\perp\cdot\boldsymbol{\kappa}\right)$ represents the increase or decrease in plasma internal energy depending on the relative direction between $\boldsymbol{\nabla}p$ and $\boldsymbol{\kappa}$. When these two vectors are in the same direction, this term is negative definite and can cause pressure-driven instabilities, corresponding to bad curvature cases.

When the two vectors are in opposite directions, this term is positive definite and plasma is stable against pressure-driven instabilities.

- $-\frac{j_\parallel}{B}(\boldsymbol{\xi}_\perp \times \boldsymbol{B}) \cdot \boldsymbol{Q}_\perp$ can have either sign representing either the increase or decrease in magnetic energy. When the term is negative, the plasma is unstable to (parallel) current-driven instabilities.

Therefore, the ideal MHD instability for a given system requires the existence of displacements that can generate sufficient negative contributions via the last two terms more than positive contributions via the first three terms of the energy integral, Eq. (676). Before we discuss each possible instability for magnetically confined plasmas, we summarize the general instabilities classifications below.

- Classifications by free-energy source:
  - Pressure-driven, *e.g.* interchange instability.
  - Current-driven, *e.g.* kink instability.
  - Flow-shear-driven, *e.g.* Kelvin-Helmholtz instability.
- Classifications by location (for fusion plasmas):
  - Internal, *e.g.* internal kink with no surface displacements.
  - External, *e.g.* external kink with finite surface displacement.
- Classifications by model:
  - Ideal MHD, *e.g.* kink instability.
  - Resistive MHD, *e.g.* tearing instability.
  - Kinetic, *e.g.* ion acoustic instability.
- Classifications by wavelength or frequency:
  - Macroscopic, *e.g.* MHD instability.
  - Microscopic, *e.g.* kinetic instability.

We will not cover kinetic or microscopic instabilities in this class.

7.1 MHD Stability of Theta-Pinch Plasmas

Consider an infinitely long theta-pinch plasma confined by axial magnetic field $B_z(r)$ as a function of radius r, generated by current in the θ direction. The radial force balance is given by

$$\frac{d}{dr}\left(p + \frac{B_z^2}{2\mu_0}\right) = 0. \tag{377}$$

Since there is no azimuthal field $B_\theta = 0$, the current along magnetic field vanishes $j_\parallel = 0$, and the field lines are straight such that $\boldsymbol{\kappa} = 0$. The energy

integral Eq. (676) becomes

$$2\delta W = \int \left[\frac{|Q_\perp|^2}{\mu_0} + \frac{B^2}{\mu_0} |\boldsymbol{\nabla} \cdot \boldsymbol{\xi}_\perp|^2 + \gamma p |\boldsymbol{\nabla} \cdot \boldsymbol{\xi}|^2 \right] dV \geq 0, \tag{378}$$

showing that theta pinches are always stable against all ideal MHD instabilities. Nonetheless, we are interested in knowing the *least stable* modes for theta-pinch plasmas.

As before, we decompose modes of displacements into different azimuthal mode numbers, m, and axial wavenumbers, k, such that

$$\boldsymbol{\xi} = \boldsymbol{\xi}(r) e^{i(m\theta + kz)}.$$

Now, we take the following two steps to minimize δW by choosing the proper $\boldsymbol{\xi} = (\xi_r, \xi_\theta, \xi_z)$ to find the least stable modes:

1. We choose a certain $\xi_\parallel (= \xi_z)$ to minimize δW by satisfying the incompressibility condition, $\boldsymbol{\nabla} \cdot \boldsymbol{\xi} = 0$ or

$$\boldsymbol{\nabla} \cdot \boldsymbol{\xi} = \frac{1}{r} \frac{\partial}{\partial r} (r \xi_r) + \frac{1}{r} \frac{\partial \xi_\theta}{\partial \theta} + \frac{\partial \xi_z}{\partial z} = 0,$$

which can be rewritten as

$$\frac{1}{r} (r \xi_r)' + \frac{im}{r} \xi_\theta + ik \xi_z = 0$$

or

$$\xi_\parallel = \frac{i}{kr} \left[(r \xi_r)' + im \xi_\theta \right]. \tag{379}$$

2. Next, we calculate $\boldsymbol{Q} = \boldsymbol{\nabla} \times (\boldsymbol{\xi}_\perp \times \boldsymbol{B})$ using

$$\begin{aligned} \boldsymbol{\xi}_\perp &= (\xi_r, \xi_\theta, 0), \\ \boldsymbol{B} &= (0, 0, B), \\ \boldsymbol{\xi}_\perp \times \boldsymbol{B} &= (\xi_\theta B, -\xi_r B, 0) \equiv \boldsymbol{A}. \end{aligned}$$

We have

$$\boldsymbol{Q}_\perp = (\boldsymbol{\nabla} \times \boldsymbol{A})_\perp = \left(\frac{1}{r} \frac{\partial A_z}{\partial \theta} - \frac{\partial A_\theta}{\partial z}, \frac{\partial A_r}{\partial z} - \frac{\partial A_z}{\partial r}, 0 \right) = ikB(\xi_r, \xi_\theta, 0).$$

Therefore, the energy integral per unit axial length, L, is given by

$$\frac{\delta W}{L} = \frac{\pi}{\mu_0} \int_0^a r dr \left[k^2 B^2 \left(|\xi_r|^2 + |\xi_\theta|^2 \right) + B^2 \left| \frac{(r\xi_r)'}{r} + \frac{im}{r} \xi_\theta \right|^2 \right], \tag{380}$$

where a is the plasma radius. Since this δW is quadratic in ξ_θ, we proceed to complete the squares for ξ_θ,

$$\begin{aligned}
&k^2 |\xi_\theta|^2 + \left| \frac{(r\xi_r)'}{r} + \frac{im}{r}\xi_\theta \right|^2 \equiv k^2 |\xi_\theta|^2 + |b + ia\xi_\theta|^2 \\
&= \left(a^2 + k^2\right) \xi_\theta^2 + b^2 + iab\xi_\theta^* - iab^*\xi_\theta \\
&= \left[\left(a^2 + k^2\right) \xi_\theta^2 + iab\xi_\theta^* - iab^*\xi_\theta + \frac{a^2 b^2}{a^2 + k^2} \right] + b^2 - \frac{a^2 b^2}{a^2 + k^2} \\
&= \left| \sqrt{a^2 + k^2}\xi_\theta - \frac{iab}{\sqrt{a^2 + k^2}} \right|^2 + \frac{k^2 b^2}{a^2 + k^2} \\
&= \frac{k^2 b^2}{a^2 + k^2},
\end{aligned}$$

which is minimized when

$$\xi_\theta = \frac{iab}{a^2 + k^2} = \frac{im}{m^2 + k^2 r^2} (r\xi_r)' . \tag{381}$$

Therefore, the energy integral in Eq. (380) reduces to

$$\frac{\delta W}{L} = \frac{\pi}{\mu_0} \int_0^a r dr k^2 B^2 \left[|\xi_r|^2 + \frac{1}{m^2 + k^2 r^2} \left| \frac{(r\xi_r)'}{r} \right|^2 \right] . \tag{382}$$

Of course, this is still positive definite, regardless of the choices for ξ_r. In the long wavelength limit, $k \to 0$, we have $\delta W \to 0$ when theta-pinches are least stable.

In this exercise, δW is minimized by incompressibility, which determines $\xi_\parallel$ as a function of $\boldsymbol{\xi}_\perp$. In the next step, the non-radial component of $\boldsymbol{\xi}_\perp$, ξ_θ in the case of theta-pinch, can be determined as a function of ξ_r to further minimize δW via a quadratic form. Then, the remaining task is to minimize δW by choosing a proper ξ_r. This strategy applies to other 1D Z-pinch and screw pinch plasmas.

7.2 MHD Stability of Z-Pinch Plasmas

In Z-pinches, current in the z-direction generates the field in the θ-direction, B_θ. The 1D equilibrium is given by

$$\frac{B_\theta}{\mu_0 r} \frac{d}{dr} (rB_\theta) + \frac{dp}{dr} = 0. \tag{383}$$

The parallel direction is now along the θ direction with $k_\parallel = m/r$. Since the first step as described in the theta-pinch section requires $k_\parallel \neq 0$, we divide our discussion below into the two cases: $m \neq 0$ and $m = 0$.

7.2.1 Z-Pinch Stability for $m \neq 0$ Mode

In this case, we can follow the same procedure that we used for θ-pinch plasmas. From the incompressibility condition, we can express $\xi_\parallel$ as

$$\xi_\parallel = \xi_\theta = \frac{i}{m}\left[(r\xi_r)' + ik\xi_z\right]. \tag{384}$$

Since

$$\begin{aligned}\boldsymbol{\xi}_\perp &= (\xi_r, 0, \xi_z)\\ \boldsymbol{B} &= (0, B, 0)\\ \boldsymbol{\xi}_\perp \times \boldsymbol{B} &= (-\xi_z B, 0, \xi_r B) \equiv \boldsymbol{A},\end{aligned}$$

we have

$$\boldsymbol{Q}_\perp = (\boldsymbol{\nabla}\times\boldsymbol{A})_\perp = \left(\frac{1}{r}\frac{\partial A_z}{\partial\theta} - \frac{\partial A_\theta}{\partial z}, 0, \frac{1}{r}\frac{\partial}{\partial r}(rA_\theta) - \frac{1}{r}\frac{\partial A_r}{\partial\theta}\right) = \frac{imB}{r}(\xi_r, 0, \xi_z).$$

Since $\boldsymbol{\kappa} = -\hat{\boldsymbol{e}}_r/r$, we have $2\boldsymbol{\xi}_\perp\cdot\boldsymbol{\kappa} = -2\xi_r/r$. We then calculate

$$\begin{aligned}\boldsymbol{\nabla}\cdot\boldsymbol{\xi}_\perp + 2\boldsymbol{\xi}_\perp\cdot\boldsymbol{\kappa} &= \frac{1}{r}(r\xi_r)' + ik\xi_z - 2\frac{\xi_r}{r}\\ &= r\frac{\partial}{\partial r}\left(\frac{\xi_r}{r}\right) + ik\xi_z,\end{aligned}$$

and $j_\parallel = 0$. Therefore, the energy integral is given by

$$\begin{aligned}\frac{\delta W}{L} &= \frac{\pi}{\mu_0}\int_0^a W(r) r dr\\ W(r) &= |Q_\perp|^2 + B^2\left|\boldsymbol{\nabla}\cdot\boldsymbol{\xi}_\perp + 2\boldsymbol{\xi}_\perp\cdot\boldsymbol{\kappa}\right|^2 - 2\mu_0(\boldsymbol{\xi}\cdot\boldsymbol{\nabla}p)(\boldsymbol{\xi}^*\cdot\boldsymbol{\kappa})\\ &= \frac{m^2B^2}{r^2}\left(|\xi_r|^2 + |\xi_z|^2\right) + B^2\left|r\left(\frac{\xi_r}{r}\right)' + ik\xi_z\right|^2 + \frac{2\mu_0 p'}{r}|\xi_r|^2\end{aligned} \tag{385}$$

As before, we complete the squares for ξ_z giving,

$$\begin{aligned}&\frac{m^2}{r^2}\xi_z^2 + \left|r\left(\frac{\xi_r}{r}\right)' + ik\xi_z\right|^2 \equiv a^2\xi_z^2 + |b + ik\xi_z|^2\\ &= (a^2+k^2)\xi_z^2 + b^2 - ibk\xi_z^* + ib^*k\xi_z\\ &= \left[(a^2+k^2)\xi_z^2 + ib^*k\xi_z - ibk\xi_z^* + \frac{b^2k^2}{a^2+k^2}\right] + b^2 - \frac{b^2k^2}{a^2+k^2}\\ &= \left|\sqrt{a^2+k^2}\xi_z - i\frac{bk}{\sqrt{a^2+k^2}}\right|^2 + \frac{a^2b^2}{a^2+k^2}\end{aligned}$$

$$= \frac{a^2 b^2}{a^2 + k^2},$$

which is minimized when

$$\xi_z = \frac{ibk}{a^2 + k^2} = \frac{ikr^3}{m^2 + k^2 r^2} \left(\frac{\xi_r}{r} \right)' . \tag{386}$$

Therefore, we have

$$\begin{aligned} W(r) &= \frac{a^2 b^2 B^2}{a^2 + k^2} + \frac{m^2 B^2}{r^2} |\xi_r|^2 + \frac{2\mu_0 p'}{r} |\xi_r|^2 \\ &= \left(2\mu_0 r p' + m^2 B^2\right) \left| \frac{\xi_r}{r} \right|^2 + \frac{m^2 r^2 B^2}{m^2 + k^2 r^2} \left| \left(\frac{\xi_r}{r} \right)' \right|^2 . \end{aligned} \tag{387}$$

The last term is positive definite and approaches zero when $k \to \infty$. For the first term to be non-negative, we need

$$2rp' + m^2 \frac{B^2}{\mu_0} \geq 0. \tag{388}$$

Using the equilibrium condition in Eq. (383),

$$p' = -\frac{B}{\mu_0 r} (rB)' ,$$

the stability condition, Eq. (388), becomes

$$\begin{aligned} -2B \frac{\partial (rB)}{\partial r} + m^2 B^2 &\geq 0 \\ -2 \left(B^2 + rB \frac{\partial B}{\partial r} \right) + m^2 B^2 &\geq 0 \\ (m^2 - 2) B^2 &\geq r \frac{\partial B^2}{\partial r}. \end{aligned} \tag{389}$$

The azimuthal field $B(r)$ is related to the total axial current within the radius r satisfying

$$\begin{aligned} 2\pi r B &= \mu_0 \pi r^2 j_0 \\ B &= \frac{\mu_0 r}{2} j_0, \end{aligned}$$

where j_0 is the averaged current density within r. Since j_0 must remain finite when $r \to 0$, we can assume that $B = \alpha r$ for sufficiently small r. The stability condition, Eq. (389), becomes

$$(m^2 - 2)\alpha^2 r^2 \geq r 2\alpha^2 r \quad \text{or}$$

$$\begin{aligned} m^2 - 2 &\geq 2 \\ m^2 &\geq 4 \\ m &\geq 2. \end{aligned}$$

Therefore, the Z-pinch plasmas are always unstable to the $m = 1$ kink, driven by the pressure gradient, as shown in Fig. 37. The magnetic field pressure is stronger in the part where the Z-pinch plasma kinks away, thus reinforcing the initial deformation.

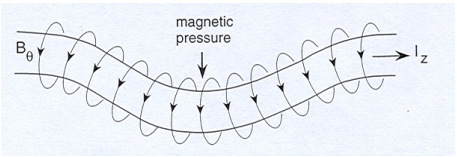

Fig. 37 Pressure-driven $m = 1$ kink instability in Z-pinch.

7.2.2 Z-Pinch Stability for $m = 0$ Mode

For $m = 0$ mode, $\xi_\parallel = \xi_\theta$ does not appear in the energy integral. Therefore, we can skip the first step of the incompressibility condition and directly go to the second step. There is no field line bending such that $\boldsymbol{Q}_\perp = 0$. There are three integrands within the energy integral which is quadratic in ξ_z,

$$W(r) = B^2 \left| r\left(\frac{\xi_r}{r}\right)' + ik\xi_z \right|^2 + \gamma\mu_0 p \left| \frac{(r\xi_r)'}{r} + ik\xi_z \right|^2 + \frac{2\mu_0 p'}{r} |\xi_r|^2 . \quad (390)$$

As usual, we can complete the squares for ξ_z and then minimize the energy integral to yield

$$W(r) = \left[\left(\frac{4\gamma B^2}{B^2/\mu_0 + \gamma p} \right) p + 2\mu_0 r p' \right] \frac{|\xi_r|^2}{r^2}. \quad (391)$$

Thus, the stability condition against $m = 0$ modes is given by (Homework 7),

$$-\frac{rp'}{p} < \frac{2\gamma B^2/\mu_0}{\gamma p + B^2/\mu_0}. \quad (392)$$

When this condition is violated, the resulting interchange instability is called sausage instability, as shown in Fig. 38. The parts with smaller cross sections have stronger B_θ due to the total current conservation. The stronger field gives a larger inward pinch force reinforcing the initial deformation. The opposite happens for the parts with larger cross sections. The Z-pinch plasma stability analysis was given by Kadomtsev in 1966.

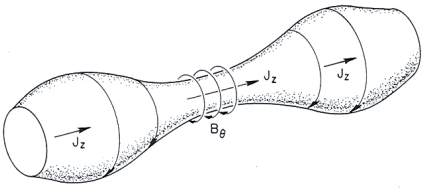

Fig. 38 Pressure-driven $m = 0$ sausage instability in Z-pinch.

7.3 MHD Stability of Screw Pinch

7.3.1 Pressure-driven instabilities

We are now ready to examine the MHD stability of a general screw pinch plasma, which can be regarded as a "straight" tokamak. The equilibrium is given by

$$\frac{B_\theta}{\mu_0 r}\frac{d}{dr}(rB_\theta) + \frac{d}{dr}\left(p + \frac{B_z^2}{2\mu_0}\right) = 0. \tag{393}$$

We will still follow the standard two-step process to minimize the energy integral but in the general configuration given above.

The displacement vector, $\boldsymbol{\xi} = (\xi_r, \xi_\theta, \xi_z)$, can be decomposed to $\boldsymbol{\xi} = (\xi_r, \eta(r), \xi_\parallel(r))$ where the parallel displacement, $\xi_\parallel$, is given by

$$\xi_\parallel = \frac{\boldsymbol{\xi}\cdot\boldsymbol{B}}{B}. \tag{394}$$

The quantity η is the third component of $\boldsymbol{\xi}$ in a direction that forms a right-hand coordinate system with the radial and the parallel directions. The first step to minimize energy integral is to determine $\xi_\parallel$ through the incompressibility condition, $\boldsymbol{\nabla}\cdot\boldsymbol{\xi} = ik_\parallel\xi_\parallel + \boldsymbol{\nabla}\cdot\boldsymbol{\xi}_\perp = 0$, leading to

$$\xi_\parallel = \frac{i}{k_\parallel}\boldsymbol{\nabla}\cdot\boldsymbol{\xi}_\perp, \tag{395}$$

where $k_\parallel$ is the parallel wavenumber,

$$k_\parallel = \frac{\boldsymbol{k}\cdot\boldsymbol{B}}{B} = \frac{kB_z + mB_\theta/r}{B}. \tag{396}$$

When $k_\parallel \neq 0$, $\xi_\parallel$ determined in this way in terms of $\boldsymbol{\xi}_\perp$ is well behaved, but questions arise on how to determine $\xi_\parallel$ at locations where $k_\parallel = 0$, which are called resonant surfaces. To overcome this difficulty, we introduce a small positive constant, $(\delta k_\parallel)^2$, to remove singularity near such surfaces by replacing Eq. (395) with

$$\xi_\parallel = \frac{ik_\parallel}{k_\parallel^2 + (\delta k_\parallel)^2}\boldsymbol{\nabla}\cdot\boldsymbol{\xi}_\perp$$

so that

$$\boldsymbol{\nabla}\cdot\boldsymbol{\xi} = \frac{(\delta k_\parallel)^2}{k_\parallel^2 + (\delta k_\parallel)^2}\boldsymbol{\nabla}\cdot\boldsymbol{\xi}_\perp \tag{397}$$

goes to zero when $(\delta k_\parallel)^2 \to 0$. In other words, by an choosing arbitrarily small $(\delta k_\parallel)^2$, plasma compressibility makes a vanishingly small contribution to energy integral even when isolated resonant surfaces exist in the plasma.

As usual, the second step, which is tedious but straightforward (Freidberg, 2014, Ch.11), is to complete the squares in terms of η and to choose

$$\eta = \frac{i}{r(k^2 + m^2/r^2)B}\left[2kB_\theta\xi_r + \left(\frac{m}{r}B_z - kB_\theta\right)\frac{d(r\xi_r)}{dr}\right]$$

to yield the minimized energy integral

$$\begin{aligned}
\frac{\delta W}{L} &= \frac{\pi}{\mu_0}\int_0^a dr\left[f\left(\frac{d\xi_r}{dr}\right)^2 + g\xi_r^2\right], \qquad (398)\\
f &= \frac{r(mB_\theta - krB_z)^2}{m^2 + k^2r^2},\\
g &= \frac{2\mu_0 k^2r^2}{m^2 + k^2r^2}p' + \frac{(mB_\theta - krB_z)^2}{r}\frac{k^2r^2 + m^2 - 1}{m^2 + k^2r^2}\\
&\quad + \frac{2k^2r^2(k^2r^2B_z^2 - m^2B_\theta^2)}{(m^2 + k^2r^2)^2},
\end{aligned}$$

where $\xi_r(r = a) = 0$ is assumed for internal modes.

Now, let us apply this to "straight" tokamaks with $L = 2\pi R_0$, where R_0 is the major radius. f and g in Eq. (398) can be written as

$$\begin{aligned}
f &= \frac{rB_\theta^2(m - nq)^2}{m^2 + k^2r^2},\\
g &= \frac{2\mu_0 k^2r^2}{m^2 + k^2r^2}p' + \frac{B_\theta^2(m - nq)^2}{r}\frac{k^2r^2 + m^2 - 1}{m^2 + k^2r^2}\\
&\quad + \frac{2k^2r^2B_\theta^2(n^2q^2 - m^2)}{(m^2 + k^2r^2)^2}, \qquad (399)
\end{aligned}$$

where $k = n/R_0$ and $q = rB_z/R_0B_\theta$ is the safety factor. It is clear that at rational surfaces, $q = m/n$, all terms vanish except the term containing pressure gradient, p', which can be negative. This non-zero term leads to the *local* interchange instability narrowly localized at the exact rational surfaces. At any distance from the rational surfaces, other terms become positive if the magnetic field has a shear or $q' \neq 0$, contributing to the stabilization of the mode. It is especially true for the term proportional to f multiplied by $d\xi_r/dr$. If ξ_r is so localized, then the value of $d\xi_r/dr$ must be large. Any finite f can effectively stabilize the local interchange instability. The detailed competition between two effects was worked out by Suydam in 1958, leading to **Suydam**

Criterion for local pressure-driven interchange stability (see Miyamoto, 2016, Ch.6 for a concise derivation),

$$\frac{rB_z^2}{\mu_0}\left(\frac{q'}{q}\right) + 8p' > 0. \tag{400}$$

Soon after, in 1960, Mercier worked out a generalized stability condition against local interchange instability called **Mercier Criterion** due to toroidal effects in the large aspect ratio limit (Freidberg, 2014, Ch.12),

$$\frac{rB_z^2}{\mu_0}\left(\frac{q'}{q}\right) + 8p'(1-q^2) > 0. \tag{401}$$

When $q > 1$, the local interchange instability is stabilized due to slightly more good curvature than bad curvature (up to the second order) near the rational surfaces when field lines trace around in the toroidal direction.

Away from the rational surfaces, however, the ideal MHD stability is determined by further minimizing Eq. (398) with respect to all possible ξ_r. The equation that ξ_r needs to satisfy can be derived using the variational principle as in the following. The integral that is to be minimized can be written as

$$I(\xi) = \int_a^b dr F(r, \xi, \xi'); \quad F = f\xi'^2 + g\xi^2. \tag{402}$$

When ξ is perturbed by a small $\delta\xi$, the change in $I(\xi)$ is given by

$$\begin{aligned}
\delta I &= I(\xi + \delta\xi) - I(\xi) \\
&= \int_a^b dr \left[\frac{\partial F}{\partial \xi}\delta\xi + \frac{\partial F}{\partial \xi'}\delta\xi'\right] \\
&= \int_a^b dr \left[\frac{\partial F}{\partial \xi}\delta\xi + \frac{\partial F}{\partial \xi'}(\delta\xi)'\right] \\
&= \int_a^b dr \delta\xi \left[\frac{\partial F}{\partial \xi} - \left(\frac{\partial F}{\partial \xi'}\right)'\right],
\end{aligned}$$

where the last step is accomplished by integration by parts,

$$\int_a^b dr \frac{\partial F}{\partial \xi'}(\delta\xi)' = \left[\frac{\partial F}{\partial \xi'}\delta\xi\right]_a^b - \int_a^b dr \left(\frac{\partial F}{\partial \xi'}\right)' \delta\xi.$$

For $I(\xi)$ to be at an extremum for arbitrary ξ, the Euler-Lagrange equation is therefore given by

$$\frac{\partial F}{\partial \xi} - \left(\frac{\partial F}{\partial \xi'}\right)' = 0,$$

leading to the desired equation for ξ,

$$\frac{d}{dr}\left(f\frac{d\xi}{dr}\right) - g\xi = 0. \tag{403}$$

Newcomb, in 1960, developed a general numerical procedure to solve this equation to find necessary and sufficient conditions for ideal MHD stability of screw pinch plasmas (Freidberg, 2014, see Ch.11 for details). Alternately, we can perform the normal mode eigenvalue analysis to calculate the growth rate for each mode using equations derived by Hain and Lüst (1958),

$$\frac{d}{dr}\left[A(r)\frac{d(r\xi)}{dr}\right] - C(r)(r\xi) = 0, \tag{404}$$

which has similar structures as in Eq. (403) with proper boundary conditions.

7.3.2 Current-driven instabilities

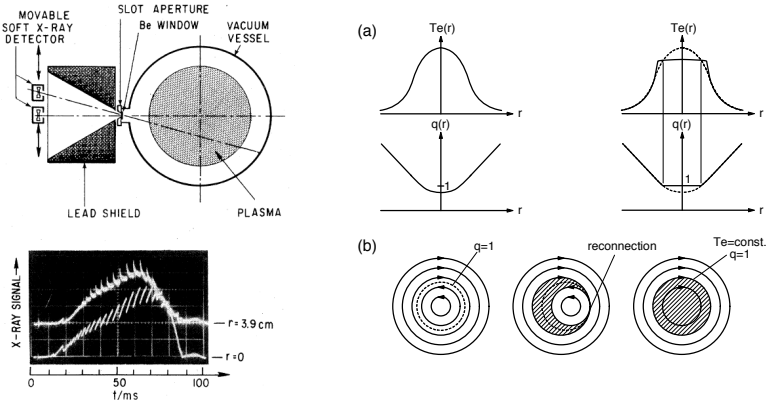

Fig. 39 Sawtooth oscillations in tokamaks (von Goeler et al, 1974) and their interpretation.

In addition to the pressure-driven instabilities, both analyses by Newcomb and Hain & Lüst include the current-driven instability. This type of instability originates from the last term of Eq. (676) and later from the last term of Eq. (399) when $q < m/n$. When the rational surface is within the plasma, the mode is called *internal* current-driven kink instabilities, which are different in nature from the pressure-driven kink instabilities that we discussed previously. A classic example is sawtooth oscillations observed in tokamaks (von Goeler et al, 1974) shown in Fig. 39. The plasma within the $q = 1$ surface with $q < 1$ is unstable to $m/n = 1/1$ kink instability, eventually leading to magnetic reconnection (see later) at the $q = 1$ surface.

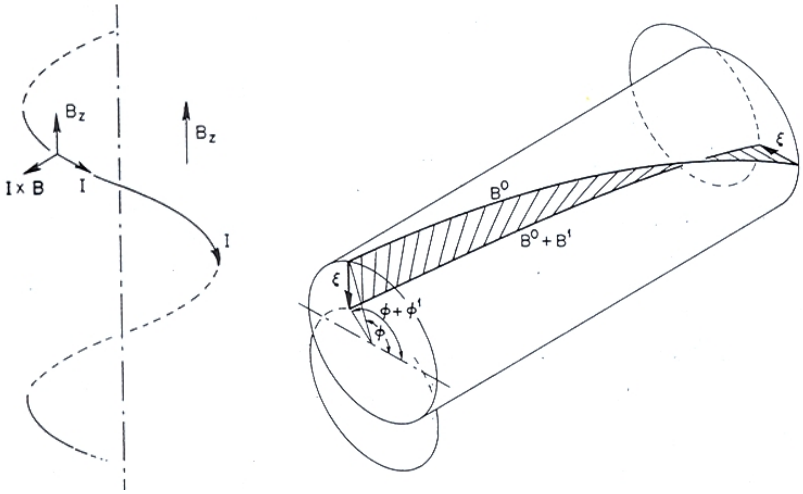

Fig. 40 Physical picture of current-driven kink instability: left by Bateman (1978) and right by Johnson et al (1958).

Current-driven kink instabilities can occur due to the rational surface outside of the plasma, with the mode being called *external* kink instabilities. In this case, the energy integral that we have discussed so far needs an addition due to the finite displacement at the plasma surface at $r = a$:

$$\frac{\delta W}{L} = \frac{\pi}{\mu_0}\int_0^a dr\left[f\left(\frac{d\xi_r}{dr}\right)^2 + g\xi_r^2\right] + \frac{\pi}{\mu_0}\left[\frac{n^2q^2 - m^2}{m^2 + k^2r^2}\right]_{r=a} B_\theta^2\xi_a^2, \qquad (405)$$

where ξ_a is the value of ξ_r at $r = a$. There are more additions to this integral due to the surface current on the plasma and the magnetic field perturbation in the vacuum region outside the plasma. We will not discuss these as they do not add more physics to this lecture and their details can be found in Chapter 11 of Freidberg (2014).

When $q_a \equiv q(a) < 1$, the surface term in Eq. (405) is negative, leading to the external 1/1 kink instability that is disruptive for plasma discharges. Demanding $q_a > 1$ places an upper limit in plasma current for a given toroidal field, commonly known as the Kruskal-Shafranov limit (Kruskal and Schwarzschild, 1954; Shafranov, 1956). Two versions of the physical picture of current-driven kink instability are shown in Fig. (40). The left version illustrates that a kink current channel can receive an additional radial force reinforcing the initial deformation. The right version shows an elaborated picture where reinforcement to the initial deformation, due to a larger poloidal field pressure, occurs only when the field line twist is larger than 90 degrees over a quarter of a wavelength, which translates to the $q < 1$ condition.

The external current-driven kink instabilities can be stabilized by a close-fit conducting wall at $r = b$, as shown in Fig. 41. The deformed plasma induces

eddy currents in the wall, and if the wall is conducting enough and close enough, the generated restoring force due to the eddy current can stabilize the instability. In practice, however, the conducting wall has a finite skin time, τ_w, beyond which the eddy currents decay while the external kink modes grow. These are called **resistive wall modes**, which can be dangerous for the long-pulse discharges common in present-day's experiments. The growth rate of resistive wall modes can be estimated (Freidberg, 2014, Ch.11) as follow:

- The external kink is stable with a superconducting wall at $r = b$: minimized energy integral is positive definite $\min(\delta W_b) > 0$.
- The external kink is unstable without wall: $\min(\delta W_\infty) < 0$.
- Growth rate γ_w is related to the skin time of a resistive wall, τ_w, as in

$$\gamma_w \tau_w = \frac{-\min(\delta W_\infty)}{\min(\delta W_b)}. \tag{406}$$

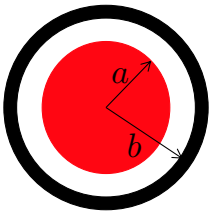

Fig. 41 A conducting wall surrounding plasma can stabilize external kink modes.

There are multiple ways to stabilize resistive wall modes:

- Active feedback by external coils with corresponding mode numbers and phase, with sufficiently fast responses;
- Plasma flow with a sufficient speed before eddy currents decay, but without causing new instabilities (flow-shear-driven, see later);
- Wall rotation with a sufficient speed.

All of these solutions are expensive and non-perfect in some ways, and thus resistive wall mode suppression is still an active area of research.

All instabilities discussed in this lecture are dangerous and can terminate discharge by causing *major disruptions*. In general, operation parameter space is constrained by current limit due to (external) kink and (internal) tearing instability and by density limit either due to radiation from high-Z impurities or pressure-driven instabilities. Some detailed discussions can be found in (Wesson, 2011, Ch.7).

7.4 Summary

- The general strategy to minimize energy integral is to remove two components of the displacement vector in terms of radial displacement, which can be solved using a differential equation with proper boundary conditions.
  - Theta-pinch stability.
  - Z-pinch stability.
  - Screw-pinch stability, as a straight tokamak.
- Suydam criterion for local pressure-drive instabilities.
- Global stability methods include Newcomb's method and eigenvalue analysis.
- Internal current-driven kink and sawtooth oscillations that are observed in tokamaks.
- External current-driven kink instabilities and resistive wall modes that are related to major disruptions.

7.5 Further Readings

- Chapter 11 (and 12) in Freidberg (2014)
- Chapter 7 in Wesson (2011)
- Chapter 6 in Miyamoto (2016)

7.6 Homework Problem Set 7

1. Sausage instability in Z-pinch plasmas.
   (a) Prove the stability condition

$$-\frac{rp'}{p} < \frac{2\gamma B_\theta^2/\mu_0}{\gamma p + B_\theta^2/\mu_0}. \tag{407}$$

   in the following two ways:
   (i) by constructing a complete square with regard to the z-component of the displacement vector based on Energy Principle.
   (ii) by using the stability condition against interchange instability,

$$\delta V \delta \left[\ln\left(PV^\gamma\right)\right] > 0 \tag{408}$$

   where δV and $\delta\left[\ln\left(PV^\gamma\right)\right]$ are differences in the volume V and the quantity $\ln\left(PV^\gamma\right)$ between two nearby flux tubes.
   (b) Is a Z-pinch plasma with uniform axial current density stable to the sausage mode?

2. Plasma confinement by a current-carrying wire.
   (a) Suppose that an ideal MHD plasma is confined by the magnetic field generated by an infinitely long, current-carrying wire. The plasma pressure is a function of radius: $P(r) \propto r^{-\alpha}$ when $r \to \infty$. What is the maximum

α for which this configuration is stable to the interchange instability? What is the profile for plasma β?

(b) Next, wrap the wire into a current-carrying ring with a radius of a. Suppose that the pressure profile $P(r) \propto r^{-\alpha}$ when $r/a \to \infty$. What is the maximum α for which this configuration is stable to the interchange instability? What is the profile for plasma β in this case? Discuss the implications for plasma confinement.

8 MHD Instabilities in Toroidal Plasmas

In this lecture, we will discuss the ideal MHD stability of toroidally confined plasmas, built on our understanding of one-dimensional cylindrical plasmas that we discussed in the previous lecture. The toroidal geometry is necessary to remove end losses that one-dimensional systems suffer from. Compared with cylindrical plasmas, toroidal screw pinches or simply toroidal pinches can be more stable, exemplified by the Mercier criterion against interchange instabilities which we have discussed briefly in the previous lecture, or more unstable, such as by ballooning instabilities. In this lecture, we discuss the following three topics on the toroidal effects:

- **Ballooning instabilities**, that occur only on the bad curvature side of a torus, while the system is interchange stable due to magnetic well or average minimum-B configuration. There are two specific types of instabilities due to toroidal effects:
  - **Edge-Localized Modes (ELM)**, that limit the "pedestal height" during the H-mode operation.
  - **External ballooning-kink modes**, that limit the plasma beta until disruptive events occur.
- **Toroidal Alfvén Eigenmodes (TAE)** and their relatives, driven by energetic ions. There exists a zoo of Alfvén modes and energetic particle modes. Their nonlinear consequences define the physics of burning plasma, one of the main subjects for the ITER project to study experimentally.
- **Vertical and horizontal instabilities of plasma positions**. These typically belong to plasma controls but can also be related to major disruptions and solar eruptions based on flux rope stability.

8.1 Ballooning Instabilities

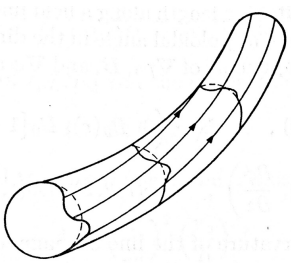

Fig. 42 Structure of a ballooning mode in a toroidal plasma from Miyamoto (2016).

As previously discussed, even when the averaged minimum-B configuration stabilizes interchange instabilities, ballooning instabilities can still occur in locations with bad magnetic curvature within a toroidal plasma. As a result,

ballooning instability effectively sets the limit of plasma beta, which we can estimate as follow.

The situation is illustrated in Fig. 42, where the instability is localized in the outboard side of a torus. In order for a field line to travel a distance of $2\pi r$, completing a full circle around the magnetic axis in the poloidal direction, it needs to travel a distance of $2\pi Rq$ in the toroidal direction. Assuming that the ballooning mode is localized only on the outboard side over 1 radian (about 57°) out of 2π radians (360°) in a full circle, the toroidal distance that a field line travels is Rq, which can be considered as an effective wavelength for the ballooning mode. Rq is often called the connection length for the field lines shorting out charge separation in the axial direction due to the ∇B drift in a simple toroidal field, which we discussed in Lecture 2.

The ballooning modes are unstable when the released plasma internal energy is larger than the increase in magnetic field energy due to the field line bending. In the energy integral, the increase of magnetic field energy can be estimated as

$$|\boldsymbol{Q}_\perp|^2 \approx |B_r|^2 \approx \left| B\frac{\xi_r}{Rq} \right|^2 \approx \left(\frac{B}{Rq}\right)^2 |\xi_r|^2 . \tag{409}$$

The released plasma internal energy can be estimated as

$$-2\left(\boldsymbol{\xi}_\perp \cdot \boldsymbol{\nabla} p\right)\left(\boldsymbol{\xi}_\perp^* \cdot \boldsymbol{\kappa}\right) \approx -2\frac{p_0}{a}\frac{1}{R}|\xi_r|^2 , \tag{410}$$

where $\nabla p \approx p_0/a$ with p_0 being the plasma pressure at the center. a is the plasma minor radius with the magnetic curvature radius defined as $1/R$. The ballooning modes are stabilized when the increase of magnetic energy is larger than the decrease of internal energy or

$$\frac{1}{\mu_0}\left(\frac{B}{Rq}\right)^2 \geq 2\frac{p_0}{aR}. \tag{411}$$

This relation leads to the beta limit,

$$\beta \equiv \frac{p_0}{B^2/2\mu_0} \leq \frac{a}{Rq^2} = \frac{\epsilon}{q^2}, \tag{412}$$

where $\epsilon \equiv a/R$ is the inverse of the aspect ratio. This simple estimate recovers the same result from a much more involved calculation in Miyamoto (2016). Taking $\epsilon = 1/3$ and $q_a = 3$, we estimate the beta limit of $1/3^3 \approx 3.7\%$, which is not too far off from the present day's tokamaks!

However, accurate analysis of the ballooning mode stability boundary turned out to be a difficult task. The reason is due to the existence of magnetic shear ($q' \neq 0$), which is crucial to stabilize ballooning (and interchange) instabilities but causes different periodicity of field lines in toroidal and poloidal directions at each radial location, illustrated in Fig. 43. Any single ballooning mode needs to have a finite radial extent to contribute meaningfully to the

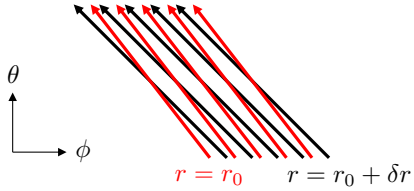

Fig. 43 When magnetic shear is finite $q' \neq 0$, field lines have different pitch angles, thus different periodicities, at different radii when looking into a toroidal plasma in the radial direction.

energy integral, thus requiring the inclusion of multiple pairs of poloidal and toroidal mode numbers (m, n). In addition, each of these modes in the toroidal system is coupled to other modes due to various geometric factors, which we will explain later in this lecture. Because of these reasons, a single ballooning mode requires a large number of mutually coupled mode number pairs (m, n). This requirement takes away the advantages of the eigenvalue analysis, which can be performed for each mode independently.

This difficulty was solved by the concept of "quasi-modes", introduced by Connor et al (1979) in the so-called ballooning formalism. The idea is to decompose the displacement vector, $\boldsymbol{\xi}(r, \theta, \phi)$, as a summation of "quasi-modes", $\bar{\boldsymbol{\xi}}(r, \theta, \phi)$, such that

$$\boldsymbol{\xi}(r, \theta, \phi) = \sum_{\substack{|m| \leq m_{\max} \\ |n| \leq n_{\max}}} \bar{\boldsymbol{\xi}}(r, \theta + 2m\pi, \phi + 2n\pi). \tag{413}$$

Unlike the standard Fourier modes, which are periodic in both θ and ϕ and defined only in the domain of $[-\pi, \pi]$, the quasi-modes are non-periodic and defined in the domains of $(-m_{\max}\pi, m_{\max}\pi)$ and $(-n_{\max}\pi, n_{\max}\pi)$. The information stored beyond the primary domain of $[-\pi, \pi]$ contains contributions from other coupled modes. When $m_{\max} = n_{\max} = \infty$, $\boldsymbol{\xi}$ decomposed in this way is periodic since shifting the summation in either m or n does not make any difference. In practice, quasi-modes are constructed with small-amplitude periodic oscillations superimposed on a non-periodic envelope that decays sufficiently fast towards zero up to $m_{\max}$ or $n_{\max}$. In this case, the periodicity of $\boldsymbol{\xi}$ is approximately satisfied since the contribution loss from the end of summation is small when m or n is shifted. In the quasi-mode decomposition, we still sum over a large number of modes as in the Fourier-mode decomposition. The difference is that all quasi-modes are the single modes defined recursively in a much larger domain than 2π! Figure 44 shows an example of quasi-mode over $[-10\pi, 10\pi]$, used to construct the full eigenfunction over $[-\pi, \pi]$ with reasonable accuracy with the corresponding mode structures in physical space (Freidberg, 2014, Ch.12).

Using quasi-modes, it is straightforward to find marginal stability, defined as

$$\boldsymbol{F}(\boldsymbol{\xi}) = 0, \tag{414}$$

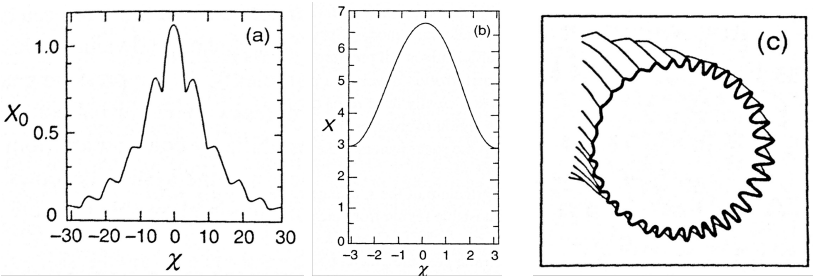

Fig. 44 From Chapter 12 of Freidberg (2014): (a) An example of quasi-mode in $[-10\pi, 10\pi]$, (b) full eigenfunction over $[-\pi, \pi]$, and (c) constructed ballooning mode structure in physical space.

where $\boldsymbol{F}$ is the force operator as a function of (r, θ, ϕ). Since the equilibrium under consideration is periodic, $\boldsymbol{F}$ is also periodic such that $\boldsymbol{F}(r, \theta + 2m\pi, \phi + 2n\pi) = \boldsymbol{F}(r, \theta, \phi)$. Applying $\boldsymbol{F}$ to $\boldsymbol{\xi}$ in Eq. (413) yields

$$\begin{aligned}\boldsymbol{F}(\boldsymbol{\xi}) &= \sum_{\substack{|m|\le m_{\max}\\ |n|\le n_{\max}}} \boldsymbol{F}(r,\theta,\phi)\bar{\boldsymbol{\xi}}(r,\theta+2m\pi,\phi+2n\pi)\\ &= \sum_{\substack{|m|\le m_{\max}\\ |n|\le n_{\max}}} \boldsymbol{F}(r,\theta+2m\pi,\phi+2n\pi)\bar{\boldsymbol{\xi}}(r,\theta+2m\pi,\phi+2n\pi)\\ &= 0.\end{aligned}$$

Since each term of the above summation has the same operator, $\boldsymbol{F}$, and the same quasi-mode, $\bar{\boldsymbol{\xi}}$, we simply have

$$\boldsymbol{F}(\bar{\boldsymbol{\xi}}) = 0, \tag{415}$$

as desired.

Nonetheless, the detailed calculation is still quite mathematically involved (Connor et al, 1979; Freidberg, 2014). However, the calculation leads to a simplified and dimensionless form of energy integral,

$$\delta W = \int \left[(1+\Lambda^2)\left(\frac{\partial X}{\partial \theta}\right)^2 - \alpha(\Lambda \sin\theta + \cos\theta) X^2 \right] d\theta, \tag{416}$$

where $\Lambda = s\theta - \alpha \sin\theta$ and X is dimensionless radial displacement. Here s and α are the dimensionless magnetic shear and the pressure gradient given by

$$\begin{aligned} s &= \frac{r}{q} q', \\ \alpha &= -\frac{2\mu_0 r^2}{R_0 B_\theta^2} p'. \end{aligned}$$

Therefore, the resulting Euler equation is given by

$$\frac{\partial}{\partial\theta}\left[\left(1+\Lambda^2\right)\frac{\partial X}{\partial\theta}\right]+\alpha(\Lambda\sin\theta+\cos\theta)X=0, \tag{417}$$

which shares the same generic form of equation for radial displacement as discussed in Lecture 7.

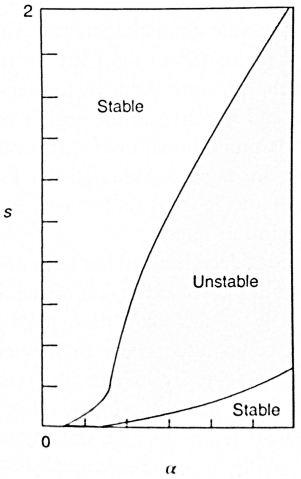

Fig. 45 From Chapter 12 of Freidberg (2014): An example $s-\alpha$ diagram for ballooning mode stability.

A particular quantitative result is shown in Fig. 45 in the format of the $s-\alpha$ diagram. A surprising feature is the existence of a "second stability" in the diagram in the limits of $s \ll 1$ and $\alpha \gg 1$. In this case, $\Lambda \approx -\alpha\sin\theta$, causing the energy integral, Eq. (416), to be

$$\delta W=\int \alpha^2\sin^2\theta\left[\left(\frac{\partial X}{\partial\theta}\right)^2+X^2\right]d\theta, \tag{418}$$

which is positive definite, implying stability. This result is rather counter-intuitive as a large pressure gradient is confined stably by the magnetic field with a small shear. Nowadays, this result is understood as the consequence of increased effective local magnetic shear at the outboard side of bad curvature locations by the large diamagnetic current (see Freidberg, 2014, Ch.12). Experimentally, whether the second stability has been convincingly demonstrated is still unclear, especially during the H-mode operation of tokamaks.

Ballooning instability sets the practical limit of plasma beta in toroidal configuration, shown by the "first stability" in the $s-\alpha$ diagram. According to Eq. (412), a lower q is preferred for a higher beta. However, from Lecture 7,

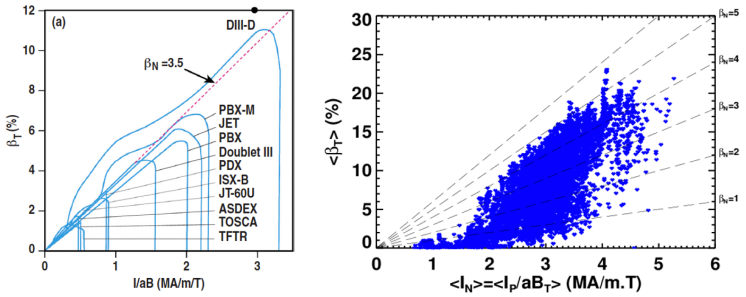

Fig. 46 Achieved beta values in various tokamaks (left) and NSTX (right).

q needs to be high to avoid current-driven kink instabilities with $q(a) > 2$ for external kink and $q(0) > 1$ for internal kink. Combining limitations from both press-driven and current-driven instabilities, a particular dimensionless figure of merit is used in present day's research

$$\beta < \beta_{\rm N} \frac{I(\text{MA})}{a(\text{m})B(\text{T})} = \beta_{\rm N} \left(\frac{I}{1\ \text{MAmp}}\right) \left(\frac{a}{1\ \text{meter}}\right)^{-1} \left(\frac{B}{1\ \text{Tesla}}\right)^{-1}. \quad (419)$$

The **beta normal**, $\beta_{\rm N}$, is given by

$$\beta_{\rm N} = 4.4\% \quad \text{Sykes limit (1974, 1983)},$$
$$\beta_{\rm N} = 2.8\% \quad \text{Troyon limit (1984)},$$

which satisfy Mercier criterion against interchange instability and internal low-n ballooning and kink modes by $q(0) > 1$. Sykes limit was derived against internal high-n ballooning modes, while Troyon limit was derived against external high-n ballooning-kink modes. A simple version of Troyon limit's derivation is given in (Wesson, 2011, Ch.6). All these derivations are for D-shaped plasmas with positive triangularity, where field lines stay more on the inboard side with good field curvature than the outboard side with bad curvature. More recently, however, there are emerging interests for cases with negative triangularity. Figure 46 shows some experimental data regarding beta limits. Note that ITER assumes $\beta_{\rm N} = 2.1$.

Edge-Localized Modes (ELMs) are driven by both large pressure gradients and current density gradients near the edge during the H-mode operation of tokamaks. The current leading theory behind ELMs is the onset of "peering-ballooning" instability as external high-n MHD modes by Snyder et al (2005). The left figure of Fig. 47 shows example data from MAST with increasing neutral beam injection power. ELMs present one of the undesirable features for H-mode operation, which otherwise is favorable for tokamakss to achieve fusion reactor conditions shown in the right figure of Fig. 47. Good confinement at the plasma edge during H-mode significantly increases the total plasma pressure by elevating the pressure on top of the pressure pedestal.

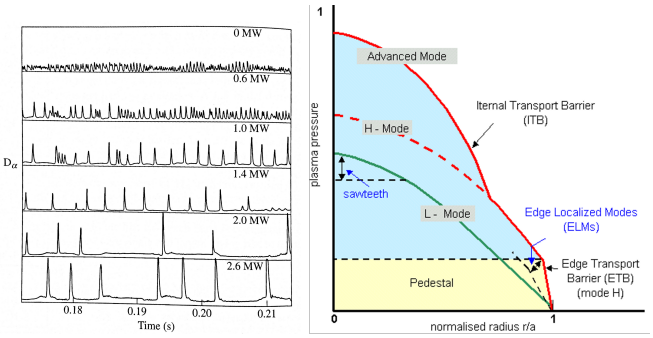

Fig. 47 Example data from MAST on ELM (left) and the pressure pedestal formed during H-mode operation of tokamaks (right).

8.2 Toroidal Alfvén Eigenmodes

The presence of sufficiently enough energetic particles can destabilize ideal MHD modes which are otherwise stable. This behavior happens during neutral beam injection (NBI) and should also occur in the upcoming burning plasmas, where a large number of charged fusion products, such as alpha particles, are born with sufficiently large energies. This area of research is relatively new and still is under development.

We begin by considering the continuum damping of Alfvén waves in an inhomogeneous plasma. In a sense, continuum damping is similar to Landau damping which occurs without dissipation but without involving particles. Consider a simple slab model of a theta-pinch plasma (Fig. 48) with a uniform B_z and density in a cold plasma extending from $x \geq 0$:

$$\begin{aligned} \boldsymbol{B} &= (0, 0, B_z), \\ p &= 0, \\ \rho &= \text{const.}. \end{aligned}$$

When a displacement vector $\boldsymbol{\xi}$ is imposed at the plasma edge at $x = 0$ with an angular frequency ω and a wavenumber vector $\boldsymbol{k} = (0, k_\perp, k_\parallel)$,

$$\boldsymbol{\xi} = \left[\xi(x), \xi_\perp(x), \xi_\parallel(x)\right] e^{-i\omega t + ik_\perp y + ik_\parallel z}, \tag{420}$$

the dependence on x can be solved as a boundary value problem.

The equation of motion is given by

$$-\omega^2 \rho \boldsymbol{\xi} = \frac{1}{\mu_0}(\boldsymbol{\nabla} \times \boldsymbol{B}) \times \boldsymbol{Q} + \frac{1}{\mu_0}(\boldsymbol{\nabla} \times \boldsymbol{Q}) \times \boldsymbol{B} - \boldsymbol{\nabla} p_1, \tag{421}$$

$$\boldsymbol{Q} = \boldsymbol{\nabla} \times (\boldsymbol{\xi} \times \boldsymbol{B}). \tag{422}$$

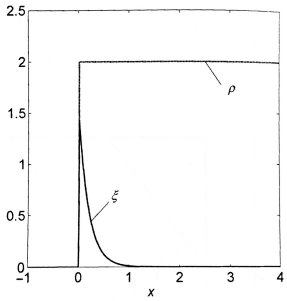

Fig. 48 A simple slab model of theta-pinch with constant density for $x \geq 0$ and exponential decay of applied ξ at $x = 0$ into the plasma.

Since we have

$$(\boldsymbol{\nabla} \times \boldsymbol{B}) \times \boldsymbol{Q} + (\boldsymbol{\nabla} \times \boldsymbol{Q}) \times \boldsymbol{B} = (\boldsymbol{Q} \cdot \boldsymbol{\nabla})\boldsymbol{B} + (\boldsymbol{B} \cdot \boldsymbol{\nabla})\boldsymbol{Q} - \boldsymbol{\nabla}(\boldsymbol{Q} \cdot \boldsymbol{B}),$$

taking the curl of Eq. (421) yields

$$\boldsymbol{\nabla} \times \left[\mu_0 \rho \omega^2 \boldsymbol{\xi} + (\boldsymbol{Q} \cdot \boldsymbol{\nabla})\boldsymbol{B} + (\boldsymbol{B} \cdot \boldsymbol{\nabla})\boldsymbol{Q}\right] = 0. \tag{423}$$

If we choose an incompressible $\boldsymbol{\xi}$ to remove continuum damping by sound waves, $\boldsymbol{\nabla} \cdot \boldsymbol{\xi} = 0$, we have

$$\begin{aligned} \boldsymbol{Q} &= (\boldsymbol{B} \cdot \boldsymbol{\nabla})\boldsymbol{\xi} - (\boldsymbol{\xi} \cdot \boldsymbol{\nabla})\boldsymbol{B} = ik_\parallel B \boldsymbol{\xi} \\ (\boldsymbol{B} \cdot \boldsymbol{\nabla})\boldsymbol{Q} &= ik_\parallel B \cdot (ik_\parallel B \boldsymbol{\xi}) = -k_\parallel^2 B^2 \boldsymbol{\xi}. \end{aligned}$$

Therefore, Eq. (423) becomes

$$\boldsymbol{\nabla} \times \left[\left(\mu_0 \rho \omega^2 - k_\parallel^2 B^2\right) \boldsymbol{\xi}\right] = 0. \tag{424}$$

If $\mu_0 \rho \omega^2 \neq k_\parallel^2 B^2$, this equation reduces to

$$\boldsymbol{\nabla} \times \boldsymbol{\xi} = 0. \tag{425}$$

The x-component of this equation and incompressibility form a set of two equations for $\xi_\perp$ and $\xi_\parallel$:

$$ik_\perp \xi_\parallel - ik_\parallel \xi_\perp = 0, \tag{426}$$

$$ik_\perp \xi_\perp + ik_\parallel \xi_\parallel = -\xi', \tag{427}$$

where the primed variables means their derivatives in x. The solution is given by

$$\xi_\perp = \frac{ik_\perp}{k^2} \xi',$$

$$\xi_\parallel = \frac{ik_\parallel}{k^2}\xi',$$

which can be substituted into the y-component of Eq. (425)

$$\frac{\partial \xi}{\partial z} - \frac{\partial \xi_\parallel}{\partial x} = 0.$$

This relation leads to a second-order differential equation in ξ,

$$\xi'' - k^2\xi = 0, \tag{428}$$

with the evanescent solution of

$$\xi = \xi(0)e^{-kx}. \tag{429}$$

The solution does not transfer energy into plasma, as illustrated in Fig. 48.

The situation changes drastically when density ρ is nonuniform, such that somewhere in plasma $\mu_0\rho(x_0)\omega^2 = k_\parallel^2 B^2$ or $F(x_0) \equiv \mu_0\rho(x_0)\omega^2 - k_\parallel^2 B^2 = 0$. In this case, we need to use Eq. (424), which can be rewritten as

$$\boldsymbol{\nabla} \times (F\boldsymbol{\xi}) = 0. \tag{430}$$

The parallel (z-component) of this equation becomes

$$\begin{aligned} \frac{\partial (F\xi_\perp)}{\partial x} - \frac{\partial (F\xi)}{\partial y} &= 0 \\ (F\xi')' - k^2 F\xi &= 0, \end{aligned} \tag{431}$$

where the solution for $\xi_\perp$ is used. We need to take care of the singularity at $x = x_0$ in Eq. (431) (Freidberg, 2014, Ch.11). The singularity location satisfies

$$\omega_A^2 = k_\parallel^2 \frac{B^2}{\mu_0\rho(x_0)} \tag{432}$$

representing a resonance absorbing all wave energy as illustrated in Fig. 49.

The situation becomes complicated in a screw pinch, where both magnetic field and density are functions of radius in general but the basic idea remains the same. The equation of motion, in this case, is given by (Wesson, 2011, Ch.6)

$$\frac{d}{dr}\left[\left(\mu_0\rho\omega^2 - F^2\right) r^3 \frac{d\xi}{dr}\right] - \left(m^2 - 1\right)\left(\mu_0\rho\omega^2 - F^2\right) r\xi + \mu_0\omega^2 r^2 \frac{d\rho}{dr}\xi = 0, \tag{433}$$

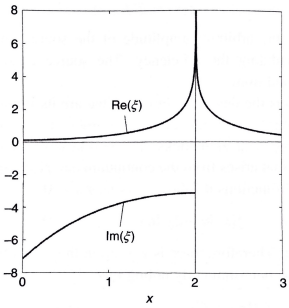

Fig. 49 Alfvén waves absorbed at resonant location in a simple slab model with inhomogeneous density.

where $F \equiv (m - nq)B_\theta/r$. A singularity can exist for each pair of (m, n) due to resonance at a particular radius where

$$\left(\frac{m - nq}{r}\right)^2 = \frac{\omega^2}{V_A^2}.$$

This equation can be solved in the same way as for Eq. (431) to obtain the continuous frequency spectrum. Examples of several modes due to the applied waves on the screw-pinch surface are shown in Fig. 50. In these cases, the wave power is expected to be absorbed in the resonant surface without penetrating beyond. In general, however, wherever the speed of fast particles, such as by NBI or fusion products, matches the wave phase speed, particle energy can be transferred to waves and consequently is damped at resonant locations.

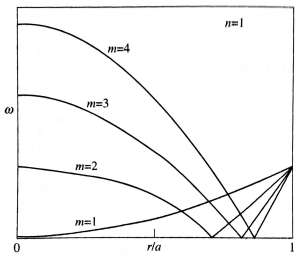

Fig. 50 From Wesson (2011): Example Alfvén wave spectra in a screw pinch plasma.

It is important to note that in cylindrical plasmas, even if some of these spectra intersect as in Fig. 50, they are independent of each other without coupling. Therefore, the resonance condition for each mode is also independent of the other. For example, the modes of (m, n) and $(m+1, n)$ have resonances of

$$\frac{\omega^2}{V_A^2} - k_{\parallel m}^2 = 0, \tag{434}$$

$$\frac{\omega^2}{V_A^2} - k_{\parallel m+1}^2 = 0, \tag{435}$$

which are often located at different radii.

However, these modes are coupled in toroidal plasmas. The coupling can be understood easily given that many quantities in toroidal plasma depend on the poloidal angle, θ. For example, the toroidal magnetic field, B_ϕ, varies as $1/R$ and can be expressed as

$$B_\phi = B_{\phi 0}\frac{R_0}{R} = B_{\phi 0}\frac{R_0}{R_0 + r\cos\theta} \approx B_{\phi 0}\left(1 - \frac{r}{R_0}\cos\theta\right),$$

where R_0 is the major radius to the center of the circular cross-section for a flux surface. As a result, the parallel wavenumber for mode (m, n) is given by

$$k_{\parallel m} = \frac{\boldsymbol{k}\cdot\boldsymbol{B}}{B} \approx \frac{1}{R}\left[n - \frac{m}{q(r)}\right] \approx \frac{1}{R_0}\left[n - \frac{m}{q(r_{m,n})}\right]\left(1 - \frac{r_{m,n}}{R_0}\cos\theta\right). \tag{436}$$

The $k_{\parallel m}$ resonance broadens due to its poloidal variations and can overlap with the broadened $k_{\parallel m+1}$ resonance at $r = r_{m+1,n}$. The coupling between the two resonances is the strongest at

$$q(r_0) = \frac{m + 1/2}{n}, \tag{437}$$

with r_0 located between $r_{m,n}$ and $r_{m+1,n}$ when $q(r)$ is monotonic in r. At this location, $k_{\parallel m} = -k_{\parallel m+1} \equiv k_\parallel$ or

$$\frac{1}{R}\left[n - \frac{m}{q(r_0)}\right] = -\frac{1}{R}\left[n - \frac{m+1}{q(r_0)}\right]. \tag{438}$$

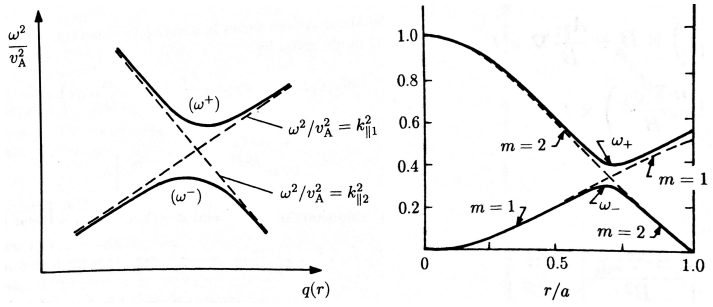

Fig. 51 From (Miyamoto, 2016, Ch.12): Illustration of coupled Alfvén resonances in toroidal plasma as a function of q or r.

Because of these couplings, the growth or damping of one mode depends on the amplitude of the other modes. An illustrative example is given in Ch.12 of Miyamoto (2016) for two modes satisfying

$$\left(\frac{\omega^2}{V_A^2} - k_{\parallel m}^2\right)\frac{dE_m}{dr} + \alpha\epsilon\frac{\omega^2}{V_A^2}\frac{dE_{m+1}}{dr} = 0, \tag{439}$$

$$\alpha\epsilon\frac{\omega^2}{V_A^2}\frac{dE_m}{dr} + \left(\frac{\omega^2}{V_A^2} - k_{\parallel m+1}^2\right)\frac{dE_{m+1}}{dr} = 0, \tag{440}$$

where α is the coupling coefficient on the order of unity with ϵ as the inverse aspect ratio. The coupled resonance condition is given by setting the determinant of the above equations equal to zero

$$\begin{vmatrix} \frac{\omega^2}{V_A^2} - k_{\parallel m}^2 & \alpha\epsilon\frac{\omega^2}{V_A^2} \\ \alpha\epsilon\frac{\omega^2}{V_A^2} & \frac{\omega^2}{V_A^2} - k_{\parallel m+1}^2 \end{vmatrix} = 0, \tag{441}$$

which yields two solutions, $\omega^{\pm}$, shown in Fig. 51. The frequency spectra have a gap that emerges around $r = r_0$ according to Eq. (437) at

$$\frac{\omega_{\pm}^2}{V_A^2} = \frac{k_{\parallel}^2}{1 \mp \alpha\epsilon}.$$

Thus, there is no resonance in the frequency gap $\omega_- < \omega < \omega_+$, which causes the continuum damping to be absent in this range. The gap allows a discrete eigenfrequency of **toroidal Alfvén eigenmode** (TAE) to be established and driven unstable by energetic particles. The detailed calculations of the stability and the growth rates using the energy principle require proper treatment of energetic particles using fluid descriptions (Miyamoto, 2016, Ch.12).

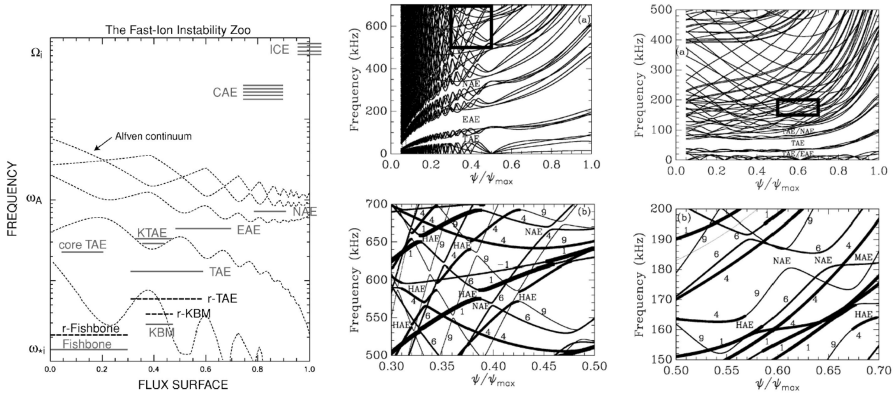

Fig. 52 Frequency spectra of Alfvén modes in tokamak (left, Heidbrink (2002)) and stellarator (right, Spong et al (2005)).

Full Name	First Name	Coupling mechanism
BAE	"beta"	Compression
TAE	"toroidicity"	m & $m+1$
EAE	"ellipticity"	m & $m+2$
NAE	"noncircular"/"triangularity"	m & $m+3$
MAE	"mirror"	n & $n+1$
HAE	"helicity"	both n's and m's

Table 3 Various Afvén eigenmodes in toroidal plasmas.

From this example, one can imagine that there should exist various coupling mechanisms between different Alfvén eigenmodes through various geometric and plasma effects. The toroidicity is just an example of them. Indeed there exists a zoo of such eigenmodes, with some (Heidbrink, 2002) categorized in Table 3. Graphically, the zoo of various Alfvén modes is typically shown in the frequency spectra, such as in Fig. 52 for both the tokamaks and stellarators.

Lastly, there exists another ideal MHD instability driven by energetic ions, called "fishbone instability", which is an internal kink instability (Ch.7 of Wesson (2011) and Ch.12 of Miyamoto (2016)).

Fast-ion-driven instabilities are part of the burning plasma physics that ITER is designed to study, as illustrated in Fig. 53. Thermal plasma, including its profile and magnetic structure, is maintained by a combination of auxiliary heating (NBI, RF), D-T fueling, current drive, and disruption controls to stabilize the MHD instabilities and to limit the transport losses. Fusion output of thermal plasma supplies the non-thermal plasma that can generate fast-ion-driven instabilities and transport to plasma edges, collected as ashes. Meanwhile, α particles can heat the thermal plasma and drive current inside of it for a sustained fusion output. These self-organization cycles can be controlled from outside such that continuous burning at a desirable level can be maintained in a steady state, while part of the fusion energy output can be used to generate electricity.

8.3 Plasma Position Instability

In Lecture 2, we discussed that a vertical magnetic field is needed to maintain toroidal plasma at a desired position, but we did not discuss its stability. Since

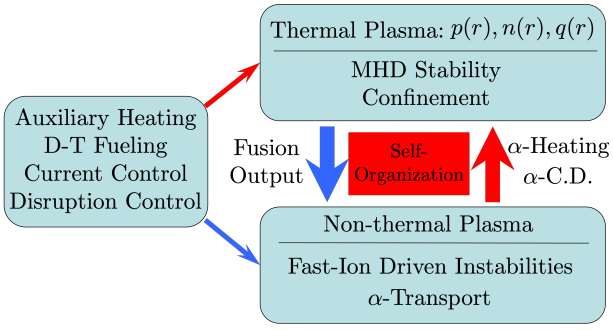

Fig. 53 Important elements of burning plasma physics for magnetically confined plasmas.

the vertical field $B_Z(R,Z)$ and the associated $B_R(R,Z)$ are generated by coils external to the plasma, it is curl-free with $\partial B_R/\partial Z = \partial B_Z/\partial R$. Below we discuss the position, both vertical and horizontal, stability in terms of the spatial profile of $B_Z(R,Z)$.

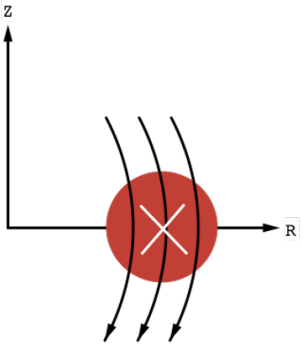

Fig. 54 Stability of toroidal plasma position depends on its vertical field profile.

Vertical stability is determined by the restoring force when the plasma's vertical position is perturbed. For the configuration shown in Fig. 54, I_p is in the positive ϕ direction, while the vertical field is in the negative Z direction. This combination provides the radially inward force to maintain plasma at its equilibrium position at (R,Z). If there is a radial magnetic field, δB_R, the vertical force is given by $F_z = -2\pi R I_p \delta B_R$. For a small vertical displacement δZ, the radial field is given by $\delta B_R = (\partial B_R/\partial Z)\delta Z$, leading to the equation of motion

$$\begin{aligned} M\frac{d^2(\delta Z)}{dt^2} &= -2\pi R I_p \frac{\partial B_R}{\partial Z}\delta Z \\ &= 2\pi I_p B_Z \left(-\frac{R}{B_Z}\frac{\partial B_Z}{\partial R}\right)\delta Z \\ &\equiv 2\pi I_p B_Z n \delta Z, \end{aligned}$$

where $\partial B_R/\partial Z = \partial B_Z/\partial R$ is used. Here, n is the vertical field decay index

$$n = -\frac{R}{B_Z}\frac{\partial B_Z}{\partial R}. \tag{442}$$

Since $I_p B_Z < 0$ here, the vertical stability demands $n > 0$.

Next, we examine horizontal stability (Miyamoto, 2016, Ch.15). According to Lecture 2, an additional vertical field B_V is needed to keep the toroidal plasma at the desired radial location with

$$B_V = -\frac{\mu_0 I_p}{4\pi R}\left(\ln\frac{8R}{a} + \Lambda - \frac{1}{2}\right), \tag{443}$$

where $\Lambda = l_i/2 + \beta_p - 1$. Since the horizontal restoring force due to $\delta B_Z - \delta B_V$ is

$$F_R = 2\pi R I_p (\delta B_Z - \delta B_V), \tag{444}$$

the equation of motion for the small perturbation in the horizontal location, δR, is given by

$$M \frac{d^2(\delta R)}{dt^2} = 2\pi R I_p \left(\frac{\partial B_Z}{\partial R} - \frac{\partial B_V}{\partial R} \right) \delta R. \tag{445}$$

Since the factors in parentheses of Eq. (443) have weak dependencies on R, we approximate $\partial B_V / \partial R$ as

$$\frac{\partial B_V}{\partial R} \approx -\frac{B_V}{R} + \frac{B_V}{I_p} \frac{\partial I_p}{\partial R} = -\frac{B_V}{R} \left(1 - \frac{R}{I_p} \frac{\partial I_p}{\partial R} \right) = -\frac{B_Z}{R} \left(1 - \frac{R}{I_p} \frac{\partial I_p}{\partial R} \right). \tag{446}$$

As the poloidal flux enclosed by the toroidal plasma ring is conserved, we have

$$\begin{aligned} \frac{\partial (L_p I_p)}{\partial R} + 2\pi R B_Z &= 0 \\ \frac{\partial I_p}{\partial R} &= -\frac{1}{L_p} \left(2\pi R B_Z + I_p \frac{\partial L_p}{\partial R} \right), \end{aligned} \tag{447}$$

where plasma self-inductance L_p is given by

$$L_p = \mu_0 R \left(\ln \frac{8R}{a} - 2 + \frac{l_i}{2} \right). \tag{448}$$

As before, we approximate $\partial L_p / \partial R \approx L_p / R$ to give

$$\begin{aligned} \frac{R}{I_p} \frac{\partial I_p}{\partial R} &= -\frac{R}{I_p L_p} \left(2\pi R B_Z + \frac{I_p L_p}{R} \right) \\ &= -1 - \frac{2\pi R^2 B_Z}{I_p L_p} \\ &= -1 - \frac{2\pi R^2 B_V}{I_p L_p} \\ &= -1 - \frac{2\pi R^2}{I_p} \frac{-\frac{\mu_0 I_p}{4\pi R} \left(\ln \frac{8R}{a} + \Lambda - \frac{1}{2} \right)}{\mu_0 R \left(\ln \frac{8R}{a} - 2 + \frac{l_i}{2} \right)} \qquad (449) \\ &\approx -\frac{1}{2}, \qquad (450) \end{aligned}$$

where $\ln(8R/a)$ is assumed to be the dominating term at a sufficiently large aspect ratio R/a in both the denominator and numerator in Eq. (449). In this

case, therefore, Eq. (445) becomes

$$M\frac{d^2(\delta R)}{dt^2} \approx 2\pi I_p B_Z \left(-n + \frac{3}{2}\right)\delta R, \tag{451}$$

where Eq. (442) was used. Thus, horizontal position stability demands $n < 3/2$. This can be understood as when the vertical field decreases too fast in the radial direction, radial displacement of plasma position runs away as an instability due to insufficient restoring force.

Combined with the vertical stability condition, the vertical field decay index (in the radial direction) needs to satisfy $0 < n < 3/2$.

8.4 Instabilities of Solar Flux Ropes

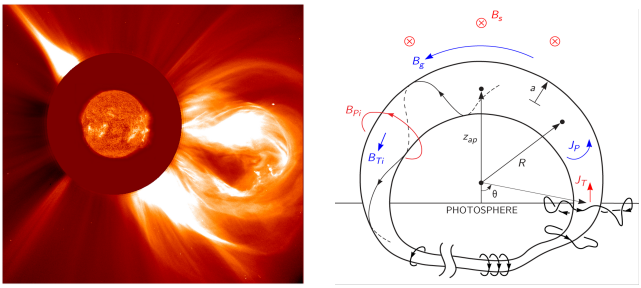

Fig. 55 From Myers (2015): (left) Coronal Mass Ejections (CMEs) measured by SOHO-LASCO-C2 on December 2, 2003. (right) Magnetic flux ropes anchored on the solar surface. Guide field B_g, strapping field B_s, and toroidal current J_T correspond to toroidal field, vertical field, and plasma current.

Coronal Mass Ejections (CMEs, see left panel of Fig. 55) are known to be the most energetic events in the solar system. Free energy in the magnetic field is accumulated in magnetic flux ropes (Gold and Hoyle, 1960) (see right panel of Fig. 55) over a long period of time in the solar corona due to the turbulent convective motion of the solar surface to which the magnetic field is anchored. The flux ropes resemble toroidal plasmas in the laboratory, with field lines helically twisted within, except these flux ropes are terminated on the solar surface rather than forming a full torus. The accumulated free energy is rapidly released via CMEs after a trigger. The CMEs propagate through the heliospheric plasma and sometimes hit Earth's magnetosphere, causing geomagnetic storms via magnetic reconnection, which will be discussed later. These storms generate beautiful aurora seen in polar areas but also can damage satellites in orbit and disrupt electric power grids on the ground. Therefore, understanding how CMEs are triggered and predicting them ahead of time, called "space weather forecast", is an important application area of heliophysics or solar and space plasma physics research.

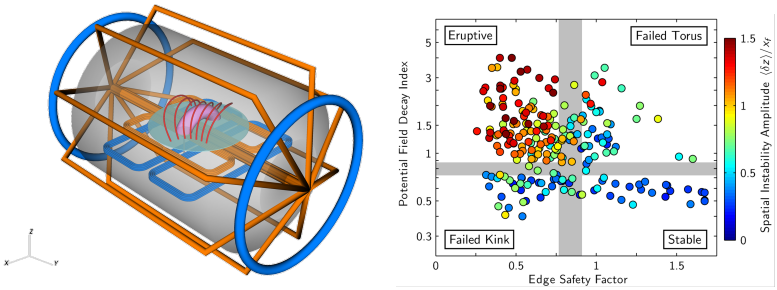

Fig. 56 From Myers et al (2015): (left) The experimental setup on MRX to study flux rope stability with different field geometry and strength. (right) Experimental stability diagram against kink and torus instabilities.

There are two primary candidates for CMEs' triggers: by magnetic reconnection (see later) and by the onset of MHD instabilities of magnetic flux ropes. Examples of MHD instabilities are the (current-driven) kink instability (Sakurai, 1976) and torus instability (Kliem and Török, 2006). The torus instability is essentially the horizontal instability that we have discussed. Even while both of these instabilities have been observed to be unstable on the sun, they "fail" to launch CMEs sometimes. The mutual relationship between these two instabilities has been studied experimentally in the Magnetic Reconnection Experiment (MRX) shown in Fig. 56. For kink instability, the observed threshold $q_a \sim 0.8$ is slightly below the Kruskal-Shafranov limit (Kruskal and Schwarzschild, 1954; Shafranov, 1956) of $q_a = 1$. On the other hand, the critical trapping field (vertical field) index of $n_{\rm cr} \sim 0.8$ is about a factor of 2 below the $n_{\rm cr} = 3/2$ we discussed above. However, it is consistent with the solar observations. The differences, however, have been figured out due to various contributing factors between setups in the lab and in the sun (Alt et al, 2021).

Figure 56 shows a highlight of the experiment with the eruption failing if only one of the instabilities is unstable. This result underlines the mutual dependence of the two MHD instabilities. Kink instability alone fails to launch CMEs due to its nonlinear saturation, while torus (horizontal) instability alone fails due to the increased magnetic tension force from its nonlinear evolution in ideal MHD (Alt, 2022). The failure of torus instability contradicted the previously conjectured Taylor relaxation (see later). These results generated a renewed interest in the solar community to investigate the ideal MHD instabilities in toroidal plasmas.

8.5 Summary

- Ballooning instability sets beta limits for toroidally confined plasmas.
  - ELM limits pedestal height during H-mode.
  - External ballooning-kink modes limit beta.
- Toroidal Alfvén Eigenmodes (TAE) and their relatives, driven by energetic ions, define the physics of burning plasma.

- Horizontal (radial) instability (and external kink instability) are common to tokamaks and solar flux ropes eruptions or CMEs.

Table 4 attempts to summarize ideal MHD instabilities and their locations for both fusion systems and space, solar, and astrophysical plasmas.

Table 4 Summary of ideal MHD instabilities in fusion plasmas and in space, solar, and astrophysical plasmas.

Instability	θ-pinch	Z-pinch	Screw pinch	Tokamak	Space, solar, astrophysics
Pressure-driven kink	No	Near axis	—	—	?
Interchange	No	Possible	Suydam	Mercier	Solar convection
Current-driven kink	—	—	$q < m/n$	$q < m/n$	Solar flux ropes
Resistive wall mode	No	Possible	Possible	Possible	—
Ballooning or Parker	No	—	—	Possible	Disk galaxies, solar convection, Earth magnetotail
Horizontal or Torus	—	—	—	Possible	Solar flux ropes

8.6 Further Readings

- Chapters 11 and 12 in Freidberg (2014)
- Chapters 6 and 7 in Wesson (2011)
- Chapters 6, 12 and 15 in Miyamoto (2016)

8.7 Homework Problem Set 8

1. Discuss the ideal MHD stability of tokamaks with positive triangularity (D-shaped plasmas) versus negative triangularity (reversed D-shaped plasmas) based on what we have learned in this class and the references that you can find from the literature. Please use a structure for a research article: title, author(s), a short abstract, introduction, body of your discussion, conclusion, and references, with a minimum length of 2 pages. Group authors are permitted.

2. Toroidal Alfvén Eigenmodes.
   (a) Using the q profile given by

$$q(x) = q_0 \left(1 + \lambda x^3\right)^{\nu}, \tag{452}$$

   with $q_0 = 1$ and $0 \leq x \leq a$, predict possible unstable Toroidal Alfvén Eigenmodes (TAEs) in terms of frequency and radial location for the case of $\alpha = 2.5$ and $\epsilon = a/R_0 = 1/3.5$. How do the predictions depend on ϵ?

(b) Sometimes observed TAE modes are used to estimate minimum q in the plasma, especially when q is not monotonic. Describe its principle and possible caveats.

9 Ideal MHD Instabilities with Flows

We have discussed ideal MHD instabilities of plasmas without flows. In this Lecture, we will focus on plasmas with an inhomogeneous flow or a sheared flow as a homogeneous flow can be removed by changing to the moving frame of the flow. In the case of sheared flows, the powerful energy principle that we have discussed does not apply as the force operator is no longer self-adjoint, and thus stability cannot be determined by simply minimizing energy integral as we have seen thus far. We revert back to normal mode analysis in this Lecture.

9.1 Kelvin-Helmholtz Instability and Magnetic Stabilization

We will begin by discussing flow shear-driven instability without any magnetic field, *i.e.* Kelvin-Helmholtz instability, followed by its stabilization by the magnetic field.

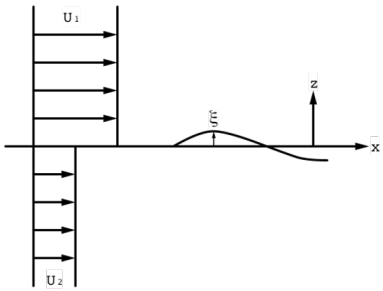

Fig. 57 Kelvin-Helmholtz instability driven by a discontinuous flow shear across $z = 0$.

The basic setup shown in Fig. 57 has an ideal flow in the x direction with a discontinuity at $z = 0$, where the instability grows with a linear perturbation. We can express the base state (equilibrium state) in flow potentials $U_1 x$ and $U_2 x$ so that

$$\boldsymbol{V}_0 = \boldsymbol{\nabla}(U_1 x) \quad \text{when } z > 0 \tag{453}$$

$$= \boldsymbol{\nabla}(U_2 x) \quad \text{when } z < 0. \tag{454}$$

We apply linear perturbation on velocity potentials, $\boldsymbol{V}_1 = \boldsymbol{\nabla}\phi_1$ or $\boldsymbol{V}_1 = \boldsymbol{\nabla}\phi_2$, and interface deformation, ξ, such that

$$\begin{aligned} \phi_1 &= \phi_1(z) e^{ik(x-ct)}, \\ \phi_2 &= \phi_2(z) e^{ik(x-ct)}, \\ \xi &= \xi e^{ik(x-ct)}, \end{aligned}$$

where k is the wavenumber in x direction and $c = \omega/k$ is the complex phase velocity. It is customary to use complex c instead of complex ω in fluid mechanics to analyze flow stability.

The incompressibility assumption leads to

$$\begin{aligned} \nabla^2\phi_1 &= 0, \\ \nabla^2\phi_2 &= 0, \end{aligned}$$

which can be solved using the boundary conditions, $\phi_1(z = \infty) = 0$ and $\phi_2(z = -\infty) = 0$, to yield

$$\begin{aligned} \phi_1 &= Ae^{-kz}, \\ \phi_2 &= Be^{kz}, \end{aligned}$$

where A and B are constants. As discussed in Lecture 4, ϕ_1 and ϕ_2 are related to interface deformation ξ by kinematic boundary conditions at the interface $z = 0$,

$$\begin{aligned} \frac{\partial\phi_1}{\partial z} &= \frac{d\xi}{dt} \approx \frac{\partial\xi}{\partial t} + U_1\frac{\partial\xi}{\partial x}, \\ \frac{\partial\phi_2}{\partial z} &= \frac{d\xi}{dt} \approx \frac{\partial\xi}{\partial t} + U_2\frac{\partial\xi}{\partial x}, \end{aligned}$$

which are linearized. Using solutions for ϕ_1 and ϕ_2, these conditions lead to expressions for A and B in terms of ξ,

$$A = -i(U_1 - c)\xi, \tag{455}$$

$$B = i(U_2 - c)\xi. \tag{456}$$

We then use Bernoulli's equation, including time dependence but without gravitational term, as discussed in Lecture 3,

$$\frac{\partial\phi_1}{\partial t} + \frac{1}{2}\left[\nabla(U_1 x + \phi_1)\right]^2 + \frac{p_1}{\rho} = c_1, \tag{457}$$

$$\frac{\partial\phi_2}{\partial t} + \frac{1}{2}\left[\nabla(U_2 x + \phi_2)\right]^2 + \frac{p_2}{\rho} = c_2, \tag{458}$$

where p_1 and p_2 are the perturbed pressures just above and below the interface while c_1 and c_2 are constants. Dynamic boundary condition demands $p_1 = p_2$ leading to

$$\frac{\partial\phi_1}{\partial t} + \frac{1}{2}U_1^2 + U_1\frac{\partial\phi_1}{\partial x} - c_1 = \frac{\partial\phi_2}{\partial t} + \frac{1}{2}U_2^2 + U_2\frac{\partial\phi_2}{\partial x} - c_2, \tag{459}$$

where the nonlinear terms have been dropped. Before perturbation, this equation simplifies to

$$\frac{1}{2}U_1^2 - c_1 = \frac{1}{2}U_2^2 - c_2,$$

which can be subtracted from Eq. (459) to yield

$$\frac{\partial \phi_1}{\partial t} + U_1 \frac{\partial \phi_1}{\partial x} = \frac{\partial \phi_2}{\partial t} + U_2 \frac{\partial \phi_2}{\partial x}. \tag{460}$$

Using solutions of ϕ_1 and ϕ_2 at $z = 0$, we have

$$A(U_1 - c) = B(U_2 - c)$$

or

$$(U_1 - c)^2 = -(U_2 - c)^2, \tag{461}$$

with the dispersion relation,

$$c = \frac{U_1 + U_2}{2} \pm \frac{i}{2}(U_1 - U_2). \tag{462}$$

Therefore, the flow is unstable if $U_1 \neq U_2$, and is called **Kelvin-Helmholtz Instability**, which was first studied by Kelvin (1871) and Helmholtz (1868) and has been observed in many places.

Next, let us examine the flow stability when a uniform magnetic field is applied. No effects are expected if the uniform field is in the y direction. When the applied magnetic field is in the z direction, B_z, it is continuously sheared by the flow, generating a field in the x direction, B_x. From the induction equation for incompressible flows,

$$\frac{\partial \boldsymbol{B}}{\partial t} = \boldsymbol{\nabla} \times (\boldsymbol{V} \times \boldsymbol{B}) = (\boldsymbol{B} \cdot \boldsymbol{\nabla})\boldsymbol{V} - (\boldsymbol{V} \cdot \boldsymbol{\nabla})\boldsymbol{B}, \tag{463}$$

the x-component of this equation is given by

$$\frac{\partial B_x}{\partial t} = B_z \frac{\partial V_x}{\partial z}, \tag{464}$$

showing that B_x grows proportional to $B_z V_x' t$ after B_z is applied at $t = 0$. V_x' is the flow shear in the magnetic field direction. This is called ω effect which will be discussed in the context of magnetic dynamo in Lecture 11. In such case, we cannot perform linear stability analysis as the base state is not steady. If we consider finite resistivity, however, B_x eventually saturates as in Hartmann flow discussed in Lecture 3, and stability analysis then can be performed upon saturation (Müller and Bühler, 2001).

However, when a uniform magnetic field $\boldsymbol{B}_0 = (B_0, 0, 0)$ is applied in the flow direction, the flow stability is altered and Kelvin-Helmholtz instability can be stabilized. It turns out that in this case the perturbed magnetic field given

by Eq. (463) does not induce electric current perturbation, $\boldsymbol{j} = (j_x, j_y, j_z)$. The j_x and j_z components vanish due to uniformity in y and equilibrium $\boldsymbol{B}_0$ does not have a y component. The remaining component j_y vanishes as

$$\begin{aligned}\mu_0 j_y &= \frac{\partial B_{x1}}{\partial z} - \frac{\partial B_{z1}}{\partial x} = -kB_{x1} - ikB_{z1} \\ &= i\,(ikB_{x1} - kB_{z1}) = i\left(\frac{\partial B_{x1}}{\partial x} + \frac{\partial B_{z1}}{\partial z}\right) = 0,\end{aligned}$$

where B_{x1} and B_{z1} are assumed to be proportional to $e^{ik(x-ct)-kz}$ for $z \geq 0$. The same conclusion holds for $z \leq 0$.

The vanishing $\boldsymbol{j} \times \boldsymbol{B}$ force then implies that its parts, magnetic tension force, $(\boldsymbol{B} \cdot \boldsymbol{\nabla})\boldsymbol{B}/\mu_0$, and magnetic pressure force, $-\boldsymbol{\nabla}(B^2/2\mu_0)$, must cancel each other if they are nonzero, and thus none of them needs to appear in Bernoulli's equations, Eqs. (457) and (458). However, the magnetic pressure needs to be added to the dynamic boundary condition of pressure balance across the interface,

$$p_1 + \frac{B_0 B_{x1}}{\mu_0} = p_2 + \frac{B_0 B_{x2}}{\mu_0}, \tag{465}$$

and therefore, the same magnetic pressure term needs to be added to Eqs. (459) and (460) but with the opposite sign (thus representing magnetic tension force in the z direction due to interface deformation) to yield

$$\frac{\partial \phi_1}{\partial t} + U_1 \frac{\partial \phi_1}{\partial x} - \frac{B_0 B_{x1}}{\mu_0 \rho} = \frac{\partial \phi_2}{\partial t} + U_2 \frac{\partial \phi_2}{\partial x} - \frac{B_0 B_{x2}}{\mu_0 \rho}. \tag{466}$$

Here B_{x1} can be calculated by using the x-component of the linearized induction equation from Eq. (463),

$$\frac{\partial B_{x1}}{\partial t} = B_0 \frac{\partial V_{x1}}{\partial x} - U_1 \frac{\partial B_{x1}}{\partial x}, \tag{467}$$

where $V_{x1} = ik\phi_1$ for $z \geq 0$. This equation leads to

$$\begin{aligned}-ikcB_{x1} &= (ik)^2 B_0 \phi_1 - ikU_1 B_{x1}, \quad \text{or} \\ B_{x1} &= -\frac{ikB_0\phi_1}{c - U_1} = kB_0\xi,\end{aligned} \tag{468}$$

where $\phi_1(z=0) = A = -i(U_1 - c)\xi$ is used. Similarly, we have

$$B_{x2} = -\frac{ikB_0\phi_2}{c - U_2} = -kB_0\xi. \tag{469}$$

Therefore, Eq. (466) becomes by defining $V_{\mathrm{A}}^2 \equiv B_0^2/\mu\rho$

$$(U_1 - c)^2 - V_{\mathrm{A}}^2 = -(U_2 - c)^2 + V_{\mathrm{A}}^2, \tag{470}$$

which can be rearranged into

$$\left(c - \frac{U_1 + U_2}{2}\right)^2 = V_\mathrm{A}^2 - \left(\frac{U_1 - U_2}{2}\right)^2. \tag{471}$$

For the flow to be stable, we must avoid complex solutions of phase velocity c, or the magnetic field needs to be strong enough such that

$$V_\mathrm{A} \geq \frac{|U_1 - U_2|}{2}. \tag{472}$$

As seen by this example, the effect of a magnetic field on flow-shear instabilities is typically stabilizing. But this is not always true and will be discussed later.

9.2 General Flow Stability

9.2.1 Orr-Sommerfeld Equation and Squire's Theorem

Instead of a special flow with a sharp jump as discussed in the previous section, here we discuss some general stability properties of a sheared flow. Consider that the base state of a flow,

$$\boldsymbol{V} = [U(y), 0, 0], \tag{473}$$

is perturbed in the 2 components in 2D:

$$\boldsymbol{V}_1 = (u, v, 0), \tag{474}$$

where u and v, as well as perturbed pressure, p_1, are assumed to be proportional to $e^{ik(x-ct)}$. The linearized equations of the motion and incompressibility are given by

$$\frac{\partial u}{\partial t} + U\frac{\partial u}{\partial x} + v\frac{\partial U}{\partial y} = -\frac{1}{\rho}\frac{\partial p}{\partial x}, \tag{475}$$

$$\frac{\partial v}{\partial t} + U\frac{\partial v}{\partial x} = -\frac{1}{\rho}\frac{\partial p}{\partial y}, \tag{476}$$

$$\frac{\partial u}{\partial x} + \frac{\partial v}{\partial y} = 0, \tag{477}$$

which lead to

$$ik(U - c)u + vU_y = -\frac{ik}{\rho}p \tag{478}$$

$$ik(U - c)v = -\frac{p_y}{\rho} \tag{479}$$

$$iku + v_y = 0, \tag{480}$$

where subscript y indicates derivative with respect to y. The incompressibility, Eq. (480), is automatically satisfied if a stream function ψ is used to represent the perturbed flow,

$$u = \psi_y \quad v = -ik\psi. \tag{481}$$

Substituting these to Eq. (478) yields

$$ik(U-c)\psi_y - ik\psi U_y = -\frac{ik}{\rho}p.$$

Taking the y-derivative of this equation gives

$$\begin{aligned} ikU_y\psi_y + ik(U-c)\psi_{yy} - ik\psi_y U_y - ik\psi U_{yy} &= -\frac{ik}{\rho}p_y \\ (U-c)\psi_{yy} - \psi U_{yy} &= -\frac{p_y}{\rho}. \end{aligned} \tag{482}$$

Equating with Eq. (479) leads to

$$(U-c)(\psi_{yy} - k^2\psi) - \psi U_{yy} = 0, \tag{483}$$

which is the inviscid version of the **Orr-Sommerfeld Equation** by Orr in 1907 and Sommerfeld in 1908, or the **Rayleigh Equation**. This is a second-order ordinary differential equation in ψ and can be solved with proper boundary conditions with c as complex eigenvalues indicating damping or growing modes for each k.

However, it is not obvious that the Orr-Sommerfeld equation explains the general stability for sheared flow as only two velocity components are perturbed. A more general perturbation should consider all the three components of velocity,

$$\boldsymbol{V}_1 = (u, v, w), \tag{484}$$

which are proportional to $e^{i(kx+mz-kct)}$. Then, the corresponding equations are given by

$$\frac{\partial u}{\partial t} + U\frac{\partial u}{\partial x} + v\frac{\partial U}{\partial y} = -\frac{1}{\rho}\frac{\partial p}{\partial x}, \tag{485}$$

$$\frac{\partial v}{\partial t} + U\frac{\partial v}{\partial x} = -\frac{1}{\rho}\frac{\partial p}{\partial y}, \tag{486}$$

$$\frac{\partial w}{\partial t} + U\frac{\partial w}{\partial x} = -\frac{1}{\rho}\frac{\partial p}{\partial z}, \tag{487}$$

$$\frac{\partial u}{\partial x} + \frac{\partial v}{\partial y} + \frac{\partial w}{\partial z} = 0, \tag{488}$$

which lead to

$$ik(U-c)u + vU_y = -\frac{ik}{\rho}p, \tag{489}$$

$$ik(U-c)v = -\frac{p_y}{\rho}, \tag{490}$$

$$ik(U-c)w = -\frac{im}{\rho}p, \tag{491}$$

$$iku + v_y + imw = 0. \tag{492}$$

Now, we apply Squire transformation to the equations above,

$$\bar{k} = \sqrt{k^2+m^2}, \tag{493}$$

$$\bar{k}\bar{u} = ku + mw, \tag{494}$$

$$\frac{\bar{p}}{\bar{k}} = \frac{p}{k}. \tag{495}$$

First, we use Eq. (494) to Eq. (492), leading to

$$i\bar{k}\bar{u} + v_y = 0, \tag{496}$$

which is identical to Eq. (480). Next, multiply Eq. (491) with m/k and add it to Eq. (489) leading to

$$i(ku+mu)(U-c) + vU_y = -\left(\frac{ik}{\rho} + \frac{im^2}{\rho k}\right)p. \tag{497}$$

Here, we use Eq. (493) first and then Eq. (495) to calculate

$$\left(\frac{ik}{\rho} + \frac{im^2}{\rho k}\right)p = \frac{ip}{\rho}\left(\frac{k^2+m^2}{k}\right) = \frac{ip}{\rho}\frac{\bar{k}^2}{k} = \frac{i\bar{k}^2}{\rho}\frac{\bar{p}}{\bar{k}} = \frac{i\bar{k}}{\rho}\bar{p}.$$

Using Eq. (494) again, Eq. (497) becomes

$$i\bar{k}(U-c)\bar{u} + vU_y = -\frac{i\bar{k}}{\rho}\bar{p}, \tag{498}$$

which is identical to Eq. (478). Lastly, taking the derivative of Eq. (495) with respect to y yields $\bar{p}_y/\bar{k} = p_y/k$, which transforms Eq. (490) to

$$i\bar{k}(U-c)v = -\frac{\bar{p}_y}{\rho}, \tag{499}$$

identical to Eq. (479). Therefore, by using the Squire transformation, the three components of 3D perturbation (u, v, w), which are the functions of (k, m, c), are converted to the two-component 2D perturbation $(\bar{u}, v, 0)$, which are the functions of $(\bar{k}, c)$. In addition, the growth of these perturbations, which are proportional to $e^{\bar{k}ct}$ in 2D, are larger than their counterparts in 3D, e^{kct}, since $\bar{k} > k$. It means that for each unstable 3D mode there exists a more unstable 2D mode! This result is known as **Squire's Theorem**, a convenient

and powerful way to analyze flow stability using Orr-Sommerfeld Equation. Both Orr-Sommerfeld Equation and Squire's Theorem are also valid for flow with a finite viscosity but in more complex forms (Kundu et al, 2015, Ch.11).

9.2.2 Rayleigh's Inflection Point Criterion and Fjørtoft's Theorem

With the inviscid Orr-Sommerfeld Equation, Eq. (483), in hand, two powerful theorems can be derived to assess the linear stability of a flow. The first one is the well-known **Rayleigh's inflection point criterion**, which we will explain below.

Equation (483) can be written as

$$\psi_{yy} - k^2\psi - \frac{U_{yy}}{U-c}\psi = 0, \tag{500}$$

as long as $U \neq c$, which is always true if the flow is unstable or $\Im(c) \neq 0$. Next, we multiply Eq. (500) with ψ^* and integrate over y. The first term becomes

$$\int \psi^*\psi_{yy}dy = [\psi^*\psi_y]_{y_1}^{y_2} - \int \psi_y^*\psi_y dy = -\int |\psi_y|^2\, dy,$$

with $\psi = 0$ at the boundaries y_1 and y_2. Therefore, we have

$$\int \left(|\psi_y|^2 + k^2\,|\psi|^2\right) dy + \int \frac{U_{yy}}{U-c}\,|\psi|^2\, dy = 0 \tag{501}$$

with its imaginary part

$$\Im(c)\int \frac{U_{yy}}{|U-c|^2}\,|\psi|^2\, dy = 0. \tag{502}$$

In order to make the last integral equal to zero, allowing $\Im(c) \neq 0$ for instability, there must exist a point in the flow $y_1 < y_0 < y_2$ where $U_{yy}(y_0) = 0$, so that the integrand between y_1 and y_0 has the opposite sign from the integrand between y_0 and y_2. The point $y = y_0$ is called the inflection point. Thus, its existence is the necessary condition for instability, which was shown by Rayleigh in 1880.

A stronger necessary condition was derived by Fjørtoft in 1950. Taking the real part of Eq. (501) yields

$$\int \frac{U_{yy}\,[U - \Re(c)]}{|U-c|^2}\,|\psi|^2\, dy = -\int \left(|\psi_y|^2 + k^2\,|\psi|^2\right) dy < 0. \tag{503}$$

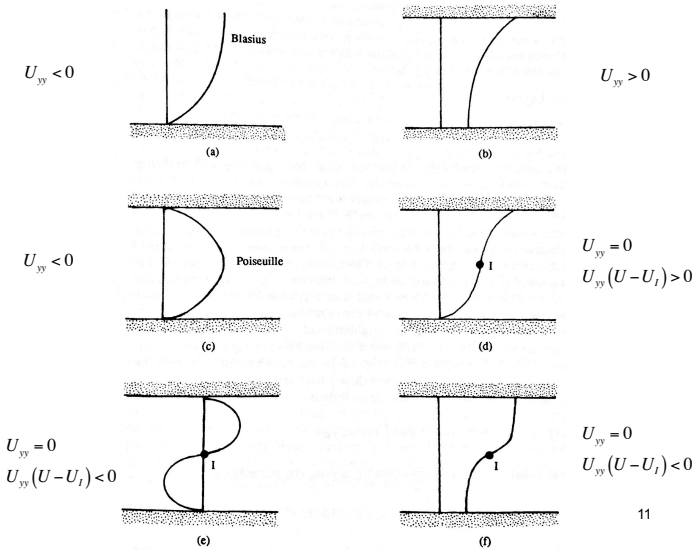

Fig. 58 Example flows to practice Rayleigh's inflection point criterion and Fjørtoft's theorem. From (Kundu et al, 2015, Ch.11).

Since the integral in Eq. (502) is zero, we can construct

$$[\Re(c) - U_I] \int \frac{U_{yy}}{|U-c|^2} |\psi|^2 \, dy = 0, \tag{504}$$

where $U_I = U(y_0)$, and add it to Eq. (503) to yield

$$\int \frac{U_{yy}\,(U - U_I)}{|U-c|^2} |\psi|^2 \, dy < 0, \tag{505}$$

or $U_{yy}\,(U - U_I) < 0$ must be true somewhere in the flow. This is an additional necessary condition for instability beyond the existence of an inflection point. Figure 58 shows several example flows which can be used as exercises to practice using Rayleigh's inflection point criterion and Fjørtoft's theorem.

9.2.3 Effects of Viscosity and Nonlinearity

So far, flow stability has been discussed without considering the effects of viscosity. Intuitively, the viscosity should stabilize the flow as it increases the cost of developing unstable modes. Indeed, it is true for many cases, such as the stability of circular Couette flow, which was first introduced in Lecture 3 and will be discussed later in this Lecture. However, the viscosity can also destabilize the flow, such as in the plane Poiseuille flow, which was also first introduced in Lecture 3 and shown in Fig. 58. The plane Poiseuille flow with a parabolic velocity profile has no inflection point within the flow, thus stable in

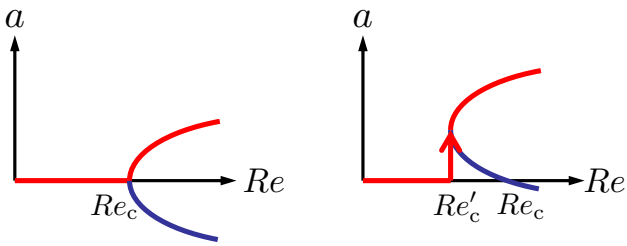

Fig. 59 (Left) Linear or supercritical bifurcation. (Right) nonlinear or subcritical transition.

the inviscid case. However, Poiseuille flow is viscously unstable with a predicted critical Reynolds number of $Re_c = 5780$ (Kundu et al, 2015, Ch.11). The counter-intuitive nature highlights that in some cases where instabilities are favored energetically, which we will discuss below. Other examples are Parker instability and ballooning instability in ideal MHD, which occur since they are energetically favored.

The linearized Navier-Stokes equation in terms of $\boldsymbol{V}_1$ is given by

$$\frac{\partial \boldsymbol{V}_1}{\partial t} + (\boldsymbol{V}_0 \cdot \boldsymbol{\nabla})\, \boldsymbol{V}_1 + (\boldsymbol{V}_1 \cdot \boldsymbol{\nabla})\, \boldsymbol{V}_0 = -\frac{\boldsymbol{\nabla} p_1}{\rho} + \nu \nabla^2 \boldsymbol{V}_1, \tag{506}$$

where $\boldsymbol{V}_0$ is the base flow velocity and p_1 is the perturbed pressure. Taking a dot product of this equation with $\boldsymbol{V}_1$ yields the rate of change for kinetic energy of the perturbation,

$$\frac{1}{2}\frac{\partial V_1^2}{\partial t} = -\boldsymbol{V}_1 \cdot (\boldsymbol{V}_0 \cdot \boldsymbol{\nabla})\, \boldsymbol{V}_1 - \boldsymbol{V}_1 \boldsymbol{V}_1 : \boldsymbol{\nabla} \boldsymbol{V}_0 - \frac{\boldsymbol{V}_1 \cdot \boldsymbol{\nabla} p_1}{\rho} + \nu \boldsymbol{V}_1 \cdot \nabla^2 \boldsymbol{V}_1, \tag{507}$$

with its total obtained by integrating over the whole flow volume. Using integration by parts, many terms of the equation above can be written in terms of surface integral, which vanish if we impose zero perturbations on the boundaries (Kundu et al, 2015, Ch.11). As a result, Eq. (507) becomes

$$\frac{1}{2}\frac{\partial}{\partial t}\int V_1^2 dV = -\int \boldsymbol{V}_1 \boldsymbol{V}_1 : \boldsymbol{\nabla} \boldsymbol{V}_0 dV - \nu \int (\boldsymbol{\nabla} \cdot \boldsymbol{V}_1)^2\, dV. \tag{508}$$

The second term on the RHS indicates the decrease of perturbation's kinetic energy due to viscosity, as expected. However, if the first term is positive and sufficiently large, due to the interaction between perturbation and flow shear that taps its free energy, the perturbation can grow, leading to instability.

The other two linear flows introduced in Lecture 3, the plane Couette flow and the pipe flow, are also linearly stable with no inflection points. They are also linearly stable, even with viscosity. However, nonlinearly, they are

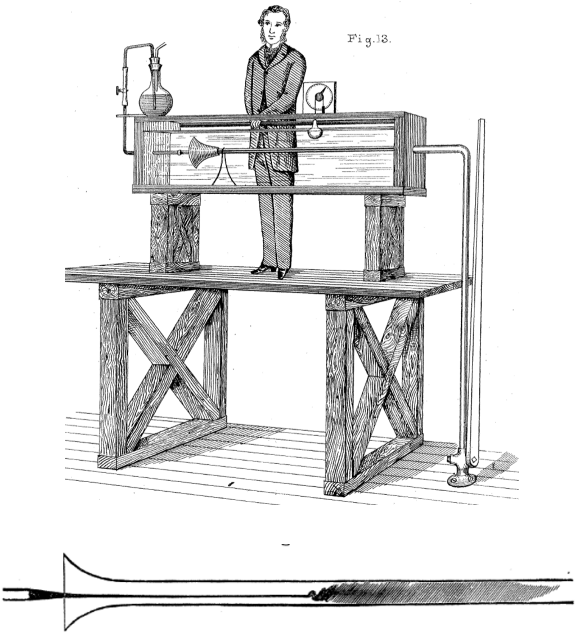

Fig. 60 (Top) Pipe flow experiments performed by Reynolds showed the onset of turbulence at low Re. (Bottom) The onset is indicated by sudden diffusion of injected ink in the flow, despite linear stability at all Re. From Reynolds (1883).

known to be unstable. Usually, nonlinear effects are expected to saturate the amplitude of linear instability. It can be phenomenologically illustrated by the following equation for a properly normalized instability amplitude a,

$$\dot{a} = \mu(Re - Re_c)a - a^3, \tag{509}$$

where μ is a normalization constant. After saturation in a steady state, $\dot{a} = 0$, the saturated amplitude is given by

$$a = \pm\sqrt{\mu\,(Re - Re_c)}. \tag{510}$$

As shown in the left panel of Fig. 59, the amplitude grows after $Re > Re_c$. In the terminology of nonlinear dynamics, the system is said to have a linear or supercritical bifurcation at Re_c to multiple states, of which only one in red is stable or realizable. (Sometimes a is defined to have a sign. In such cases, the blue solution can also be realizable.)

When the system is described with an additional nonlinear term proportional to a^2 instead of Eq. (509), we have

$$\dot{a} = \mu(Re - Re_c)a + \beta a^2 - a^3, \tag{511}$$

where β is a constant. The solution is given by

$$a = \frac{1}{2}\left(\beta \pm \sqrt{\beta^2 + 4\mu\,(Re - Re_c)}\right), \tag{512}$$

which has finite-amplitude solutions at a lower Re where

$$Re_c' = Re_c - \frac{\beta^2}{4\mu}. \tag{513}$$

Therefore, if there exists a proper finite amplitude or nonlinear perturbation, the system can be unstable by transitioning via the path indicated in red on the right panel of Fig. 59. In this case, the system is said to have a nonlinear or subcritical bifurcation at Re_c', and the instability is often termed *nonlinear instability* as opposed to linear instability, which we have discussed throughout this class. In the case of plane Poiseuille flow, the predicted nonlinear critical Reynolds number is $Re_c' = 2510$, smaller than the linear critical Reynolds number at $Re_c = 5780$, but agrees better with experimental results (Kundu et al, 2015, Ch.11).

Both the plane Couette flow and pipe flow can be destabilized by finite-amplitude perturbations. A well-known case is the pipe flow experiment performed by Reynolds in 1883 (Reynolds, 1883), shown in Fig. 60. The transition to turbulence typically occurs at $Re \sim 2000$ and can be maintained laminar at Re as high as 5×10^4 shown by Reynolds. Above that, the flow eventually becomes turbulent due to nonlinear effects.

In civil engineering, pipe flows have been long accepted to be turbulent. In 1944, Princeton Hydraulic Engineering professor, Lewis Moody, published a graphical chart known now as the Moody Diagram shown (Moody, 1944) in Fig. 61, where the effective friction of pipe flow is plotted against the Reynolds number for various roughness of the pipe's inner wall. The friction factor is proportional to the pressure drop needed to maintain the desired averaged flow,

$$f = -\frac{Dp'}{\rho \bar{U}^2/2},$$

where D is pipe diameter, p' is pressure gradient along the pipe, and $\bar{U}$ is the flow speed averaged over the pipe cross-section. The nonlinear transition from laminar to turbulent flow occurs around $Re \sim 2000 - 3000$, with the friction factors gradually asymptote to constant values for a given pipe wall roughness. Aside from engineering applications, the detailed physics of nonlinear transition to turbulence remains a hot topic in the communities of fluid dynamics and nonlinear dynamics but is rarely studied in MHD.

9.3 Stability of Rotating Flow

Nearly all celestial bodies, including Earth, rotate; so do most of the astrophysical (and geophysical) fluids and plasmas. The importance of rotation in

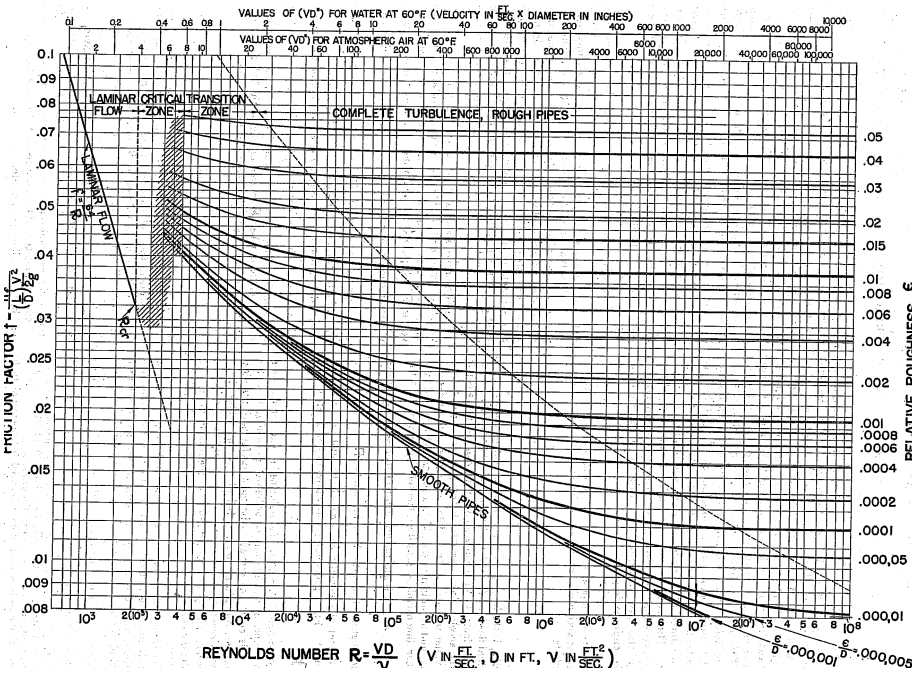

Fig. 61 Moody Diagram on the friction of pipe flow as functions of Reynolds number and pipe inner wall roughness from Moody (1944).

dynamics can be quantified by the Rossby number, defined as the ratio of inertial force to Coriolis force

$$Ro \equiv \frac{|\boldsymbol{V} \cdot \boldsymbol{\nabla} \boldsymbol{V}|}{|\boldsymbol{\Omega} \times \boldsymbol{V}|} = \frac{V^2/L}{V\Omega} = \frac{V}{L\Omega}, \tag{514}$$

where V, L, and Ω are the characteristic velocity, length scale, and angular frequency of the rotation, respectively. When $Ro \gg 1$, we can neglect the effect of rotation, while for $Ro \ll 1$, the rotation effect dominates. The Rossby number is scale-dependent, *i.e.*, for the same characteristic V and Ω, flows at small scales are not affected by rotation, while the opposite is true on large scales. This explains that the Earth's rotation effect can be ignored in small-scale laboratory experiments, while it is important in large-scale flow phenomena in the ocean and atmosphere, or geophysical fluids in general. In this subsection, we discuss flows in the low Ro regimes where rotation plays a dominant role.

9.3.1 Taylor-Proudman Theorem and Inertial Waves

Since a rotating frame of reference is not an inertial frame, additional terms due to the acceleration appear in the Navier-Stokes equation

$$\frac{\partial \boldsymbol{V}}{\partial t} + (\boldsymbol{V}\cdot\boldsymbol{\nabla})\,\boldsymbol{V} = -\frac{1}{\rho}\boldsymbol{\nabla}p + \nu\nabla^2\boldsymbol{V} + \boldsymbol{\Omega}\times(\boldsymbol{r}\times\boldsymbol{\Omega}) - 2\boldsymbol{\Omega}\times\boldsymbol{V}, \tag{515}$$

where the last two terms represent centrifugal and Coriolis forces, respectively. Under *a solid body rotation*, $\boldsymbol{\Omega}$, the centrifugal force can be written as an effective gravity force since

$$\boldsymbol{\Omega}\times(\boldsymbol{r}\times\boldsymbol{\Omega}) = \frac{1}{2}\boldsymbol{\nabla}\left[(\boldsymbol{r}\times\boldsymbol{\Omega})^2\right], \tag{516}$$

where $\boldsymbol{r}$ is the position vector from a point along the rotation axis, and $-(\boldsymbol{r}\times\boldsymbol{\Omega})^2/2$ serves as an effective gravitational potential. In the large Ω limit, the dominant terms of Eq. (515) are Coriolis force and pressure force. They are in balance,

$$2\boldsymbol{\Omega}\times\boldsymbol{V} = -\frac{1}{\rho}\boldsymbol{\nabla}p, \tag{517}$$

called **geostrophic flow**, commonly seen in geophysical fluids as in a typical weather map. Assuming incompressibility, taking the curl of the above equation leads to

$$\begin{aligned}\boldsymbol{\nabla}\times(\boldsymbol{\Omega}\times\boldsymbol{V}) &= 0\\ &= (\boldsymbol{\Omega}\cdot\nabla)\,\boldsymbol{V} - (\boldsymbol{V}\cdot\nabla)\,\boldsymbol{\Omega} + \boldsymbol{V}\,(\boldsymbol{\nabla}\cdot\boldsymbol{\Omega}) - \boldsymbol{\Omega}\,(\boldsymbol{\nabla}\cdot\boldsymbol{V})\\ &= (\boldsymbol{\Omega}\cdot\nabla)\,\boldsymbol{V}\end{aligned}$$

since $\boldsymbol{\Omega}$ is constant. This means that $\boldsymbol{V}$ does not vary in the direction of $\boldsymbol{\Omega}$, or flow tends to be two-dimensional, uniform along the $\boldsymbol{\Omega}$ direction. Much like the situation where plasma tends to be two-dimensional and uniform along a strong magnetic field! This is called **Taylor-Proudman theorem** proposed by Proudman in 1916 and shown by G.I. Taylor experimentally in 1922-1923.

Rotation introduces new waves. Adding time derivative to Eq. (517) yields

$$\frac{\partial \boldsymbol{V}}{\partial t} + 2\boldsymbol{\Omega}\times\boldsymbol{V} = -\frac{1}{\rho}\boldsymbol{\nabla}p. \tag{518}$$

The curl of this equation gives

$$\frac{\partial \boldsymbol{\omega}}{\partial t} = 2\,(\boldsymbol{\Omega}\cdot\nabla)\,\boldsymbol{V}, \tag{519}$$

where $\boldsymbol{\omega} \equiv \boldsymbol{\nabla} \times \boldsymbol{V}$ is vorticity. Since $\boldsymbol{\nabla} \times \boldsymbol{\omega} = \boldsymbol{\nabla}(\boldsymbol{\nabla} \cdot \boldsymbol{V}) - \nabla^2 \boldsymbol{V} = -\nabla^2 \boldsymbol{V}$, by taking another curl operation on Eq. (519), we have

$$-\frac{\partial\left(\nabla^2 \boldsymbol{V}\right)}{\partial t} = 2\left(\boldsymbol{\Omega} \cdot \boldsymbol{\nabla}\right)\boldsymbol{\omega}. \tag{520}$$

Taking a time derivative of this equation leads to

$$\frac{\partial^2\left(\nabla^2 \boldsymbol{V}\right)}{\partial t^2} = -2\left(\boldsymbol{\Omega} \cdot \boldsymbol{\nabla}\right)\frac{\partial \boldsymbol{\omega}}{\partial t} = -4\left(\boldsymbol{\Omega} \cdot \boldsymbol{\nabla}\right)^2 \boldsymbol{V}, \tag{521}$$

where Eq. (519) is used again. As before, we use normal mode decomposition of plane waves in the form of $e^{i(\boldsymbol{k}\cdot\boldsymbol{x}-\omega t)}$. Eq. (521) leads to a dispersion relation of **inertial waves**,

$$\omega^2 k^2 = 4\left(\boldsymbol{\Omega} \cdot \boldsymbol{k}\right)^2$$

or

$$\omega = \pm\frac{2\boldsymbol{\Omega} \cdot \boldsymbol{k}}{k} = \pm 2\Omega\cos\theta, \tag{522}$$

where θ is the angle between $\boldsymbol{\Omega}$ and $\boldsymbol{k}$. Note that the frequencies of inertial waves are limited to $\pm 2\Omega$, as the restoring force is from the Coriolis force, $2\boldsymbol{\Omega} \times \boldsymbol{V}$, which arises due to angular momentum conservation. The energy of inertial waves is carried by the group velocity

$$\boldsymbol{V}_g = \frac{\partial \omega}{\partial \boldsymbol{k}} = \pm\frac{2\left[k^2\boldsymbol{\Omega} - \left(\boldsymbol{\Omega} \cdot \boldsymbol{k}\right)\boldsymbol{k}\right]}{k^3}, \tag{523}$$

which is mostly directed along the $\boldsymbol{\Omega}$ direction, consistent with the implication of the Taylor-Proudman theorem. The magnetic field parallel to $\boldsymbol{\Omega}$ adds Alfvén wave dynamics to inertial waves in ideal MHD, leading to the dispersion relation of magneto-Coriolis (MC) waves,

$$\omega = \pm\frac{\boldsymbol{\Omega} \cdot \boldsymbol{k}}{k} \pm \sqrt{\left(\frac{\boldsymbol{\Omega} \cdot \boldsymbol{k}}{k}\right)^2 + \left(\boldsymbol{k} \cdot \boldsymbol{V}_\mathrm{A}\right)^2}, \tag{524}$$

which has two branches: fast and slow MC waves (see Homework 9).

9.3.2 Centrifugal Instability and Taylor-Couette Flow

Solid-body rotations do not have free energy for instabilities—differential rotations, as in many astrophysical plasmas, do. The stability of differentially rotating, unmagnetized, inviscid fluid is governed by Rayleigh's criterion against centrifugal instability (Rayleigh, 1916), similar to the interchange instability that we discussed earlier.

Consider two fluid rings with equal mass in a differentially rotating inviscid fluid: ring 1 rotates at angular velocity Ω_1 at $r = r_1$, and ring 2 at angular

velocity Ω_2 at $r = r_2$. Since the fluid is inviscid, circulation by each ring Γ is conserved per Kelvin's circulation theorem discussed in Lecture 3,

$$\Gamma = \oint_{r=r} \boldsymbol{V} \cdot \boldsymbol{dl} = 2\pi r^2 \Omega, \tag{525}$$

which is proportional to angular momentum per unit mass or the specific angular momentum, $L = r^2\Omega$. The kinetic energy per unit mass is

$$\frac{1}{2}V^2 = \frac{1}{2}r^2\Omega^2 = \frac{1}{2}\frac{L^2}{r^2}. \tag{526}$$

Now we interchange ring 1 and ring 2 with regard to their radial locations while conserving their angular momenta. After the interchange, ring 1 with the angular momentum of L_1 is at $r = r_2$, while ring 2 with the angular momentum of L_2 is at $r = r_1$. The flow is stable if the change in energy is positive by the interchange,

$$\frac{1}{2}\left(\frac{L_2^2}{r_1^2} + \frac{L_1^2}{r_2}\right) - \frac{1}{2}\left(\frac{L_1^2}{r_1^2} + \frac{L_2^2}{r_2}\right) = \frac{1}{2}\left(L_2^2 - L_1^2\right)\left(\frac{1}{r_1^2} - \frac{1}{r_2^2}\right) > 0, \tag{527}$$

which is equivalent to the condition

$$\frac{dL^2}{dr} > 0. \tag{528}$$

Therefore, the flow is stable if angular momentum is an increasing function of radius. This condition is called **Rayleigh's criterion** (Rayleigh, 1916).

Therefore, the stability of circular Couette flow, driven by two concentric, infinitely long cylinders (also introduced in Lecture 3), depends on the relative magnitude of angular momentum between inner and outer cylinders. The flow is centrifugally stable if $r_1^2\Omega_1 < r_2^2\Omega_2$ when cylinders are co-rotating. Finite viscosity, in this case, is stabilizing, so even if Rayleigh's criterion is violated, the flow is still stable when Re is sufficiently low. G.I. Taylor derived a

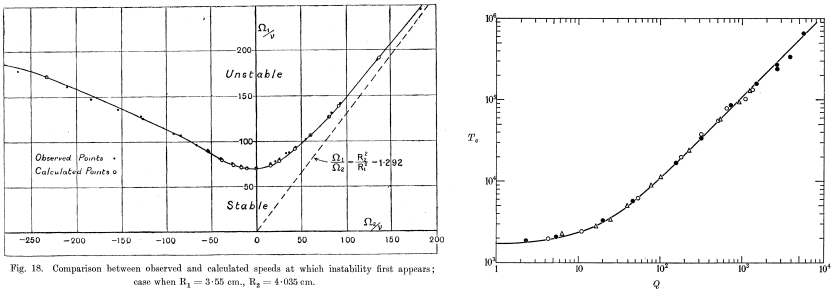

Fig. 62 Hydrodynamic stability of Taylor-Couette flow by Taylor (1923) and its magnetic stabilization by Donnelly and Ozima (1962).

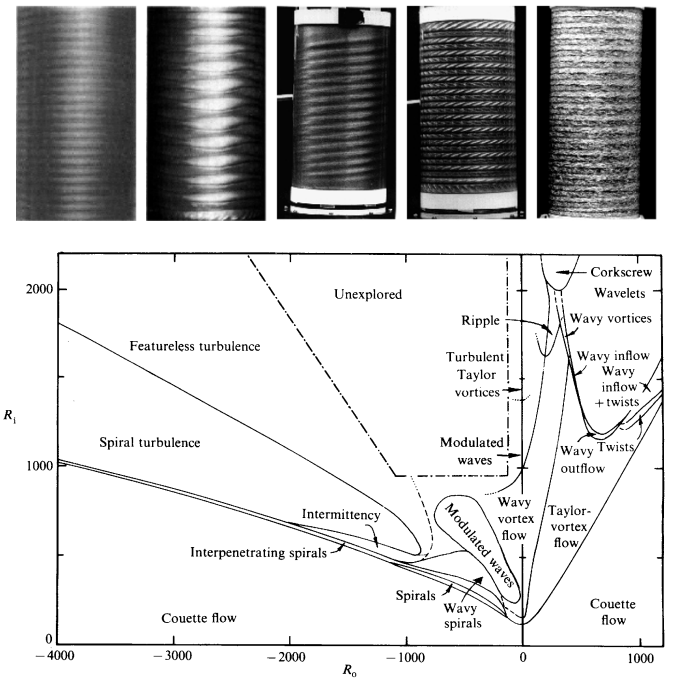

Fig. 63 Different flow regimes after the first instability appears by Andereck et al (1986).

set of differential equations by taking into account finite viscosity and solved them numerically without modern computers with non-slip boundary conditions on the surface of inner and outer cylinders. He also performed careful experiments using the now-called Taylor-Couette cells (Taylor, 1923) by injecting inks to determine the onset of centrifugal instability. Experimental and numerical results agree nearly perfectly, as shown in the left panel of Fig. 62, effectively validating the non-slip boundary conditions.

A magnetic field imposed along the rotation axis can stabilize centrifugal instability. This has been worked out theoretically by Chandrasekhar (1961) and confirmed experimentally (Donnelly and Ozima, 1962), with excellent agreements shown in the right panel of Fig. 62. Here the critical Taylor number, T_c, for the onset of centrifugal instability is proportional to the square of the Reynolds number, while Q, the Chandrasekhar number, is proportional to the square of Alfvén speed.

The nonlinear regimes above the first instability turned out to be very rich with various bifurcations and transition towards full turbulence when Re is increased, as shown in Fig. 63. These regimes are continuously being studied even after 100 years (Lueptow et al, 2023a,b) since G.I. Taylor's 1923 paper due to their richness in terms of nonlinear dynamics and their applications.

9.4 Stability of Keplerian Flows

Accretion disks are disk-like flows where gas, plasma, and dust particles rotate around and gradually fall on the central object. Disk-like structures naturally form due to the conservation of angular momentum but not its energy which escapes due to, *i.e.*, radiation. Important energetic astrophysical processes occur in accretion disks, including the formation of stars and planets, mass transfer and novae in binary star systems, and energy release in active galactic centers around a supermassive black hole that has mass as large as 10^9 of solar mass and is as luminous as 10^{14} of our Sun, the brightest steady source in the Universe. The energy released by accretion can be as efficient as converting up to $\sim 25\%$ of rest mass energy through falling in gravitational potential wells in compact objects (neutron stars and black holes), compared to only $\sim 10^{10}$ by chemical reaction, $\sim 0.08\%$ by nuclear fission, and $\sim 0.4\%$ by D-T fusion.

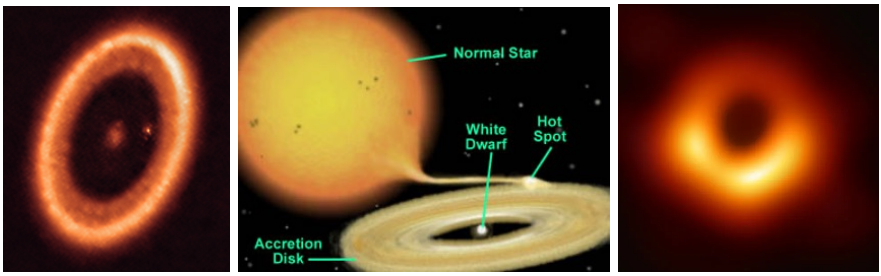

Fig. 64 (Left) planet-forming star PDS70 by ALMA. (Middle) mass transfer in binary system. (Right) M87 supermassive backhole image by Event Horizon Telescope.

The flow profile in accretion disks closely follows Kepler's Third Law: "The square of the orbital period of a planet is directly proportional to the cube of the semi-major axis of its orbit" or

$$\Omega(r) = \frac{\sqrt{GM}}{r^{3/2}} \tag{529}$$

for circular orbits with G as the gravitational constant and M as the central object mass. The kinetic energy of a mass m at r is

$$K = \frac{1}{2} m \left(r\Omega\right)^2 = \frac{GMm}{2r}, \tag{530}$$

with its gravitational potential energy

$$\Phi = -\frac{GMm}{r} \tag{531}$$

such that the total energy is given by

$$E = K + \Phi = -\frac{GMm}{2r} < 0. \tag{532}$$

Therefore, by falling deeper through the gravitational potential through accretion, more energy is released, even if the orbital kinetic energy gets larger.

However, mass cannot simply fall in the gravitational potential due to angular momentum conservation, just as Earth does not simply fall onto the Sun due to its finite angular momentum. Therefore, the only way for a mass to fall onto the central object or accrete to release energy is to transfer its angular momentum to other masses, conserving the total angular momentum. This can be demonstrated by the following thought experiment.

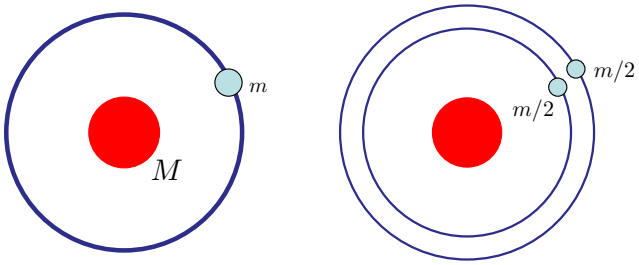

Fig. 65 (Left) A mass of m orbiting around the central mass of M. (Right) The mass m splits into two halves with equal masses but unequal angular momenta.

Consider a mass of m orbiting with an angular frequency of Ω at a distance r from the central mass M. This mass carries an angular momentum and energy of

$$J_0 = mr^2\Omega = m\sqrt{r}, \tag{533}$$

$$E_0 = -\frac{m}{2r}. \tag{534}$$

Here, the constant GM is taken as unity to simplify the problem. Now, the mass m is split into two, each having half of the mass, angular momentum, and energy such that

$$\frac{J_0}{2} = \frac{m}{2}\sqrt{r} \tag{535}$$

$$\frac{E_0}{2} = -\frac{m}{4r}. \tag{536}$$

If one half gains angular momentum by δJ, the other half loses the same δJ. As a result, the total angular momentum will be conserved. However, the radius of the half mass that gains angular momentum needs to increase by δr_1, while

the radius of the half mass which loses angular momentum needs to decrease by δr_2 in such a way that

$$\frac{J_0}{2} + \delta J = \frac{m}{2}\sqrt{r + \delta r_1} \tag{537}$$

$$\frac{J_0}{2} - \delta J = \frac{m}{2}\sqrt{r - \delta r_2}. \tag{538}$$

Dividing these equations by Eq. (535) yields

$$\left(1 + \frac{2\delta J}{J_0}\right)^2 = \frac{r + \delta r_1}{r}, \tag{539}$$

$$\left(1 - \frac{2\delta J}{J_0}\right)^2 = \frac{r - \delta r_2}{r}, \tag{540}$$

which can be used to calculate the total energy

$$\begin{aligned} -\frac{m}{4(r+\delta r_1)} - \frac{m}{4(r-\delta r_2)} &= -\frac{m}{4r}\left(\frac{r}{r+\delta r_1} + \frac{r}{r-\delta r_2}\right) \\ &= -\frac{m}{4r}\left[\left(1 + \frac{2\delta J}{J_0}\right)^{-2} + \left(1 - \frac{2\delta J}{J_0}\right)^{-2}\right] \\ &\approx -\frac{m}{2r}\left[1 + 3\left(\frac{2\delta J}{J_0}\right)^2\right] < E_0. \end{aligned} \tag{541}$$

As a result, by transferring angular momentum from one part of the mass to the other part, the part losing angular momentum can lower its orbit while the part gaining angular momentum raises its orbit while releasing gravitational energy. This process repeats and eventually leads to accretion, with the majority of the mass possessing little angular momentum forming a star at the center. The masses carrying most of the angular momentum orbits the central object as the planets, far from the star. This is what happened to our solar system.

This radially outward transport of angular momentum can happen by molecular viscosity of accretion disk flow but at a very slow time scale. The diffusion time over 1 AU distance is $\tau \sim R^2/\nu$ where $R = 1.5 \times 10^{11}$m and $\nu \sim 10^4 \text{m}^2/\text{s}$. The values give $\tau \sim 10^{18}\text{s} \sim 10^{10}$year, which is longer than the age of the Universe! Therefore, we need an enhanced effective viscosity by orders of magnitude in order to explain the observed star formation on the order of millions of years (Shakura and Sunyaev, 1973). The usual suspect of such an enhancement is turbulence as in the pipe flow, but the question here is, what is the driving mechanism for turbulence?

Unfortunately, Keplerian flows are stable against centrifugal instability because Rayleigh's criterion is satisfied due to their positive radial gradient of angular momentum, $L \propto \sqrt{r}$ per Eq. (529). Since viscosity is stabilizing here as well, therefore, we are left with two main possibilities: instability driven

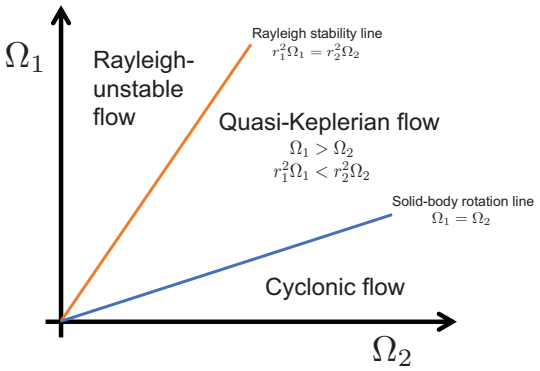

Fig. 66 Different flow regimes of Taylor-Couette flow in the parameter space of angular speeds of inner and outer cylinders from Ji and Goodman (2023).

by nonlinearity or by the magnetic field. Both of these effects have only been studied recently (Ji and Goodman, 2023) despite the long history of rotating flow research, which historically focused on centrifugal instability. The relevant regime here is the quasi-Keplerian regime where angular velocity decreases with radius while angular momentum increases with radius, as shown in Fig. 66 for Taylor-Couette flows.

There are enough reasons to believe nonlinearity can indeed destabilize (quasi-)Keplerian flows: there is sufficient free energy in the flow shear when the Reynolds numbers are enormous (at least 10^{13}) in any moderate solar system. There are also plenty of examples of such systems that are nonlinearly unstable, such as pipe flows, which we discussed before. This motivated a large wave of intensive research to look for nonlinear instabilities, including some experiments which claimed to have found such instabilities that turned out to be the cases where turbulence is driven by Ekman circulation due to rigid endcaps of Taylor-Couette flow (Ji and Goodman, 2023). Ekman circulation is explained conceptually in Fig. 67, where a cup of tea can stop in about 10 seconds after being spun up by a spoon, while even viscous spin down should take minutes. More detailed descriptions of Ekman circulation are given in

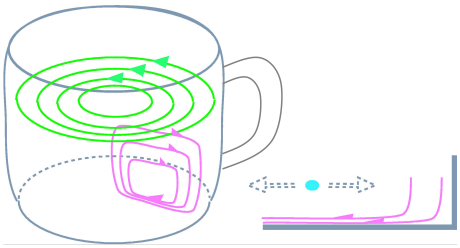

Fig. 67 Ekman circulation in the spinning tea in a cup. In the bulk of tea, centrifugal force is balanced by pressure force from the outer wall. However, near the bottom of the teacup, where viscous force is non-negligible, tea rotates at a slower rate leading to smaller centrifugal force. On the other hand, the pressure force from the outer wall is still large, pushing the tea toward the center of the cup to generate Ekman circulation in purple.

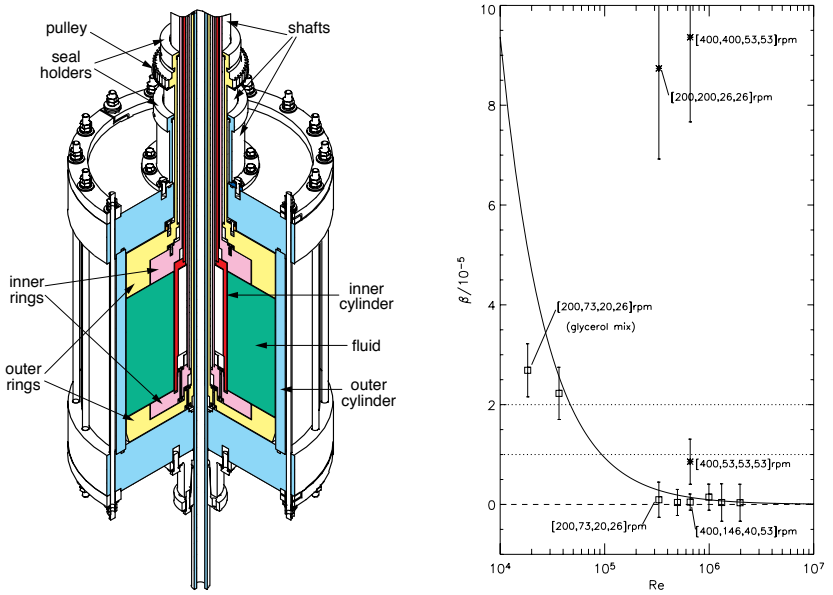

Fig. 68 From Ji et al (2006): (Left) Princeton MRI experiment which contains segmented and independently rotatable end rings to minimize Ekman circulation. (Right) Measured Reynolds stress is indistinguishable from zero and shows no sign of turbulence with the proper choice of end ring speeds up to shear Reynolds numbers above 10^6. Large stresses can be measured for non-optimal choices of end ring speeds or at low Reynolds numbers. The solid line represents viscous stresses.

(Kundu et al, 2015, Ch.13). Ekman circulation is effective in transporting angular momentum, removing the energetic needs for instabilities. In practice, endcaps are typically placed far from the bulk of Taylor-Couette flows. However, their influences extend to large distances along the rotation axis, especially when the system is rapidly rotating at a small Ro, according to the Taylor-Proudman theorem that we discussed already.

After proper care was taken by using segmented and independently rotatable rings (Ji et al, 2006) to remove Ekman effects, there have been no signs of turbulence from experiments and simulations in (quasi-)Keplerian flows at Reynolds numbers as large as 10^6, see Fig. 68. This is true even with active perturbations. This is quite remarkable as there are no other known shear flows that remain laminar at such large Reynolds numbers. However, the reason why (quasi-)Keplerian flows are so robustly stable is still unclear. Interestingly, the flow structure outside the major hurricane eyes is also in the quasi-Keplerian regime (Mallen and Montgomery, 2005). There are speculations that this has to do with the constraints coming from the angular momentum conservation in the time evolution of perturbation energy (Balbus et al, 1996), which is absent in linear flows such as pipe flows, but a powerful mathematical theorem seems to be in order (Ji and Goodman, 2023).

9.5 MagnetoRotational Instability (MRI)

Even the (quasi-)Keplerian flows are robustly stable in hydrodynamics. Their stability changes drastically with a very weak magnetic field. When such a field is imposed axially—along the rotation axis, an ideal MHD instability called (standard) MagnetoRotational Instability or MRI arises. MRI was first derived by Velikhov (1959) and Chandrasekhar (1960). It did not get any attention for its astrophysical importance until Balbus and Hawley (1991). There are other versions of MRI: Helical MRI (HMRI) with a helical magnetic field in both axial and azimuthal magnetic field; Azimuthal MRI (AMRI) with a purely azimuthal field. Both HMRI and AMRI are unstable at much lower Rm than SMRI, but they are stable for Keperian flows, see Ji and Goodman (2023), and will not be discussed here.

The standard MRI can be illustrated using a spring-mass analog, shown in Fig. 69. Similar to the situation shown in Fig. 65, two masses are split but connected by a spring this time, mimicking the effects of a connecting magnetic field. The mass perturbed radially inward gains angular speed, while the mass perturbed radially outward loses angular speed. Therefore, the spring is stretched, pulling the inner mass and transferring its angular momentum to the outer mass. With less angular momentum, the inner mass drifts further to the lower orbit closer to the center, while the outer mass, with more angular momentum, drifts to a higher orbit away from the center. The movement stretches the spring further, transferring more angular momentum between two masses and creating a runaway process. The process results in instability as a purely growing mode in the local rotating frame. When the spring is too strong, the system oscillates but is stable.

In fact, this runaway process can be demonstrated by constructing a set of equations in terms of x and y, defined as linear displacement of the mass in the local radial and flow directions, respectively (Balbus, 2009). We assume that the unperturbed location is at $r = r_0$ with $\Omega(r_0) = \Omega_0$. The equation of motion is given by

$$\frac{\partial \boldsymbol{V}}{\partial t} + (\boldsymbol{V}\cdot\boldsymbol{\nabla})\,\boldsymbol{V} + 2\boldsymbol{\Omega}_0 \times \boldsymbol{V} = -\frac{\partial \Phi(r)}{\partial r}\hat{\boldsymbol{r}} + r\Omega_0^2\hat{\boldsymbol{r}}, \tag{542}$$

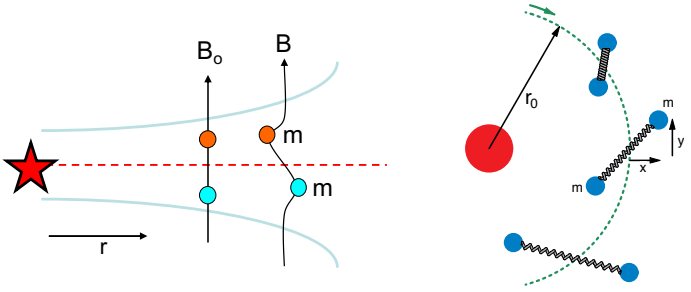

Fig. 69 Side view (left) and top view (right) of a spring-mass analogue of standard MRI.

where the last two terms are centripetal and centrifugal forces, which are in balance when unperturbed. $\hat{\boldsymbol{r}}$ is radial unit vector with $\boldsymbol{V} = (\dot{x}, \dot{y})$. The centripetal force is determined by the scalar potential, which is the gravitation potential in accretion disks or pressure in the laboratory. The magnitude must be in the form of $-r\Omega^2(r)$ in order to keep the mass in orbit. When the mass is perturbed, the perturbed centripetal force is given by

$$\begin{aligned}\left[-\frac{d\Phi}{dr}\right]_{r_0+x} - \left[-\frac{d\Phi}{dr}\right]_{r_0} &= \left[-r\Omega^2\right]_{r_0+x} - \left[-r\Omega^2\right]_{r_0} \\ &\approx -x\left(\Omega_0^2 + r_0\frac{d\Omega^2}{dr}\right), \end{aligned} \tag{543}$$

where $d\Omega^2/dr$ is taken at r_0. The perturbed centrifugal force is simply $x\Omega_0^2$, so the combined perturbed radial force is

$$-xr_0\frac{d\Omega^2}{dr}. \tag{544}$$

Therefore, the desired set of equations is given by

$$\ddot{x} - 2\Omega_0\dot{y} = -xr_0\frac{d\Omega^2}{dr} - Kx, \tag{545}$$

$$\ddot{y} + 2\Omega_0\dot{x} = -Ky, \tag{546}$$

where $K \geq 0$ is the spring constant. Assuming $x, y \propto e^{\gamma t}$, the equations above become

$$\left(\gamma^2 + r_0\frac{d\Omega^2}{dr} + K\right)x - 2\Omega_0\gamma y = 0, \tag{547}$$

$$2\Omega_0\gamma x + \left(\gamma^2 + K\right)y = 0, \tag{548}$$

leading to the dispersion relation

$$\gamma^4 + (2K + \kappa^2)\gamma^2 + K\left(K + r_0\frac{d\Omega^2}{dr}\right) = 0, \tag{549}$$

where the *epicyclic frequency*, κ, is given at r_0 by

$$\kappa \equiv 4\Omega_0^2 + r_0\frac{d\Omega^2}{dr} = \frac{1}{r^3}\frac{d\left(r^4\Omega^2\right)}{dr}. \tag{550}$$

When $K = 0$, Eq. (549) reduces to $\gamma^2 = -4\Omega_0^2$ in solid body rotation, recovering the inertial waves discussed earlier. When $K \neq 0$, one of the solutions of Eq. (549), which corresponds to the destabilized slow magneto-Coriolis

waves (Homework 9), is given by

$$2\gamma^2 = \sqrt{\left(2K+\kappa^2\right)^2 - 4K\left(K + r_0\frac{d\Omega^2}{dr}\right)} - \left(2K+\kappa^2\right). \tag{551}$$

Since $K \geq 0$, the stability requires $\gamma^2 < 0$, which is satisfied when

$$K + r_0\frac{d\Omega^2}{dr} > 0. \tag{552}$$

However, K can be arbitrarily small (but remains positive), simplifying the condition to

$$\frac{d\Omega^2}{dr} > 0, \tag{553}$$

which contrasts the stability condition, Eq. (528), for centrifugal instability. Even if this condition is violated, i.e., the system is unstable with a weak spring, but with a sufficiently strong spring or sufficiently large K can satisfy Eq. (552) and stabilizes the system as expected.

Interestingly, the spring-mass analog of MRI, shown in Fig. 69, has been actually demonstrated in the laboratory (Hung et al, 2019). It was shown that the "mass" indeed follows the trajectory predicted by the equations above.

Now consider the ideal MHD model of a thin accretion disk where the radial extent is much larger than the vertical height, $r \gg h$, such that radial variations (or effective "k_r") can be ignored when compared with the vertical variations k_z. The base flow state and magnetic field are given by

$$\boldsymbol{V_0} = [0, r\Omega(r), 0], \tag{554}$$

$$\boldsymbol{B_0} = [0, 0, B]. \tag{555}$$

The incompressible ideal MHD equations in the *rest frame* are

$$\frac{\partial \boldsymbol{B}}{\partial t} = \boldsymbol{\nabla} \times (\boldsymbol{V} \times \boldsymbol{B}), \tag{556}$$

$$\frac{\partial \boldsymbol{V}}{\partial t} + (\boldsymbol{V}\cdot\boldsymbol{\nabla})\,\boldsymbol{V} = \frac{(\boldsymbol{B}\cdot\boldsymbol{\nabla})\,\boldsymbol{B}}{\mu_0\rho} - \frac{1}{\rho}\boldsymbol{\nabla}\left(p + \frac{B^2}{2\mu_0}\right), \tag{557}$$

$$\boldsymbol{\nabla}\cdot\boldsymbol{B} = 0, \tag{558}$$

$$\boldsymbol{\nabla}\cdot\boldsymbol{V} = 0. \tag{559}$$

We assume all linear quantities $\boldsymbol{B}_1 = (B_r, B_\theta, B_z)$, $\boldsymbol{V}_1 = (V_r, V_\theta, V_z)$, and p_1 are axisymmetric and proportional to $e^{\gamma t - ikz}$. We also ignore the curvature terms B_z and V_z since $r \gg h$. The resulting set of linear equations is given by

$$\gamma B_r = -ikBV_r \tag{560}$$

$$\gamma B_\theta = -ikBV_\theta + r\frac{\partial\Omega}{\partial r}B_r \tag{561}$$

$$\gamma V_r - 2\Omega V_\theta = -i\frac{kB}{\mu_0\rho}B_r \tag{562}$$

$$\gamma V_\theta + \frac{\kappa^2}{2\Omega}V_r = -i\frac{kB}{\mu_0\rho}B_\theta, \tag{563}$$

which leads to the MRI dispersion relation (Balbus and Hawley, 1991),

$$\gamma^4 + \left(2k^2V_\mathrm{A}^2 + \kappa^2\right)\gamma^2 + k^2V_\mathrm{A}^2\left(k^2V_\mathrm{A}^2 + r\frac{\partial\Omega^2}{\partial r}\right) = 0. \tag{564}$$

This equation is identical to Eq. (549) for the spring-mass analog, with the spring constant $k^2V_\mathrm{A}^2$ replacing K. Again, the same Eq. (553) gives the stability condition, meaning that (quasi-)Keplerian flows are unstable for a weak field while stable if the field is too strong, as expected.

In the case of MRI, finite viscosity and resistivity are stabilizing, with the corresponding dispersion relation given by Ji et al (2001),

$$\left[\left(\gamma + \nu k^2\right)\left(\gamma + \eta k^2\right)\right]^2 + \kappa^2\left(\gamma + \eta k^2\right)^2 + r\frac{d\Omega^2}{dr}k^2V_\mathrm{A}^2 = 0. \tag{565}$$

We can show that this equation reduces to the ideal MHD version when $\nu = \eta = 0$. Unlike in the ideal MHD, where a small but finite magnetic field can destabilize MRI, a dissipative MHD system requires a magnetic field and Rm beyond some thresholds to trigger MRI. This is because the magnetic field can be detached from the fluid due to diffusion if the field is too weak or too diffusive. These requirements were used to design the Princeton MRI experiment based on a magnetized liquid metal Taylor-Couette flow device, with the amplitude of SMRI shown in Fig. 68 as a function of dimensions, speeds, and magnetic field strength.

However, adding an axial magnetic field enhances Ekman effects from the endcaps on the bulk flow. When the magnetic field is strong enough or when the Rossby number is low enough, equivalently rotation is fast enough, the speed gap on the endcaps induces a free shear layer in the bulk flow, as implied by the Taylor-Proudman theorem. The induced layer is unstable to Kelvin-Helmholtz instability. Fortunately, it turned out that the parameter space does not overlap with the parameter space for MRI.

Also, fortunately, it turned out that the enhanced Ekman effects can be advantageous. The free energy for MRI comes from the radial flow shear maintained viscously by inner and outer cylinders, which is weak due to large Reynolds numbers. Electrically conducting endcaps, coupled with an axial magnetic field, are used to enhance the injection of free energy, increasing the MRI amplitudes significantly to be detectable. Another advantage of Ekman cells is that they induce the onset of the MRI cell in the same polarity at lower Rm values during the so-called imperfect bifurcation than the perfect bifurcation without Ekman cells. Combining these factors, the standard MRI has been successfully detected (Wang et al, 2022), as shown in Fig. 70. The MRI

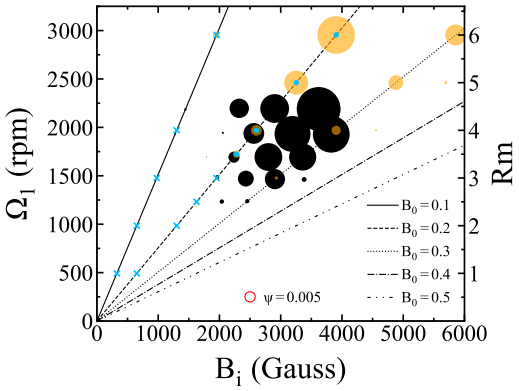

Fig. 70 From (Wang et al, 2022): The amplitude of standard MRI radial magnetic field amplitude (circle diameter) from the Princeton MRI experiment (black filled circles) and 3D simulations (orange) in the parameter space of imposed magnetic field B_i and inner cylinder angular speed Ω_1. The red circle indicates 0.5% of B_i. Blue crosses (stable) and dots (unstable) show predictions from the global linear analysis. B_0 is Lehnert number defined as $(B_i/\sqrt{\mu_0\rho})/(r_1\Omega_1)$.

appears in the expected place in the parameter space of imposed field (not too weak nor too strong) and inner cylinder speed (only above a threshold value). This was only after more than 20 years of effort working out many important details (Ji and Goodman, 2023). Currently the nonlinear consequences of transporting angular momentum in the radially outward direction and the detailed bifurcation physics are being studied. The experimental confirmation places MRI on firm ground as it is being used widely in astrophysical modeling, with some of them being directly compared with observations, such as Event Horizon Telescope.

Additional effects beyond ideal MHD become important. In protoplanetary accretion disks, Hall effects and ambipolar diffusion effects (due to neutral particles) can be dominant. In these cases, MHD models that includes Hall effects or neutral particle fluid must be used. In accretion disks around black holes or neutron stars, special and general relativity become important requiring the MHD models to include those effects when appropriate. In these hot plasmas, kinetic effects can be important. Yet, there are no particular fluid models that can model kinetic effects in these plasmas. In Lecture 1, some of these MHD models have been mentioned briefly.

9.6 Summary

- Kelvin-Helmholtz Instability, caused by flow shear, can be stabilized by a parallel magnetic field.
- Orr-Sommerfeld equation governs the linear stability of the general sheared flow.
- Squire's theorem is a powerful tool to reduce 3D and 3-component perturbation analysis to 2D and 2-component analysis.

- Rayleigh's inflection point criterion and Fjørtoft's theorem can provide easy-to-use guidance on the linear stabilityof a flow.
- Both viscosity and nonlinear effects can either be stabilizing or destabilizing.
  - Nonlinear or subcritical transition to turbulence in pipe flows.
- Taylor-Proudman theorem and inertial waves in rapidly rotating flows.
- Centrifugal instability and Taylor-Couette flow.
- Accretion disk stability problem and its nonlinear stability.
- MRI is supposed to work universally in accretion disks but has only been confirmed recently in the lab.
- Applying magnetic field to a sheared flow can lead to four possibilities: (1) do nothing, (2) generate unsteady magnetic field which is eventually saturated by finite resistivity as in Hartmann flow, (3) stabilize shear flow instability as in Kelvin-Helmholtz instability, (4) destabilize otherwise stable flow as in MRI.

9.7 Further Readings

- Chapters 11 and 13 in Kundu et al (2015)
- Chapter 7 in Kulsrud (2005)
- Review paper by Ji and Goodman (2023)

9.8 Homework Problem Set 9

1. Solution symmetry for inviscid Orr-Sommerfeld equation (or the Rayleigh equation) for the base state of $\underline{V} = [U(y), 0, 0]$.
   (a) Show that the y component of the perturbation velocity, $v = v(y)\exp[ik(x - ct)]$ satisfies

$$(U - c)\left(v_{yy} - k^2 v\right) - U_{yy} v = 0. \tag{566}$$

   (b) Show that if c is an eigenvalue of Eq.(566) under proper boundary conditions, then so is the conjugate $c^* = c_r - ic_r$. What aspect of Eq.(566) allows this results to be valid?
   (c) Let $U(y)$ be antisymmetric, so that $U(y) = -U(-y)$. Demonstrate that if $c(k)$ is an eigenvalue, then $-c(k)$ is also an eigenvalue. Explain the result physically in terms of the possible directions of propagation of perturbations in such an antisymmetric flow.
   (d) Let $U(y)$ be symmetric, so that $U(y) = U(-y)$. Show that in this case v is either symmetric (aka sausage instability) or antisymmetric (aka kink or sinuous instability) about $y = 0$.

2. Magnetocoriolis waves.
   (a) Use the plane wave approximation to derive the dispersion relation for fast and slow magnetocoriolis waves.

(b) Show that it recovers inertial waves when the magnetic field vanishes and recovers Alfvén waves when there is no rotation.
(c) Discuss wave properties and the meanings of "fast" and "slow" in the limit of
  (i) weak magnetic field
  (ii) slow rotation

3. Maximum growth rate of magnetorotational instability (MRI).
Suppose that the base state is given by $\boldsymbol{B} = (0, 0, B)$ and $\boldsymbol{V} = (0, r\Omega(r), 0)$. Perturb only B_r, B_θ, V_r, and V_θ in the form proportional to $\exp(\gamma t - ikz)$.
(a) Invoke the thin disk approximation ($k \gg 1/r$) to show that the perturbation is incompressible. Verify that the perturbed field satisfies $\nabla \cdot \boldsymbol{B} = 0$.
(b) Derive the linearized equations from the induction equation and equation of motion in the thin disk limit:

$$\gamma B_r = -ikV_r B \tag{567}$$

$$\gamma B_\theta = -ikV_\theta B + \frac{d\Omega}{d\ln r} B_r \tag{568}$$

$$\gamma V_r - 2\Omega V_\theta = -i\frac{kB}{\mu_0 \rho} B_r \tag{569}$$

$$\gamma V_\theta + \frac{\kappa^2}{2\Omega} V_r = -i\frac{kB}{\mu_0 \rho} B_\theta \tag{570}$$

where $\kappa^2 = (1/r^3) d(r^4\Omega^2)/dr$ and ρ is mass density.
(c) Prove that the dispersion relation is given by

$$\gamma^4 + \left(\kappa^2 + 2(kV_A)^2\right)\gamma^2 + (kV_A)^2\left((kV_A)^2 + \frac{d\Omega^2}{d\ln r}\right) = 0 \tag{571}$$

where $V_A = B/\sqrt{\mu_0 \rho}$.
(d) MRI exists only when $d\Omega^2/d\ln r < 0$, but it can be stabilized by a strong B or V_A. What is the minimum V_A to stabilize MRI?
(e) Prove that the maximum growth rate is given by

$$\gamma_{max} = \frac{1}{2}\left|\frac{d\Omega}{d\ln r}\right| \tag{572}$$

when

$$(kV_A)^2 = -\left(\frac{1}{4} + \frac{\kappa^2}{16\Omega^2}\right)\frac{d\Omega^2}{d\ln r}. \tag{573}$$

What is the maximum growth rate for Keplerian flows?

4. (Bonus problem) Stability of magnetized shear flow.

(a) On page 4 of this lecture notes, there is a sentence that says "No effects are expected if the uniform field is in the y direction." This sentence refers to the case shown in Fig. 57 where the flow is in the x direction and sheared in the z direction with a magnetic field imposed in the y direction. Is this sentence correct? Why?

(b) However, this statement seems to contradict the MRI case with the flow in the θ (x) direction, shear in the r (z) direction, and magnetic field in the z (y) direction. The directions in parentheses are the corresponding directions shown in Fig. 57. Compare the two cases regarding their MHD stability. (Hint: refer to Balbus et al (1996).)

10 Tearing Instability and Magnetic Reconnection

In previous lectures, we have discussed various ideal instabilities in dissipationless fluids and plasmas. They are driven by free energies in magnetic field, plasma pressure, and flow shear. When multiple free energies exist simultaneously, the combined effects from them sometimes can lead to interesting, even surprising, outcomes. Pressure driven interchange instabilities can be stabilized by a magnetic shear which contains magnetic free energy, as quantified by Suydam criterion. Similarly, a large pressure gradient can lead to second stability to ballooning instability via increased magnetic shear generated by large diamagnetic current. Sheared flow, which can be unstable by itself, can stabilize current-driven instabilities (e.g. Shumlak and Hartman, 1995) or pressure-driven instabilities (e.g. Biglari et al, 1990). Magnetic field can certainly stabilize flow shear driven instabilities, as in Kelvin-Helmholtz instabilities, but can also destabilize otherwise stable shear flow without magnetic field, as in MRI. There might be more interesting combinations that are still waiting to be explored.

However, there exist another important player in deciding stability of a particular system: finite dissipation. In Lecture 9, we briefly discussed effects of finite viscosity which can be stabilizing or destabilizing, depending on the modification that its existence brings to the overall energetics of linear perturbation. A similar situation exists for finite resistivity, or dissipation in magnetic field in general. We begin this lecture by discussing resistive tearing instability, followed by magnetic reconnection to which tearing instability eventually leads, and has wide applications to space, solar, and astrophysical plasmas as well as fusion plasmas.

10.1 Resistive Tearing Instability

Finite resistivity can destabilize plasmas which are otherwise stable to all ideal MHD instabilities by "tearing" or breaking and reconnecting its magnetic field, which is unallowed in ideal MHD. This class of instabilities are called resistive tearing instabilities (Furth et al, 1963). We begin this topic by discussing ideal

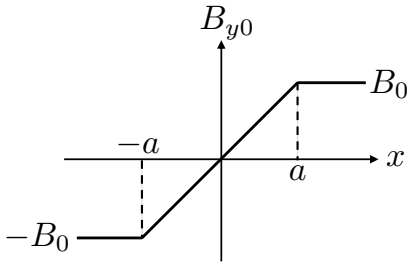

Fig. 71 Equilibrium magnetic field profile for tearing instability analysis.

MHD *stability* of an infinitely long current sheet, followed by the resisitive effects that can lead to an instability.

10.1.1 Ideal MHD Stability of an Infinitely Long Current Sheet

Consider a magnetostatic equilibrium given by

$$\boldsymbol{B}_0 = [0, B_{y0}(x), B_{z0}(x)], \tag{574}$$

where $B_{y0}(x)$ is shown in Fig. 71, reversing its magnitude from $-B_0$ to B_0 across $x = 0$ linearly within $|x| < a$. This corresponds to a constant current density of $j_{z0} = B_0/a\mu_0$ in the z direction over $|x| < a$. The exact profile of $B_{z0}(x)$ is unimportant as it does not enter the tearing mode analysis explicitly, but its strength, combined with plasma pressure profile $p(x)$, enters the force balance in the x direction. In either case, tearing instability occurs at resonant surfaces where the wavenumber vector $\boldsymbol{k}$ is perpendicular to the local magnetic field so that $\boldsymbol{k}\cdot\boldsymbol{B} = 0$ to minimize the energy increase due to field-line bending as in interchange instability. At resonant surface $x = 0$ where $B_{y0} = 0$, the wavenumber vector takes the form of $\boldsymbol{k} = (0, k, 0)$ so that all perturbations (B_x, B_y, V_x, V_y) can be assumed to be proportional to

$$e^{i(ky-\omega t)}$$

where ω is complex frequency. For simplicity, we consider the case of $B_{z0} = 0$, as well as incompressible perturbations with uniform density ρ as we typically do when analyzing ideal MHD stability.

Since magnetic curvature vector $\boldsymbol{\kappa}$ and parallel current $j_\parallel$ are zero, this system is obviously stable to ideal MHD perturbations as all the terms of the energy integral [Eq. (6) in Lecture 7] are either zero or positive definite. However, it is still insightful to show the ideal MHD stability more explicitly as the following.

The first-order, incompressible ideal MHD equations for $\boldsymbol{B}_1 = (B_x, B_y, 0)$ and $\boldsymbol{V}_1 = (V_x, V_y, 0)$ are given by

$$\frac{\partial \boldsymbol{B}_1}{\partial t} = \boldsymbol{\nabla}\times(\boldsymbol{V}_1\times\boldsymbol{B}_0) = (\boldsymbol{B}_0\cdot\boldsymbol{\nabla})\,\boldsymbol{V}_1 - (\boldsymbol{V}_1\cdot\boldsymbol{\nabla})\,\boldsymbol{B}_0, \tag{575}$$

$$\rho\frac{\partial \boldsymbol{V}_1}{\partial t} = \frac{1}{\mu_0}\left[(\boldsymbol{B}_0\cdot\boldsymbol{\nabla})\,\boldsymbol{B}_1 + (\boldsymbol{B}_1\cdot\boldsymbol{\nabla})\,\boldsymbol{B}_0\right] - \boldsymbol{\nabla}\left(p_1 + \frac{B_{y0}B_y}{\mu_0}\right), \tag{576}$$

$$\boldsymbol{\nabla}\cdot\boldsymbol{B}_1 = 0, \tag{577}$$

$$\boldsymbol{\nabla}\cdot\boldsymbol{V}_1 = 0. \tag{578}$$

From the x-component of the induction equation Eq. (575), B_x can be expressed by V_x,

$$B_x = -\frac{k}{\omega}B_{y0}V_x. \tag{579}$$

Combined with Eqs. (577) and (578), we can also express B_y and V_y in terms of V_x, respectively,

$$B_y = \frac{i}{k} B_x' = -\frac{i}{\omega} \left(B_{y0} V_x\right)' \tag{580}$$

$$V_y = \frac{i}{k} V_x', \tag{581}$$

where prime denotes derivative with respect to x. Therefore, Eq. (576) can be expressed in term of V_x alone, in addition to the existing p_1, which however can be removed by taking curl of the equation to yield

$$\rho \frac{\partial \left(\boldsymbol{\nabla} \times \boldsymbol{V}_1\right)}{\partial t} = \frac{1}{\mu_0} \boldsymbol{\nabla} \times \left[\left(\boldsymbol{B}_0 \cdot \boldsymbol{\nabla}\right) \boldsymbol{B}_1 + \left(\boldsymbol{B}_1 \cdot \boldsymbol{\nabla}\right) \boldsymbol{B}_0\right] \equiv \frac{1}{\mu_0} \boldsymbol{\nabla} \times \boldsymbol{A}. \tag{582}$$

Here the vector $\boldsymbol{A}$ is given by

$$A_x = ikB_{y0} B_x = -i \frac{k^2}{\omega} B_{y0}^2 V_x$$

$$A_y = ikB_{y0} B_y + B_{y0}' B_x = \frac{k}{\omega} B_{y0}^2 V_x'.$$

The z-component of Eq. (582) then reads

$$-i\mu_0 \rho\omega \left(V_y' - ikV_x\right) = A_y' - ikA_x \tag{583}$$

which simplifies to

$$\mu_0 \rho \frac{\omega}{k} \left(V_x'' - k^2 V_x\right) = \frac{k}{\omega} \left[\left(B_{y0}^2 V_x'\right)' - k^2 B_{y0}^2 V_x\right] \tag{584}$$

or

$$\left[\left(\mu_0 \rho\omega^2 - k^2 B_{y0}^2\right) V_x'\right]' - k^2 \left(\mu_0 \rho\omega^2 - k^2 B_{y0}^2\right) V_x = 0.$$

To obtain the energy equation for V_x, multiply the above equation with V_x^* and integrate it over x from $-\infty$ to ∞. Integrating by part, the first term becomes

$$\begin{aligned}
&\int_{-\infty}^{\infty} V_x^* \left[\left(\mu_0 \rho\omega^2 - k^2 B_{y0}^2\right) V_x'\right]' dx \\
&= V_x^* \left(\mu_0 \rho\omega^2 - k^2 B_{y0}^2\right) V_x' \Big|_{-\infty}^{\infty} - \int_{-\infty}^{\infty} V_x^{*\prime} \left(\mu_0 \rho\omega^2 - k^2 B_{y0}^2\right) V_x' dx \\
&= -\int_{-\infty}^{\infty} \left(\mu_0 \rho\omega^2 - k^2 B_{y0}^2\right) \left|V_x'\right|^2 dx.
\end{aligned} \tag{585}$$

Therefore, we have the energy equation for V_x,

$$\int_{-\infty}^{\infty} \left(\mu_0 \rho\omega^2 - k^2 B_{y0}^2\right) \left(\left|V_x'\right|^2 + k^2 \left|V_x\right|^2\right) dx = 0, \tag{586}$$

which demands ω^2 be real, and thus ω be either real or pure imaginary. When ω is pure imaginary, $\omega = i\gamma$ and $\omega^2 = -\gamma^2$, and the left hand side of Eq. (586) would be negative definite, and thus, such solutions cannot satisfy Eq. (586) with a finite amplitude. Therefore, possible solutions for ω need to be real, corresponding to stable oscillations due to shear Alfvén waves, $V_{\rm ph}^2 = (\omega/k)^2 = B_{y0}^2/\mu_0\rho$, as discussed in Lecture 3. However, the situation here is more similar to the continuous Alfvén wave damping when $V_{\rm ph}^2 \neq B_{y0}^2/\mu_0\rho$ anywhere in the plasma or the resonance absorption of Alfvén wave when $V_{\rm ph}^2 = B_{y0}^2/\mu_0\rho$ at somewhere in the plasma, as discussed in Lecture 8. In any cases, the plasma is stable to all ideal MHD instabilities.

10.1.2 Resistive Inner Layer and Tearing Instability

However, the ideal MHD models are not necessarily a good approximation everywhere even resistivity is small or Lundquist number, $S \to \infty$. The resistive effects can be important at locations such as thin "boundary layers", which can be internal to plasma in this case (and thus sometime called "internal layers" or "inner layers"), similar to the thin shock layers where dissipation is important as discussed in Lecture 4. When resistivity dominates, these layers are often called resistive layers sandwiched by ideal regions.

Existence of such resistive inner layers in the above system is self-evident by examining inductive equation, Eq. (575), but with the resistive diffusion term included. Instead of Eq. (579), its x-component is given by

$$\omega B_x \approx -kB_{y0}V_x + i\frac{\eta}{\mu_0}B_x'', \tag{587}$$

where magnetic diffusion is taken to be dominated by the gradient in the x-direction. Regardless how small the resistivity is, the resistive term eventually dominates the ideal term when sufficiently close to $x = 0$ since $B_{y0} = (B_0/a)x$. Note that adding the diffusion term in Eq. (587) introduces a phase shift between B_x and V_x, which is absent in Eq. (579). So if we treat B_x real, V_x will need to be complex.

As in the case of shock waves, the jump condition for magnetic field, $[\boldsymbol{B}\cdot\boldsymbol{n}] = 0$ ($\boldsymbol{n}$ is normal unit vector to the layer), or $[B_x] = 0$. This means that B_x needs to be continuous across $x = 0$ but does not need to vanish. A non-vanishing B_x across $x = 0$ connects field lines between two ideal regions outside of the resistive inner layer, breaking or "tearing" the frozen-in magnetic field in ideal MHD plasmas, as expected from the finite resitivity despite its smallness. Thus, such instabilities are termed "resistive tearing instability" (Furth et al, 1963).

In contrast to the normal magnetic component B_x, there are no jump conditions for the tangential component B_y to satisfy. In fact, the jump in B_y or $[B_y]$, corresponding to first-order current in the z direction $\mu_0 j_z = [B_y]$, can remain finite with either signs. According to Eq. (580), $[B_y] \propto [B_x']$ and

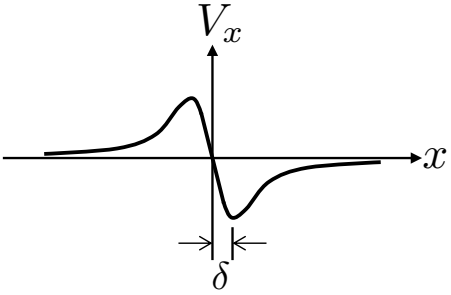

Fig. 72 Illustration of the V_x solution which peaks at $x = \delta$.

we can define a new parameter Δ' across $x = 0$,

$$\Delta' \equiv \frac{[B_x']}{B_x}, \tag{588}$$

whose sign determines the stability of resistive tearing mode and can be calculated by integrating field structures in ideal regimes, as shall shown below. In short, B_x needs to be continuous across $x = 0$, but not B_x', which in term determines resistive tearing stability.

It is attempting to estimate the inner layer thickness δ by simply equating the left-hand side of Eq. (587) with the diffusion term on its right-hand side, but it is not as straightforward as V_x is expected to accelerate towards the inner layer where effective diffusion of B_{y0} occurs. In other words, the two terms on the right-hand side of Eq. (587) are roughly in balance resulting in a slow growth (or in the so-called small-Δ' regime; see below). The equation for V_x in the inner layer can be derived from Eq. (583) with the y-derivatives (the terms containing k) ignored since the x-derivative terms dominate in the inner layer,

$$\mu_0 \rho \frac{\omega}{k} V_x'' \approx A_y', \tag{589}$$

where Eq. (581) is used as before, but A_y' needs to be evaluated to include resistive effects,

$$\begin{aligned} A_y &= ikB_{y0}B_y + B_{y0}'B_x = -B_{y0}B_x' + B_{y0}'B_x \\ A_y' &= -B_{y0}B_x'' + B_{y0}''B_x = -B_{y0}B_x'' \\ &= i\frac{\mu_0}{\eta} B_{y0}\left(kB_{y0}V_x + \omega B_x\right) \end{aligned} \tag{590}$$

where $B_{y0}'' = 0$ since $B_{y0} = B_0(x/a)$ and also $B_{y0} \propto x$ in general in the inner layer. In the above equation, B_x'' is substituted using Eq. (587). By defining

$\omega = i\gamma$, therefore, we have

$$\gamma\eta\rho V_x'' = kB_{y0}(kB_{y0}V_x + i\gamma B_x). \tag{591}$$

As implied by $[B_x] = 0$, we can take B_x as a constant within the inner layer. This is often called constant-ψ (flux) approximation (Furth et al, 1963). In this case, we can observe the following several important characteristics of Eq. (591):

- Away from the inner layer, $V_x'' \to 0$, so V_x should decrease as $V_x \approx -i\gamma B_x/(kB_{y0}) \propto 1/x$.
- Solution V_x is odd in x, since V_x needs to flip its sign when x flips its sign.
- Further more by symmetry, $V_x(0) = 0$, leading to a sketch of the solution illustrated in Fig. 72, and thus, V_x must peak at some distance $x = \delta$.
- Δ', which is determined by the outer ideal regions, needs to be matched to the inner layer solution through integrating Eq. (587) across the layer,

$$\Delta' = \frac{[B_x']}{B_x} = \frac{\mu_0}{i\eta}\int\left(i\gamma + \frac{B_0}{B_x}\frac{x}{a}kV_x\right)dx, \tag{592}$$

where $V_x(x)$ is determined by Eq. (591).

Now, we are ready to estimate δ as the inner layer thickness by balancing the left-hand side of Eq. (591) with the first term of its right-hand side [which is equivalent to balance the two terms on the right-hand side of Eq. (587)],

$$\gamma\eta\rho\frac{V_x}{\delta^2} \simeq k^2B_{y0}^2(\delta)V_x = k^2B_0^2\frac{\delta^2}{a^2}V_x.$$

This leads to

$$\frac{\delta}{a} \simeq \sqrt[4]{\frac{\gamma\eta\rho}{(ka)^2B_0^2}}, \tag{593}$$

showing that δ increases with η as expected but only very slowly. Using δ, we can introduce normalized variables,

$$X = \frac{x}{\delta}$$
$$U = \left(\frac{\delta}{a}\right)\left(\frac{B_0}{B_x}\right)\left(\frac{V_x}{i\gamma/k}\right)$$

to rewrite Eq. (591) into

$$U'' = X\,(1 + XU) \tag{594}$$

where $'$ denotes derivative with respect to X. Using X and U, Δ' is given by

$$\Delta' = \mu_0\sqrt[4]{\frac{\gamma^5\rho a^2}{\eta^3k^2B_0^2}}\int_{-\infty}^{\infty}(1 + XU)\,dX \tag{595}$$

where the integration part gives $\simeq 2.12$ using the corresponding solution of Eq. (594) (Goldston and Rutherford, 1995, Ch. 20). Therefore, positive values of Δ' correspond to instabilities that are otherwise absent without a finite resistivity, as termed *resistive teating instabilities*. The growth rate can be calculated by rewriting the above equation,

$$\gamma = 0.55 \sqrt[5]{\frac{\Delta'^4 \eta^3 k^2 B_0^2}{\rho a^2 \mu_0^4}} = 0.55 \frac{(\Delta' a)^{4/5} (ka)^{2/5}}{\tau_{\rm A}^{2/5} \tau_{\rm R}^{3/5}}, \tag{596}$$

where Alfvén transit time $\tau_{\rm A}$ and resistive diffusion time $\tau_{\rm R}$ of the current sheet are defined,

$$\tau_{\rm A} \equiv \frac{a}{V_{\rm A}} \quad \text{and} \quad \tau_{\rm R} \equiv \frac{\mu_0 a^2}{\eta}, \tag{597}$$

respectively. Accordingly, the inner layer thickness δ scales as

$$\frac{\delta}{a} = 0.86 \left(\frac{\Delta' a}{k^2 a^2}\right)^{1/5} \left(\frac{\tau_{\rm A}}{\tau_{\rm R}}\right)^{2/5} = 0.86 \left(\frac{\Delta' a}{k^2 a^2}\right)^{1/5} \frac{1}{S^{2/5}}. \tag{598}$$

Here Lundquist number S is defined as ratio of $\tau_{\rm R}$ to $\tau_{\rm A}$. The hallmark of resistive tearing instabilities is that their growth rate is much slower than that of ideal MHD instabilities ($\propto \tau_{\rm A}^{-1}$) but much faster than the resistive diffusion ($\propto \tau_{\rm R}^{-1}$).

10.1.3 Calculation of Δ'

As we have seen, the tearing instability growth rate is determined by Δ' which is in term determined by the properties of the outer ideal region of the plasma. More specifically, Δ' can be calculated by using the z-component of vorticity equation, Eq. (584), but expressed in magnetic field B_x rather than velocity V_x,

$$\mu_0 \rho \left(\frac{\omega}{k}\right)^2 \left[\left(\frac{B_x}{B_{y0}}\right)'' - k^2 \frac{B_x}{B_{y0}}\right] = \left[B_{y0}^2 \left(\frac{B_x}{B_{y0}}\right)'\right]' - k^2 B_{y0} B_x. \tag{599}$$

Equation (599) above can be solved with proper boundary conditions for B_x to calculate Δ', since B_{y0} is given. Since the tearing instability growth rate, $\omega = i\gamma$, is much slower than the ideal MHD timescale, the inertial terms on the left-hand side of Eq. (599) can be ignored. This is also regarded as the small-Δ' approximation (Furth et al, 1963). In this case, Eq. (599) becomes simply

$$\left[B_{y0}^2 \left(\frac{B_x}{B_{y0}}\right)'\right]' - k^2 B_{y0} B_x = 0, \tag{600}$$

which can be solved for the configuration given in Fig. 71. For $x > a$, $B_{y0} = B_0$ is a constant, and for $0 < x < a$, $B_{y0} = B_0(x/a)$, and in both cases, Eq. (600)

becomes simply

$$B_x'' = k^2 B_x. \tag{601}$$

The solution for $x > 0$ is given by

$$B_x = \begin{cases} Ae^{kx} + Be^{-kx} & \text{for } 0 < x < a \\ Ce^{-kx} & \text{for } a < x \end{cases} \tag{602}$$

where A, B and C are related via matching the solution at $x = a$

$$\begin{aligned} [B_x]_{x=a} &= 0 \\ \left[\left(\frac{B_x}{B_{y0}}\right)'\right]_{x=a} &= 0. \end{aligned}$$

The first condition simply leads to

$$Ae^{ka} + Be^{-ka} = Ce^{-ka}. \tag{603}$$

For $0 < x < a$, we have

$$\begin{aligned} \left(\frac{B_x}{B_{y0}}\right)'\Bigg|_{x=-a} &= \left(\frac{Ae^{kx} + Be^{-kx}}{B_0(x/a)}\right)'\Bigg|_{x=-a} \\ &= \left(\frac{Ake^{kx} - Bke^{-kx}}{B_0(x/a)} - \frac{Ae^{kx} + Be^{-kx}}{B_0(x^2/a)}\right)\Bigg|_{x=-a} \\ &= \frac{A(ka-1)e^{ka} - B(ka+1)e^{-ka}}{B_0 a}, \end{aligned}$$

and for $x > a$, we have

$$\left(\frac{B_x}{B_{y0}}\right)'\Bigg|_{x=+a} = \left(\frac{Ce^{-kx}}{B_0}\right)'\Bigg|_{x=+a} = -\frac{Ckae^{-ka}}{B_0 a}.$$

Equating them yields second relation between A, B and C,

$$A(ka-1)e^{ka} - B(ka+1)e^{-ka} = -Ckae^{-ka}. \tag{604}$$

Multiplying Eq. (603) with $(ka+1)$ and adding it to Eq. (604) relates A to C while multiplying Eq. (603) with $(ka-1)$ and subtracting it from Eq. (604) relates B to C,

$$A = \frac{C}{2ka}e^{-2ka}; \qquad B = \frac{C}{2ka}(2ka-1). \tag{605}$$

By symmetry, the solution for $x < 0$ has the same functional form with x replaced by $-x$ and same coefficients A, B and C. Therefore, we have

$$B_x = \begin{cases} Ae^{kx} + Be^{-kx} & \text{for } 0 < x < a \\ Ae^{-kx} + Be^{kx} & \text{for } -a < x < 0 \end{cases} \tag{606}$$

$$B'_x = \begin{cases} Ake^{kx} - Bke^{-kx} & \text{for } 0 < x < a \\ -Ake^{-kx} + Bke^{kx} & \text{for } -a < x < 0. \end{cases} \tag{607}$$

Using Eq. (605), Δ' can be calculated then as

$$\Delta' a = \frac{a\,[B'_x]_{x=0}}{B_x} = 2ka\frac{A-B}{A+B} = 2ka\frac{e^{-2ka} - 2ka + 1}{e^{-2ka} + 2ka - 1} \tag{608}$$

as shown graphically in Fig. 73 as a function of ka.

When k is sufficiently small, Δ' is positive so resistive tearing modes are unstable. More specifically in the $k \to 0$ limit, $\Delta' a$ increases as $2/(ka)$. Then the growth rate [Eq. (596)] and inner layer thickness [Eq. (598)] become

$$\gamma = 0.55\frac{(\Delta' a)^{4/5}\,(ka)^{2/5}}{\tau_{\rm A}^{2/5}\tau_{\rm R}^{3/5}} = \frac{0.96}{(ka)^{2/5}\,\tau_{\rm A}^{2/5}\tau_{\rm R}^{3/5}}, \tag{609}$$

$$\frac{\delta}{a} = 0.86\left(\frac{\Delta' a}{k^2a^2}\right)^{1/5}\frac{1}{S^{2/5}} = \frac{0.99}{(ka)^{3/5}\,S^{2/5}}, \tag{610}$$

respectively. This can be understood as a competition between magnetic energy increase due to field line bending in the outer ideal regions and magnetic energy decrease due to resistive diffusion in the inner resistive layer. Longer the wavelengths magnetic field lines are bent less, and thus lead to less the

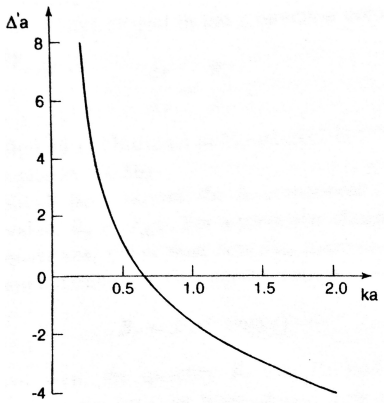

Fig. 73 Δ' as a function of k for the equilibrium shown in Fig. 71 from Goldston and Rutherford (1995).

magnetic energy increase. Resistive tearing instability grows when wavelength is sufficiently long, and grows faster at longer wavelength. The situation is similar to Parker instability (see Lecture 6) which grows only at sufficiently long wavelengths when reduction of gravitational potential energy is larger than magnetic energy increase due to field line bending.

However, there arise two potential issues for the above analysis if k is too small or the wavelengths are too long. First, Δ' diverges as k^{-1} when $k \to 0$, as shown in Fig. 73. The tearing growth rate also increases with Δ', and eventually the assumption of small-Δ' approximation breaks down such that the inertial terms on the left-hand side of Eq. (599) cannot be ignored for the Δ' calculation. This is the so-called large-Δ' regime.

The second potential issue of the $k \to 0$ limit is when the corresponding wavelengths reach to the system scale. On the system scale, however, the 1D equilibrium model shown in Fig. 574 is no longer a good approximation of realistic cases. The magnetic field direction (y direction) needs to be either periodic as in toroidally confined plasmas or line-tied as in solar corona, rather than extends to infinity, while the cross-field direction (x direction) corresponds to the radial direction in the toroidally confined plasmas. For example, $x = 0$ can correspond to the $q = 1$ surface in tokamaks with the central $q(0) < 1$. Thus, the $x < 0$ region in this case refers to the plasma within the $q = 1$ flux surface while the $x > 0$ region refers to the plasma between the $q = 1$ surface and plasma boundary. The ideal MHD stability of such systems can be significantly modified due to periodic or line-tied boundary conditions. In Lecture 7, internal kink instability was discussed for the cylindrical plasmas in which plasma displacement is localized only within the $q = 1$ surface, or equivalently localized only on the $x < 0$ side, breaking the symmetry with respect to $x = 0$. The tearing instability can occur regardless ideal MHD stability. Thus, the ideal MHD instability can couple with or can "drive" resistive tearing instability, as a consequence, the approximations used in the above analysis, including the constant-ψ approximation and small-Δ' approximation, need to be revised. This was done first by Coppi et al (1976) and more discussions can be found in (White, 2014, Ch. 5).

Scaling laws for the tearing instability growth rate, γ, can be derived in this large-Δ' regime without detailed analysis to illustrate the different physics. Consider the case when the plasma only on one side of the current sheet is unstable to ideal MHD instabilities. The unstable displacement or B_x changes sharply across $x = 0$, violating constant-ψ or constant-B_x approximation, and with a large Δ' and growth rate. Thus, the diffusion of non-uniform B_x dominates the right hand side of Eq. (587), leading to the estimate of inner layer thickness δ

$$i\gamma B_x \sim i\frac{\eta}{\mu_0}\frac{B_x}{\delta^2}$$

or

$$\frac{\delta}{a} \sim \frac{1}{(\gamma\tau_R)^{1/2}}. \tag{611}$$

On the other hand, according to Eq. (584) without terms involving k^2 but keeping inertial terms in the large-Δ' approximation, the inner layer thickness δ can be also estimated by

$$\mu_0 \rho \gamma^2 V_x'' \sim k^2 B_0^2 \left(\frac{\delta}{a}\right)^2 V_x''$$

leading to

$$\frac{\delta}{a} \sim \frac{\gamma \tau_{\rm A}}{ka}. \tag{612}$$

Equating Eq. (611) with Eq. (612) yields

$$\gamma \sim \frac{(ka)^{2/3}}{\tau_{\rm A}^{2/3} \tau_{\rm R}^{1/3}} \tag{613}$$

$$\frac{\delta}{a} \sim \frac{1}{(ka)^{1/3}} \left(\frac{\tau_{\rm A}}{\tau_{\rm R}}\right)^{1/3} = \frac{1}{(ka)^{1/3}} \frac{1}{S^{1/3}}, \tag{614}$$

with faster growth rates compared with Eq. (609), as expected, but still hybrid between $\tau_{\rm A}^{-1}$ and $\tau_{\rm R}^{-1}$. Therefore, Eqs. (609) and (613) are the growth rate in the small and large Δ' limits of resistive tearing instability.

10.1.4 Magnetic Island and Nonlinear Evolution

A consequence of resistive tearing instability is to break and rejoin (or reconnect) magnetic field lines by changing its connectivity. This change is topological for the magnetic field lines and can be shown conveniently in 2D by using magnetic field stream function or flux function, $\psi(x, y)$, defined as

$$\boldsymbol{B} = (B_x, B_y) \equiv \boldsymbol{\nabla}\psi \times \boldsymbol{z} = \left(\frac{\partial \psi}{\partial y}, -\frac{\partial \psi}{\partial x}\right) \tag{615}$$

where $\boldsymbol{z}$ is unit vector in the z direction. Since $\boldsymbol{B} \cdot \boldsymbol{\nabla}\psi = 0$, magnetic field lines follow contour lines of ψ. We can write

$$\psi = \psi_0 + \psi_1 \tag{616}$$

where ψ_0 is the equilibrium flux function and ψ_1 is the growing flux function due to resistive tearing instability. Limiting to $|x| < a$ and integrating B_{y0} over x from $x = 0$, ψ_0 is given by

$$\psi_0(x, y) = -\int_0^x B_{y0} dx = -\frac{1}{2}\frac{B_0}{a} x^2,$$

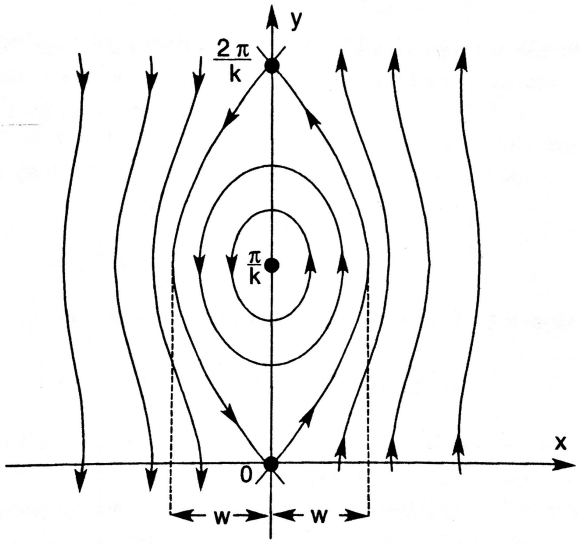

Fig. 74 Magnetic island within the inner layer due to resistive tearing instability from Goldston and Rutherford (1995).

while integrating $B_x = B_{x0}e^{\gamma t}\sin ky$ over y in the constant-ψ case (constant B_{x0}) yields

$$\psi_1(x,y) = \int B_x dy = -\frac{B_{x0}}{k}e^{\gamma t}\cos ky$$

with the integration constant chosen to be zero here. By defining $\bar{\psi}_0 = -(1/2)B_0 a$ and $\bar{\psi}_1 = -(B_{x0}/k)e^{\gamma t}$, the contour plot of

$$\psi(x,y) = \bar{\psi}_0\left(\frac{x}{a}\right)^2 + \bar{\psi}_1\cos ky \tag{617}$$

is shown in Fig. 74 where a *magnetic island* is formed as field lines are broken and rejoined (or reconnected) due to tearing instability. Therefore, *magnetic reconnection* is a natural consequence of tearing instability.

The field lines represented by the flux contours of $\psi = \bar{\psi}_1$ are rather special,

$$\bar{\psi}_0\left(\frac{x}{a}\right)^2 + \bar{\psi}_1(\cos ky - 1) = 0,$$

which has solutions of

$$x = \begin{cases} 0 & \text{when } ky = 0 \text{ or } 2\pi \\ w & \text{when } ky = \pi, \end{cases} \tag{618}$$

where w is width of the magnetic island,

$$\frac{w}{a} = \sqrt{\frac{2\bar{\psi}_1}{\psi_0}} = 2\sqrt{\frac{1}{ka}\frac{B_{x0}}{B_0}}e^{\gamma t/2}. \tag{619}$$

Thus, the $\psi = \bar{\psi}_1$ contours are called *separatrix* defining the edge of the island by separating reconnected field lines from those still unreconnected. For obvious reasons, the points $(x, y) = (0, 0)$ or $(x, y) = (0, 2\pi/k)$ are called X-points or X-lines extending in the z direction and the point $(x, y) = (0, \pi)$ is called O-point or O-line.

The island width grows exponentially as linear tearing instability [see Eq. (619)] and when w reaches the inner layer thickness δ, either based on Eq. (598) or Eq. (614) both of which are thin due to large values of S, the linear treatment described thus far between outer ideal region and inner resistive layer is invalid. When nonlinear forces are taken into account in the small-Δ' regime, slower algebraic growth (as opposed to fast linear exponential growth) of island has been predicted by Rutherford (1973), often referred as *Rutherford Regime*. The nonlinear theory has been extended to the large-Δ' regime by Waelbroeck (1989), who further predicted that this slow growth is followed by a rapid X-point collapse (Waelbroeck, 1993), during which an intense current sheet is formed sustaining quasi-steady magnetic reconnection. The full range of this time evolution from linear, nonlinear, X-point collapse, current sheet reconnection (see below), and eventually island saturation has been studied numerically (Loureiro et al, 2005).

10.2 Magnetic Reconnection

Magnetic reconnection has been an intense subject since 1950s when first quantitative model, called Sweet-Parker model in a current sheet (Sweet, 1958; Parker, 1957), was developed. Magnetic reconnection occurs nearly in all magnetized plasmas across the universe ranging from Earth's magnetosphere, to solar flares, to magnetized neutron stars, as well as in magnetically confined plasmas. Figure 75 illustrates four such examples involving current sheets which are highlighted in blue. A survey of plasmas where reconnection is considered to occur was given by Ji and Daughton (2011).

The realization that magnetic reconnection might be responsible for the efficient release of accumulated magnetic energy began with the observation of solar flares (Giovanelli, 1946). The transiently enhanced emission due to electron temperature increase typically lasts minutes to hours. This is very long compared to the Alfvén transit time $\tau_A = L/V_A \approx 2$ seconds for a magnetic field of 100 Gauss in a plasma of electron density $n = 10^{15}\text{m}^{-3}$ over $L = 10,000$ km. Therefore, solar flares are not an ideal MHD process. On the other hand, the resistive diffusion time is extremely long, $\tau_R = \mu_0 L^2/\eta \approx 10^{14}$ seconds (~ 3 million years!) with coronal electron temperature of $T_e = 100$ eV. Therefore, it is natural to invoke processes like tearing instability or magnetic reconnection to explain solar flares.

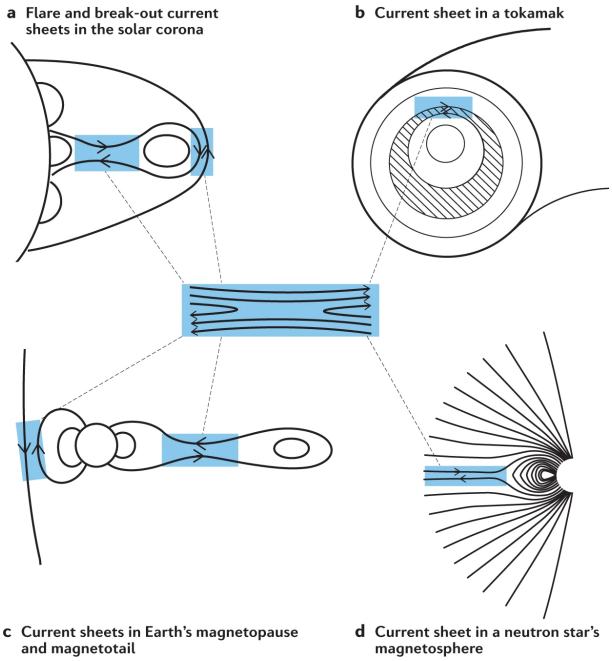

Fig. 75 Examples of magnetic reconnection involving current sheets from Ji et al (2022).

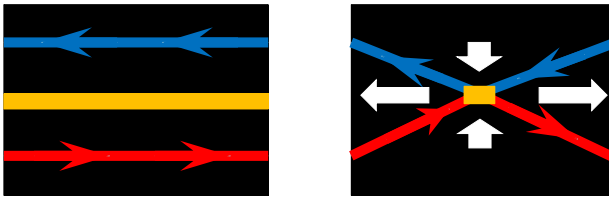

Fig. 76 Left panel: Diffusion of oppositely directed magnetic field lines (blue and red lines) in an infinitely-long, one-dimensional line (orange). Right panel: Diffusion occurs only in a localized spot (orange) in two-dimensional space, associated with inflows and outflows (white arrows).

The efficiency of reconnection in reducing magnetic energy in 2D can be appreciated from Fig. 76. In the one dimensional system shown in the left panel, magnetic energy is reduced only through slow diffusion within an infinitely long diffusion line in orange. In the two dimensional system shown in the right panel, magnetic energy is reduced not only in the diffusion spot in orange but also through generating fast outflows by magnetic tension force after reconnection. This point can be made also by examining the time change rate of magnetic energy in a volume of V,

$$\frac{\partial}{\partial t}\left(\frac{B^2}{2\mu_0}\right) = -\int \boldsymbol{E}\cdot\boldsymbol{J}dV - \int (\boldsymbol{E}\times\boldsymbol{B})\cdot d\boldsymbol{S},$$

where S is the surface of V and $\boldsymbol{E} \times \boldsymbol{B}$ is Poynting vector representing energy flux of an electromagnetic field. The volume change rate is represented by $\boldsymbol{E} \cdot \boldsymbol{J}$ which can be written by using resistive MHD law,

$$\boldsymbol{E} \cdot \boldsymbol{J} = -(\boldsymbol{V} \times \boldsymbol{B}) \cdot \boldsymbol{J} + \eta J^2 = (\boldsymbol{J} \times \boldsymbol{B}) \cdot \boldsymbol{V} + \eta J^2$$

where the second term on the right-hand side denotes resistive dissipation of magnetic energy. The first term of the right-hand side, however, represents the change in magnetic energy due to the work done by magnetic field on plasmas. In one dimension where only magnetic diffusion is possible, the primary way to reduce magnetic energy is via resistive dissipation while in two dimensions where magnetic reconnection becomes possible, the primary way to reduce magnetic energy is via the work done by magnetic field on plasma by generating fast flows.

Following Ji et al (2022), magnetic reconnection is described below in three stages of its research, each focusing on a particular aspect of magnetic reconnection: MHD, kinetic, and multiple-scale.

10.2.1 Reconnection in Collisional MHD Plasmas

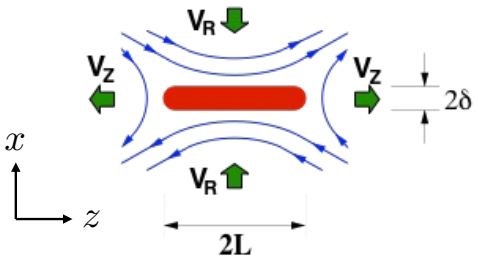

Fig. 77 Sweet-Parker model of magnetic reconnection.

The Stage 1 of magnetic reconnection research from its outset in 1950s until 1990s was primarily motivated by solar flare observation and was based on MHD models. The MHD description is justified for the solar atmospheric plasma due to its large size even it is thin and hot with long mean free paths, see Lecture 1. A leading theory based on a two-dimensional current sheet was developed by Peter Sweet (Sweet, 1958) and Gene Parker (Parker, 1957), illustrated in Fig. 77 where the X-line is located at $(x, z) = (0, 0)$. The reconnecting field component, B_z, reverses its direction across a current sheet (in red) with a length of $2L$ in the z direction and a width of 2δ in the x direction. Magnetic field lines move along the x direction into the current sheet from upstream with an inflow speed of V_R, get reconnected within the current sheet, and then move along the z direction away from the current sheet towards downstream

with an outflow speed of V_z. For symmetric reconnection where mirror symmetry applies between two upstreams and also two downstreams, the X-line is the stagnation point of plasma flow in and out of the current sheet.

The other assumptions used in Sweet-Parker model are: (1) reconnection is in a steady state, *i.e.* all time derivatives are ignored; (2) plasma is incompressible; and (3) plasma has the classical Spitzer resistivity, $\eta_{\rm Spitzer}$. Note that the guide field, the magnetic field component along the electric current, B_y, does not enter the Sweet-Parker analysis described below.

The induction equation reads

$$\frac{\partial \boldsymbol{B}}{\partial t} = \boldsymbol{\nabla} \times (\boldsymbol{V} \times \boldsymbol{B}) + \frac{\eta_{\rm Spitzer}}{\mu_0} \nabla^2 \boldsymbol{B}$$

where in steady state the left-hand side vanishes. Balancing the two terms on the right-hand side with the recognition that the dominant gradient is in the x direction,

$$\frac{V_R B_z}{\delta} \approx \frac{\eta_{\rm Spitzer}}{\mu_0} \frac{B_z}{\delta^2},$$

leading to an equation for the reconnection inflow V_R

$$V_R \approx \frac{\eta_{\rm Spitzer}}{\mu_0 \delta}. \tag{620}$$

This relation can be understood as magnetic field diffuses more rapidly with thinner current sheet δ resulting in faster reconnection inflow V_R.

The continuity equation for plasma mass density ρ,

$$\frac{\partial \rho}{\partial t} + \boldsymbol{\nabla} \cdot (\rho \boldsymbol{V}) = 0,$$

reduces in the steady state ($\partial \rho / \partial t = 0$) with incompressibilility (spatially uniform ρ) to

$$\rho V_R L \approx \rho V_z \delta$$

or

$$V_R \approx \frac{\delta}{L} V_z. \tag{621}$$

This relation can be understood as reconnection proceeds faster with thicker current sheet δ as plasma can flow through the current sheet more rapidly.

Notice that the opposite dependence of V_R on δ between Eqs. (620) and (621). As a compromise, multiplying these two equations to eliminate δ in favor of inflow V_R yields

$$V_R^2 = \frac{\eta_{\rm Spitzer}}{\mu_0 L} V_z,$$

which leads to

$$\frac{V_R}{V_Z} = \frac{\delta}{L} = \sqrt{\frac{\eta_{\rm Spitzer}}{\mu_0 L V_z}}. \tag{622}$$

In order to determine the outflow V_Z, the equation of motion,

$$\rho\left[\frac{\partial}{\partial t}+(\boldsymbol{V}\cdot\boldsymbol{\nabla})\,\boldsymbol{V}\right]=\boldsymbol{j}\times\boldsymbol{B}-\boldsymbol{\nabla}p, \tag{623}$$

needs to be applied along the symmetry lines of $z=0$ and $x=0$. Integrating Eq. (623) along $z=0$ from upstream to the flow stagnation point of $(0,0)$ yields

$$p_{\rm up}+\frac{1}{2}\rho V_R^2+\frac{B_z^2}{2\mu_0}\approx p_0 \tag{624}$$

where $p_{\rm up}$ and p_0 are plasma pressure at upstream and at X-line, respectively. The magnetic tension force is ignored here due to large magnetic curvature of reconnecting field line moving towards the current sheet. Furthermore, the second term representing dynamic pressure of inflow speed, $(1/2)\rho V_R^2$, is small compared with the upstream magnetic pressure (third term). Integration from the stagnation point towards the downstream yields

$$p_0\approx p_{\rm down}+\frac{1}{2}\rho V_z^2 \tag{625}$$

where both magnetic pressure term and magnetic tension term are ignored due to smallness of the reconnected field component, B_x, compared to B_z. $p_{\rm down}$ is plasma pressure at downstream. Combining Eqs. (624) and (625) leads to

$$p_{\rm up}+\frac{B_z^2}{2\mu_0}\approx p_{\rm down}+\frac{1}{2}\rho V_z^2$$

which is simply

$$V_z\approx V_{\rm A} \tag{626}$$

if $p_{\rm up}=p_{\rm down}$ and the Alfvén speed is defined as $V_{\rm A}\equiv B_z/\sqrt{\mu_0\rho}$. According to Eq. (622), therefore, the normalized reconnection inflow speed or reconnection rate, as well as the current sheet thinkness, is given by

$$\frac{V_R}{V_{\rm A}}=\frac{\delta}{L}=\sqrt{\frac{\eta_{\rm Spitzer}}{\mu_0 L V_{\rm A}}}=\frac{1}{\sqrt{S}},\qquad S\equiv\frac{\mu_0 L V_{\rm A}}{\eta_{\rm Spitzer}}=\frac{\tau_{\rm R}}{\tau_{\rm A}} \tag{627}$$

where S is the usual Lundquist number. Then the predicted reconnection time $\tau_{\rm rec}$ by Sweet-Parker model is given by

$$\tau_{\rm rec}\equiv\frac{L}{V_R}=\frac{L}{V_{\rm A}}\frac{V_{\rm A}}{V_R}=\tau_{\rm A}\sqrt{S}=\tau_{\rm A}\sqrt{\frac{\tau_{\rm R}}{\tau_{\rm A}}}=\sqrt{\tau_{\rm R}\tau_{\rm A}}. \tag{628}$$

In other words, the reconnection time is simply the geometric mean of resistive time and Alfvénic time. Such an elegant prediction, unfortunately, does not explain the observed solar flare time. Using the numbers used above, $\tau_{\rm A}$=2

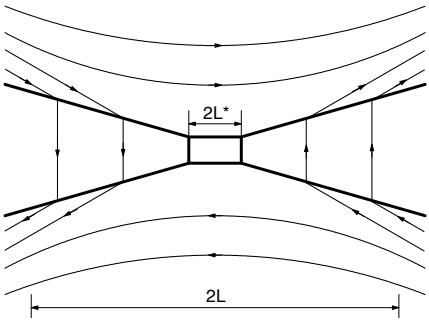

Fig. 78 Petschek model of magnetic reconnection.

seconds and $\tau_{\rm R} = 10^{14}$ seconds, $\tau_{\rm rec}$ is predicted to be $\sim 10^7$ which is still much longer than the typical observation of $10^2 - 10^3$ seconds.

Subsequently therefore, finding faster reconnection mechanisms than Sweet-Parker model has been a primary objective of magnetic reconnection research. Since the steady state reconnection rate is determined by the current sheet geometry [see Eq. (621)], the slow reconnection is due to the bottleneck requirement that all plasma needs to pass through a narrow and long current sheet in Sweet-Parker model, which takes L as the system size. Thus, there exist only two ways to accelerate reconnection process: thicker current sheet (larger δ) or shorter current current (smaller L). However, larger δ slows down magnetic diffusion at the X-line [see Eq. (620)] which is required for magnetic reconnection. Petschek (1964) instead proposed to shorten the current sheet from L to L^* as shown in Fig. 78 to accelerate reconnection. Shorter the L^* faster the rate, but there should be some practical limits in minimizing L^* since a short L^* would significantly distort upstream magnetic field. For example, as an extreme case when L^* is as short as δ, the symmetry between upstream and downstream is essentially restored, resembling the X-line area in vacuum without electric current and thus no dissipation of magnetic field energy. Therefore, L^* should be much shorter than L so that magnetic reconnection is fast while L^* should be much longer than δ to effective dissipate magnetic energy. Petschek derived a minimum L^* to preserve a certain level of upstream-downstream asymmetry while without significantly distorting the upstream magnetic field. Nonetheless, two pairs of shock structures along the separatrices are needed to be introduced to join the distorted or stressed field geometry due to the shortened current sheet. The plasma existing at end of the current sheet $L*$ enters a flow channel which opens up towards downstream, avoiding the bottleneck effect. The corresponding maximum reconnecton rate to the minimum L^* was predicted to be

$$\frac{V_R}{V_{\rm A}} \sim \frac{1}{\ln S}, \tag{629}$$

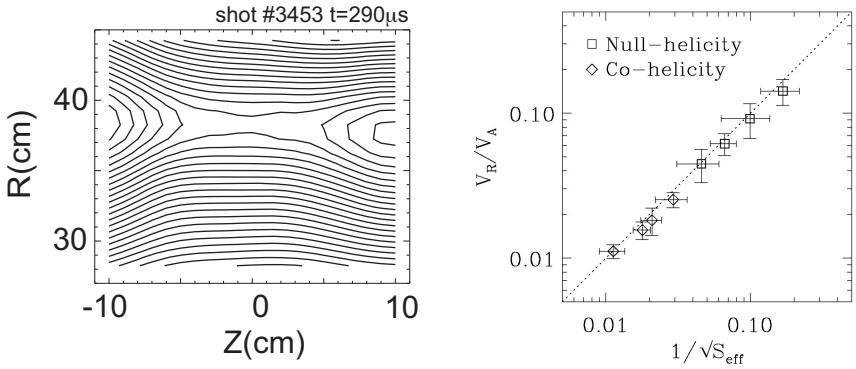

Fig. 79 Experimental confirmation of Sweet-Parker model on Magnetic Reconnection Experiment (MRX: (left panel) measured magnetic structure around diffusion region and (right panel) measured reconnection rate versus model prediction. Here $S_{\rm eff}$ is defined to take into account other effects beyond the standard assumptions mentioned above. From Ji et al (1998).

which is much closer to the observed reconnection rates. As a further result, not all plasma needs to pass through the shortened current sheet; the majority of it instead goes through the shocks while gets heated. The shock structures are necessarily slow shock type (see Lecture 4) which reduces the strength of parallel component of magnetic field from upstream to downstream to aid the reconnection process by dissipating magnetic energy.

In the next several decades, Petschek model had been essentially regarded as the solution for fast reconnection until serious numerical tests became possible (Biskamp, 1986) to disapprove it. To this date, Petschek model has been reproduced numerically only with the so-called locally enhanced "anomalous resistivity" (see below) and has not been confirmed experimentally. In contrast, Sweet-Parker model has been not only reproduced numerically but also confirmed experimentally (Ji et al, 1998), see Fig. 79.

10.2.2 Reconnection in Kinetic Plasmas

The failure of both Sweet-Parker model and Petschek model motivated the Stage 2 research of magnetic reconnection, which began in 1990s and is still ongoing in 2020s, in an attempt to search of fast reconnection mechanisms beyond the MHD description of plasmas. As discussed in Lecture 1, when the relevant length becomes comparable to plasma kinetic scales such as ion skin depth, d_i, or ion sound gyro-radius, ρ_s, the physics beyond MHD description needs to be taken into account by using generalized Ohm's law

$$\boldsymbol{E}+\boldsymbol{V}\times\boldsymbol{B}=\eta_{\rm Spitzer}\boldsymbol{j}+\frac{\boldsymbol{j}\times\boldsymbol{B}}{en}-\frac{\boldsymbol{\nabla}p_e}{en}-\frac{\boldsymbol{\nabla}\cdot\boldsymbol{\Pi}_e}{en}-\frac{m_e}{e}\frac{d\boldsymbol{V}_e}{dt}, \tag{630}$$

where the full electron pressure tensor is expressed as a sum of diagonal isotropic pressure tensor and stress tensor which include off-diagonal pressure tensor: $\boldsymbol{P}_e\equiv p_e\boldsymbol{I}+\boldsymbol{\Pi}_e$ ($\boldsymbol{I}$ is unit tensor).

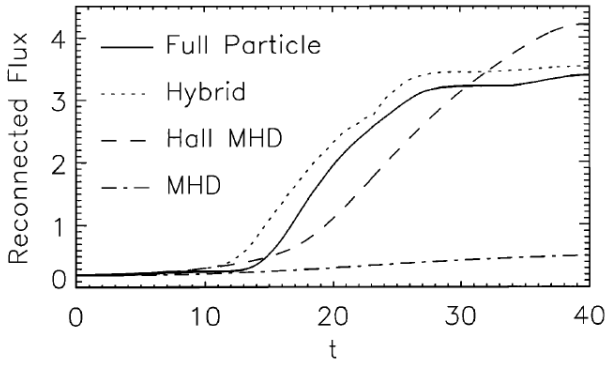

Fig. 80 Reconnected magnetic flux over time using different numerical models by GEM challenge from Birn et al (2001). The slope of these curves represent reconnection rate.

Since the shortest scale for reconnection is the current sheet thickness, δ, and the longest plasma kinetic scale is d_i or ρ_s, the MHD description remains valid when $\delta \gg (d_i \text{ or } \rho_s)$. When this condition is violated, at least one additional term in the generalized Ohm's law. Eq. (630) needs to be kept. A major milestone of the Stage 2 reconnection research was achieved by the so-called GEM (Geospace Environment Modeling) challenge (Birn et al, 2001) when various versions of the generalized Ohm's law was implemented numerically, see Fig. 80. Only the MHD model gives slow reconnection as expected from Sweet-Parker model while all other models give fast reconnection. Since the Hall MHD model only includes the Hall term ($\boldsymbol{j} \times \boldsymbol{B}/en$) which is common to other models, the physics enabled by the Hall term is regarded as essential for fast kinetic reconnection.

The origin of the Hall term can be understood easily if we express $\boldsymbol{j} = en(\boldsymbol{V}_i - \boldsymbol{V}_e) \approx en(\boldsymbol{V} - \boldsymbol{V}_e)$ to rewrite Hall MHD Ohm's law

$$\boldsymbol{E} + \boldsymbol{V} \times \boldsymbol{B} = \eta_{\text{Spitzer}} \boldsymbol{j} + \frac{\boldsymbol{j} \times \boldsymbol{B}}{en} \tag{631}$$

as

$$\boldsymbol{E} + \boldsymbol{V}_e \times \boldsymbol{B} = \eta_{\text{Spitzer}} \boldsymbol{j}$$

which is simply electron momentum equation without pressure force and initial terms. Omitting the Hall term in the Ohm's law, therefore, is equivalent to demanding that ions and electrons move together in resistive MHD models. (Note that this is different from demanding zero electric current as it is determined instead by Ampere's law in the standard MHD models.) In contrast, electrons are allowed to move differently from ions by following Eq. (631) in the Hall MHD models.

Allowing different movement between ions and electrons can achieve fast reconnecton on kinetic scales, as illustrated in Fig. 81 (left panel) in the case of anti-parallel reconnection or without a guide field. When plasma flows towards X-line from upstream, ions become demagnetized first, in the ion diffusion region or IDR owing to their larger mass, and turn towards downstream

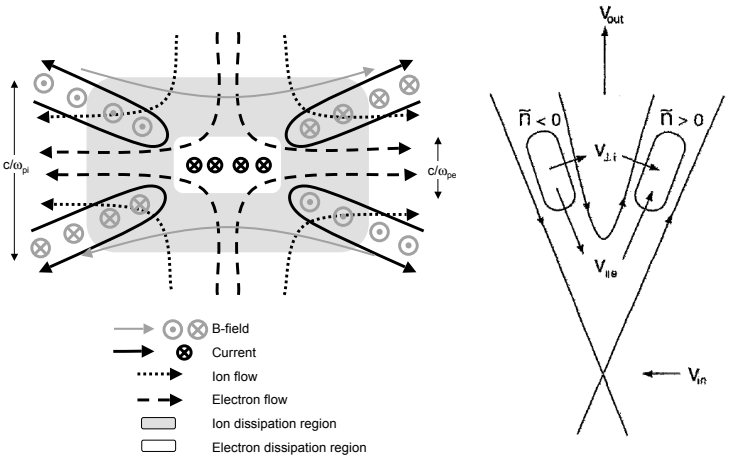

Fig. 81 (left panel) Schematics of ion and electron diffusion regions (IDR and EDR) of kinetic reconnection without a guide field from Drake and Shay (2007). (right panel) Schematics of ion and electron flows during guide field reconnection from Kleva et al (1995).

(dotted lines). Electrons are still magnetized and continue to flow together with magnetic field towards X-line until they are demagnetized in the electron diffusion region or EDR, before they turn towards downstream (dashed lines). The width of IDR and EDR are typically on the order of d_i and d_e, respectively. The differential movement between ions and electrons within the reconnection plane around separatrices areas generate the in-plane electric current (solid lines) and therefore out-of-the-plane magnetic field component in a quadrupolar pattern, which become a hallmark of Hall effect during kinetic fast reconnection. They have been successfully detected in space (Mozer et al, 2002) and in the laboraotory (Ren et al, 2005).

By this configuration fast reconnection can be achieved due to the following two factors. First, magnetic field diffuses effectively in the narrower EDR where electrons dominate while plasma flows with a large flux in the wider IDR where ions dominate to avoid the bottleneck effect. This is in contrast to Sweet-Parker model in MHD where the same current sheet width applies to both magnetic field diffusion and plasma flow forming a bottleneck. Second, since the plasma flows bypass the X-line within IDR without passing through EDR, a deficiency in plasma pressure develops at the X-line which sucks in the upstream magnetic field (Liu et al, 2022) and opens up the outflow channel in a way similar to Petschek model but without shock structures.

The above physics picture of fast kinetic reconnection needs some modifications when a strong guide field is present, which is typical in fusion plasmas. Ions do not become unmagnetized in the diffusion regions so they are not free to move across field lines directly following the in-plane electric field as during anti-parallel reconnection. Instead, they move across field lines in IDR by ion polarization drift due to *spatially inhomogeneous* electric field, $\boldsymbol{V}_{\text{polarization}} \propto d\boldsymbol{E}_{\text{in-plane}}/dt = (\boldsymbol{V}_{\text{E}} \cdot \boldsymbol{\nabla})\boldsymbol{E}_{\text{in-plane}}$ in steady state. Here

$\boldsymbol{V}_{\rm E} = \boldsymbol{E} \times \boldsymbol{B}/B^2$ is the $E \times B$ drift velocity. The ion cross field drift generates density or pressure inhomogeneity along the field lines which balances parallel electric field, as illustrated in Fig. 81 (right panel). Therefore, the isotropic pressure term needs to be added to the Hall MHD Ohm's law in the case of guide field reconnection,

$$\boldsymbol{E} + \boldsymbol{V} \times \boldsymbol{B} = \eta_{\rm Spitzer}\boldsymbol{j} + \frac{\boldsymbol{j} \times \boldsymbol{B}}{en} - \frac{\boldsymbol{\nabla} p_e}{en}, \tag{632}$$

where $\boldsymbol{E}_\perp$ is balanced by the Hall term as before while $E_\parallel$ is balanced by parallel electron pressure gradient in IDR. The existence of density quadrupolar structures during fast guide field reconnection have been confirmed as recent as in space (Øieroset et al, 2016) and in the laboraroty (Fox et al, 2017).

A last piece of the puzzle for fast kinetic reconnection is the last two terms in the generalized Ohm's law, Eq. (630). These two terms, especially the second last term for the gradient of off-diagonal pressure tensor, become important in EDR (Vasyliunas, 1975) when the resitivty is small such as in collisionless plasmas in Earth's magnetosphere. Unmagnetized electrons in EDR are subject to free acceleration by reconnection electric field, generating large off-diagonal pressure gradient during their transit time in EDR. This effect has been demonstrated numerically (Cai and Lee, 1997) and confirmed in space (Torbert et al, 2018) by the most advanced NASA mission called Magnetospheric MultiScale (MMS) mission. A competing alternative to this dissipation mechanism is the so-called "anomalous resistivity" based on 3D kinetic instabilities (Papadopoulos, 1977) which was used to reproduce Petschek-like solutions but its existence is still unclear despite numerous reports on the detection of various kinetic waves. A more systematic review of laboratory study of diffusion regions of kinetic reconnection is given recently by Ji et al (2023) including the detected various kinetic waves and energy conversion process from magnetic field to plasma.

10.2.3 Multiple-Scale Reconnection and Phase Diagram

The success in realizing fast magnetic reconnection in kinetic plasmas has appeared to have solved the fast reconnection problem. However, it turned out that the kinetic fast reconnection solution does not scale up with system size. In the above solar flare example, kinetic scale $d_i \sim 10$ m, which is a million time shorter than system size of $L = 10^7$ m. When scaling up with system size on the order of $100d_i$, the kinetic solution becomes unstable as the current sheet lengthens and eventually breaks up to generate the so-called "plasmoids" (Daughton et al, 2006). Plasmoids are considered to be magnetic islands in two dimensions as a consequence of tearing instability as discussed earlier in this Lecture but "resistivity" needs to be replaced by kinetic dissipation mechanisms discussed above in collisionless plasmas. Once plasmoids are formed via kinetic tearing instability, there exists no longer a single X-line and magnetic reconnection can occur simultaneously at multiple X-lines, and

often plasmoids are dynamic, *i.e.* they are continuously formed, merged and ejected out of the current sheet.

The status of magnetic reconnection research from its Stage 1 and Stage 2 therefore can be summarized as in the following. In MHD plasmas, Sweet-Parker model is valid but predicts only slow reconnection incompatible with the observation. In kinetic plasmas, fast reconnection can indeed occur but the model is only applicable to small plasmas. Therefore, the challenge is to find way(s) to combine these models, which are valid in certain parameter ranges, into one single, self-consistent model to explain fast reconnection in plasmas with high S and large sizes. This is in fact a multi-scale challenge as discussed in Lecture 1, involving fluid MHD scales and various kinetic scales simultaneously, with large separations between them. Therefore, the final Stage 3 of magnetic reconnection research, which began in 2000s, is to study multi-scale nature of magnetic reconnection in large sizes and at high S.

It turned out that the laminar single X-line Sweet-Parker solution also does not scale up with Lundquist number S. When S is sufficiently high, the current sheet is long and narrow as its aspect ratio δ/L scales as $S^{-1/2}$, and thus unstable to resistive tearing instability or "plasmoid" instability (Shibata and Tanuma, 2001) with multiple X-lines. Note that Sweet-Parker reconnecting current sheet is different from the static current sheet shown in Fig. 71 that we discussed earlier in this Lecture. The reconnection outflow in the current sheet can be stabilizing as it can shear apart of linear perturbation but it turned out that such effects are unimportant.

A sufficiently long current sheet is unstable to resistive tearing modes over a wide range of wavenumber, k. In the large-k limit, the small-Δ' regime applies with growth rate decreasing as $k^{-2/5}$ [Eq. (609)]. In the small-k limit, the opposite large-Δ' regime applies with the growth rate increasing as $k^{2/3}$ [Eq. (613)], as illustrated in Fig. 82. Therefore, maximum growth rate $\gamma_{\max}$ is given by equating two growth rate equations to yield,

$$\gamma_{\max}\tau_{Aa} = S_a^{-1/2} \tag{633}$$

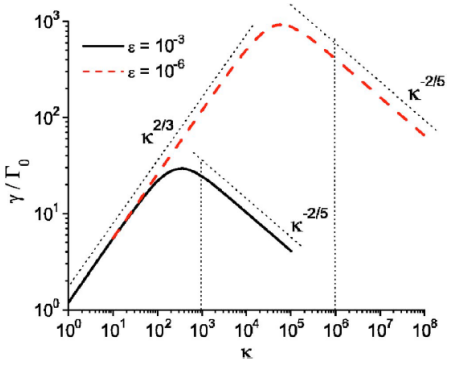

Fig. 82 Growth rate of tearing instability as a function of wavenumber for a long current sheet from Loureiro et al (2007).

$$k_{\max} a = S_a^{-1/4}, \tag{634}$$

where $\tau_{\mathrm{A}a}$ and S_a are Alfvén time and Lundquist number defined based on the current sheet thickness, a, which is δ in the Sweet-Parker model. After translating these definitions for those used in Sweet-Parker model, the above equations become

$$\gamma_{\max} \tau_{\mathrm{A}} = S^{1/4} \tag{635}$$

$$k_{\max} L = S^{3/8}. \tag{636}$$

As expected, the number of plasmoids increases with S as the current sheet gets longer. The maximum growth rate also increases with S, meaning that the Sweet-Parker current sheet becomes increasingly unstable. This naturally leads to an important question on what is the critical S_{c}, beyond which the Sweet-Parker solution begins to break down and the current sheet stops to lengthen. Suppose that at $S = S_{\mathrm{c}}$, $\gamma_{\max}\tau_{\mathrm{A}} = S_{\mathrm{c}}^{1/4} = 10 \gg 1$, we have $S_{\mathrm{c}} \approx 10^4$ which has been confirmed numerically (Samtaney et al, 2009). The resultant reconnection rate is therefore fast $S_{\mathrm{c}}^{-1/2} \approx 0.01$ for all $S \geq S_{\mathrm{c}}$, as confirmed by nonlinear numerical simulation by Bhattacharjee et al (2009), see Fig. 83 (left panel).

If Sweet-Parker current sheet aspect ratio $\delta/L = S^{-1/2}$ is actually unattainable for $S > S_{\mathrm{c}}$ due to plasmoid instability, then a natural question arises:

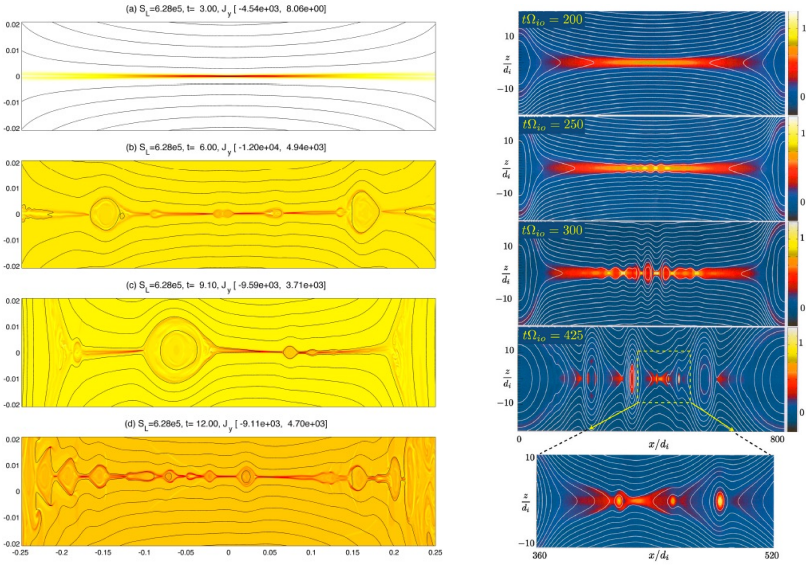

Fig. 83 (left panel) Breakdown of Sweet-Parker current sheet due to plasmoid instability in MHD from Bhattacharjee et al (2009). (right panel) Breakdown of Sweet-Parker current sheet due to plasmoid instability in collisional Particle-In-Cell simulation resulting in kinetic reconnection between plasmoids. From Daughton et al (2009).

what is the attainable current sheet aspect ratio? Rewriting Eq. (633), we have

$$\gamma_{\max}\left(\frac{\delta}{V_A}\right) = \left(\frac{\mu_0 \delta V_A}{\eta}\right)^{-1/2}$$
$$\gamma_{\max}\left(\frac{L}{V_A}\right) = \left(\frac{L}{\delta}\right)^{3/2}\left(\frac{\mu_0 L V_A}{\eta}\right)^{-1/2}$$
$$\gamma_{\max}\tau_A = \left(\frac{L}{\delta}\right)^{3/2} S^{-1/2}. \tag{637}$$

If we demand $\gamma_{\max}\tau_A$ is a constant, independent of S, the current sheet thickness needs to scale with

$$\frac{\delta}{L} = S^{-1/3} \tag{638}$$

which is much wider than Sweet-Parker current sheet when $S \to \infty$. This has been predicted theoretically (Pucci and Velli, 2014) and confirmed numerically (Huang et al, 2017). The corresponding $k_{\max}$ is given by

$$k_{\max} L = S^{1/6} \tag{639}$$

instead of $k_{\max} L = S^{3/8}$ by Eq. (636).

During the fully nonlinear stage of plasmoid instability of a reconnecting current sheet, new current sheets develop between plamoids but with lower Lundquist numbers. If these new current sheets are sufficiently long and thin or equivalently their Lundquist numbers are sufficiently large and above S_c, these new current sheets can be unstable also to plasmoid instability, which can lead to the next generation of plasmoids if the same conditions are satisfied. Thus, a fractal hierarchy of nested current sheets and plamoids emerges (Shibata and Tanuma, 2001) as illustrated in Fig. 84. As the current sheet length and thickness get shorter each level down, the fractal hierarchy can be terminated only in two ways:

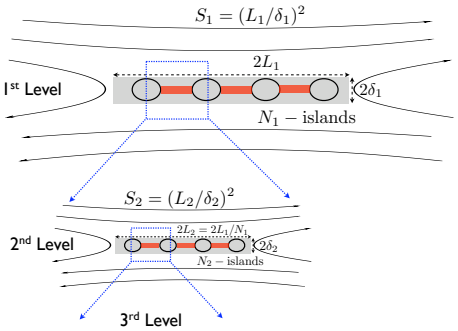

Fig. 84 A fractal hierarchy model of multiscale reconnecting current sheet due to plasmoid instability. From Ji and Daughton (2011).

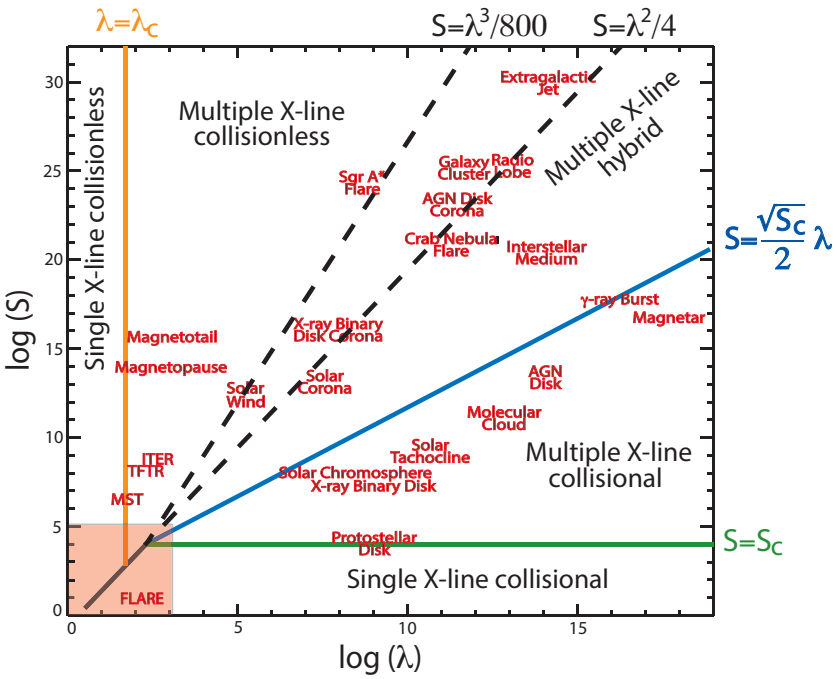

Fig. 85 A magnetic reconnection phase diagram, originally from Ji and Daughton (2011) and updated by Ji and Daughton (2022). The locations from a survey for fusion, space, and astrophysical plasmas where reconnection is considered to occur are displayed. The area covered by FLARE device is also shown.

- When the Lundquist number of current sheets goes below S_c such that single X-line Sweet-Parker reconnection proceeds without plasmoid instability as described in the Stage 1 research;
- When the current sheet thickness goes below ion kinetic scales (d_i or ρ_s depending on guide field) such that single X-line kinetic reconnection proceeds as described in the Stage 2 research.

In either of these two cases, the reconnection rate (which can be defined in several ways here) always remains fast in the range of 0.1-0.01, meeting the requirements for a multi-scale solution for fast reconnection in space and astrophysical plasmas. Based on the above descriptions, a magnetic reconnection "phase diagram" (Ji and Daughton, 2011) has been constructed in the parameter space of normalized plasma size λ (to ion kinetic scale) and Lundquist number S, see Fig. 85. Here, "collisionless" refers to the situation where kinetic reconnection dominates while "collisional" refers to the fluid MHD physics dominates. "multiple X-line" refers to multiple reconnection diffusion regions generated by plasmoid instability.

There are five different reconnection "phases" or regimes. When $S < S_c$ or $\lambda < \lambda_c$ (where λ_c is critical size for kinetic plasmoids instability), reconnection

proceeds following single X-line Sweet-Parker or kinetic models, respectively. Other three phases are plasmoid-mediated, multiple X-line regimes:

- "multiple X-line collisional" refers to the case where collisional MHD description remains valid throughout but current sheet is unstable to collisional plasmoid instability. The plasmoid hierarchy is terminated by single X-line collisional Sweet-Parker reconnection.
- "multiple X-line collisionless" refers to the case where kinetic description remains valid throughout but current sheet is unstable to kinetic plasmoid instability. The plasmoid hierarchy is terminated by single X-line kinetic reconnection.
- "multiple X-line hybrid" refers to the case where on larger scales collisonal MHD description is valid in the plasmoid hierarchy but it is terminated by kinetic reconnection on smaller scales. A mixture of fluid and kinetic physics is required to model the reconnection process as a whole.

Therefore, the multi-scale reconnection solution based on plasmoid instability has five distinct phases depending on the location in the phase diagram. [Note that an additional single X-line electron-only reconnection regime has emerged recently (e.g. Phan et al, 2018) and ions are decoupled from the reconnection process due to small system sizes, see Ji et al (2022) for more details.] The two dashed black lines are based on different current sheet aspect ratio scaling: $S = \lambda^3/800$ and $S = \lambda^2/4$ correspond respectively to the marginal stability scaling $\delta/L = S^{-1/3}$ and Sweet-Parker scaling $\delta/L = S^{-1/2}$, as described above. The boundary (blue line) between multiple X-line collisional and multiple X-line hybrid phases depends on plamoid number scaling on S, and the line $S = \sqrt{S_c}\lambda/2$ is for the case of linear scaling with respect to S (Ji and Daughton, 2011).

A survey of plasmas from fusion to space and astrophysics where magnetic reconnection is considered to occur was performed and their locations in the phase diagram are also shown in Fig. 85. There is some but very limited evidence on plasmoids in reconnecting current sheets. In order to provide the first laboratory access to these new regimes, Facility for Laboratory Reconnection Experiments (FLARE) has been constructed (Ji et al, 2018) and currently is being upgraded at PPPL. There exist a large number of major outstanding questions on magnetic reconnection (Ji et al, 2020) and many of them can be studied on FLARE for the first time in the new multi-scale regimes. The recent "roadmap" review (Ji et al, 2022) called out the following three particular questions in solving the reconnection problem in the near term: how does multiscale coupling work? how does reconnection start or onset? and how is magnetic field energy converted to flow, thermal and non-thermal energies partitioning between ions and electrons? A concerted effort is warranted to address these questions between communities of plasma physics, fusion, space, solar and astrophysics using theory, simulation, observation, laboratory experiment, as well as emerging data science techniques.

10.3 Summary

- Finite resistivity can stabilize but can also destabilize otherwise ideal MHD stable equilibria by inducing a new class of MHD instabilities: resistive tearing instability.
- Resistive tearing instability is determined by Δ' which is a jump condition for the inner resistive layer, and can be calculated in the ideal MHD regions. Positive Δ' corresponds to instability.
- The growth rate of tearing instability is hybrid between the inverse of ideal and resistive time scales.
- A consequence of resistive tearing instability is the growth of magnetic islands, and the nonlinear effects become important when the island width is larger than the inner layer width.
- Sweet-Parker model is valid in 2D MHD but predicts slow reconnection while Petschek model predicts fast reconnection but is still unconfirmed.
- Kinetic reconnection is fast by avoiding the bottleneck effect via different motions between ions and electrons, but does not scale up to large scales.
- A multi-scale model based on plasmoid instability of reconnecting current sheet has been proposed to explain fast reconnection in fusion plasmas and throughout the universe in a reconnection phase diagram.

10.4 Further Readings

- Chapters 20 in Goldston and Rutherford (1995) on resistive tearing instability.
- Review paper by Yamada et al (2010) on magnetic reconnection in general.
- Review paper by Ji et al (2023) on laboratory study of kinetic reconnection.
- "Roadmap" review paper by Ji et al (2022) on future magnetic reconnection research.
- Community white paper by Ji et al (2020) on major questions on magnetic reconnection.

10.5 Homework Problem Set 10

1. Tearing mode with rigid conducting walls.

   Place rigid conducting walls at $x = \pm b$ ($b > a$) into the case that we have gone through duing the class.

   (a) Do you expect the plasma to be more, or less, stable to the tearing modes? Why?

   (b) Calculate $\Delta' a$ for this case. Is this expectation confirmed by your expression for $\Delta' a$?

2. Plasmoid instability of Sweet-Parker current sheet.

   If S is sufficiently large, the Sweet-Parker current sheet is known to be unstable to resistive tearing instability, which is often called plasmoid instability.

(a) Apply what we have learned in Lecture 10 to this case to show that the growth rate is given by

$$\gamma\tau_A' = 0.61S^{2/5} \tag{640}$$

where τ_A' is the Alfvén time defined for the reconnection problem, $\tau_A' = L/V_A$, instead of $\tau_A = a/V_A$ defined for tearing instability problem (a is the half-width of current sheet, and is called δ in the reconnection problem). Effects due to finite flow within the current sheet are ignored for simplicity.

(b) Equation (640) shows that the growth rate increases with S, called "super-Alfvénic", which seems to contradict with the essence of tearing instability: it grows on a time scale between ideal and resisitive scales. Does this make sense? Explain.

(c) When S is sufficiently small, plasmoid instability should be stable. What is the maximum S at which the Sweet-Parker current sheet is stable?

11 Magnetic Dynamo

11.1 The Dynamo Problem

The physical process through which magnetic field is generated and sustained is called magnetic dynamo or simply dynamo. The dynamo problem predates the emergence of modern plasma physics and has been mostly based on Navier-Stokes equations with Lorentz force and induction equation added. The energy source for the magnetic field growth is typically from flow energy but other forms of energy are also possible (see below). The interest in geodynamo emerged since the realization that geomagnetic fields last much longer than the diffusion time of a given initial field (on the order of 200,000 years) while the liquid inner core is hotter than the Curie temperature removing permanent magnets as a possible explanation. The interests further surged when ancient geomagnetic fields (paleomagnetism) have been found to have exhibited chaotic reversals. Similar stories were told for solar dynamo and galactic dynamo when magnetic fields are found on the Sun and in the galaxy. In particular, solar dynamo generates magnetic field, exhibiting a 22 year cycle during which dipole field flips its polarity twice to return to its original orientation (see Fig. 86). In contrast, galactic magnetic fields are static on the observational timescale and one of example is shown in Fig. 87 for a well-known spiral galaxy. By now magnetic fields have been observed nearly everywhere in the universe, including moons around planets, accretion disks, and jets on the stellar scales or galactic scales, and the magnetic dynamo stands as a common physics problem across many fields of physics including plasma physics, fluid dynamics, geophysics, solar physics, and astrophysics.

Mechanical dynamos are commonly found. They began with Michael Faraday's homopolar dynamo in 1831, see Fig. 88, eventually leading to modern

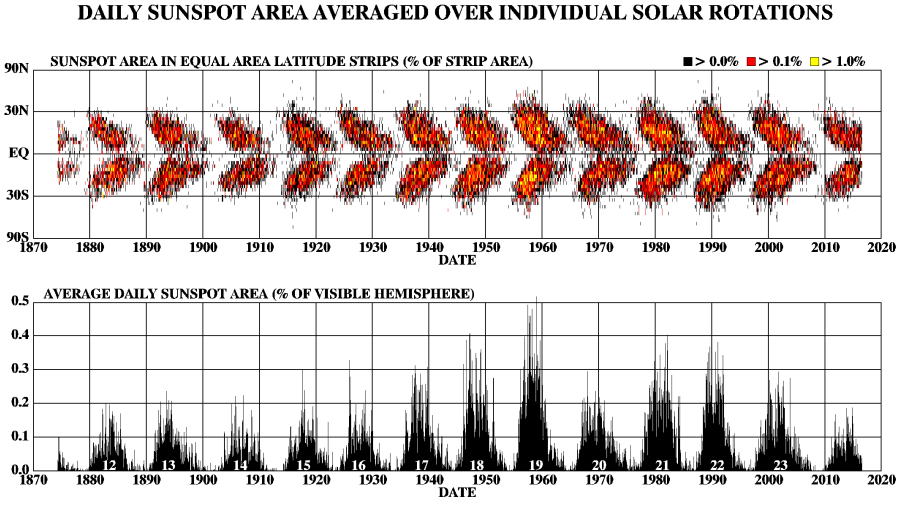

Fig. 86 "The butterfly diagram" of sunspots.

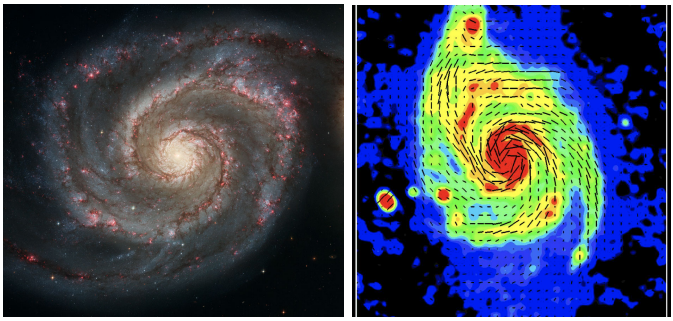

Fig. 87 (left panel) M51 spiral galaxy by Hubble space telescope (right panel) radio emission superimposed with magnetic field vector from polarization measurements. The length of magnetic field vectors is proportional to polarized intensity. From Beck (2000).

electricity production but with essentially the same principle. An electrically conducting disk rotates at angular velocity ω with a wire connecting its center at $r = 0$ to its edge at $r = a$. The electric current flowing in the wire is I, which proportionally generates a magnetic field B_z at the disk surface, and therefore a flux threading the disk Φ,

$$\Phi = \alpha I. \tag{641}$$

The electric voltage drop between the disk edge and center due to electromotive force is given by

$$\int_0^a r\omega B_z dr = \omega \int_0^a B_z r dr = \frac{\omega\Phi}{2\pi} = \frac{\omega\alpha}{2\pi} I, \tag{642}$$

leading to a circuit equation,

$$L\frac{dI}{dt} + RI = \frac{\omega\alpha}{2\pi} I, \tag{643}$$

where L and R are inductance and resistance of the wire, respectively. Assuming $I \propto e^{\gamma t}$, Eq. (643) leads to the solution to the growth rate γ,

$$\gamma = \frac{\alpha}{2\pi L}\left(\omega - \frac{2\pi R}{\alpha}\right). \tag{644}$$

In order to have a positive growth rate of the current (and thus the magnetic field), α needs to have an appropriate sign (so that induced current can reinforce the original field, as opposed to reduce the original field) and ω is above a critical value of $\omega_c = 2\pi R/\alpha$. The former condition represents the requirement for the wire to take an appropriate path to reinforce the initial magnetic field while the latter condition represents the requirement for a sufficiently large injection rate of mechanical energy to overcome diffusion. Both requirements carry over to dynamo action in plasmas; first one corresponds to the

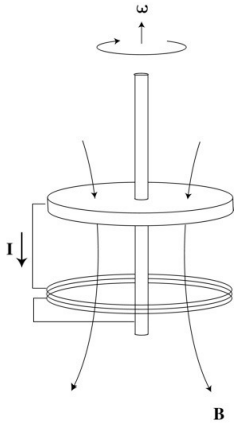

Fig. 88 Homopolar dynamo.

requirement for a right type of flow and second one corresponds to sufficient flow energy inject to overcome magnetic diffusion.

However, there is a major difference between mechanical dynamos and dynamos in plasmas. In plasmas, there are no physical wires to constrain the path for electric current to flow; it is determined by structure and dynamics of the "homogeneous" plasma flow. For this reason, dynamos in plasmas are called "homogeneous dynamos". The challenge of homogeneous dynamos is to realize and understand magnetic field generation by flow when the (return) current paths are unconstrained in electrically conducting plasmas. In general the flow here can result from an instability due to other free energy source, such as convective instability in stars and MRI in accretion disks, or can be simply prescribed in steady state, such as in theory and numerical simulation, or can be driven as in laboratory experiments. There have been tremendous progress in the dynamo research during its long history but the problem is still largely unsolved at least in the MHD context. Several important concepts and development will be described below, followed by some relevant laboratory efforts.

11.2 Kinematic Dynamo versus Nonlinear Dynamo

In the MHD framework, the dynamo problem is defined as the study of mechanism(s) by which magnetic field is created and sustained against dissipation from flow of electrically conducting media. For a given flow field, $\boldsymbol{V}$, under specified boundary conditions, *the kinematic dynamo* problem poses as a linear eigenmode problem to seek unstable solutions of a vector equation for $\boldsymbol{B}$,

$$\frac{\partial \boldsymbol{B}}{\partial t} = \boldsymbol{\nabla} \times (\boldsymbol{V} \times \boldsymbol{B}) + \frac{\eta}{\mu_0} \nabla^2 \boldsymbol{B}. \tag{645}$$

The subject volume is generally in three dimensions but two of dimensions are typically decomposed in Fourier space to form a one-dimensional eigenmode

problem in radial direction, with mode numbers in other two directions appearing in coefficients. We note that this is a rather common technique in linear stability analysis as shown for many times in this Lecture Notes. These two coordinates are axial and azimuthal in cylindrical coordinate while azimuthal and polar in spherical coordinate.

The ratio of the two terms on the right-hand side of Eq. (645) defines magnetic Reynolds number,

$$R_m \equiv \frac{\mu_0 V_0 L_0}{\eta}, \tag{646}$$

where V_0 and L_0 are characteristic flow magnitude and space scale, respectively. Note that this R_m is fundamentally distinguished from Lundquist number, S, whose definition is based on Alfvén speed, V_A, instead of V_0. Magnetic Reynolds number quantifies how much magnetic field generation driven by sheared flow against magnetic diffusion while Lundquist number quantifies how "ideal" the plasma is, or how much magnetic field is frozen-in to plasma, against magnetic diffusion. For a static but magnetized plasma as in magnetic fusion, magnetic Reynolds number vanishes while Lundquist number is large. In a flowing but unmagnetized plasma as in astrophysics, Lundquist number vanishes while magnetic Reynolds number is large.

As illustrated in the example of mechanical dynamos, there always exist a critical speed for a given flow under certain boundary conditions, above which magnetic dynamos occur. (Needless to say, the flow needs to be sheared; otherwise it can be transformed out by moving to the flow frame.) This critical speed can be expressed in terms of dimensionless critical magnetic Reynolds number, R_{mc}. The simplest known kinematic dynamo is by Ponomarenko (1973), in which an infinitely long cylinder is embedded in a static, infinitely large conducting medium. The cylinder rotates around its axis rigidly and translates along its axis with a constant speed to form a helical flow pattern. A magnetic dynamo is excited if magnetic Reynolds number, defined using cylinder radius and surface speed, is above a critical value of $R_{mc} = 17.7$.

Motivated by this theory, an actual liquid sodium experiment was built in Riga, Latvia, and operated to successfully generate magnetic field, see Fig. 89. A helical flow was generated by a propeller along a cylinder with a return flow in a larger cylinder, which is embedded in a static liquid sodium. The critical Rm for magnetic field generation was measured to be close to the theoretically predicted values. An example run is shown in Fig. 89. Magnetic field measured by a Hall senor grows exponentially from a small seed field once the propeller rotation rate is above the critical value. Another successful dynamo experiment, Von Karman Sodium (VKS) experiment, was performed in Cadarache, France where two von-Karman type vortices in liquid sodium are stirred by the counter-rotation of two magnetic (iron) bladded disks in a cylinder (Monchaux et al, 2007).

In an actual flow like the one shown above, however, kinematic dynamo is only an approximation when magnetic field is relatively weak or is still

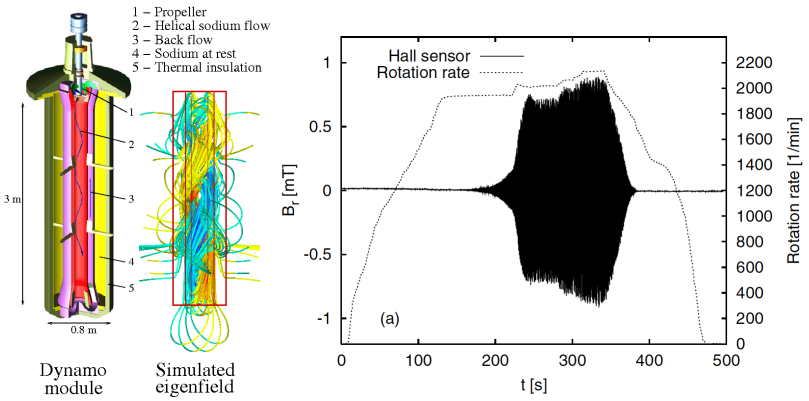

Fig. 89 Riga dynamo. From Gailitis et al (2001).

in its linear growth phase. When magnetic field grows to a large amplitude, nonlinear effects appear to begin to modify the flow. This effect manifests as a non-negligible Lorentz force in the equation of motion,

$$\rho\left(\frac{\partial \boldsymbol{V}}{\partial t}+\boldsymbol{V}\cdot\boldsymbol{\nabla}\boldsymbol{V}\right)=-\boldsymbol{\nabla}p+\boldsymbol{j}\times\boldsymbol{B}+\nu\nabla^2\boldsymbol{V}. \tag{647}$$

Eventually, the modified flow generates magnetic field less effectively and is balanced with diffusion to achieve nonlinear saturation. When both equations, Eqs. (645) and (647), are simultaneously solved, the solution is said as *nonlinear dynamo* which is a much more difficult problem than the kinematic dynamo counterpart, and has attracted much attention over a long time.

11.3 Slow Dynamo versus Fast Dynamo

Another important characteristic of a given dynamo is the time scale on which magnetic field is generated and sustained. When the magnetic field growth time is on the order of or related to the resistive diffusion time, the dynamo is said to be "slow". The previously mentioned homopolar dynamo, Ponomarenko dynamo, and most likely the geodynamo are examples of slow dynamos. Different conductivity leads to different growth rate.

In contrast, when the magnetic field growth time is independent of resistive diffusion time, the dynamo is said to be "fast". An illustrative example of fast dynamos has been given by Vainshtein and Zel'dovich (1972), known as Stretch-Twist-Fold dynamo, is shown in Fig. 90. When a flux tube [Fig. 90(a)] is stretched twice long, the field strength doubles while cross-sectional area shrinks to half to conserve its flux. Then one end of the flux tube is twisted by 180 degrees against the other end [Fig. 90(b)], and is folded on the other half doubling cross-sectional area to get back to the original value, but magnetic flux is doubled [Fig. 90(c)]. This process works on the dynamic time scale of the flow, independent of the resistive time scale, is qualified as a fast dynamo process. However, there is a paradox in this illustrative example. The large

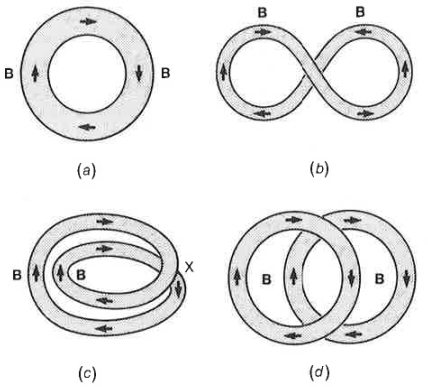

Fig. 90 Stretch-Twist-Fold fast dynamo. From Roberts (1994).

field gradient area, marked "X" in Fig. 90(c), can cause magnetic reconnection smoothing out flux tubes as shown in Fig. 90(d). This last step actually involves resistive diffusion, in contradiction with the definition of a fast dynamo, but on a much shorter spatial scale.

This paradox is shared by the solar dynamo. Evidently, the 22 year cycle, being much shorter than the resistive diffusion time, demands a fast dynamo mechanism. But if there exists no field diffusion, these rapid 22 year cycles of solar dynamo would generate a train of repeated magnetic patterns piling up somewhere in the sun, eventually triggering resistive reconnection to smooth out local field gradients. In other words, fast dynamo is necessarily accompanied by resistive diffusion somewhere in the system in order to achieve quasi-steady-state, but resistive diffusion is the trademark of slow dynamo! Therefore if we focus on this resistive diffusion aspect, we might want to also call solar dynamo a slow dynamo. These examples illustrate the complex and multifaceted nature of a dynamo in nature.

11.4 Cowling's Anti-dynamo Theorem

One milestone result of the long history of dynamo theory is due to Cowling (1934). The Cowling's anti-dynamo theorem states "*an axisymmetric magnetic field cannot be sustained by dynamo*". The formal proof is rather lengthy and will not be reproduced here. Instead a heuristic version is given below.

Any axisymmetric magnetic field can be decomposed to toroidal and poidal components, $\boldsymbol{B}_t$ amd $\boldsymbol{B}_p$, respectively. As before such in Lecture 2, $\boldsymbol{B}_p$ can be expressed in terms of a stream function or flux function ψ, $\boldsymbol{B}_p = \boldsymbol{\nabla} \times \psi$, such that the divergence free condition of $\boldsymbol{\nabla} \cdot \boldsymbol{B} = 0$ is satisfied. The equal-potential contours of ψ form closed loops in any finite-length systems as illustrated in Fig. 91 where there must exist at least one extremum. These extrema correspond to poloidal null points where $\boldsymbol{B}_p = 0$. The toroidal component of Ohm's

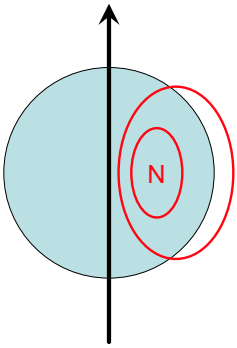

Fig. 91 Cowling anti-dynamo theorem.

law at these null points becomes

$$E_t + (\boldsymbol{V} \times \boldsymbol{B})_t = E_t + \boldsymbol{V}_p \times \boldsymbol{B}_p = E_t = \eta j_t > 0. \tag{648}$$

By using Faraday's law, $\partial \boldsymbol{B}/\partial t = -\boldsymbol{\nabla} \times \boldsymbol{E}$, the time change rate of the poloidal flux enclosed by a null line circle is given by

$$\frac{\partial}{\partial t} \int \boldsymbol{B}_p \cdot d\boldsymbol{S} = -\oint E_t dl = -2\pi R_{null} \eta j_t < 0, \tag{649}$$

where the surface S is enclosed by the loop l at the null point, whose radius is R_{null}. Therefore, the enclosed poloidal flux by a null point circle in any axisymmetric magnetif fields cannot be sustained and must decay in time.

This theorem highlighted the difficulty of the dynamo problem, especially to those who were seeking steady state axisymmetric field solutions, motivated by the fact that the actually observed magnetic fields in planets are more or less axisymmetric dipoles. However, it is commonly accepted now that this anti-dynamo theorem does not really apply since none of these observed fields are exactly asymmetric nor in a true steady state. Note that this theorem is only about the magnetic field generated by dynamo and should not be confused with any constraints on the velocity field that induces dynamo. In kinematic dynamo models, axisymmetric flows are often prescribed, but the resulted magnetic fields are usually non-axisymmetric and time dependence as exemplified in Ponomarenko dynamo as well as the Riga dynamo experiment (Fig. 89).

11.5 Biermann Battery Effects

Cowling's theorem does not apply outside of MHD models. In fact, axisymmetric magnetic fields can be generated and sustained in models where generalized Ohm's law is valid. One such example is Biermann battery effects (Biermann, 1950). If we keep only the electron pressure term on the right-hand side, the

generalized Ohm's law reads

$$\boldsymbol{E} + \boldsymbol{V} \times \boldsymbol{B} = -\frac{\boldsymbol{\nabla} P_e}{e n_e}. \tag{650}$$

Therefore, Faraday's law becomes

$$\begin{aligned} \frac{\partial \boldsymbol{B}}{\partial t} &= \boldsymbol{\nabla} \times (\boldsymbol{V} \times \boldsymbol{B}) + \boldsymbol{\nabla} \times \left(\frac{\boldsymbol{\nabla} P_e}{e n_e} \right) \\ &= \boldsymbol{\nabla} \times (\boldsymbol{V} \times \boldsymbol{B}) - \frac{\boldsymbol{\nabla} n_e \times \boldsymbol{\nabla} T_e}{e n_e}, \end{aligned} \tag{651}$$

where the last term can be nonzero under certain conditions. Biermann (1950) considered that a seed magnetic field can be generated from this term at an early stage of the universe. Without a seed, regardless how small it might be, magnetic field cannot grow because the zero field solution identically satisfies the kinematic dynamo equation, Eq. (645).

Biermann battery effects are readily realized in the laboratory by shining a high-power laser on a solid target to generate axisymmetric fields. An example is illustrated in Fig. 92. When a powerful laser reaches the target, it heats the solid matter and ionizes it to plasma. The electron density gradient naturally points into the target along the laser direction. On the other hand, the electron temperature gradient points radially inwards due to the laser heating. Their cross product is in the azimuthal direction, generating an azimuthal magnetic field as shown in Fig. 92. This azimuthal field is axisymmetric.

The magnetic field generated by Biermann battery effects can be strong on the order of MegaGauss or 100 T, but plasma β is still high ($> 10 - 100$) due to high plasma density. Thus these magnetic fields can be treated as tracers of plasma inhomogeneity and their measurements can help characterize plasma dynamic evolution. The Biermann fields are also used to study flow-driven magnetic reconnection in high-β plasmas (Nilson et al, 2006).

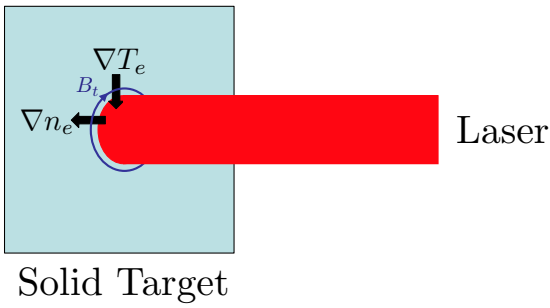

Fig. 92 Biermann battery magnetic field from laser-target interaction.

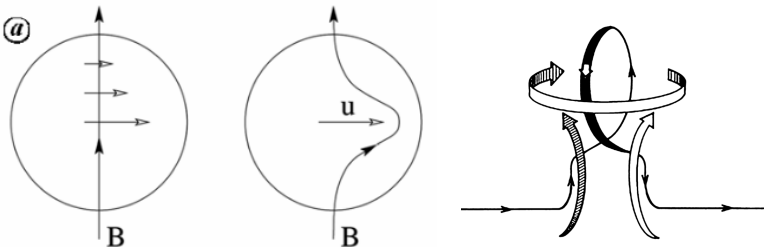

Fig. 93 $\alpha-\omega$ dynamo model. (left two panels) Shared toroidal flow can generate tororidal field from poloidal field. (right panel) A rising plumes in a rotating fluid is twisted by Coriolis force to generate poloidal field from toroidal field. From Parker (1970).

11.6 Parker's $\alpha-\omega$ Dynamo Model

Cowling's anti-dynamo theorem paused a challenge in dynamo research for nearly two decades before Parker's landmark $\alpha-\omega$ dynamo model was introduced (Parker, 1955) to explain geodynamo. The ω effect is the generation of the field component along the flow direction due to flow shear, as discussed in Lecture 9 where magnetic field effects were assessed to influence flow stability. Figure 93 illustrates a case where a toroidal field is generated out of an initial poloidal field by a sheared toroidal flow.

The α-effect, however, is less straightforward. It requires both convection and rotation. Convectively unstable plumes arise against gravity bringing magnetic field with them, as also illustrated in Fig. 93. The background rotation introduces a Coriolis force which twists the rising plumes outside of the plane of the page to form a cyclonic fluid updraft. If the twist is 90°, poloidal field is generated out of the original toroidal field. This effect is less effective for smaller or larger angle of the twist, which depends on relative strength between convection and rotation, but the qualitative idea does not change. The sinking convective plumes twist in the opposite direction but generate similar poloidal fields. A sea of these twisted plumes can merge through magnetic reconnection at large field gradient locations, similar to the case illustrated in the Stretch-Twist-Fold fast dynamo in Fig. 90, to form large-scale poloidal field that was imposed at the beginning. This completes the circle of the $\alpha-\omega$ dynamo process to amplify magnetic fields with both torodial and poloidal components, close to those observed in nature. The proposal of this model essentially revived the dynamo research which continues to this day.

An important element introduced by Parker's $\alpha-\omega$ dynamo model is about the role of small-scale motions as part of the α effects. Small-scale magnetic fields are quickly generated by these small-scale plumes, which can break down to motions at even smaller scale (as part of turbulent cascade, see Lecture 12). Motions at smaller scales typically have shorter time scales to evolve, which can in turn generate magnetic fields at smaller spatial scales at a faster rate. Thus,

the generation of small-scale fields is quite rapid, and is called (fast) *small-scale dynamo* or *fluctuation dynamo*, and has been formulated to derive its spectra since Kulsrud and Anderson (1992). The small-scale dynamo research has seen rapid progress in recently years mainly due to advances in numerical simulations, and some part of it has been realized in the laboratory.

11.7 Large-scale Dynamo and Mean-field Theory

Parker's $\alpha - \omega$ dynamo model invoked an important concept to generate large-scale fields out of small-scale fields of convecting plumes. This generation process can, but does not have to, rely on the reconnection process. The large-scale field can be readily obtained by simply *averaging* over small-scale fields. This led to another landmark of the dynamo research: the so-called mean-field theory, or mean-field dynamo theory since it focuses on dynamo problem (Steenbeck et al, 1966).

The key assumption behind the mean-field theory is the scale separation between large and small scales, so that every quantity, a, can be split to the mean part, a_0, and fluctuation (or turbulent) part, $\widetilde{a}$,

$$a = a_0 + \widetilde{a}, \tag{652}$$

where the average is taken over the large scale so by definition

$$a_0 \equiv \langle a \rangle\,; \quad \langle \widetilde{a} \rangle \equiv 0. \tag{653}$$

Applying this procedure to both $\boldsymbol{V} = \boldsymbol{V}_0 + \widetilde{\boldsymbol{V}}$ and $\boldsymbol{B} = \boldsymbol{B}_0 + \widetilde{\boldsymbol{B}}$ in the induction equation yields

$$\frac{\partial \left(\boldsymbol{B}_0 + \widetilde{\boldsymbol{B}}\right)}{\partial t} = \boldsymbol{\nabla} \times \left[\left(\boldsymbol{V}_0 + \widetilde{\boldsymbol{V}}\right) \times \left(\boldsymbol{B}_0 + \widetilde{\boldsymbol{B}}\right)\right] + \frac{\eta}{\mu_0} \nabla^2 \left(\boldsymbol{B}_0 + \widetilde{\boldsymbol{B}}\right). \tag{654}$$

Taking the $\boldsymbol{V}_0$ frame (so that $\boldsymbol{V}_0 = 0$), and averaging this equation over the large scale leads to

$$\frac{\partial \boldsymbol{B}_0}{\partial t} = \boldsymbol{\nabla} \times \left\langle \widetilde{\boldsymbol{V}} \times \widetilde{\boldsymbol{B}} \right\rangle + \frac{\eta}{\mu_0} \nabla^2 \boldsymbol{B}_0, \tag{655}$$

where an important cross term $\left\langle \widetilde{\boldsymbol{V}} \times \widetilde{\boldsymbol{B}} \right\rangle \equiv \boldsymbol{\mathcal{E}}$ represents the contribution to growth of large-scale magnetic field by turbulent electromotive force (EMF) due to small-scale fluctuations in velocity and magnetic field. Then the critical question is how to evaluate this turbulent EMF, $\boldsymbol{\mathcal{E}}$.

Steenbeck et al (1966) made a series of simplifying assumptions to derive several important results of the mean-field dynamo theory. One of such assumption is to express fluctuating magnetic field in terms of velocity fluctuations. Subtracting Eq. (655) from Eq. (654) and ignoring the resistive term

yields

$$\begin{aligned}\frac{\partial \widetilde{\boldsymbol{B}}}{\partial t} &= \boldsymbol{\nabla}\times\left(\widetilde{\boldsymbol{V}}\times\boldsymbol{B}_0\right)+\boldsymbol{\nabla}\times\left(\widetilde{\boldsymbol{V}}\times\widetilde{\boldsymbol{B}}-\left\langle\widetilde{\boldsymbol{V}}\times\widetilde{\boldsymbol{B}}\right\rangle\right)\\ &\approx \boldsymbol{\nabla}\times\left(\widetilde{\boldsymbol{V}}\times\boldsymbol{B}_0\right)\end{aligned} \tag{656}$$

where the second term on the right-hand side is dropped by the so-called "quasilinear approximation" or "second-order smoothing". Then $\widetilde{\boldsymbol{B}}$ can be calculated by integrating along fluid element trajectory,

$$\widetilde{\boldsymbol{B}}(\boldsymbol{r},t)=\int_{-\infty}^{t}dt'\boldsymbol{\nabla}\times\left[\widetilde{\boldsymbol{V}}(\boldsymbol{r}',t')\times\boldsymbol{B}_0\right],$$

where $\boldsymbol{r}'$ points to the location of the subject fluid element at t'. The resultant turbulent EMF is calculated by

$$\boldsymbol{\mathcal{E}}=\left\langle\widetilde{\boldsymbol{V}}\times\widetilde{\boldsymbol{B}}\right\rangle=\int_{-\infty}^{t}dt'\left\langle\widetilde{\boldsymbol{V}}\times\left[\boldsymbol{\nabla}\times\left(\widetilde{\boldsymbol{V}}\times\boldsymbol{B}_0\right)\right]\right\rangle.$$

Under further assumptions of isotropic, homogeneous, and imcompressible turbulence of $\widetilde{\boldsymbol{V}}$, the above calculations yield (Chap. 13, Kulsrud, 2005)

$$\boldsymbol{\mathcal{E}}=\alpha\boldsymbol{B}_0-\beta\boldsymbol{\nabla}\times\boldsymbol{B}_0+... \tag{657}$$

where

$$\alpha=-\frac{1}{3}\int_{-\infty}^{t}dt'\left\langle\widetilde{\boldsymbol{V}}\cdot\left(\boldsymbol{\nabla}\times\widetilde{\boldsymbol{V}}\right)\right\rangle=-\frac{\tau}{3}\left\langle\widetilde{\boldsymbol{V}}\cdot\widetilde{\boldsymbol{\omega}}\right\rangle \tag{658}$$

$$\beta=-\frac{1}{3}\int_{-\infty}^{t}dt'\left\langle\widetilde{\boldsymbol{V}}\cdot\widetilde{\boldsymbol{V}}\right\rangle=\frac{\tau}{3}\left\langle\widetilde{V}^2\right\rangle. \tag{659}$$

Here $\left\langle\widetilde{\boldsymbol{V}}\cdot\widetilde{\boldsymbol{\omega}}\right\rangle$ and $\left\langle\widetilde{V}^2\right\rangle$ are turbulent kinetic helicity (see below) and turbulent energy, respectively, and τ is turbulent correlation time. All of these are statistical properties of small-scale velocity fluctuations. In other words, large-scale dynamos are determined by small-scale turbulence. This is a remarkable result.

Physically, α represents a turbulent EMF along the mean field to drive the electric current on the large scale. This twists up the mean field lines helically as in a screw pinch. This corresponds to the α-effect in Parker's $\alpha-\omega$ dynamo model. The plumes, represented by $\widetilde{\boldsymbol{V}}$, are associated with a twist due to Coriolis force from rotation, represented by $\widetilde{\boldsymbol{\omega}}$. $\widetilde{\boldsymbol{V}}$ and $\widetilde{\boldsymbol{\omega}}$ are in the same direction leading to a finite α-effect per Eq. (658). As shown in Fig. 93, if the twist angle is between 0° and 180°, the twisted field line requires an electric current along the original field line. This is an expected result by the

parallel component of $\boldsymbol{\mathcal{E}}$ along $\boldsymbol{B}_0$, or the α-effect of the mean-field dynamo theory. In contrast, the β component in $\boldsymbol{\mathcal{E}}$ appears as a coefficient of mean electric current, along side of the regular resistivity in Eq. (655). Thus, β represents turbulent mixing of the mean magnetic field by small-scale velocity fluctuations. Note that the turbulent mixing can naturally lead to (but does not automatically guarantee) magnetic reconnection to smooth out field gradient. See the discussion at the end of Sec.11.3 on fast dynamo.

Like kinematic dynamo problem, the classic mean-field dynamo theory does not taken into account feedback of dynamo effects (α and β effects) into the equation of motion for velocity. The full nonlinear problem including the feedback is a subject of modern mean-field dynamo theory. As it turns out, the nonlinear problem is closely related to the simplifying assumptions that were used: the natural systems are not homogeneous as they are bounded in space as in any astrophysical objects with specific boundary conditions; they are not isotropic as they are convectively unstable against gravity and they are typically rotating; and they have large-scale flow shear as in accretion disks. In addition, the expansion coefficients in Eq. (657), α and β, are not necessarily only scalars, and they are 3×3 tensors in general. Relaxing each of the above assumptions is often reflected in appearance of specific matrix elements of the α and β tensors as well as different associated nonlinear feedback channels. A comprehensive understanding of dynamo process on the large scale demands systematic investigations of each of these effects and their combinations. Despite the long history and significant progress, therefore, the large-scale dynamo problem is still largely unsolved.

11.8 Laboratory Detection of α Effect

On the other hand, the α-effects due to turbulent EMF have been directed measured in magnetized plasma experiments. As discussed in Lecture 2, there is a class of magnetically confined plasma experiments in toroidal geometry called Reversed Field Pinches (RFP), similar to tokamaks but with an order of magnitude larger plasma current, and thus at much lower safety factor $q \ll 1$. At such low q values, RFP is unstable to many current-driven instabilities as discussed in Lecture 7 to exhibit large-amplitude fluctuations, but remarkably the plasma discharge as a whole does not suffer major disruptions or terminations. Due to their large plasma currents, the poloidal field is comparable to toroidal field which interestingly reverses it direction between the plasma core to edge. Externally, a large inductive torodial electric field is applied by an Ohmic transformer to drive the large plasma current. Projecting this external toroidal electric field along the magnetic field yields a radial profile of $E_\parallel$ reversing it sign from the plasma core to edge, as shown in Fig. 94. However, the resistive electric field, $\eta j_\parallel$, remains the same sign, creating a mismatch between two electric fields.

This mismatch can be balanced by the turbulent EMF or more precisely the α effect as explained below. For a resistive MHD Ohm's law of $\boldsymbol{E}+\boldsymbol{V}\times\boldsymbol{B} = \eta\boldsymbol{j}$,

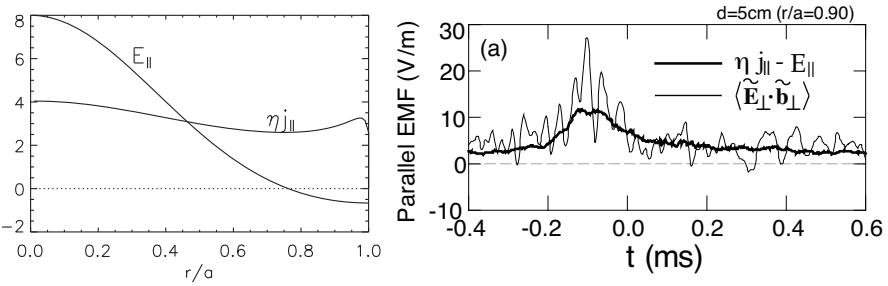

Fig. 94 Detection of α-effect on a Reversed Field Pinch (RFP) plasma. (left panel) Steady state radial profiles of externally applied parallel electric field $E_\parallel$ and parallel resistive electric field $\eta j_\parallel$. A significant parallel electric field is needed to balance them. (right panel) Measured parallel component of turbulent EMF or α-effect (thick line) can explain the mismatch between external electric field $E_\parallel$ and resistive electric field (thin line) as a function of time at a fixed radial location. From Ji et al (1994); Ji and Prager (2002).

its mean and turbulent parts are given by

$$\boldsymbol{E}_0 + \boldsymbol{V}_0 \times \boldsymbol{B}_0 + \boldsymbol{\mathcal{E}} = \eta \boldsymbol{j}_0 \tag{660}$$

$$\widetilde{\boldsymbol{E}} + \widetilde{\boldsymbol{V}} \times \boldsymbol{B}_0 + \boldsymbol{V}_0 \times \widetilde{\boldsymbol{B}} + \widetilde{\boldsymbol{V}} \times \widetilde{\boldsymbol{B}} - \boldsymbol{\mathcal{E}} = \eta \widetilde{\boldsymbol{j}} \tag{661}$$

where $\boldsymbol{\mathcal{E}} = \left\langle \widetilde{\boldsymbol{V}} \times \widetilde{\boldsymbol{B}} \right\rangle$. Taking the parallel component of the mean electric field equation, Eq. (660), leads to

$$E_{0\parallel} + \frac{\boldsymbol{\mathcal{E}} \cdot \boldsymbol{B}_0}{B_0} = \eta j_{0\parallel}, \tag{662}$$

where the second term on the left-hand side represents the α effect per Eq. (657). This α can be expressed as

$$\alpha = \frac{\boldsymbol{\mathcal{E}} \cdot \boldsymbol{B}_0}{B_0^2} = \frac{\left\langle \widetilde{\boldsymbol{V}} \times \widetilde{\boldsymbol{B}} \right\rangle \cdot \boldsymbol{B}_0}{B_0^2} = -\frac{\left\langle \left(\widetilde{\boldsymbol{V}} \times \boldsymbol{B}_0 \right) \cdot \widetilde{\boldsymbol{B}} \right\rangle}{B_0^2},$$

where $\widetilde{\boldsymbol{V}} \times \boldsymbol{B}_0$ can be substituted via Eq. (661),

$$\widetilde{\boldsymbol{V}} \times \boldsymbol{B}_0 = -\widetilde{\boldsymbol{E}} - \boldsymbol{V}_0 \times \widetilde{\boldsymbol{B}} - \widetilde{\boldsymbol{V}} \times \widetilde{\boldsymbol{B}} + \boldsymbol{\mathcal{E}} + \eta \widetilde{\boldsymbol{j}}.$$

Taking dot product of the above equation with $\widetilde{\boldsymbol{B}}$ removes second and third terms on the right-hand side, and then taking averaging removes the fourth term. The remaining first term and fifth term lead to

$$\alpha = \frac{\left\langle \widetilde{\boldsymbol{E}} \cdot \widetilde{\boldsymbol{B}} \right\rangle}{B_0^2} - \frac{\left\langle \eta \widetilde{\boldsymbol{j}} \cdot \widetilde{\boldsymbol{B}} \right\rangle}{B_0^2} = \frac{\left\langle \widetilde{\boldsymbol{E}}_\perp \cdot \widetilde{\boldsymbol{B}}_\perp \right\rangle}{B_0^2} - \frac{\left\langle \eta \widetilde{\boldsymbol{j}}_\perp \cdot \widetilde{\boldsymbol{B}}_\perp \right\rangle}{B_0^2} \approx \frac{\left\langle \widetilde{\boldsymbol{E}}_\perp \cdot \widetilde{\boldsymbol{B}}_\perp \right\rangle}{B_0^2}, \tag{663}$$

where $\widetilde{E}_{\parallel} = \eta \widetilde{j}_{\parallel}$ is used for the second equal sign. Both $\widetilde{\boldsymbol{E}}_{\perp}$ and $\widetilde{\boldsymbol{B}}_{\perp}$ due to MHD instabilities were actually measured at approximately the same spatial location for their correlation study (Ji et al, 1994). One of the results at a fixed location but as a function of time is shown in Fig. 94, in good agreement with the expectation from Eq. (662). Therefore, the MHD instabilities in RFP generate properly correlated velocity and magnetic fluctuations so that the resultant turbulent EMF can drive the required parallel equilibrium current to cause toroidal magnetic field to reverse its direction for the RFP configuration. Often, the α effect observed in RFP is called the RFP dynamo. Similar α effects are also observed in spheromaks (Al-Karkhy et al, 1993).

Even the required spatial scale separation in the large-scale astrophysical dynamo does not apply in RFP, the actual detection of α-effects in a real physical system is still a significant step for the mean field theory in general. It confirms that the principal idea behind mean-field theory is valid, at least when the temporal scale separation applies between the slowly varying mean field profiles and rapid fluctuations due MHD instabilities. Since there are no fundamental distinctions between spatial and temporal scale separations in terms of mean-field theory, it is a reasonable expectation that the mean-field theory should be valid for the large-scale dynamo problem. Nonetheless, each of simplifying assumptions of classic mean-field dynamo theory should be carefully examined for any specific cases before actual application. Since each application is specific, there may exist many different types of the dynamo solutions as opposed to one particular dynamo solution applicable universally everywhere.

In the case of the RFP dynamo, the assumption of turbulence isotropy is violated as the external Ohmic drive by transformer uniquely points one particular toroidal direction relative to the toroidal field or a particular sign of field line twist (magnetic helicity, see Lecture 12). Furthermore, there exist a radially inward flux of electromagnetic energy (Poyngting flux) by the Ohmic drive which is balanced in steady state by a radially outward flux of plasma energy due to dissipation of magnetic field energy by reconnection and turbulence. The mean-field theory under these particular conditions exhibits certain properties which might be relevant to astrophysical dynamos (Ji, 1999). In any cases, availability of laboratory experiments and feasibility of numerical simulations with sufficient scale separations will ultimately determine the validity and applicability of mean-field theory of large-scale dynamos.

11.9 Summary

- Magnetic dynamo, or generation of magnetic field by plasma motion, is a fundamental MHD process in planets, stars, astrophysical plasmas, as well as in some of fusion plasmas.
- Kinematic dynamo problems deal with linear growth of magnetic field but feedback by Lorentz force on velocity field needs to taken into account in the nonlinear dynamo problems.

- The field growth on the resistive time scale is called slow dynamo, which are the cases of geodynamo or laboratory dynamo, but solutions of fast dynamo, such as the scratch-twist-fold example, are needed to explain many astrophysical dynamos such as solar dynamo.
- Cowling's anti-dynamo theorem prohibits a subclass of the desired dynamo solutions but Biermann battery effects circumvent its application by including physics beyond classic MHD, such as during laser-target interaction.
- Parker's $\alpha-\omega$ dynamo model brought up a specific scenario for fast dynamo, involving both small-scale and large-scale fields, which may work in general for convectively unstable rotating plasmas. The small-scale dynamo has attracted attension in recent years.
- Mean-field theories provide a practical framework to describe the growth of large-scale field out of small-scale turbulence but need to adapt to each specific situation to make further progress.
- The α effects of turbulent electromotive force (EMF) has been successfully detected in magnetically confined plasmas.

11.10 Further Readings

- Chapters 13 in Kulsrud (2005).
- Review chapter by Roberts (1994).
- Review paper by Ji and Prager (2002) on the α-effect detected in Reversed Field Pinch or RFP.

12 Magnetic Self-Organization and MHD Turbulence

As the last lecture of our course, a concise introduction to two outstanding and inter-connected subjects are given: magnetic self-organization and MHD turbulence. MHD turbulence emerged from its hydrodynamic counterpart with additional insights based on physics of MHD while the concept of magnetic self-organization has been developed relatively independently but it turned out to be closely related to MHD turbulence, as well as magnetic reconnection and dynamo that we have discussed in previous Lectures.

12.1 Magnetic Self-Organization

12.1.1 Non-equilibrium Thermodynamics and Self-organization

It should be recognized and appreciated that a large portion of the modern physics is built on the premise of equilibrium thermodynamics. This is unfortunate because the physical world around us is *not* really in a thermodynamic equilibrium and yet the physics of non-equilibrium thermodynamics is *still* underdeveloped despite its long history. As a result for a practical purpose, we often than not *pretend* as if the laws of equilibrium thermodynamics still applies in non-equilibrium thermodynamics. This fundamental fraud is widespread in physics in general; and plasma physics including the subject of this lecture on magnetohydrodynamics is not an exception. Most of the topics discussed thus far in this lecture, such as MHD models, MHD equilibrium, the concept of energy principle and its associated various instabilities, are all subject to a suspicion that they might be invalid after all, despite of the mounting evidence that they actually work, as we discussed throughout in this class.

This paradoxical situation is sometime explained as the assumption of thermodynamic equilibrium may be valid *locally* even the global system is not in

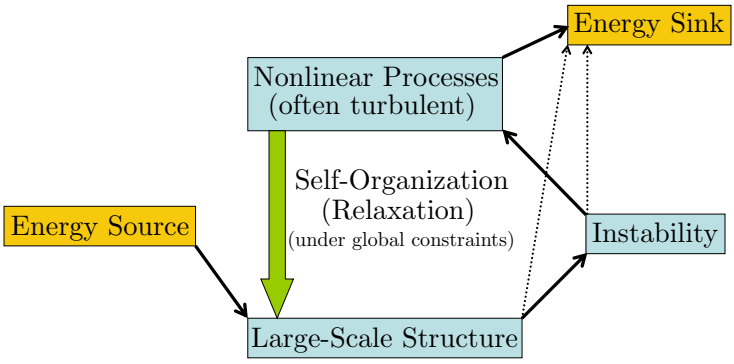

Fig. 95 Self-organization or relaxation process of an open system which has energy source and sink.

a thermodynamic equilibrium. This is to state that thermodynamic variables, such as temperature and entropy, are well defined locally, even they may vary on a global scale in an inhomogeneous system seen in fusion devices or astrophysical objects. It should be noted that the inhomogeneity here is closely related to the fact that the system is open – being able to take in or release matters, momentum or energy either through its boundary or volumically such as radiation. With constant input from outside, these open systems are often called *driven* systems.

Then, without a solid physics foundation from non-equilibrium thermodynamics an unsettling but important question naturally arise: what decides the *global* inhomogeneity or structure of such a non-equilibrium system, which is open and driven? This question motivates the concept of self-organization or relaxation which is illustrated graphically in Fig. 95. The large-scale structure receives energy input from the outside and is unstable leading to nonlinear processes that are often turbulent. The nonlinear processes "relax" the original large-scale structure (the green arrow) to reach its quasi-steady state by shedding excess energy to energy sink leaving the system. The large-scale structure and instability can also possibly dissipate energy to energy sink indicated by the dotted arrows.

However, such self-organization processes are subject to global constraints. In magnetized systems with large Lundquist numbers, total magnetic flux is well conserved. In fact, ideal MHD systems have infinite numbers of globally conserved quantities. One such constraint is conservation of magnetic helicity.

12.1.2 Conservation of Magnetic Helicity

Magnetic helicity of a magnetized plasma is defined as

$$K \equiv \int (\boldsymbol{A} \cdot \boldsymbol{B})\, dV \tag{664}$$

where V is the volume of the subject plasma and $\boldsymbol{A}$ is a vector potential of magnetic field $\boldsymbol{B}$, $\boldsymbol{B} = \boldsymbol{\nabla} \times \boldsymbol{A}$. The value of K quantifies how much magnetic field lines in V are topologically inter-knotted or inter-linked with itself. To illustrate this, imagine that there are two thin flux tubes, Φ_1 occupying volume V_1 and Φ_2 occupying volume V_2, topologically inter-linked as shown in Fig. 96. Since the incremental volume dV can be written as $dV = \boldsymbol{S} \cdot d\boldsymbol{l}$ where $\boldsymbol{S}$ is a vector pointing along a thin flux tube and its magnitude is the thin tube's cross-sectional area. $d\boldsymbol{l}$ is the incremental length vector along the thin flux tube. Then, magnetic helicity of this two-flux-tube system can be computed as

$$\begin{aligned} K &= \int_{V_1} (\boldsymbol{A} \cdot \boldsymbol{B})\, dV + \int_{V_2} (\boldsymbol{A} \cdot \boldsymbol{B})\, dV \\ &= \int_{V_1} (\boldsymbol{B} \cdot \boldsymbol{S})\, (\boldsymbol{A} \cdot d\boldsymbol{l}) + \int_{V_2} (\boldsymbol{B} \cdot \boldsymbol{S})\, (\boldsymbol{A} \cdot d\boldsymbol{l}) \end{aligned}$$

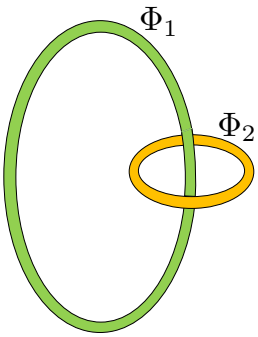

Fig. 96 Magnetic helicity: topological linkage of two flux tubes.

$$\begin{aligned} &= \Phi_1 \int_{V_1} \boldsymbol{A} \cdot d\boldsymbol{l} + \Phi_2 \int_{V_2} \boldsymbol{A} \cdot d\boldsymbol{l} \\ &= \Phi_1 \Phi_2 + \Phi_2 \Phi_1 = 2\Phi_1 \Phi_2. \end{aligned} \tag{665}$$

Here $\int_{V_1} \boldsymbol{A} \cdot d\boldsymbol{l} = \Phi_2$ since the loop integration along V_1 encircles flux tube Φ_2. If two flux tubes are not topologically inter-linked instead, $\int_{V_1} \boldsymbol{A} \cdot d\boldsymbol{l} = 0$. The same operation applies to the integration over V_2. Thus, the value of K represents whether these two flux tubes are inter-linked in this system.

There might be questions on whether such a definition of magnetic helicity, Eq. (664), is physically sound as it uses vector potential which is gauge-dependent while any physical quantities should be gauge-independent. In other words, K should not change under the gauge transformation $\boldsymbol{A} \to \boldsymbol{A} + \boldsymbol{\nabla}\chi$, where χ is a scalar potential. This demands the change in magnetic helicity, ΔK, under such transformation vanish,

$$\Delta K = \int (\boldsymbol{B} \cdot \boldsymbol{\nabla}\chi)\, dV = \int \boldsymbol{\nabla} \cdot (\chi \boldsymbol{B})\, dV = \int \chi \boldsymbol{B} \cdot d\boldsymbol{S} = 0, \tag{666}$$

where $\boldsymbol{S}$ is the surface of V. There are three ways to satisfy the gauge invariance Eq. (666):

- In singly connected volumes, $\boldsymbol{B}$ needs to be tangent everywhere on $\boldsymbol{S}$ so $\boldsymbol{B} \cdot d\boldsymbol{S} = 0$.
- In doubly connected volumes like a torus, $\boldsymbol{B} \cdot d\boldsymbol{S} = 0$ alone is insufficient to guarantee the gauge invariance due to the linkage between toroidal flux, Φ, of the torus and (unspecified) poloidal flux, Ψ, threading the center hole of the torus. Removal of this unknown linkage is needed for K defined by Eq. (664) to be gauge invariant, $K' = K - \Phi\Psi$.
- When $\boldsymbol{B} \cdot d\boldsymbol{S} \neq 0$, magnetic field lines are connected to outside of the subject volume with unknown linkages. In such cases, the unknown linkages

need to be removed from the definition by using the concept of relative helicity (Berger and Field, 1984).

Magnetic helicity is a conserved quantity in ideal MHD. This can be shown as in the following. Taking time derivative of Eq. (664) while using $\boldsymbol{E} = -\boldsymbol{\nabla}\phi - \partial\boldsymbol{A}/\partial t$ and Faraday's Law yields

$$\begin{aligned}\frac{\partial K}{\partial t} &= \int \left(\frac{\partial \boldsymbol{A}}{\partial t}\cdot\boldsymbol{B} + \boldsymbol{A}\cdot\frac{\partial \boldsymbol{B}}{\partial t}\right) dV \\ &= -\int (\boldsymbol{E}\cdot\boldsymbol{B} + \boldsymbol{B}\cdot\boldsymbol{\nabla}\phi + \boldsymbol{A}\cdot\boldsymbol{\nabla}\times\boldsymbol{E})\, dV \\ &= -2\int \boldsymbol{E}\cdot\boldsymbol{B} dV + \int (\phi\boldsymbol{B} + \boldsymbol{A}\times\boldsymbol{E})\, dV. \end{aligned} \tag{667}$$

In deriving the last step, we used vector identities,

$$\begin{aligned}\boldsymbol{\nabla}\cdot(\phi\boldsymbol{B}) &= \phi\boldsymbol{\nabla}\cdot\boldsymbol{B} + \boldsymbol{B}\cdot\boldsymbol{\nabla}\phi \\ &= \boldsymbol{B}\cdot\boldsymbol{\nabla}\phi \\ \boldsymbol{\nabla}\cdot(\boldsymbol{E}\times\boldsymbol{A}) &= \boldsymbol{A}\cdot\boldsymbol{\nabla}\times\boldsymbol{E} - \boldsymbol{E}\cdot\boldsymbol{\nabla}\times\boldsymbol{A} \\ &= \boldsymbol{A}\cdot\boldsymbol{\nabla}\times\boldsymbol{E} - \boldsymbol{E}\cdot\boldsymbol{B}. \end{aligned}$$

In ideal MHD, $\boldsymbol{E}\cdot\boldsymbol{B}$ vanishes identically, leaving only surface integral terms in the right-hand side of Eq. (667) which represents *flux of magnetic helicity*. However, the surface integral terms can only transport magnetic helicity across space and cannot generate nor destroy it. Thus, magnetic helicity is conserved. In reality, magnetic helicity conservation has been experimentally verified during magnetic self-organization or relaxation (Ji et al, 1995) as explained below.

12.1.3 Minimum Energy State

The origin of the problem traces back to the ZETA (Zero Energy Thermonuclear Assembly) device as a toroidal pinch experiment that was built during early days of fusion research of 1950s in UK. Against the common expectation from the $q_a > 1$ Kruskal-Shafranov limit (Kruskal and Schwarzschild, 1954; Shafranov, 1956) (see Lecture 7), the plasma current in ZETA was much larger resulting in $q_a \ll 1$, yet the plasma was observed to be "quiescent" implying the global stability, after a violent phase with large fluctuations. The relative stability was observed to be accompanied with the reversal of toroidal magnetic field from plasma center to edge, and thus the configuration was dubbed "Reversed Field Pinch" or RFP (see Lecture 2 for various confinement concepts). Figure 97 shows example measurements from a later device called HBTX-1A in UK. Poloidal field is large (comparable to toroidal field) due to large plasma current compared to tokamaks while the toroidal component changes its sign between core and edge. Here comes J.B. Taylor who took

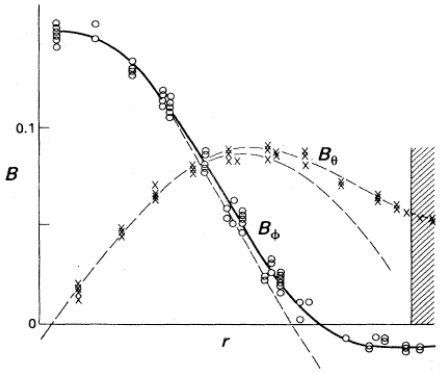

Fig. 97 Experimentally measured and theoretically predicted profiles of magnetic field from HBTX-1A RFP device from Taylor (1986).

a note on the "quiescence" and considered its implication that the RFP configuration is an energetically preferred state or minimum energy state (Taylor, 1974).

The minimum energy states or relaxed states can be derived in several different ways. A simplest way is to minimize magnetic energy,

$$W = \frac{1}{2\mu_0}\int B^2 dV, \tag{668}$$

subject to the constraints of Gauss's law $\boldsymbol{\nabla}\cdot\boldsymbol{B}=0$ and ideal MHD Ohm's law $\boldsymbol{E}+\boldsymbol{V}\times\boldsymbol{B}=0$. Under these conditions, from Lecture 4, we have the change in $\boldsymbol{B}$ or $\delta\boldsymbol{B}$ due to displacement $\boldsymbol{\xi}$ is given by $\delta\boldsymbol{B}=\boldsymbol{\nabla}\times(\boldsymbol{\xi}\times\boldsymbol{B})$. Therefore, the change in W or δW can be computed as

$$\begin{aligned}\delta W &= \frac{1}{\mu_0}\int \boldsymbol{B}\cdot\boldsymbol{\delta B}dV = \frac{1}{\mu_0}\int \boldsymbol{B}\cdot\boldsymbol{\nabla}\times(\boldsymbol{\xi}\times\boldsymbol{B})\,dV \\ &= -\frac{1}{\mu_0}\int \boldsymbol{\xi}\cdot(\boldsymbol{B}\times\boldsymbol{\nabla}\times\boldsymbol{B})\,dV = \int \boldsymbol{\xi}\cdot(\boldsymbol{j}\times\boldsymbol{B})\,dV.\end{aligned} \tag{669}$$

According to variational principle, for W to take an extremum including minimum, $\delta W=0$ for all possible $\boldsymbol{\xi}$. This demands $\boldsymbol{j}\times\boldsymbol{B}=0$ or *Lorentz force-free* or simply *force-free* in Eq. (669). Therefore, minimum energy force-free field can be expressed as

$$\boldsymbol{\nabla}\times\boldsymbol{B}=\lambda(\boldsymbol{r})\boldsymbol{B} \tag{670}$$

where $\lambda(\boldsymbol{r})$ is a scalar function of spatial location $\boldsymbol{r}$. Taking divergence operation of Eq. (670) yields

$$0=\lambda\boldsymbol{\nabla}\cdot\boldsymbol{B}+\boldsymbol{B}\cdot\boldsymbol{\nabla}\lambda(\boldsymbol{r})=\boldsymbol{B}\cdot\boldsymbol{\nabla}\lambda(\boldsymbol{r}) \tag{671}$$

which means that λ must be a constant along each field line. Note, however, that λ does not have to be a constant across different field lines.

12.1.4 Taylor's Relaxation Theory

However, the ideal MHD condition does not apply during the RFP relaxation when large fluctuations due to violent instabilities are observed, indicative of highly turbulent state of plasma including resistive processes like magnetic reconnection. Clearly, a different constraint is needed in the place of ideal MHD and magnetic helicity is certainly a candidate. Using resistive MHD Ohm's law, $\boldsymbol{E} + \boldsymbol{V} \times \boldsymbol{B} = \eta \boldsymbol{j}$, we have

$$\begin{aligned} \frac{\partial K}{\partial t} &= -2\eta \int \boldsymbol{j} \cdot \boldsymbol{B} dV \\ \frac{\partial W}{\partial t} &= -\eta \int j^2 dV, \end{aligned}$$

where surface terms are ignored because they represent transport across space without affecting conservation properties. Both magnetic helicity and magnetic energy decay on the resistive time scale, but for fluctuations on a small scale, δ, expressed in the corresponding wavenumber $k \equiv 2\pi/\delta$,

$$\begin{aligned} \frac{\partial K}{\partial t} &= -2\eta k B_k^2 \\ \frac{\partial W}{\partial t} &= -\eta k^2 B_k^2, \end{aligned}$$

where B_k is magnetic fluctuation amplitude on the scale k. If δ is determined by the current sheet thickness of Sweet-Parker reconnection with Lundquist number of $S \propto \eta^{-1}$ (see Lecture 10), we have

$$k \propto \delta^{-1} \propto S^{1/2} \propto \eta^{-1/2},$$

which leads to

$$\frac{\partial K}{\partial t} \propto -2\eta^{1/2} B_k^2 \tag{672}$$

$$\frac{\partial W}{\partial t} \propto -B_k^2. \tag{673}$$

Therefore, when $\eta \to 0$, magnetic helicity dissipation diminishes while magnetic energy dissipation remains finite. This consideration motivates the conjecture that magnetic energy is minimized while magnetic helicity is conserved during relaxation.

Yet there is still another conceptual difficulty to apply conservation of magnetic helicity. Magnetic topology should be preserved if magnetic helicity is conserved, but in a turbulent plasma undergoing magnetic reconnection, magnetic topology should be altered. Magnetic helicity of each flux tube should not be conserved due to the change in local connectivity of magnetic field lines. For example, the two flux tubes illustrated in Fig. 96 are initially topologically

linked but can become detached from each other through magnetic reconnection. In order to satisfy these two seemingly contradicting requirements — on the one hand magnetic helicity should be conserved when $\eta \to 0$ while on the other hand magnetic helicity should not be conserved locally where reconnection occurs — the plasma relaxation involving reconnection can be considered to re-distribute magnetic helicity within the plasma while conserving its total magnetic helicity (Taylor, 1974). In fact, the total magnetic helicity conservation has been experimentally confirmed, and the corresponding magnetic helicity flux has also been measured to transport magnetic helicity in space (Ji et al, 1995).

Taylor's theory states that the quiescent RFP configuration corresponds to a relaxed state with a minimum magnetic energy, W defined by Eq. (668), for a given total magnetic helivity, K defined by Eq. (96). This can be solved by using variational principle, $\delta(W-\mu K)=0$, where μ is the Lagrange multiplier. Focusing only on the integral of W and K, we have

$$\begin{aligned}\delta\left(B^2-\mu\boldsymbol{A}\cdot\boldsymbol{B}\right) &= 2\boldsymbol{B}\cdot\delta\boldsymbol{B}-\mu\delta\boldsymbol{A}\cdot\boldsymbol{B}-\mu\boldsymbol{A}\cdot\delta\boldsymbol{B}\\ &= 2\boldsymbol{B}\cdot(\boldsymbol{\nabla}\times\delta\boldsymbol{A})-\mu\delta\boldsymbol{A}\cdot\boldsymbol{B}-\mu\boldsymbol{A}\cdot(\boldsymbol{\nabla}\times\delta\boldsymbol{A})\\ &= 2\boldsymbol{\nabla}\cdot(\delta\boldsymbol{A}\times\boldsymbol{B})+2\delta\boldsymbol{A}\cdot\boldsymbol{\nabla}\times\boldsymbol{B}-\mu\delta\boldsymbol{A}\cdot\boldsymbol{B}\\ &\quad -\mu\boldsymbol{\nabla}\cdot(\delta\boldsymbol{A}\times\boldsymbol{A})-\mu\delta\boldsymbol{A}\cdot\boldsymbol{B}\\ &= \boldsymbol{\nabla}\cdot(2\delta\boldsymbol{A}\times\boldsymbol{B}-\mu\delta\boldsymbol{A}\times\boldsymbol{A})+2\delta\boldsymbol{A}\cdot(\boldsymbol{\nabla}\times\boldsymbol{B}-\mu\boldsymbol{B})\end{aligned}$$

where the surface terms vanish as $\delta\boldsymbol{A}$ can be set to zero there. To guarantee $\delta\left(B^2-\mu\boldsymbol{A}\cdot\boldsymbol{B}\right)=0$ for all possible $\delta\boldsymbol{A}$, the solution needs to be a force-free field,

$$\boldsymbol{\nabla}\times\boldsymbol{B}-\mu\boldsymbol{B}=0. \tag{674}$$

Note that this force-free field is distinguished from the force-free field by Eq. (670) where λ is a function of space while μ is a spatial constant. An important feature of all force-free fields is that plasma pressure gradient identically vanishes as $\boldsymbol{\nabla}p=\boldsymbol{j}\times\boldsymbol{B}=0$, which is *undesirable* for plasma confinement, unfortunately.

Since μ is a constant, applying curl operation to Eq. (674) leads to an eigenvalue problem,

$$\begin{aligned}&\boldsymbol{\nabla}\times(\boldsymbol{\nabla}\times\boldsymbol{B}-\mu\boldsymbol{B})=\boldsymbol{\nabla}\times\boldsymbol{\nabla}\times\boldsymbol{B}-\mu\boldsymbol{\nabla}\times\boldsymbol{B}=-\nabla^2\boldsymbol{B}-\mu^2\boldsymbol{B}\\ &=-\left(\nabla^2+\mu^2\right)\boldsymbol{B}=0,\end{aligned} \tag{675}$$

which can be solved in cylindrical coordinate (R,θ,Z) assuming axisymmetry to yield the well-known Bessel function solutions,

$$\begin{cases}B_R &= 0\\ B_Z &= B_0 J_0(\mu R)\\ B_\theta &= B_0 J_1(\mu R)\,.\end{cases}$$

Here B_Z and B_θ correspond to toroidal and poloidal fields, respectively. J_0 and J_1 are Bessel function of the first kind. By choosing a proper eigenvalue of μ, the force-free solution matches well the experimental measurements in RFP plasmas, see Fig. 97. In addition to RFP, there is another class of magnetic confinement configurations called spheromaks (see Lecture 2) which also exhibit similar relaxation or self-organization behaviors and have magnetic field profiles close force-free solutions but in spherical coordination (Taylor, 1986).

12.1.5 Relation with Energy Principle and Self-organization

By definition, minimum energy states, if static, should be stable against all ideal MHD instabilities that have been discussed. Here we examine it via energy principle described in Lecture 5 but using a specific form of the energy integral given in Lecture 7, reproduced here:

$$2\delta W = \int \left[\frac{|Q_\perp|^2}{\mu_0} + \frac{B^2}{\mu_0} |\boldsymbol{\nabla}\cdot\boldsymbol{\xi}_\perp + 2\boldsymbol{\xi}_\perp\cdot\boldsymbol{\kappa}|^2 + \gamma p\,|\boldsymbol{\nabla}\cdot\boldsymbol{\xi}|^2 \right.$$
$$\left. -2\,(\boldsymbol{\xi}_\perp\cdot\boldsymbol{\nabla}p)\,(\boldsymbol{\xi}_\perp\cdot\boldsymbol{\kappa}) - \frac{j_\parallel}{B}\,(\boldsymbol{\xi}_\perp\times\boldsymbol{B})\cdot\boldsymbol{Q}_\perp \right] dV, \tag{676}$$

where $\boldsymbol{Q}$ and $\boldsymbol{\xi}$ are perturbed magnetic field, $\boldsymbol{B}_1$ (while $\boldsymbol{B}$ is unperturbed magnetic field), and displacement vector, respectively. As discussed in Lecture 7, first three terms are positive definitive, contributing to stability. The second last term vanishes as $\boldsymbol{\nabla}p = 0$ for force-free fields. The only remaining question is about the last term.

By comparing $\boldsymbol{B}_1 \equiv \boldsymbol{Q} = \boldsymbol{\nabla}\times(\boldsymbol{\xi}\times\boldsymbol{B})$ and the definition of $\boldsymbol{B}_1 = \boldsymbol{\nabla}\times\boldsymbol{A_1}$ where $\boldsymbol{A}_1$ is perturbed vector potential, we have $\boldsymbol{A}_1 = \boldsymbol{\xi}\times\boldsymbol{B}$, leading to

$$\begin{aligned}\boldsymbol{A}_{1,\parallel} &= 0\\ \boldsymbol{A}_{1,\perp} &= \boldsymbol{\xi}\times\boldsymbol{B}.\end{aligned}$$

Furthermore from Eq. (674), we have $j_\parallel/B = \mu/\mu_0$ which is a spatial constant and can be taken out of the integration. Therefore, the last term of the energy integral becomes

$$-\int \left[\frac{j_\parallel}{B}\,(\boldsymbol{\xi}_\perp\times\boldsymbol{B})\cdot\boldsymbol{Q}_\perp\right] dV$$
$$= -\frac{j_\parallel}{B}\int \boldsymbol{A}_{1,\perp}\cdot\boldsymbol{B}_{1,\perp}dV = -\frac{j_\parallel}{B}\int \boldsymbol{A}_1\cdot\boldsymbol{B}_1 dV = 0, \tag{677}$$

where the last step is due to the fact that magnetic helicity is conserved despite the perturbation in ideal MHD. Thus, the energy integral $\delta W \geq 0$ for all

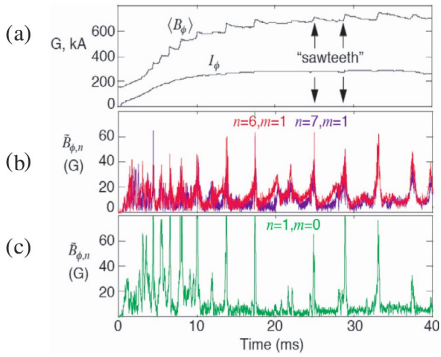

Fig. 98 Repeated relaxation events ("sawteeth") observed in a modern RFP device. From Prager et al (2005).

possible $\boldsymbol{\xi}$, confirm the expectation that (static) force-free minimum energy states are indeed stable against all ideal MHD instabilities.

From the above analysis, it seemed that minimum energy states should be ideal for magnetic confinement because of their stability. Unfortunately, this is not completely true. The reasons are not only due to the fact that force-free fields cannot support pressure gradient which is needed for confinement as mentioned before. This is also due to the observation that the "quiescent" phase of the RFP plasma is not sustained in modern RFP experiments and one example is shown in Fig. 98 for repeated relaxation events over time. After each event, the internal $\mu = j_\parallel/B$ profile flattens towards a relaxed state, but soon followed by peaking of the μ profile over time due to faster diffusion of $j_\parallel$ at plasma edge where electron temperature is lower. When the μ profile is sufficiently nonuniform, MHD instabilities (perhaps ideal instabilities coupled with tearing modes in the large-Δ' regime, see Lecture 10) are triggered to initiate the next relaxation events. The process repeats. The overall picture of the repeated relaxation events is illustrated as magnetic self-organization in Fig. 95.

The concept of magnetic relaxation or self-organization has been applied to solar corona where magnetic energy is released while conserving magnetic helicity. The often observed helical structures on the solar surface can be regarded as a consequence of relaxation which can shed magnetic energy but not helicity (Rust and Kumar, 1996). Over time, magnetic helicity accumulates and eventually reaches the limit beyond which violent instability occurs leading to coronal mass ejection (Zhang et al, 2006). The force-free field is the standard model now used to extrapolate field structures from the measured magnetic field vector on the solar photosphere to the solar corona for MHD stability analysis and numerical simulation. It also meets the requirement that the plasma β is low in corona. In this context, when a constant j/B is used, the force-free field is referred to as Linear Force-Free Field or LFFF. Otherwise, it is referred to as Nonlinear Force-Free-Field or NLFFF.

12.2 MHD Turbulence

The nonlinear processes described above for magnetic self-organization often involves dynamics across multiple scales which are sometimes called plasma turbulence in general. In this last part of this class, a concise introduction is given for plasma turbulence in the MHD regime.

12.2.1 Effects of Turbulence

Turbulence is a universal phenomenon long recognized in fluid dynamics. There is a famous quote (Goldstein, 1969) from a renowned physicist Sir Horace Lamb nearly a century ago in 1932: "I am an old man now, and when I die and go to Haven there are two matters on which I hope enlightenment. One is quantum electrodynamics and the other is turbulence. About the former, I am really rather optimistic." This speaks for the complex nature of turbulence which is still an unsolved problem despite significant progress made over the decades. Several important concepts and results of hydrodynamic turbulence are discussed below to serve as a starting point to introduce MHD turbulence.

It makes a good sense to use mean-field theory for the study of turbulence, which typically exhibits seemingly "random" fluctuations from its mean quantities. Statistical methods, such as averaging and correlation, can be applied to any measured quantify $V(t)$, to obtain

$$\begin{aligned} V &= \langle V \rangle + \widetilde{V} \\ R(\tau) &= \langle V(t)V(t+\tau) \rangle \end{aligned}$$

where averaging $< ... >$ is applied over the time so $\langle V \rangle$ is the average of V. τ is the time lag for the autocorrelation function $R(\tau)$ which can be normalized,

$$r(\tau) \equiv \frac{\langle V(t)V(t+\tau) \rangle}{\langle V^2 \rangle} \leq 1, \tag{678}$$

where the latter inequality is due to *Schwartz inequality*. In addition to autocorrelation, a cross-correlation between two quantities $U(t)$ and $V(t)$ can be defined as $C(\tau) \equiv \langle U(t)V(t+\tau) \rangle$, as well as its normalized version. According to Eq. (678), $r(0) = 1$, and normally $r(\infty) = 0$ indicating that memory is lost with sufficient time lag, as one outstanding characteristics of turbulence. Therefore, an integral time scale T can be defined as

$$T \equiv \int_0^\infty r(\tau) d\tau, \tag{679}$$

as a measure of the memory of the turbulence. This T can be used to estimate the so-called "eddy viscosity", an effective dissipation coefficient due to turbulence. The molecular or classical viscosity is estimated as

$$\nu_{\text{molecule}} \sim l_{\text{mfp}}^2 T_{\text{collision}}^{-1} \tag{680}$$

where $l_{\rm mfp}$ is the mean-free-path and $T_{\rm collision}$ is collision time. Then T can be regarded as an effective "collision" time to lose memory in turbulence, and thus the corresponding eddy viscosity can be estimated as

$$\nu_{\rm eddy} \sim l_{\rm eddy}^2 T^{-1} \tag{681}$$

where $l_{\rm eddy}$ is the smallest eddy size of the turbulence.

The above average and correlation procedures are performed over the time, but they can be also applied in space for spatial correlation and integral spatial scale or the so-called correlation length. In practice, however, it is much more common to have measurements with high temporal resolutions then with spatial resolutions. If a frozen spatial structure passes the measurement point, the temporal variation reflects the spatial variation by replacing t by x/U_0, where U_0 is the advection speed. This assumption of frozen structures is called *Taylor's hypothesis*. Having measurements at multiple spatial points can avoid using this hypothesis as done by space MMS mission to study magnetic reconnection as mentioned in Lecture 10.

In Lecture 11, we discussed mean-field dynamo theory in which the large-scale magnetic field can grow out from the turbulent EMF due to small-scale dynamics. The same procedure can be applied to large-scale flow leading to an equation similar to Eq. (655),

$$\frac{\partial \boldsymbol{V}_0}{\partial t} + (\boldsymbol{V}_0 \cdot \boldsymbol{\nabla})\, \boldsymbol{V}_0 = -\frac{\boldsymbol{\nabla} P_0}{\rho} + \nu \nabla^2 \boldsymbol{V}_0 - \boldsymbol{\nabla} \cdot \left\langle \widetilde{\boldsymbol{V}} \widetilde{\boldsymbol{V}} \right\rangle, \tag{682}$$

where the last term is Reynolds stress (Kundu et al, 2015, Ch.12) due to turbulence. Here $\boldsymbol{V}_0 \equiv \langle \boldsymbol{V} \rangle$ and $P_0 \equiv \langle P \rangle$ while density ρ is assumed to be uniform in an incompressible flow. Therefore, the mean flow can be generated or dissipated by turbulence.

In MHD, similar procedures can be performed to add the standard Lorentz force due to large-scale magnetic field and Maxwell stress due to turbulence in the right-hand side of Eq. (682),

$$\frac{\boldsymbol{j}_0 \times \boldsymbol{B}_0}{\rho} + \boldsymbol{\nabla} \cdot \left\langle \frac{\widetilde{\boldsymbol{B}} \widetilde{\boldsymbol{B}}}{\mu_0 \rho} \right\rangle.$$

The latter is similar to the α-effect and β-effect on the large-scale magnetic field in the mean-field dynamo theory.

12.2.2 Cascade and Kolmogorov's -5/3 Law

As an important concept of turbulence, the cascade process was introduced a century ago by Richardson (1922) and is illustrated in Fig. 100 where energy spectra, S, of turbulence as a function of scale or wavenumber, k, are shown. Energy is injected on the large system scales (small k) and is dissipated on the small scales (large k). In between these two ends of the scales, energy flows from

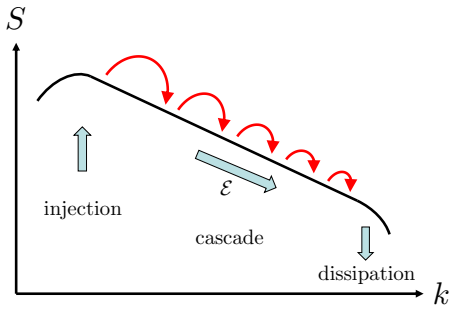

Fig. 99 Energy injection, cascade and dissipation in turbulence.

large scales to small scales in a self similar fashion. In other words, from the system scale larger eddies break down to smaller eddies, which further break down to even smaller eddies in a similar way, and the process repeats until the scale reaches dissipation scale. The cascade process should be scale-invariant, i.e., the exact same process is occurring everywhere in the k space, except at two ends. This demands the spectral functions in the k space be power laws, $S \propto k^x$ where x is a (negative) constant, as compared to, e.g., exponential functions which always have a characteristic scale, as k_0 in $\exp(-k/k_0)$. The power-law part of the spectra is also called *inertial range* of the spectra. The scale-invariant nature of cascade process provides a much desirable flexibility for turbulence to connect energy injection scale to dissipation scale regardless the separation between these scales. Thus, probably it is not an overstatement that the cascade process makes turbulence a universal phenomenon across many disciplines.

Kolmogorov (1941) made further progress in turbulence theory by discovering $x = -5/3$ for the energy spectra which is referred commonly to Kolmogorov spectrum. This can be derived from dimensional analysis as below. The energy spectra should depend on only two parameters, wavenumber k and energy cascade flux $\mathcal{E}$,

$$S(k, \mathcal{E}) \propto k^x \mathcal{E}^y, \tag{683}$$

where k has a dimension of $[k] = L^{-1}$ and $\mathcal{E}$ has the dimension of $V \cdot \nu\nabla^2 V$ since $\nu\nabla^2 V$ represents the energy dissipation:

$$[\mathcal{E}] = \frac{L}{T} \cdot \frac{L^2}{T} \cdot \frac{1}{L^2} \cdot \frac{L}{T} = \frac{L^2}{T^3}.$$

From the definition of S, $\langle V^2 \rangle = \int S dk$, $[S] = L^3 T^{-2}$. Therefore, the dimensions of Eq. (683) become

$$\frac{L^3}{T^2} \propto \left(\frac{1}{L}\right)^x \left(\frac{L^2}{T^3}\right)^y,$$

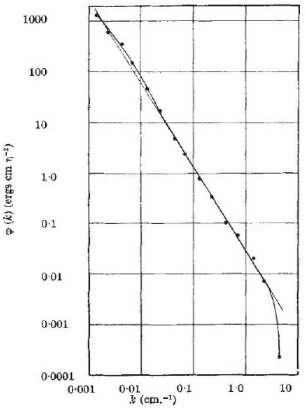

Fig. 100 Measured turbulent energy spectrum in a sea-water channel at $Re = 4 \times 10^7$, confirming Kolmogorov's -5/3 law. From Grant et al (1959).

which leads to

$$\begin{aligned} 3 &= -x + 3y \\ -2 &= -3y \end{aligned}$$

with the solution of $x = -5/3$ and $y = 2/3$. More precisely,

$$S = C_K k^{-5/3} \mathcal{E}^{2/3}, \tag{684}$$

where $C_K = 1.6 - 1.7$ is Kolmogotov constant (Kolmogorov, 1941). This is known as *Kolmogorov's -5/3 law*. However, this Kolmogorov's -5/3 law was not confirmed in experiments nor observations for a long time until Grant et al (1959) due to the difficulties in generating high Re turbulence in the laboratory.

The Kolmogorov's -5/3 law can be derived also by the following phenomenological arguments (Biskamp, 2003, Ch.5). The energy contained in eddies of each size, $l_n \sim k_n^{-1}$, is $S_n \sim (\delta V_n)^2$ where δV_n is turbulent velocity amplitude at l_n. The cascade hypothesis is that the energy transfer is essentially local in k space, i.e., energy from eddies of one size l_n can be transferred by distortion only to the next size, l_{n+1}, over the eddy turnover time,

$$\tau_n \sim \frac{l_n}{\delta V_n}.$$

Therefore, the energy cascade flux is given by

$$\mathcal{E} \sim \frac{S_n}{\tau_n} \sim \frac{(\delta V_n)^2}{l_n/\delta V_n} = \frac{(\delta V_n)^3}{l_n} \tag{685}$$

which can be rewritten to

$$\delta V_n \sim \mathcal{E}^{1/3} l_n^{1/3} \sim \mathcal{E}^{1/3} k_n^{-1/3}. \tag{686}$$

We can express energy spectrum in terms of wavenumber spectrum, $S_n \sim S_k dk_n$, where $dk_n \sim k_n$. Therefore, with the use of Eq. (686), we have

$$S_k(\text{Kol}) \sim \frac{S_n}{dk_n} \sim \frac{S_n}{k_n} \sim \frac{(\delta V_n)^2}{k_n} \sim \mathcal{E}^{2/3} k_n^{-5/3} = \mathcal{E}^{2/3} k^{-5/3}, \tag{687}$$

which recovers the Kolmogorov's -5/3 law, Eq. (684).

This cascade concept complements well the self-organization concept (see Fig. 95) introduced earlier this lecture. The energy source is on the global large scales while the energy sink is on the local dissipation scales. The instability leads to turbulence in which energy cascades toward dissipation scale. However, the self-organization or relaxation process, through which the large-scale structures are modified, is not part of the cascade process discussed above. More specifically, the turbulent cascade does not capture the physics of self-organization. During self-organization, the large-scale magnetic field is generated or modified via turbulent EMF as in mean-field dynamo theory and the mean flow is modified by Reynolds stress. This requires that energy is transferred from small scales to large scale, in the opposite direction of cascade. This is called *inverse cascade*, which distinguishes from the normal cascade in the classical picture of Kolmogorov turbulence. The inverse cascade occurs in both hydrodynamics and MHD.

12.2.3 Effects of Large-scale Field and Elsässer Fields

A sufficiently strong mean (guide) magnetic field alters the hydrodynamic turbulence in a fundamental way. We can appreciate this by the following excise. In ideal MHD, the cross helicity, H, defined as

$$H = \int \boldsymbol{V} \cdot \boldsymbol{B} dV,$$

is conserved (see Homework). As in Taylor's relaxation theory, we attempt to minimize the combined magnetic energy and flow energy while conserving cross helicity using variational principle, $\delta(W - \lambda H) = 0$. Here λ is the Langrange multiplier, and W here is defined as

$$W = \int \left(\frac{\rho V^2}{2} + \frac{B^2}{2\mu_0} \right) dV.$$

Thus, we have

$$\delta(W - \lambda H) = \delta \left[\int \left(\frac{\rho V^2}{2} + \frac{B^2}{2\mu_0} \right) dV - \lambda \int \boldsymbol{V} \cdot \boldsymbol{B} dV \right]$$

$$= \int \delta \boldsymbol{V} \cdot (\rho \boldsymbol{V} - \lambda \boldsymbol{B})\, dV - \int \delta \boldsymbol{B} \cdot \left(\frac{\boldsymbol{B}}{\mu_0} - \lambda \boldsymbol{V} \right) dV.$$

To guarantee $\delta(W - \lambda H) = 0$ for all possible $\delta \boldsymbol{V}$ and $\delta \boldsymbol{B}$, we need to salmultanuously satisfy,

$$\rho \boldsymbol{V} = \lambda \boldsymbol{B} = 0 \quad \text{and} \quad \frac{\boldsymbol{B}}{\mu_0} = \lambda \boldsymbol{V}.$$

Eliminating λ by taking ratio of the above two equations leads to the solution,

$$\boldsymbol{V} = \pm \frac{\boldsymbol{B}}{\sqrt{\mu_0 \rho}}, \tag{688}$$

i.e., the plasma flows along the magnetic field at Alfvén speed. This is called Alfvénic state which is a minimum-energy state that MHD plasmas tend to relax towards with sufficiently large flow and magnetic field. The Alfvénic states have equal flow energy and magnetic energy, which is said to have equipartition between field and flow. The tendency that plasmas have to align flow to its magnetic field (or vice versa) is referred to as dynamic alignment, that has been observed numerically, as well as in solar wind especially when close to the Sun. This reminds us about rotational discontinuity and Alfvén mode shock solutions that we discussed in Lecture 4. They represent unique cases that exist only in MHD with sufficiently large flow and field. In addition, this also reminds us about alignment of electric current $\boldsymbol{j}$ to magnetic field in the force-free field when magnetic energy is minimized while conserving magnetic helicity in static MHD plasmas, as mentioned earlier in this Lecture.

Given that Alfvénic states are preferred states for the magnetized MHD plasmas, it is convenient to introduce Elsässer variables (Elsasser, 1950) defined as

$$\boldsymbol{Z}^{\pm} \equiv \boldsymbol{V} \pm \frac{\boldsymbol{B}}{\sqrt{\mu_0 \rho}} \tag{689}$$

which quantify how far from the preferred Alfvénic states. $\boldsymbol{Z}^{\pm} = 0$ represent exact Alfvénic states. The aforementioned total energy and cross helicity can be written in terms of $\boldsymbol{Z}^{\pm}$ as well. Using incompressible, visco-resistive MHD equations,

$$\frac{\partial \boldsymbol{V}}{\partial t} + (\boldsymbol{V} \cdot \boldsymbol{\nabla})\, \boldsymbol{V} = -\boldsymbol{\nabla} \left(\frac{P}{\rho} + \frac{B^2}{2\mu_0 \rho} \right) + \frac{1}{\mu_0 \rho} (\boldsymbol{B} \cdot \boldsymbol{\nabla})\, \boldsymbol{B} + \frac{\nu}{\rho} \nabla^2 \boldsymbol{V} \tag{690}$$

$$\frac{\partial \boldsymbol{B}}{\partial t} + (\boldsymbol{V} \cdot \boldsymbol{\nabla})\, \boldsymbol{B} = (\boldsymbol{B} \cdot \boldsymbol{\nabla})\, \boldsymbol{V} + \frac{\eta}{\mu_0} \nabla^2 \boldsymbol{B} \tag{691}$$

$$\boldsymbol{\nabla} \cdot \boldsymbol{B} = 0 \tag{692}$$

$$\boldsymbol{\nabla} \cdot \boldsymbol{V} = 0, \tag{693}$$

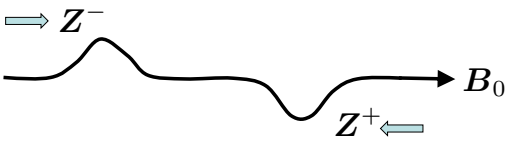

Fig. 101 Counter-propagating Alfvén waves.

the governing equations for $\boldsymbol{Z}^{\pm}$ can be derived (see Homework),

$$\frac{\partial \boldsymbol{Z}^{\pm}}{\partial t} + \left(\boldsymbol{Z}^{\mp} \cdot \boldsymbol{\nabla}\right) \boldsymbol{B}^{\pm} = -\boldsymbol{\nabla}\left(\frac{P}{\rho} + \frac{B^2}{2\mu_0 \rho}\right) + \frac{1}{2}\left(\frac{\nu}{\rho} + \frac{\eta}{\mu_0}\right) \nabla^2 \boldsymbol{Z}^{\pm} + \frac{1}{2}\left(\frac{\nu}{\rho} - \frac{\eta}{\mu_0}\right) \nabla^2 \boldsymbol{Z}^{\mp} \tag{694}$$

$$\boldsymbol{\nabla} \cdot \boldsymbol{Z}^{\pm} = 0. \tag{695}$$

In the ideal limit, Eq. (694) can be linearlized around a uniform $\boldsymbol{B}_0$ to yield,

$$\frac{\partial \boldsymbol{Z}^{\pm}}{\partial t} \mp \left(\boldsymbol{B}_0 \cdot \boldsymbol{\nabla}\right) \boldsymbol{Z}^{\pm} = 0, \tag{696}$$

which has solutions of $\boldsymbol{Z}^-(x - B_0 t)$ representing Alfvén waves propagating along $\boldsymbol{B}_0$ and $\boldsymbol{Z}^+(x + B_0 t)$ representing Alfvén waves propagating along $-\boldsymbol{B}_0$. Nonlinear interaction between counter-propagating Alfvén waves represented by Elsässer variables, as illustrated in Fig. 101, is a leading theory for solar wind heating, and also serves as the foundation of Iroshnikov-Kraichnan MHD turbulence theory which will be discussed next.

12.2.4 Iroshnikov-Kraichnan Theory and Goldreich-Sridhar Theory

In this subsection, a brief introduction is given for two leading and often competing theories for MHD turbulence. The first theory is by Iroshnikov (1964) and Kraichnan (1965), independently. The second theory is jointly by Sridhar and Goldreich (1994); Goldreich and Sridhar (1995).

The Iroshnikov and Kraichnan (IK) theory assumes a large-scale, strong background magnetic field, $\boldsymbol{B}_0$. Turbulence is due to collisions (or nonlinear interactions) of counter-propagating Alfvén waves, represented by Elsässer variables, $\boldsymbol{Z}^{\pm}$. Due to the strong $\boldsymbol{B}_0$, Alfvénic transit time, τ_A, is short compared with eddy turnover time, τ_l, at scale l,

$$\tau_A \sim \frac{l}{V_A} \ll \tau_l \sim \frac{l}{\delta Z_l},$$

and thus, distortion of eddies is small by each collision,

$$\frac{\Delta\delta Z_l}{\delta Z_l} = \frac{\tau_A}{\tau_l} \ll 1.$$

In order to transfer energy to the next scale, many collisions are needed via a diffusive process,

$$\tau_d \sim \left(\frac{\delta Z_l}{\Delta\delta Z_l}\right)^2 \tau_A = \frac{\tau_l^2}{\tau_A} = \frac{lV_A}{(\delta Z_l)^2},$$

which leads to the energy cascade flux,

$$\mathcal{E} \sim \frac{S_l}{\tau_d} \sim \frac{(\delta Z_l)^4}{lV_A} \sim \frac{k\,(\delta Z_l)^4}{V_A},$$

or

$$(\delta Z_l)^2 \sim \mathcal{E}^{1/2} V_A^{1/2} k^{-1/2}.$$

Using this, we have energy spectrum by the IK theory,

$$S_k(\mathrm{IK}) \sim \frac{S_l}{k} \sim \frac{(\delta Z_l)^2}{k} \sim \mathcal{E}^{1/2} V_A^{1/2} k^{-3/2}. \tag{697}$$

The spectral indexes are noticeably different from Kolmogorov theory.

The Goldreich-Sridhar (GS) theory also assumes a large-scale, strong background magnetic field, $\boldsymbol{B}_0$, but takes the note that the turbulence should be anisotropic with wavenumber perpendicular to $\boldsymbol{B}_0$ much larger than its parallel counterpart, $k_\perp \gg k_\parallel$. In the limit of large $\boldsymbol{B}_0$, turbulence should become essentially 2D. This is in contrast to IK and Kolmogorov theories, both of which assume isotropic turbulence.

To appreciate the development of spectral anisotropy, we begin with the so-called weak turbulence regime where turbulence is generated by interactions of waves propagating in the opposite directions $\boldsymbol{Z}_k^{\pm}$ along $\boldsymbol{B}_0$ but with wave frequency, $\omega = \pm k_\parallel V_A$, is unchanged. The three wave interaction needs to satisfy

$$\boldsymbol{k}_3 = \boldsymbol{k}_1 + \boldsymbol{k}_2 \tag{698}$$

$$\omega_3 = \omega_1 + \omega_2 \tag{699}$$

where wave 1 and 2 are parent waves while wave 3 is daughter wave. Focusing on the relations for parallel wavenumbers, they need to simultaneously satisfy

$$k_{\parallel 3} = k_{\parallel 1} + k_{\parallel 2} \tag{700}$$

$$\pm k_{\parallel 3} = k_{\parallel 1} - k_{\parallel 2} \tag{701}$$

where the first equation comes from the parallel component of Eq. (698) while the second equation takes into account of counter-propagating parent waves from Eq. (699). The only solutions for Eqs. (700) and (701) are $k_{\parallel 1} = 0$ or $k_{\parallel 2} = 0$, and thus, $k_{\parallel 3}$ cannot increase beyond $k_{\parallel 1}$ and $k_{\parallel 2}$, i.e., cascade does not occur in the parallel direction. In contrast, the perpendicular wavenumber of daughter waves can freely increase as in hydrodynamic turbulence, leading to the rapid development of turbulence anisotropy.

The above discussion, however, does not apply to strong turbulence in which interactions are not wave-like. Nonetheless, anisotropic nature of MHD turbulence with a strong $\boldsymbol{B}_0$ can still persist. This can be intuitively understood as in the following. Consider an eddy with perpendicular scale of $l_\perp$ and parallel scale of $l_\parallel$. The eddy turnover time in the perpendicular direction is given by $\tau_{l_\perp} \sim l_\perp / \delta Z_{l_\perp}$ during which the eddy's influence propagates along $\boldsymbol{B}_0$ with V_A. Therefore, $l_\parallel$ should be determined by

$$l_\parallel \sim V_A \tau_{l_\perp} = \frac{V_A l_\perp}{\delta Z_{l_\perp}}, \tag{702}$$

or

$$\frac{l_\parallel}{V_A} = \frac{l_\perp}{\delta Z_{l_\perp}} \tag{703}$$

which states that Alfvénic transit time over $l_\parallel$ is equal to eddy turnover time over $l_\perp$ in the perpendicular direction. This is often referred to as "critical balance" assumption (Goldreich and Sridhar, 1995). This assumption naturally leads to anisotropy with respect to $\boldsymbol{B}_0$, since the eddy's aspect ratio from the above equations is

$$\frac{l_\parallel}{l_\perp} = \frac{V_A}{\delta Z_{l_\perp}} \tag{704}$$

where V_A is more or less a constant decided by B_0 while turbulent velocity $\delta Z_{l_\perp}$ is a function of the perpendicular scale $l_\perp$ which typically gets weaker at smaller scales. Therefore, eddies get progressively more anisotropic – elongated along the large-scale magnetic field – at smaller scales. In contrast, in IK or Kolmogorov theories, the velocity along the parallel direction is the same as in the perpendicular direction, and thus, they assume isotropy.

In the GS theory, the energy cascade mainly takes place in the perpendicular direction and its flux is given the same way as Kolmogorov, c.f., Eq. (685),

$$\mathcal{E} \sim \frac{S_{l_\perp}}{\tau_{l_\perp}} \sim \frac{(\delta Z_{l_\perp})^3}{l_\perp} \tag{705}$$

which leads to the same spectrum but only in the perpendicular direction,

$$S_{\perp k}(\mathrm{GS}) \sim \mathcal{E}^{2/3} k_\perp^{-5/3}. \tag{706}$$

The parallel spectrum is determined by the perpendicular spectrum since

$$l_\parallel \sim \frac{V_A l_\perp}{\delta Z_{l_\perp}} \sim \frac{V_A l_\perp^{2/3}}{\mathcal{E}^{1/3}}, \tag{707}$$

where Eq. (705) is used. This can be rewritten as

$$l_\perp \sim \frac{l_\parallel^{3/2}\mathcal{E}^{1/2}}{V_A^{3/2}}, \tag{708}$$

which can be substituted to Eq. (706) yields the parallel spectrum,

$$S_{\parallel k}(\mathrm{GS}) \sim \mathcal{E}^{3/2} V_A^{-5/2} k_\parallel^{-5/2} \tag{709}$$

Note that $k_\parallel \sim l_\parallel^{-1}$ and $k_\perp \sim l_\perp^{-1}$, respectively. Indeed, the parallel spectrum steepens faster than the perpendicular spectrum progressively at larger k or smaller scales, as expected from the previous discussion.

12.2.5 Final Remarks on Turbulence

Turbulence is an important but complicated subject, so is the MHD turbulence. Only a small subset of its contents have been discussed by this introductory lecture. There are so much to be learned and researched. For example, a finite global rotation will introduce another direction of potential anisotropy, so does stratification which arises in compressible plasmas under gravity. Boundary conditions can be influential as well, as we learned before, especially in the laboratory settings. Any combinations of these effects can certainly lead to new and surprising results. As a fundamental aspect of plasma physics, here we aim to seek its university, but we should not forget that turbulence forms a core topic by itself in non-equilibrium thermodynamics which was briefly discussed at the beginning of this Lecture. Therefore, understanding universal physics of MHD turbulence can potentially contribute to our knowledge in broader non-equilibrium thermodynamics.

We would like to end of this Lecture by listing a few motivating observational evidence of turbulence in plasmas. The first two figures in Fig. 102 show turbulence results from solar wind measurements which indeed exhibit the desired power-law dependence of energy spectra. Both of them show a power-law indexes of ~ -1.6, which is indeed close to $-5/3$ (predicted by Kolmogorov and IK theories), but it is not too far from $-3/2$ (predicted by GS theory). A subtle but important technical difficulty should be recognized that measuring parallel energy spectra is hard in reality – both because precise determination of the direction of large-scale magnetic field using *in-situ* data is nontrivial and also anisotropic turbulence will be dominated by perpendicular spectra which have much larger power and can mask the information on parallel fluctuations.

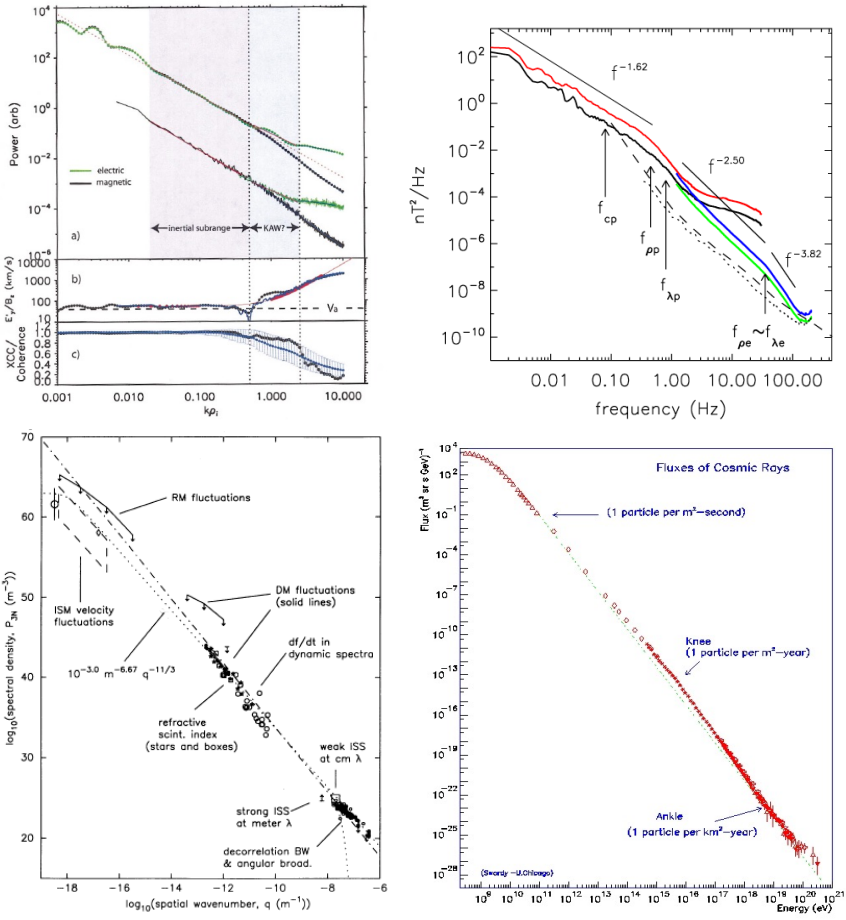

Fig. 102 (top left) Measurements of electric field (green) and magnetic field (black) in solar wind turbulence. Dotted and solid lines are -5/3 power law lines. From Bale et al (2005). (top right) Measurements of parallel (black) and perpendicular (red) magnetic field in solar wind turbulence. From (Sahraoui et al, 2009). (bottom left) Measurements of electron density fluctuations in local interstellar medium. From (Armstrong et al, 1995). (bottom right) Cosmic ray flux as a function of particle energy. Credit: Simon Swordy from University of Chicago.

The last two figures in Fig. 102 display astrophysical measurements on electron density fluctuations in interstellar medium and cosmic ray flux. Both exhibit striking power law dependence over many more decades. The former is certainly very close to the predicted index of $-5/3$, and can be regarded as an extended version of Fig. 100 in supporting Kolmogorov's $-5/3$ law. The latter figure on cosmic ray flux as a function of their energy exhibits another power law, which can be regarded as a by-product of turbulence, but a subtlety is that collisionless shocks (Lecture 4) and magnetic reconnection (Lecture 10) can also contribute to generation of energetic particles with power-law

dependence. Multiscale magnetic reconnection, sometime termed as "turbulent reconnection", as discussed towards end of Lecture 10, has merged recently as another potentially important contributor to particle acceleration in the Universe (Ji et al, 2022).

12.3 Summary

- Self-organization is an important topical area in non-equilibrium thermodynamics which is still in its development.
- Magnetic helicity, conserved in ideal MHD, quantifies how much field lines are inter-knotted or inter-linked with itself, but its definition needs care due to the gauge-invariant requirement.
- RFP configuration is explained as a force-free field of a minimum energy state by Taylor's relaxation theory while conserving magnetic helicity.
- The force-free states are stable according to energy principle, consistent with being minimum energy states.
- RFP in realty exhibits repeated sawtooth cycles due to gradual deviation from force-free states followed by rapid relaxation events, termed magnetic self-organization.
- Hydrodynamic turbulence is still an unsolved problem especially on its effects on large-scale flows, but many of its energy spectra are explained by Kolmogorov's -5/3 law based on turbulent cascade.
- Effects due to large-scale field are important in MHD turbulence which can be conveniently treated by Elsässer fields, especially on counter-propagating Alfvén waves.
- Iroshnikov-Kraichnan theory for istropic turbulence and Goldreich-Sridhar theory for anisotropic turbulence are two leading and competing theories, each with supporting evidence.

12.4 Further Readings

- Chapter 12 in Kundu et al (2015).
- Chapter 5 in Biskamp (2003).

12.5 Homework Problem Set 11-12

1. Minimum energy states.
   (a) Incompressible MHD equations are given by

$$\rho\left(\frac{\partial}{\partial t}+\boldsymbol{V}\cdot\boldsymbol{\nabla}\right)\boldsymbol{V} = -\boldsymbol{\nabla}p+\boldsymbol{j}\times\boldsymbol{B}+\nu\nabla^2\boldsymbol{V} \tag{710}$$

$$\frac{\partial\boldsymbol{B}}{\partial t} = \boldsymbol{\nabla}\times(\boldsymbol{V}\times\boldsymbol{B})+\frac{\eta}{\mu_0}\nabla^2\boldsymbol{B} \tag{711}$$

$$\boldsymbol{\nabla}\cdot\boldsymbol{V} = 0 \tag{712}$$

$$\boldsymbol{\nabla}\cdot\boldsymbol{B} = 0 \tag{713}$$

where ρ, η and ν are constants. Dot $\boldsymbol{V}$ to Eq.(710) and $\boldsymbol{B}/\mu_0$ to Eq.(711), then add them together to derive the decay rate of total energy decay $E = (1/2)\int(\rho V^2 + B^2/\mu_0)dV$,

$$\frac{dE}{dt} = -\eta \int j^2 dV - \nu \int \omega^2 dV \tag{714}$$

where surface terms are ignored and $\boldsymbol{\omega} = \boldsymbol{\nabla} \times \boldsymbol{V}$.

(b) Repeat the same procedure with dotting Eq.(710) with $\boldsymbol{B}/\sqrt{\mu_0\rho}$ and Eq.(711) with $\sqrt{\rho/\mu_0}\boldsymbol{V}$ to yield the decay rate of total cross helicity $K = \sqrt{\rho/\mu_0}\int \boldsymbol{V}\cdot\boldsymbol{B}dV$,

$$\frac{dK}{dt} = -\sqrt{\mu_0\rho}\left(\frac{\eta}{\mu_0} + \frac{\nu}{\rho}\right)\int \boldsymbol{j}\cdot\boldsymbol{\omega}dV, \tag{715}$$

where the surface terms are ignored.

(c) Derive the decay rate of total magnetic helicity $H = \int \boldsymbol{A}\cdot\boldsymbol{B}dV$,

$$\frac{dH}{dt} = -2\eta \int \boldsymbol{j}\cdot\boldsymbol{B}dV, \tag{716}$$

where the surface terms are ignored and $\boldsymbol{A}$ is the vector potential.

(d) Find minimum energy states by using the variational principle, based on the assumption that K and H decay slower than E. Discuss the physical implications of your results.

2. Alfvénic turbulence.

Studies of Alfvénic turbulence, which is of great interest in astrophysical and space plasmas, often begin from the incompressible visco-resistive MHD equations (that is, the MHD equations including viscosity and resistivity).

(a) Define the Elsässer variables $\boldsymbol{Z}^{\pm} = \boldsymbol{V} \pm \boldsymbol{B}/\sqrt{\mu_0\rho_0}$ and obtain the equations governing the time-evolution of these variables.

(b) Assume a uniform background magnetic field $\boldsymbol{B} = B_0\hat{\boldsymbol{z}}$ in a homogeneous plasma. Show that an arbitrary, uni-directional Alfvén wave is an exact solution of the nonlinear ideal MHD equations.

References

Al-Karkhy A, Browning PK, Cunningham G, et al (1993) Observations of the magnetohydrodynamic dynamo effect in a spheromak plasma. Phys Rev Lett 70(12):1814–1817. https://doi.org/10.1103/PhysRevLett.70.1814

Alt A (2022) Laboratory study of the stability of solar-relevant, arched, line-tied magnetic flux ropes. PhD thesis, Princeton University

Alt A, Myers CE, Ji H, et al (2021) Laboratory Study of the Torus Instability Threshold in Solar-relevant, Line-tied Magnetic Flux Ropes. Astrophys J 908(1):41

Andereck C, Liu S, Swinney H (1986) Flow regimes in a circular couette system with independently rotating cylinders. J Fluid Mech 164:155

Anderson JE (1963) Magnetohydrodynamic shock waves. MIT Press, Cambridge, MA

Armstrong JW, Rickett BJ, Spangler SR (1995) Electron Density Power Spectrum in the Local Interstellar Medium. Astrophys J 443:209. https://doi.org/10.1086/175515

Balbus S (2009) Magnetorotational instability. Scholarpedia 4:2409. https://doi.org/10.4249/scholarpedia.2409

Balbus S, Hawley J (1991) A powerful local shear instability in weakly magnetized disks. i - linear analysis. Astrophys J 376:214–222

Balbus SA, Hawley JF, Stone JM (1996) Nonlinear stability, hydrodynamical turbulence, and transport in disks. Astrophys J 467:76–86

Bale SD, Kellogg PJ, Mozer FS, et al (2005) Measurement of the Electric Fluctuation Spectrum of Magnetohydrodynamic Turbulence. Physical Review Letters 94(21):215002. https://doi.org/10.1103/PhysRevLett.94.215002

Bateman G (1978) MHD instabilities. Cambridge University Press, Cambridge, UK

Beck R (2000) Magnetic fields in normal galaxies. Philosophical Transactions of the Royal Society of London Series A: Mathematical, Physical and Engineering Sciences 358(1767):777–796. https://doi.org/10.1098/rsta.2000.0558

Berger MA, Field GB (1984) The topological properties of magnetic helicity. Journal of Fluid Mechanics 147:133–148. https://doi.org/10.1017/S0022112084002019

Bernstein IB, Frieman EA, Kruskal MD, et al (1958) An Energy Principle for Hydromagnetic Stability Problems. Proceedings of the Royal Society of London Series A 244(1236):17–40

Bhattacharjee A, Huang Y, Yang H, et al (2009) Fast reconnection in high-lundquist-number plasmas due to the plasmoid instability. Phys Plasmas 16:112,102

Biermann L (1950) Über den Ursprung der Magnetfelder auf Sternen und im interstellaren Raum (miteinem Anhang von A. Schlüter). Zeitschrift Naturforschung Teil A 5:65

Biglari H, Diamond PH, Terry PW (1990) Influence of sheared poloidal rotation on edge turbulence. Physics of Fluids B 2(1):1–4. https://doi.org/10.1063/1.859529

Birn J, Drake J, Shay M, et al (2001) Geomagnetic Environmental Modeling (GEM) Magnetic Reconnection Challenge. Journal of Geophysical Research 106(A3):3715. https://doi.org/10.1029/1999JA900449

Biskamp D (1986) Magnetic reconnection via current sheet. Physics of Fluids 29:1520

Biskamp D (2003) Magnetohydrodynamic Turbulence. Cambridge University Press

Braginskii S (1965) Transport processes in a plasma. Rev Plasma Phys 1:205

Bulanov SV, Pegoraro F, Sakharov AS (1992) Magnetic reconnection in electron magnetohydrodynamics. Physics of Fluids B 4(8):2499–2508. https://doi.org/10.1063/1.860467

Cai HJ, Lee LC (1997) The generalized Ohm's law in collisionless magnetic reconnection. Physics of Plasmas 4:509. https://doi.org/10.1063/1.872178

Chandrasekhar S (1960) The stability of non-dissipative couette flow in hydromagnetics. Proc Nat Acad Sci 46:253–257

Chandrasekhar S (1961) Hydrodynamic and Hydromagnetic Stability. Oxford University Press.

Connor JW, Hastie RJ, Taylor JB (1979) High mode number stability of an axisymmetric toroidal plasma. Proc R Soc Lond A 365:1–17

Coppi BM, Galvao R, Pellat R, et al (1976) Resistive kink modes. Sov J Plasma Phys 2:533

Cowling TG (1934) The stability of gaseous stars. Mon Not R Astron S 94:768–782. https://doi.org/10.1093/mnras/94.8.768

Daughton W, Scudder J, Karimabadi H (2006) Fully kinetic simulations of undriven magnetic reconnection with open boundary conditions. Phys Plasmas 13:072,101

Daughton W, Roytershteyn V, Albright B, et al (2009) Transition form collisional to kinetic reconnection in large-scale plasmas. Phys Rev Lett 103:065,004

Davidson RC (2001) Physics of Nonneutral Plasmas. Imperial College Press, London

Donnelly RJ, Ozima M (1962) Experiments on the stability of flow between rotating cylinders in the presence of magnetic field. Proc R Soc Lond A 266:272–286

Drake J, Shay M (2007) Fundamentals of collisionless reconnection. In: Birn J, Priest ER (eds) Reconnection of magnetic fields : magnetohydrodynamics and collisionless theory and observations. Cambridge University Press, Cambridge, UK, p 87

Dupree T (1963) Kinetic theory of plasma and the electromagnetic field. Phys Fluids 6:1714. https://doi.org/10.1063/1.1711014

Elsasser WM (1950) The Hydromagnetic Equations. Physical Review 79(1):183–183. https://doi.org/10.1103/PhysRev.79.183

Fox W, Sciortino F, von Stechow A, et al (2017) Experimental verification of the role of electron pressure in fast magnetic reconnection with a guide field. Physical Review Letters 118:125,002. https://doi.org/10.1103/PhysRevLett.118.125002

Freidberg JP (2014) Ideal MHD. Cambridge University Press, Cambridge, UK

Furth H, Killeen J, Rosenbluth M (1963) Finite-resistivity instabilities of a sheet pinch. Physics of Fluids 6:459

Gailitis A, Lielausis O, Platacis E, et al (2001) Magnetic Field Saturation in the Riga Dynamo Experiment. Phys Rev Lett 86(14):3024–3027. https://doi.org/10.1103/PhysRevLett.86.3024

Giovanelli R (1946) A theory of chromospheric flares. Nature 158:81

Goedbloed H, Poedts S (2004) Principles of Magnetohydrodynamics. Cambridge University Press, Cambridge, UK

Gold T, Hoyle F (1960) On the origin of solar flares. Mon Not R Astron S 120:89

Goldreich P, Sridhar S (1995) Toward a Theory of Interstellar Turbulence. II. Strong Alfvenic Turbulence. Astrophys J 438:763. https://doi.org/10.1086/175121

Goldstein S (1969) Fluid Mechanics in the First Half of this Century. Annual Review of Fluid Mechanics 1:1–29

Goldston R, Rutherford P (1995) Introduction to Plasma Physics. Institute of Physics Publishing, Bristol and Philadelphia

Grant HL, Moilliet A, Stewart RW (1959) A Spectrum of Turbulence at Very High Reynolds Number. Nature 184:808–810. https://doi.org/10.1038/184808b0

Gurnett DA, Bhattacharjee A (2017) Introduction to Plasma Physics. Cambridge University Press, Cambridge, UK

Hain K, Lüst R (1958) Zur Stabilität zylindersymmetrischer Plasmakonfigurationen mit Volumenströmen. Zeitschrift Naturforschung Teil A 13(11):936–940

Hain K, Lüst R, Schlüter A (1957) Zur Stabilität eines Plasmas. Zeitschrift Naturforschung Teil A 12(10):833–841

Heidbrink W (2002) Alpha particle physics in a tokamak burning plasma experiment. Physics of Plasmas 9:2113

Huang YM, Comisso L, Bhattacharjee A (2017) Plasmoid instability in evolving current sheets and onset of fast reconnection. The Astrophysical Journal 849:75. https://doi.org/10.3847/1538-4357/aa906d

Hung DMH, Blackman EG, Caspary KJ, et al (2019) Experimental confirmation of the standard magnetorotational instability mechanism with a spring-mass analogue. Communications Physics 2:7

Iroshnikov PS (1964) Turbulence of a Conducting Fluid in a Strong Magnetic Field. Soviet Astronomy 7:566

Ji H (1999) Turbulent Dynamos and Magnetic Helicity. Phys Rev Lett 83(16):3198–3201. https://doi.org/10.1103/PhysRevLett.83.3198

Ji H, Daughton W (2011) Phase diagram for magnetic reconnection in heliophysical, astrophysical, and laboratory plasmas. Phys Plasmas 18(11):111207. https://doi.org/10.1063/1.3647505

Ji H, Daughton W (2022) Preface for frontiers of magnetic reconnection research in heliophysical, astrophysical, and laboratory plasmas. Physics of Plasmas 29(7):070,401. https://doi.org/10.1063/5.0104925

Ji H, Goodman J (2023) Taylor–couette flow for astrophysical purposes. Phil Trans R Soc A 381:20220,119. https://doi.org/https://doi.org/10.1098/rsta.2022.0119

Ji H, Prager SC (2002) The α dynamo effects in laboratory plasmas. Magnetohydrodynamics 38:191–210. https://doi.org/10.22364/mhd.38.1-2.15, https://arxiv.org/abs/astro-ph/0110352 [astro-ph]

Ji H, Almagri AF, Prager SC, et al (1994) Time-resolved observation of discrete and continuous magnetohydrodynamic dynamo in the reversed-field pinch edge. Phys Rev Lett 73(5):668–671. https://doi.org/10.1103/PhysRevLett.73.668

Ji H, Prager SC, Sarff JS (1995) Conservation of Magnetic Helicity during Plasma Relaxation. Phys Rev Lett 74(15):2945–2948. https://doi.org/10.1103/PhysRevLett.74.2945

Ji H, Yamada M, Hsu S, et al (1998) Experimental test of the sweet-parker model of magnetic reconnection. Physical Review Letters 80:3256. https://doi.org/10.1103/PhysRevLett.80.3256

Ji H, Goodman J, Kageyama A (2001) Magnetorotational instability in a rotating liquid metal annulus. Mon Not R Astron Soc 325:L1–L5

Ji H, Burin M, Schartman E, et al (2006) Hydrodynamic turbulence cannot transport angular momentum effectively in astrophysical disks. Nature 444:343–346

Ji H, Cutler R, Gettelfinger G, et al (2018) The FLARE Device and Its First Plasma Operation. In: APS Meeting Abstracts, p CP11.020

Ji H, Alt A, Antiochos S, et al (2020) Major scientific challenges and opportunities in understanding magnetic reconnection and related explosive phenomena throughout the universe. 2004.00079

Ji H, Daughton W, Jara-Almonte J, et al (2022) Magnetic reconnection in the era of exascale computing and multiscale experiments. Nat Rev Phys 4:263–282. https://doi.org/10.1038/s42254-021-00419-x

Ji H, Yoo J, Fox W, et al (2023) Laboratory Study of Collisionless Magnetic Reconnection. Space Science Reviews 219:76. https://doi.org/10.1007/s11214-023-01024-3

Johnson JL, Oberman CR, Kulsrud RM, et al (1958) Some Stable Hydromagnetic Equilibria. Physics of Fluids 1(4):281–296

Kivelson MG, Russell CT (1995) Introduction to Space Physics. Cambridge University Press, Cambridge, UK

Kleva R, Drake J, Waelbroeck F (1995) Fast reconnection in high temperature plasmas. Physics of Plasmas 2:23. https://doi.org/10.1063/1.871095

Kliem B, Török T (2006) Torus instability. Phys Rev Lett 96:255,002

Klimontovich YL (1967) The Statistical Theory of Non-Equilibrium Processes in a Plasma. MIT, Cambridge, Mass.

Kolmogorov A (1941) The Local Structure of Turbulence in Incompressible Viscous Fluid for Very Large Reynolds' Numbers. Akademiia Nauk SSSR Doklady 30:301–305

Kraichnan RH (1965) Inertial-Range Spectrum of Hydromagnetic Turbulence. Physics of Fluids 8(7):1385–1387. https://doi.org/10.1063/1.1761412

Krall NA, Trivelpiece AW (1973) Principles of plasma physics. McGraw-Hill, New York

Kruskal M, Schwarzschild M (1954) Some Instabilities of a Completely Ionized Plasma. Proceedings of the Royal Society of London Series A 223(1154):348–360

Kulsrud RM (2005) Plasma physics for astrophysics. Princeton University Press, Princeton

Kulsrud RM, Anderson SW (1992) The Spectrum of Random Magnetic Fields in the Mean Field Dynamo Theory of the Galactic Magnetic Field. Astrophys J 396:606. https://doi.org/10.1086/171743

Kundu P, Cohen I, Dowling D (2015) Fluid Mechanics, 6th Ed. Academic Press, New York, originally published in 1990

Landau LD, Lifshitz EM (1960) Electrodynamics of continuous media. Pergamon Press, Oxford, UK

Laval G, Mercier C, Pellat R (1965) Necessity of the energy principles for magnetostatic stability. Nuclear Fusion 5(2):156

Liu YH, Cassak P, Li X, et al (2022) First-principles theory of the rate of magnetic reconnection in magnetospheric and solar plasmas. Communications Physics 5. https://doi.org/10.1038/s42005-022-00854-x

Loureiro NF, Cowley SC, Dorland WD, et al (2005) X-point collapse and saturation in the nonlinear tearing mode reconnection. Physical Review Letters 95. https://doi.org/10.1103/PhysRevLett.95.235003

Loureiro NF, Schekochihin AA, College K, et al (2007) Instability of current sheets and formation of plasmoid chains. Physics of Plasmas 14. https://doi.org/10.1063/1.2783986

Lueptow R, Hollerbach R, Serre E (2023a) Taylor–couette and related flows on the centennial of taylor's seminal philosophical transactions paper: part 1. Phil Trans R Soc A 381:20220,140. https://doi.org/https://doi.org/10.1098/rsta.2022.0140

Lueptow R, Hollerbach R, Serre E (2023b) Taylor–couette and related flows on the centennial of taylor's seminal philosophical transactions paper: part 2. Phil Trans R Soc A 381:20220,359. https://doi.org/https://doi.org/10.1098/rsta.2022.0359

Mallen KJ, Montgomery MT (2005) Reexamining the near-core radial structure of the tropical cyclone primary circulation: Implications for vortex resiliency. JOURNAL OF THE ATMOSPHERIC SCIENCES 62:408

Mestel L, Spitzer JL. (1956) Star Formation in Magnetic Dust Clouds. Monthly Notices of the Royal Astronomical Society 116(5):503–514. https://doi.org/10.1093/mnras/116.5.503

Miyamoto K (2016) Plasma Physics for Controlled Fusion, 2nd Ed. Springer-Verlag, Berlin Heidelberg

Monchaux R, Berhanu M, Bourgoin M, et al (2007) Generation of a magnetic field by dynamo action in a turbulent flow of liquid sodium. Physical Review Letters 98. https://doi.org/10.1103/PhysRevLett.98.044502

Moody L (1944) Friction factors for pipe flow. Transactions of the ASME 66:671 – 684

Mozer FS, Bale S, Phan TD (2002) Evidence of diffusion regions at a subsolar magnetopause crossing. Physical Review Letters 89:015,002. https://doi.org/10.1103/PhysRevLett.89.015002

Müller U, Bühler L (2001) Magnetofluiddynamics in Channels and Containers. Springer-Verlag, Berlin Heidelberg New York

Myers C (2015) Laboratory study of the equilibrium and eruption of line-tied magnetic flux ropes in the solar corona. PhD thesis, Princeton University

Myers CE, Yamada M, Ji H, et al (2015) A dynamic magnetic tension force as the cause of failed solar eruptions. Nature 528(7583):526–529

Nilson PM, Willingale L, Kaluza MC, et al (2006) Magnetic Reconnection and Plasma Dynamics in Two-Beam Laser-Solid Interactions. Physical Review Letters 97(25):255001

Øieroset M, Phan TD, Haggerty C, et al (2016) MMS observations of large guide field symmetric reconnection between colliding reconnection jets at the center of a magnetic flux rope at the magnetopause. Geophysical Research Letters 43(1):5536–5544. https://doi.org/10.1002/2016GL069166

Papadopoulos K (1977) A review of anomalous resistivity for the ionosphere. Reviews of Geophysics and Space Physics 15:113. https://doi.org/10.1029/RG015i001p00113

Parker EN (1955) Hydromagnetic Dynamo Models. Astrophys J 122:293. https://doi.org/10.1086/146087

Parker EN (1957) Sweet's mechanism for merging magnetic fields in conducting fluids. J Geophys Res 62(4):509–520

Parker EN (1958) Dynamics of the Interplanetary Gas and Magnetic Fields. Astrophys J 128:664. https://doi.org/10.1086/146579

Parker EN (1966) The Dynamical State of the Interstellar Gas and Field. Astrophys J 145:811

Parker EN (1967) The Dynamical State of the Interstellar Gas and Field. III. Turbulence and Enhanced Diffusion. Astrophys J 149:535

Parker EN (1970) The Generation of Magnetic Fields in Astrophysical Bodies. I. The Dynamo Equations. Astrophys J 162:665. https://doi.org/10.1086/150697

Petschek H (1964) Magnetic field annhilation. NASA Spec Pub 50:425

Phan TD, Eastwood JP, Shay MA, et al (2018) Electron magnetic reconnection without ion coupling in Earth's turbulent magnetosheath. Nature 557(7):202–206

Ponomarenko YB (1973) Theory of the hydromagnetic generator. Journal of Applied Mechanics and Technical Physics 14(6):775–778. https://doi.org/10.1007/BF00853190

Prager SC, Adney J, Almagri A, et al (2005) Overview of results in the MST reversed field pinch experiment. Nucl Fusion 45:276–+

Pucci F, Velli M (2014) Reconnection of quasi-singular current sheets: The "ideal" tearing mode. Astrophysical Journal Letters 780. https://doi.org/10.1088/2041-8205/780/2/L19

Rayleigh L (1916) On the dynamics of rotating fluid. Proc R Soc Lond A 93:148–154

Ren Y, Yamada M, Gerhardt S, et al (2005) Experimental Verification of the Hall Effect during Magnetic Reconnection in a Laboratory Plasma. Physical Review Letters 95(5):055,003. https://doi.org/10.1103/PhysRevLett.95.055003

Reynolds O (1883) An experimental investigation of the circumstances which determine whether the motion of water shall be direct or sinuous, and of the law of resistance in parallel channels. Phil Trans Roy Soc 174:935–982

Richardson LF (1922) Weather prediction by numerical process. University Press

Roberts PH (1994) Fundamentals of Dynamo Theory. In: Lectures on Solar and Planetary Dynamos, p 1

Rust DM, Kumar A (1996) Evidence for helically kinked magnetic flux ropes in solar eruptions. Astrophys J Lett 464:L199

Rutherford PH (1973) Nonlinear growth of the tearing mode. Physics of Fluids 16:1903–1908. https://doi.org/10.1063/1.1694232

Sahraoui F, Goldstein ML, Robert P, et al (2009) Evidence of a Cascade and Dissipation of Solar-Wind Turbulence at the Electron Gyroscale. Physical Review Letters 102(23):231102. https://doi.org/10.1103/PhysRevLett.102.231102

Sakurai T (1976) Magnetohydrodynamic interpretation of the motion of prominences. Publications of Astronomical Society of Japan 28(2):177–198

Samtaney R, Loureiro N, Uzdensky D, et al (2009) Formation of plasmoid chains in magnetic reconnection. Physical Review Letters 103(10):105,004

Schwarzschild K (1906) On the equilibrium of the Sun's atmosphere. Nachrichten von der Königlichen Gesellschaft der Wissenschaften zu Göttingen Math-phys Klasse 195:41–53

Shafranov V (1956) The stability of a cylindrical gaseous conductor in a magnetic field. The Soviet Journal of Atomic Energy 1:709

Shafranov V (1966) Plasma Equilibrium in a Magnetic Field. Reviews of Plasma Physics 2:103

Shakura N, Sunyaev R (1973) Black holes in binary systems. observational appearance. Astron Astrophys 24:337–355

Shibata K, Tanuma S (2001) Plasmoid-induced-reconnection and fractal reconnection. Earth Planets Space 53:473

Shumlak U, Hartman CW (1995) Sheared flow stabilization of the m = 1 kink mode in z pinches. Physical Review Letters 75:3285

Snyder PB, Wilson HR, Xu XQ (2005) Progress in the peeling-ballooning model of edge localized modes: Numerical studies of nonlinear dynamicsa). Physics of Plasmas 12(5):056115

Solov'ev L (1968) The Theory of Hydromagnetic Stability of Toroidal Plasma Configurations. Sov Phys JETP 26:400

Spong D, Sanchez R, Weller A (2005) Shear Alfvén continua in stellarators. Physics of Plasmas 10:3217

Sridhar S, Goldreich P (1994) Toward a Theory of Interstellar Turbulence. I. Weak Alfvenic Turbulence. Astrophys J 432:612. https://doi.org/10.1086/174600

Steenbeck M, Krause F, Rädler KH (1966) Berechnung der mittleren LORENTZ-Feldstärke $\boldsymbol{v} \times \boldsymbol{B}$ für ein elektrisch leitendes Medium in turbulenter, durch CORIOLIS-Kräfte beeinflußter Bewegung. Zeitschrift Naturforschung Teil A 21:369. https://doi.org/10.1515/zna-1966-0401

Sweet PA (1958) The neutral point theory of solar flares. In: IAU Symp. in Electromagnetic Phenomena in Cosmical Physics, ed. B. Lehnet (New York: Cambridge Univ. Press), p 123

Taylor G (1923) Stability of a viscous liquid contained between two rotating cylinders. Philos Trans R Soc Lond A 223:289–343

Taylor JB (1974) Relaxation of Toroidal Plasma and Generation of Reverse Magnetic Fields. Phys Rev Lett 33:1139–1141

Taylor JB (1986) Relaxation and magnetic reconnection in plasmas. Review of Modern Physics 58:741

Torbert RB, Burch JL, Phan TD, et al (2018) Electron-scale dynamics of the diffusion region during symmetric magnetic reconnection in space. Science 362(6421):1391–1395. https://doi.org/10.1126/science.aat2998

Vainshtein SI, Zel'dovich YB (1972) Origin of magnetic fields in astrophysics (turbulent "dynamo" mechanisms). Soviet Physics Uspekhi 15(2):159. https://doi.org/10.1070/PU1972v015n02ABEH004960

Vasyliunas V (1975) Theoretical models of field line merging, i. Rev Geophys Space Phys 13:303. https://doi.org/10.1029/RG013i001p00303

Velikhov EP (1959) Stability of an ideally conducting liquid flowing between cylinders rotating in a magnetic field. Sov Phys JETP 36:995–998

von Goeler S, Stodiek W, Sauthoff N (1974) Studies of Internal Disruptions and m=1 Oscillations in Tokamak Discharges with Soft-X-Ray Tecniques. Physical Review Letters 33:1201–1203

Waelbroeck FL (1989) Current sheets and nonlinear growth of the m=1 kink-tearing mode. Physics of Fluids B 1:2372–2380. https://doi.org/10.1063/1.859172

Waelbroeck FL (1993) Onset of the sawtooth crash. Physical Review Letters 70:3259–3262

Wang Y, Gilson E, Ebrahimi F, et al (2022) Observation of axisymmetric standard magnetorotational instability in the laboratory. Phys Rev Lett 129:115,001

Wesson J (2011) Tokamaks, 4th Ed. Oxford University Press, Oxford, UK

White R (2014) The Theory of Toroidally Confined Plasmas, Third Edition. Imperial College Press, London

Yamada M, Kulsrud R, Ji H (2010) Magnetic reconnection. Rev Mod Phys 82:603. https://doi.org/10.1103/RevModPhys.82.603

Zhang M, Flyer N, Low BC (2006) Magnetic field confinement in the corona: The role of magnetic helicity accumulation. The Astrophysical Journal 644(1):575. https://doi.org/10.1086/503353, URL https://dx.doi.org/10.1086/503353